UNIVERSITÉ DE GENÈVE

Département de physique

nucléaire et corpusculaire

IFIC (CSIC & Universitat de València)

FACULTÉ DES SCIENCES

Professeur A. Blondel

Docteur A. Cervera Villanueva

Extraction of kaon production cross-sections in HARP

THÈSE

présentée à la Faculté des sciences de l'Université de Genève

pour obtenir le grade de Docteur ès sciences, mention physique

par

Raphaël Schroeter

de Suisse, originaire de Eischoll (VS)

Thèse N° 4296

UNIVERSITÉ DE GENÈVE

FACULTÉ DES SCIENCES

Doctorat ès sciences
Mention physique

Thèse de *Monsieur Raphaël SCHROETER*

intitulée :

"Extraction of Kaon Production Cross-sections in HARP"

La Faculté des sciences, sur le préavis de Messieurs A. BLONDEL, professeur ordiniaire et directeur de thèse (Département de physique nucléaire et corpusculaire) A. CERVERA VILLANUEVA, docteur et codirecteur de thèse (Instituto de Física Corpuscular Universitat de Valencia, Consejo Superior de Investigaciones Científicas, Valencia, España), D. RAPIN, professeur titutlaire (Département de physique nucléaire et corpusculaire), J. J. GOMEZ CADENAS, professeur (Edificios Institutos de Investigación, Universitat de Valencia, España) et de Madame G. CATANESI (Istituto Nazionale Fisica Nucleare, Sezione di Bari, Italia), autorise l'impression de la présente thèse, sans exprimer d'opinion sur les propositions qui y sont énoncées.

Genève, le 10 mars 2011

Thèse - 4296 -

Le Doyen, Jean-Marc TRISCONE

N.B.- La thèse doit porter la déclaration précédente et remplir les conditions énumérées dans les "Informations relatives aux thèses de doctorat à l'Université de Genève".

Thesis advisors

Anselmo Cervera Villanueva, Alain Blondel

Author

Raphaël Schroeter

Extraction of kaon production cross-sections in HARP

Abstract

Precise measurements of secondary yields in hadron-nucleus collisions in the few GeV/c region are relevant to several areas of particle physics, particularly experimental neutrino physics. In particular, measurements made at HARP can have a direct impact on the detailed understanding of the neutrino fluxes of several accelerator-based neutrino experiments, including the K2K experiment in Japan and MiniBooNE and SciBooNE at Fermilab. HARP took data with these exact beam energies and target materials using both thin and thick targets.

Strange particle production in the forward direction must be well known when trying to determine the ν_e background in a ν_μ beam, since K_{e3} decays of $K^\pm$ and K_L^0 constitute an irreducible background in the search of the $\nu_\mu \to \nu_e$ oscillations. This applies particularly to experiments such as MiniBooNE where G4 simulations showed that kaon decays contribute to more than 40% of the total intrinsic ν_e background of the beam.

A complete analysis method has been developed to extract the total positive kaon differential production cross-sections from the 12.9GeV/c protons on aluminum target data set.

Résumé

Nous savons que les neutrinos sont massifs et oscillent grâce aux résultats d'environ dix expériences couvrant plus de deux décennies de recherche intense et mesurant des neutrinos produits dans le soleil, l'atmosphère, à partir de réacteurs nucléaires et de faisceaux artificiels.

Le but de l'expérience HARP est de mesurer des sections efficaces de production de hadrons produits dans l'interaction d'un faisceau de protons ou de pions de différentes énergies (1.5-15 GeV/c) dans des cibles de différents matériaux.

HARP couvre un angle solide le plus large possible en utilisant plusieurs combinaisons de détecteurs. Les grands angles sont couverts par une Chambre à Projection Temporelle dans laquelle sont disposées les cibles. La région à petits angles (vers l'avant), elle, est couverte par un spectromètre. L'expérience a étudié sept cibles de matériau solide pour couvrir l'intervalle de nombre atomique entre 4 et 82. Les cibles sélectionnées ont une épaisseur comprise entre 2% et 5% de la longueur d'interaction nucléaire pour minimiser l'effet de possibles ré-interactions dans la cible ou de distorsion des traces due à la diffusion multiple.

Parmi les cibles solides, HARP a mesuré les sections efficaces de production de hadrons produits dans les répliques des cibles employées dans les expériences K2K et Miniboone en utilisant un faisceau de protons réglé à l'énergie correspondante. L'utilisation de HARP comme expérience auxiliaire de mesure d'hadro-production est justifiée par le fait que la fraction la plus importante des neutrinos du faisceau est produite par la désintégration de pions positifs. L'évaluation précise du contenu en saveur du faisceau de neutrinos produit par K2K et MiniBooNE nécessite donc une mesure fiable et précise des sections efficaces différentielles de production des hadrons sur tout l'angle solide mesuré par HARP. Il n'est en effet pas possible de se fier entièrement aux simulations pour prédire les flux de neutrinos. Ces dernières fournissent des prédictions pouvant varier de 50 à 100% selon les modèles de production de hadrons utilisés.

La production de particules étranges vers l'avant (à petit angle) doit être bien comprise lorsqu'on veut quantifier le bruit de fond composé de ν_e dans un faisceau de ν_μ. En effet, la désintégration de type K_{e3} des $K^\pm$ et K_L^0 produit un bruit de fond irréductible dans le faisceau lorsque l'on mesure les oscillations $\nu_\mu \to \nu_e$. Ceci est particulièrement vrai

pour l'expérience MiniBooNE dont les simulations montrent que la désintégration des kaons contribue jusqu'à 40% du bruit de fond ν_e dans faisceau.

Le but de l'analyse présentée dans ce rapport de thèse est de mesurer la section efficace doublement différentielle, en p (impulsion) et θ (angle de production) des kaons positifs produits dans la collision de protons de 12.9 GeV/c d'impulsion sur une cible mince d'aluminium (5% de la longueur d'interaction nucléaire). La section efficace doublement différentielle normalisée donnée dans le référentiel du laboratoire pour un bin (p, θ) est donnée par:

$$\frac{\mathrm{d}^2\sigma^{K^+}}{\mathrm{d}p\,\mathrm{d}\Omega}(p,\theta) = \frac{1}{N_{\text{p.o.t.}}} \cdot \frac{A}{N_A\,\rho\,t} \cdot \frac{1}{\Delta p\,\Delta\Omega} \cdot N^{K^+}(p,\theta)$$

La partie principale de notre analyse repose sur une méthode d'identification des particules à partir des traces reconstruites par le spectromètre. Cette dernière nous permet de mesurer la production brute des pions, kaons et protons produits dans la cible. Pour cela, nous fitons les distributions de la vitesse β des particules avec un modèle complexe qui tient compte simultanément des pions, kaons et protons dans un bin d'énergie et d'angle reconstruits donné. La variable β est définie comme d/tc où d et t sont respectivement la longueur de la trace et le temps mesuré par le détecteur de temps de vol (TOF) entre le moment où la particule a été produite et le moment où elle a atteint le TOF. Le détecteur Cherenkov peut être utilisé pour rejeter les pions d'impulsion supérieure à 2.75 GeV/c des distributions β afin d'extraire de manière optimale le pic des kaons dans l'intervalle en impulsion où ce dernier se superpose avec le pic des pions. Cela à pour effet d'améliorer la fiabilité de l'algorithme de fit et de réduire l'incertitude sur le taux de kaons mesuré.

Plusieurs corrections sont appliquées dans notre analyse à différents niveaux. Certaines lors du remplissage des distributions β et d'autres directement sur la mesure de la production brute des particules. Les corrections sont classées en trois catégories: efficacité du signal, bruit de fond et migration de bin à bin entre les quantités reconstruites et finales. Les corrections sont fonctions soit de variables reconstruites ou finales et sont appliquées à des étapes spécifiques de l'analyse.

Nous modélisons le spectre β en combinant plusieurs fonctions de densité de probabilité (FDP) correspondant à chaque type de particule. La FDP générale tient compte de la résolution intrinsèque du TOF, de la résolution en impulsion du détecteur, de la largeur du bin en impulsion reconstruite et de la variation du taux de production des particules à l'intérieur d'un bin. Il est crucial de s'assurer de la stabilité et de la convergence de

l'algorithme de fit. Pour cela nous fixons par étape certains paramètres des FDP. Le nombre de particules mesuré dans un bin reconstruit (p', θ') est donné par l'intégrale de la FDP correspondante sur l'intervalle β.

Une étude complète des erreurs assignées aux mesures est présentée. Les incertitudes de type statistique et systématique provenant des différentes corrections ou paramètres de fit sont calculées à partir de méthodes analytiques ou basées sur le Monte Carlo. Ces incertitudes sont finalement combinées pour estimer la précision des mesures des sections efficaces obtenues.

Contents

List of Figures

List of Tables

Remerciements

pu choisir à chaque fois la page dans notre livre d'entrainement. Avec vous j'ai acquis une excellente force physique mais surtout la force mentale nécessaire pour terminer cette thèse. Rien ne sera jamais pareil sans vous à mes côtés dans la ligne d'eau. Et n'oubliez pas, 'Los vasos con hielo y limon'. Swim smooth!

Merci Juan José Gomez Cadenas. Il y a peu de personnes qui soient aussi passionnées que passionnantes. Tu en fais partie, sans aucun doute. Tu es une source d'inspiration infinie!

Un grand merci à vous tous qui m'entourez en dehors de ma vie professionnelle. Vous savez qui vous êtes. Jamais je n'aurais eu la force d'achever un travail de si grande envergure sans votre soutien inconditionnel et votre absolue confiance en moi. Vous êtes les personnes qui jamais n'avez douté un instant. Vous êtes les pierres angulaires de cette thèse car vous avez compris bien avant moi que la dimension de ce travail dépassait largement le seul monde de la physique. Merci infiniment, Suzy, Camille, Yiorgos. Et Priyanthi, ton souvenir continue de m'inspirer.

Finalement je tiens à remercier Anselmo Cervera Villanueva, mon co-directeur de thèse. Il n'y a pas de mots qui peuvent décrire l'importance de ton savoir, de ton aide, de ton support et de tes encouragements, jour après jour, durant toutes ces années de doctorat. C'est en grande partie grâce à toi que j'ai pu achever ce travail de thèse et je t'en suis infiniment reconnaissant.

Chapter 1

Neutrino Physics

In the Standard Model (SM), neutrinos were introduced as massless particles. However, it is more natural to expect them to be massive, since there is no symmetry principle or gauge invariance requiring neutrinos to have vanishing masses. Moreover, we know that all other fermions, quarks and charged leptons are massive. Oscillation experiments have proven in the last years that neutrinos have indeed a mass, and consequently it is a must to extend the SM to take this fact into account. It turns out that neutrinos are very light with respect to the other fermions, and this striking qualitative feature needs to be understood. Furthermore, the issue of the actual nature of neutrino mass also arises when extending the SM. Whereas the charged leptons are Dirac particles, distinct from their antiparticles, neutrinos may be the ultimate neutral fermions, as envisioned by Majorana, identical to their antiparticles. The see-saw mechanism is the most simple scenario explaining why neutrinos are so light, and it predicts Majorana neutrinos.

Along this chapter, we review the possible ways in which the SM can be modified or extended in order to accommodate massive neutrinos, leading to leptonic mixing and neutrino oscillation. We also discuss about the so-called Dirac or Majorana nature of the neutrinos. The phenomenology of massive neutrinos has been described in several works, although in the current document we mainly follow [1, 2].

1.1   Introduction

It was the process of nuclear beta decay which led Pauli to postulate the neutrino's existence. It was known that an element could change its place on the periodic table via the

emission of an electron

$$(A, Z) = (A, Z + 1) + e^-, \tag{1.1}$$

but a series of experiments showed that the electron is emitted with a continuous energy spectrum, which is inconsistent with a 2-body decay of a nucleon at rest. This implied non-conservation of energy and led Pauli to suggest a "desperate way out". He postulated that an unseen neutral particle was also being emitted in the decay and carrying away the missing energy. Many believed the electron and this new "neutron", as Pauli first called it, were part of the nucleus and were simply ejected in the process of beta decay.

In 1934, Enrico Fermi placed this new particle into his theoretical framework of the weak force [3] and gave it the name we use today, "neutrino". In Fermi's theory the interaction was assumed to occur at a single space-time point with the neutron emitting a proton, electron and neutrino (actually what we now know is the electron antineutrino):

$$n \to p + e^- + \overline{\nu}_e \tag{1.2}$$

and was formulated as a vector×vector current interaction based on analogy to electrodynamics. The approach enabled H. Bethe and R. Peierls to calculate the rate of the inverse process [4]:

$$\overline{\nu}_e + p \to n + e^+ \tag{1.3}$$

and suddenly a process by which to detect the neutrino was discovered. This is the approach F. Reines and C. Cowen used to detect electron antineutrinos produced at the Savannah River nuclear power reactor in South Carolina [5].

Soon afterward, a major breakthrough in the understanding of the weak force arrived when T.D. Lee and C.N. Yang suggested that the weak force may violate parity [6]. Then, in 1957, C.S. Wu et al. experimentally confirmed that parity is, in fact, maximally violated by weak interactions [7]. This led to the very successful (V-A) formulation of the weak interaction by R. Feynman and M. Gell-Mann as well as by E.C.G. Sudarshan and R.E. Marshak in 1958 [8, 9]. In the theory, the weak interaction is described by equal amounts of vector and axial vector coupling which effectively picks out the left-handed helicity component ($H \equiv \overrightarrow{p} \cdot \overrightarrow{S} / |\overrightarrow{p}|$ where $\overrightarrow{p}$ and $\overrightarrow{S}$ are the momentum and spin of the particle, respectively) of the massless neutrino and incorporates the observed parity violation.

Another surprise came in 1962 when L. Lederman, M. Schwartz, J. Steinberger and collaborators discovered a second type of neutrino [10] distinct from the one which participated in the reactions 1.2 and 1.3. Their experiment was the first to use the accelerator-based neutrino beam method and led to the discovery of the muon neutrino. The tau neutrino, predicted to exist after Lederman's experiment, would have to wait until 2000 to be observed experimentally [11]. However long before the ν_τ was directly detected, leptons were now thought to be grouped in families with lepton flavor (L_e, L_μ, L_τ) being a conserved quantity. The development of this family structure was an important step and led to the formation of the fermion doublets introduced below.

1.2 Introducing Massive neutrinos to the Standard Model

The major success of the Standard Model is the connection between forces mediated by spin-1 particles and local (gauge) symmetries. The strong, weak and electromagnetic interactions are connected to $SU(3)$, $SU(2)$ and $U(1)$ gauge groups, respectively, being the characteristics of the different interactions explained by the symmetry which they are related to. Thus, the SM is based on the gauge group:

$$\mathrm{G_{SM} = SU(3)_C \times SU(2)_L \times U(1)_Y,} \tag{1.4}$$

where SU(3) belongs to the color group of quantum chromodynamics; SU(2) to the weak isospin; and U(1) to the hypercharge. That is, the strong, weak and electromagnetic interactions.

In the standard model individual lepton charges ($L_e = 1$ for e^- and ν_e and $L_e = -1$ for e^+, and $\bar{\nu}_e$ and analogously for L_μ and L_τ) are conserved. Thus, processes such as $\mu^+ \rightarrow e^+ + \gamma$, or $K_L \rightarrow e^\pm + \mu^\mp$ are forbidden. Indeed, there is no experimental evidence of such processes. Based on these empirical facts, the standard model places the left-handed components of the charged lepton and neutrino fields into the doublets of the group $SU(2)_L$,

$$L_L = \begin{pmatrix} \nu_\ell \\ \ell_L \end{pmatrix}_L , \ \ell = e, \mu, \tau , \tag{1.5}$$

while the right-handed components of the charged lepton fields are singlets. The right-handed components of the neutrino fields are *absent* in the standard electroweak model by definition.

$L_L(1, 2, -\frac{1}{2})$ $Q_L(3, 2, \frac{1}{6})$	$E_R(1, 1, -1)$	$U_R(3, 1, \frac{2}{3})$	$D_R(3, 1, -\frac{1}{3})$
$\begin{pmatrix} \nu_e \\ e \end{pmatrix}_L \quad \begin{pmatrix} u \\ d \end{pmatrix}_L$	e_R	u_R	d_R
$\begin{pmatrix} \nu_\mu \\ \mu \end{pmatrix}_L \quad \begin{pmatrix} c \\ s \end{pmatrix}_L$	μ_R	c_R	s_R
$\begin{pmatrix} \nu_\tau \\ \tau \end{pmatrix}_L \quad \begin{pmatrix} t \\ b \end{pmatrix}_L$	τ_R	t_R	b_R

Table 1.1: Matter contents of the Standard Model. Numbers in parenthesis represent the corresponding charges under the group given by the formula 1.4.

Thus, the matter content of the SM remains as shown in Table 1.1. As can be seen, there are three matter fermion generations. Each one consists of five different representations of the SM gauge group. The elementary particles are arranged as doublets for chiral left-handed fields and singlets for right-handed fields except for neutrinos (ν_ℓ). These are fermions that have neither strong nor electromagnetic interactions, i.e., they are singlets of $SU(3)_C \times U(1)_Y$. These three neutrinos that have weak interactions are known as *active*.

In order to provide masses to fermions in the SM, the model also contains a single Higgs boson doublet, ϕ with charges $(1, 2, 1/2)$, whose vacuum expectation value breaks the gauge symmetry,

$$\langle \phi \rangle = \begin{pmatrix} 0 \\ \frac{v}{\sqrt{2}} \end{pmatrix} \quad \implies \quad G_{SM} \to SU(3)_C \times U(1)_{EM}. \tag{1.6}$$

This is the only piece of the SM which still misses experimental confirmation. In the SM, fermion masses arise from the Yukawa interactions which couple a right-handed fermion with

its left-handed doublet and the Higgs field,

$$- \mathcal{L}_{\text{Yukawa}} = Y_{ij}^d \bar{Q}_{Li} \phi D_{Rj} + Y_{ij}^u \bar{Q}_{Li} \tilde{\phi} U_{Rj} + Y_{ij}^\ell \bar{L}_{Li} \phi E_{Rj} + \text{h.c.} \qquad (1.7)$$

(where $\tilde{\phi} = i\tau_2 \phi^\star$) which after spontaneous symmetry breaking (Higgs mechanism) lead to charged fermion masses

$$m_{ij}^f = Y_{ij}^f \frac{v}{\sqrt{2}}. \qquad (1.8)$$

However, since no right-handed neutrinos exist in the model, the Yukawa interactions leave the neutrinos massless. Furthermore, neutrino masses cannot arise either from loop corrections, according to the following considerations. The SM gauge symmetries and particle content induce an accidental global symmetry (*i.e.*, it is not imposed):

$$\text{G}_{\text{SM}}^{\text{global}} = \text{U}(1)_B \times \text{U}(1)_{L_e} \times \text{U}(1)_{L_\mu} \times \text{U}(1)_{L_\tau}. \qquad (1.9)$$

$\text{U}(1)_B$ is the baryon number symmetry and $\text{U}(1)_{L_e, L_\mu, L_\tau}$ are the three lepton flavor symmetries, with total lepton number given by $L = L_e + L_\mu + L_\tau$. Loop corrections cannot provide neutrino masses because the only possible neutrino mass term that can be constructed with the SM fields is the bilinear $\bar{L}_L L_L^C$ which violates the total lepton symmetry by two units. Being the total lepton number a global symmetry of the model, L-violating terms cannot be induced by loop corrections.

Regarding interactions between neutrinos and their corresponding charged leptons, we have in the SM charged current (CC) and neutral currents (NC):

$$- \mathcal{L}_{\text{CC}} = \frac{g}{\sqrt{2}} \sum_\ell \bar{\nu}_{L\ell} \gamma^\mu \ell_L^- W_\mu^+ + \text{h.c.} \qquad (1.10)$$

$$- \mathcal{L}_{\text{NC}} = \frac{g}{2 \cos \theta_W} \sum_\ell \bar{\nu}_{L\ell} \gamma^\mu \nu_{L\ell} Z_\mu^0. \qquad (1.11)$$

It is important to notice here that studies of $e^+ e^-$ annihilation at the Z-resonance peak have determined the invisible width of the Z boson, caused by its decay into unobservable channels. One can interpret this width as a measurement of the number of neutrino active flavors: $N_\nu = 2.984 \pm 0.008$ is obtained from the four LEP experiments [12]. Therefore, it can be concluded that there are just three active neutrinos with masses of less than $M_Z/2$. Besides these three active neutrino flavors there could be other neutrinos which do not participate in weak interactions. Such neutrinos are called *sterile*. This kind of neutrinos is defined as having no SM gauge interactions (singlets of the full SM gauge group). Notice

that as defined, the SM contains no sterile neutrinos.

Summarizing all the above discussion, one can say that neutrinos are deemed to be massless in the SM, and the individual lepton numbers, as well as the total one, are strictly conserved. With the fermionic content and gauge symmetry of the SM one cannot construct a renormalizable mass term for the neutrinos. In order to introduce a neutrino mass, one must either extend the particle contents of the model or abandon the gauge invariance and/or renormalizability. Concerning experimental tests, observation of neutrino oscillations proves non-conservation of neutrino flavor and the massive nature of these particles, leading to physics beyond the Standard Model.

Introducing massive neutrinos

In a field theory of neutrinos the mass is determined by the mass term in the Lagrangian. Since the right-handed neutrinos are absent in the standard electroweak model, one can add more possibilities by adding to the three known neutrino fields $\nu_{\ell L}$ new fields corresponding to sterile neutrinos ν_{si}. Keeping the gauge symmetry and the particle contents of the SM, and assuming an arbitrary number m of sterile neutrinos, one can construct two types of mass terms:

$$-\mathcal{L}_{M_\nu} = M_{Dij}\bar{\nu}_{si}\nu_{Lj} + \frac{1}{2}M_{Nij}\bar{\nu}_{si}\nu_{sj}^c + \text{h.c..} \qquad (1.12)$$

where ν^c indicates a charge conjugated field, $\nu^c = C\bar{\nu}^T$ and C is the charge conjugation matrix. M_D is a complex $m \times 3$ matrix and M_N is a symmetric matrix of dimension $m \times m$.

The first term is what we call a Dirac mass term, analogous to the mass term of charged leptons. It conserves the total lepton number, but it might violate the individual lepton flavor numbers.

The second term is a Majorana mass term which breaks the total lepton number conservation by two units. It is allowed only if the neutrinos have no additive conserved charges of any kind.

In general Equation 1.12 can be rewritten as:

$$-\mathcal{L}_{M_\nu} = \frac{1}{2}\overline{\vec{\nu}^c}M_\nu\vec{\nu} + \text{h.c.}, \qquad (1.13)$$

where

$$M_\nu = \begin{pmatrix} 0 & M_D^T \\ M_D & M_N \end{pmatrix}, \tag{1.14}$$

and $\vec{\nu} = (\vec{\nu}_L, \vec{\nu}_s^c)^T$ is a (3+m)-dimensional vector. The matrix M_ν is complex and symmetric. It can be diagonalized by a unitary matrix of dimension $(3+m)$, V^ν, so that

$$(V^\nu)^T M_\nu V^\nu = \text{diag}(m_1, m_2, \ldots, m_{3+m}). \tag{1.15}$$

The corresponding 3+n eigenstates ν_M represent Majorana neutrinos, obeying the condition:

$$\nu_M = \nu_M^c \tag{1.16}$$

Now, depending on the scale of M_N, one can analyze different cases:

Dirac neutrinos:

this happens when $M_N = 0$, so second term in Equation 1.12 vanishes, and therefore there is lepton number symmetry in the model. The quantum number L distinguishes a neutrino from an anti-neutrino. For $m = 3$ we can identify the three sterile neutrinos with the right-handed component of a four-spinor neutrino field. In this case the Dirac mass term can be diagonalized with two 3×3 unitary matrices, V^ν and V_R^ν as:

$$V_R^{\nu\dagger} M_D V^\nu = \text{diag}(m_1, m_2, m_3). \tag{1.17}$$

The neutrino mass term can be written as:

$$-\mathcal{L}_{M_\nu} = \sum_{k=1}^{3} m_k \bar{\nu}_{Dk} \nu_{Dk} \tag{1.18}$$

where

$$\nu_{Dk} = (V^{\nu\dagger} \vec{\nu}_L)_k + (V_R^{\nu\dagger} \vec{\nu}_s)_k, \tag{1.19}$$

so the weak-doublet components of the neutrino fields are

$$\nu_{Li} = L \sum_{j=1}^{3} V_{ij}^\nu \nu_{Dj}, \qquad i = 1, 3. \tag{1.20}$$

In this case the SM is not a good low-energy effective theory since both the matter content and the assumed symmetries are different. In addition, there is no explanation to the fact that neutrino masses are much lighter than the corresponding charged fermion masses, although in this case all acquire their mass via the same mechanism.

Majorana neutrinos in the Seesaw model:

in this case M_N is much higher than the scale of electroweak symmetry breaking $\langle \phi \rangle$. The diagonalization of M_ν leads to three light, ν_l, and m heavy, N, neutrinos:

$$-\mathcal{L}_{M_\nu} = \frac{1}{2} \bar{\nu}_l M^l \nu_l + \frac{1}{2} \bar{N} M^h N \tag{1.21}$$

with

$$M^l \simeq -V_l^T M_D^T M_N^{-1} M_D V_l, \qquad M^h \simeq V_h^T M_N V_h \tag{1.22}$$

and

$$V^\nu \simeq \begin{bmatrix} \left(1 - \frac{1}{2} M_D^\dagger M_N^{*-1} M_N^{-1} M_D \right) V_l & M_D^\dagger M_N^{*-1} V_h \\ -M_N^{-1} M_D V_l & \left(1 - \frac{1}{2} M_N^{-1} M_D M_D^\dagger M_N^{*-1} \right) V_h \end{bmatrix} \tag{1.23}$$

where V_l and V_h are 3×3 and $m \times m$ unitary matrices respectively. So the heavier are the heavy states, the lighter are the light ones. Also as seen from Equation 1.23 the heavy states are mostly right-handed while the light ones are mostly left-handed. Both the light and the heavy neutrinos are Majorana particles. In this case the SM is a good effective low energy theory. For further details, see [13].

Light sterile Majorana neutrinos:

this happens if the scale of some eigenvalues of M_N is not higher than the electroweak scale. As in the case with $M_N = 0$, the SM is not even a good low energy effective theory: there are more than three light neutrinos, and they are admixtures of doublet and singlet fields.

From experimental data, we know that neutrinos masses are much smaller than the masses of the associated lepton in the weak isodoublet (Equation 1.5). Even the mass of the lightest charged lepton (the electron) is at least 10^5 times larger than the neutrino mass. Such a large factor is difficult to explain unless within some symmetry principle, and thus the assumption that neutrinos are Majorana particles arises. Moreover, several theoretical models explaining neutrinos masses lead to the conclusion that neutrinos are massive Majorana fermions.

Neutrino mixing

If neutrinos are massive particles and there is neutrino mixing, the left-handed components of the neutrino fields $\nu_{\alpha L}$ ($\alpha = e, \mu, \tau, s_1, s_2, \ldots$) are unitary linear combinations

of the left-handed components of the n (Dirac or Majorana) neutrino fields ν_k ($k = 1, \ldots, n$) with masses m_k:

$$\nu_{\alpha L} = \sum_{k=1}^{n} U_{\alpha k} \nu_{kL}.$$

(1.24)

The number n of massive neutrinos is 3 for the cases with only three active flavour neutrinos. The number n is more than three in the case of a Dirac-Majorana mass term with a mixing of both active and sterile neutrinos.

In particular, if there are only three neutrinos, U is a 3×3 unitary matrix analogous to the CKM matrix for the quarks. It is known as the PMNS matrix to Pontecorvo, Maki, Nakagawa and Sakata. It can be written in terms of six independent parameters: three mixing angles and three phases. If neutrinos are Dirac particles, two phases can be eliminated by redefinition of the massive states. For Majorana neutrinos, this is not possible.

In the case of Majorana neutrinos, the PMNS matrix can be conveniently parametrized as:

$$U = \begin{pmatrix} 1 & 0 & 0 \\ 0 & c_{23} & s_{23} \\ 0 & -s_{23} & c_{23} \end{pmatrix} \begin{pmatrix} c_{13} & 0 & s_{13}e^{-i\delta} \\ 0 & 1 & 0 \\ -s_{13}e^{i\delta} & 0 & c_{13} \end{pmatrix} \cdot$$
$$\begin{pmatrix} c_{21} & s_{12} & 0 \\ -s_{12} & c_{12} & 0 \\ 0 & 0 & 1 \end{pmatrix} \begin{pmatrix} e^{i\alpha_1} & 0 & 0 \\ 0 & e^{i\alpha_2} & 0 \\ 0 & 0 & 1 \end{pmatrix}$$

(1.25)

where $c_{ij} \equiv \cos\theta_{ij}$ and $s_{ij} \equiv \sin\theta_{ij}$. The angles θ_{ij} can be taken without loss of generality to lie in the first quadrant, $\theta_{ij} \in [0, \pi/2]$ and the phases $\delta, \alpha_i \in [0, 2\pi]$. The presence of these phases causes the violation of CP invariance in the lepton sector. The two Majorana phases $\alpha_{1,2}$ affect only lepton number violating processes and are very hard to measure (oscillation experiments are not sensitive to them). Since in this parameterization of the mixing matrix the CP-violating phase δ is associated with s_{13}, it is clear that CP violation is negligible in the lepton sector if the mixing angle θ_{13} is small.

PMNS matrix parameterization of Equation (1.25) can be understood as a 3D rotation matrix, product of three independent rotations, one in the plane 23, another in the plane 12 and a third that connects both (Figure 1.1). As it will be described in chapter 2, the current experimental data can be accommodated to this 3-ν scheme. Atmospheric neutrino experiments are sensitive to the mixing angle θ_{23} (and thus to the rotation in the plane 23), while solar neutrino experiments can measure θ_{12} (rotation in the plane 12).
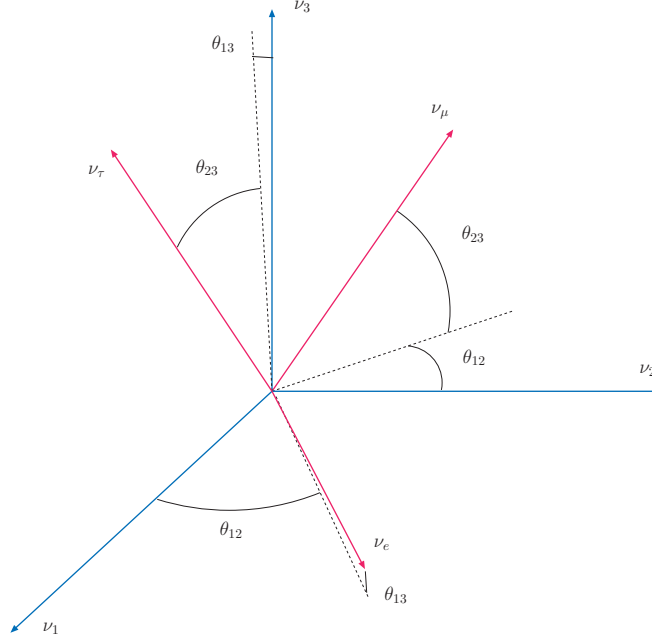
Figure 1.1: Neutrino mixing scheme.

1.3   Neutrino oscillations in vacuum

In the case of massive neutrinos, the weak eigenstates, ν_α, produced in weak interactions are, in general, linear combinations of the mass eigenstates ν_i:

$$|\nu_\alpha\rangle = \sum_{i=1}^{n} U_{\alpha i}^* |\nu_i\rangle \tag{1.26}$$

where n is the number of light neutrino species and U is the mixing matrix. After traveling a distance L, a neutrino originally produced with a flavor α evolves as:

$$|\nu_\alpha(t)\rangle = \sum_{i=1}^{n} U_{\alpha i}^* |\nu_i(t)\rangle, \tag{1.27}$$

and it can be detected in the charged-current (CC) interaction

$$\nu_\alpha(t)N' \rightarrow \ell_\beta N$$

with a probability

$$P_{\alpha\beta} = |\langle \nu_\beta | \nu_\alpha(t)\rangle|^2 = |\sum_{i=1}^{n}\sum_{j=1}^{n} U_{\alpha i}^* U_{\beta j} \langle \nu_j | \nu_i(t)\rangle|^2. \tag{1.28}$$

Using the standard approximation that $|\nu\rangle$ is a plane wave

$$|\nu_i(t)\rangle = e^{-iE_i t}|\nu_i(0)\rangle,$$

that neutrinos are relativistic with $p_i \simeq p_j \equiv p \simeq E$,

$$E_i = \sqrt{p_i^2 + m_i^2} \simeq p + \frac{m_i^2}{2E}, \tag{1.29}$$

and the orthogonality relation $\langle \nu_j | \nu_i \rangle = \delta_{ij}$, we get the following transition probability:

$$P_{\alpha\beta} = \delta_{\alpha\beta} - 4 \sum_{i<j}^{n} \mathrm{Re}[U_{\alpha i} U_{\beta i}^* U_{\alpha j}^* U_{\beta j}] \sin^2 X_{ij}$$

$$+ 2 \sum_{i<j}^{n} \mathrm{Im}[U_{\alpha i} U_{\beta i}^* U_{\alpha j}^* U_{\beta j}] \sin 2X_{ij}, \tag{1.30}$$

where

$$X_{ij} = \frac{(m_i^2 - m_j^2)L}{4E}. \tag{1.31}$$

The first line in (1.30) is CP conserving while the second one is CP violating and has opposite sign for neutrinos and antineutrinos. This transition probability has an oscillatory behavior, with amplitudes that are proportional to elements in the mixing matrix and oscillation lengths

$$L_{0,ij}^{\mathrm{osc}} = \frac{4\pi E}{\Delta m_{ij}^2}, \tag{1.32}$$

where $\Delta m_{ij}^2 \equiv m_i^2 - m_j^2$.

Thus, in order to undergo flavour oscillations, neutrinos must have different masses and they must mix. Also, as can be seen from Equation (1.30), the Majorana phases cancel out in the oscillation probability as expected because flavour oscillation is a total lepton number conserving process.

When neutrinos propagate in dense matter, the interaction with the medium affects their properties and the corresponding effects can be observed in oscillation experiments. Although this is an interesting issue, it is out of the scope of this work. For further details, we refer to [1].

Chapter 2

Experimental Approaches to
Neutrino Physics

The experimental studies aiming to understand neutrino nature can be divided into two different fields. First, neutrino oscillation experiments aim to measure the oscillation parameters appearing in the three first terms of Eq.1.25. Depending on the neutrino energy and the distance between the neutrino source and the detectors, one is able to measure one or another parameter. This is why we distinguish between different kinds of neutrino oscillation experiments, being sensitive to the solar, atmospheric or interference regimes.

The following sections summarize different experimental approaches to neutrino physics, from the oscillation experiments to those experiments looking for the absolute mass scale and the nature of neutrino masses. An extended description of these experiments and their results can be found at [1].

2.1   Neutrino oscillations

Neutrino oscillations experiment are characterized by the typical neutrino energy E_ν and by the distance L between neutrino source and detector. In order to be sensitive to a given value of Δm_{ij}^2, the experiment has to be set up with $E/L \approx \Delta m_{ij}^2$.

Oscillation experiments can be divided into four categories, depending of the neutrino source under study. Typically, each neutrino source implies a given range of energy and a distance between the source and the detector (as an example, solar neutrinos have

much longer flight distances than atmospheric neutrinos), although for neutrinos generated on Earth one has some freedom to choose the source-detector distance L. Consequently, oscillation experiments are sensitive to a certain set of oscillation parameters, depending on the neutrino source.

According to the above criteria, we have the following type of experiments:

- solar neutrinos

- atmospheric neutrinos

- reactor neutrinos

- accelerator neutrinos

In the case of reactor and accelerator experiments, one can set L depending on the range of Δm^2 to be explored. This is why we distinguish between short and long baseline (LBS and SBL) experiments. Furthermore, oscillation in atmospheric neutrinos can be analyzed in a wide range of L, since one can detect neutrinos coming from the top of the detector (they travel about 15 km in the atmosphere), or neutrinos coming from the bottom (they have traversed the full diameter of the Earth). Table 2.1 shows the typical parameters of L and E_ν, and the corresponding values of Δm^2, for the kinds of experiments listed above.

Concerning experimental issues, PMNS matrix in Eq. 1.25 can be understood as the convolution of three different terms (apart from the Majorana phases, which cannot be observed by oscillation experiments). Each term (or rotation, as explained in section 1.2) contains the mixing angle controlling one of the so-called *oscillation sectors*: atmospheric, solar and interference. Thus, first sub-matrix in Eq. 1.25 holds the angle which can be measured in atmospheric and accelerator neutrinos (at long baselines) experiments:

$$U_{atm} = \begin{pmatrix} 1 & 0 & 0 \\ 0 & c_{23} & s_{23} \\ 0 & -s_{23} & c_{23} \end{pmatrix} \tag{2.1}$$

and we use the following convection for the mixing angle: $\theta_{23} \equiv \theta_{atm}$.

On the other hand, solar and reactor neutrino experiments are sensitive to the parameter in third term of Eq. 1.25, that is, to the solar sector:

Experiment	L (m)	E (MeV)	Δm^2 (eV^2)
Solar	10^{10}	1	10^{-10}
Atmospheric	$10^4 - 10^7$	10^2–10^5	$10^{-1} - 10^{-4}$
Reactor SBL	$10^2 - 10^3$	1	$10^{-2} - 10^{-3}$
Reactor LBL	$10^4 - 10^5$		$10^{-4} - 10^{-5}$
Accelerator SBL	10^2	10^3–10^4	> 0.1
Accelerator LBL	$10^5 - 10^6$	10^4	$10^{-2} - 10^{-3}$

Table 2.1: Characteristic values of L and E_ν for various types of neutrino experiments and the corresponding ranges of Δm^2 which can be explored. SBL and LBL stand for short and long baselines.

$$U_{sol} = \begin{pmatrix} c_{12} & s_{12} & 0 \\ -s_{12} & c_{12} & 0 \\ 0 & 0 & 1 \end{pmatrix} \tag{2.2}$$

In this work we use the following convection for the corresponding mixing angle: $\theta_{12} \equiv \theta_{sol}$.

Finally, mixing or interference between atmospheric and solar sectors is controlled by the second term in Eq. 1.25:

$$U_{inter} = \begin{pmatrix} c_{13} & 0 & s_{13}e^{-i\delta} \\ 0 & 1 & 0 \\ -s_{13}e^{i\delta} & 0 & c_{13} \end{pmatrix} \tag{2.3}$$

Summarizing, the current experimental data can be fit to a 3-ν scenario: two mixing angles (θ_{sol} and θ_{atm}) and two mass square differences ($\Delta m^2_{\mathrm{sol}}$ and $\Delta m^2_{\mathrm{atm}}$) are measured by solar and atmospheric experiments respectively.

The third mixing angle (θ_{13}) is known to be small or even null. Therefore, one is allowed to analyze atmospheric and solar data assuming a two-neutrino scenario within

good approximation. For a two-neutrino case, the overall mixing matrix depends on a single parameter (θ_{sol} or θ_{atm}),

$$U = \begin{pmatrix} \cos\theta & \sin\theta \\ -\sin\theta & \cos\theta \end{pmatrix} , \qquad (2.4)$$

and there is a single mass-squared difference Δm^2 (Δm^2_{sol} or Δ^2_{atm}). Then $P_{\alpha\beta}$ of Eq. 1.30 takes the well known form

$$P_{\alpha\beta} = \delta_{\alpha\beta} - (2\delta_{\alpha\beta} - 1) \sin^2 2\theta \sin^2 X . \qquad (2.5)$$

The physical parameter space is covered with $\Delta m^2 \geq 0$ and $0 \leq \theta \leq \frac{\pi}{2}$ (or, alternatively, $0 \leq \theta \leq \frac{\pi}{4}$ and either sign for Δm^2).

Neutrino oscillation experiments usually analyze their data inside this scenario of only two-flavour neutrino oscillation.

2.1.1 Solar neutrinos

Solar neutrinos are electron neutrinos produced in the thermonuclear reactions which generate the solar energy. All the reaction chains result in the overall fusion of protons into ^{4}He:

$$4p \rightarrow^4 \text{He} + 2e^+ + 2\nu_e + \gamma, \qquad (2.6)$$

where the energy release is $Q = 4m_p - m_{^4\text{He}} - 2m_e \simeq 26$ MeV. It is mostly radiated through the photons and only a small fraction is carried by the neutrinos, $\langle E_{2\nu_e} \rangle = 0.59$ MeV. Due to their low energy, neutrinos from this fusion are not easy to detect. Neutrinos coming from the following secondary reactions were the first to be observed:

$$^7\text{Be} + e^+ \rightarrow^7 \text{Li} + \nu_e , \quad E_\nu = 0.86 \ MeV \qquad (2.7)$$

$$^8\text{B} + e^+ \rightarrow^8 \text{Be}^* + e^+ + \nu_e , \quad E_\nu < 15 \ MeV \qquad (2.8)$$
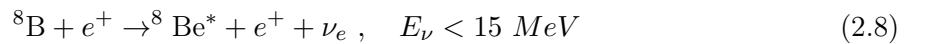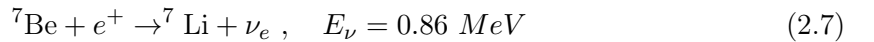
The so-called solar neutrino problem [14, 15] came from the fact that several experiments observed a solar neutrino flux Φ^{obs} that was smaller than the predicted by the Standard Solar Model (SSM) [16]. Moreover, different experiments have shown different deficits, indicating that the effect is energy dependent. Figure 2.1 shows the solar ν_e fluxes as predicted by the SSM. The following list summarizes results from solar neutrino experiments since 1968:
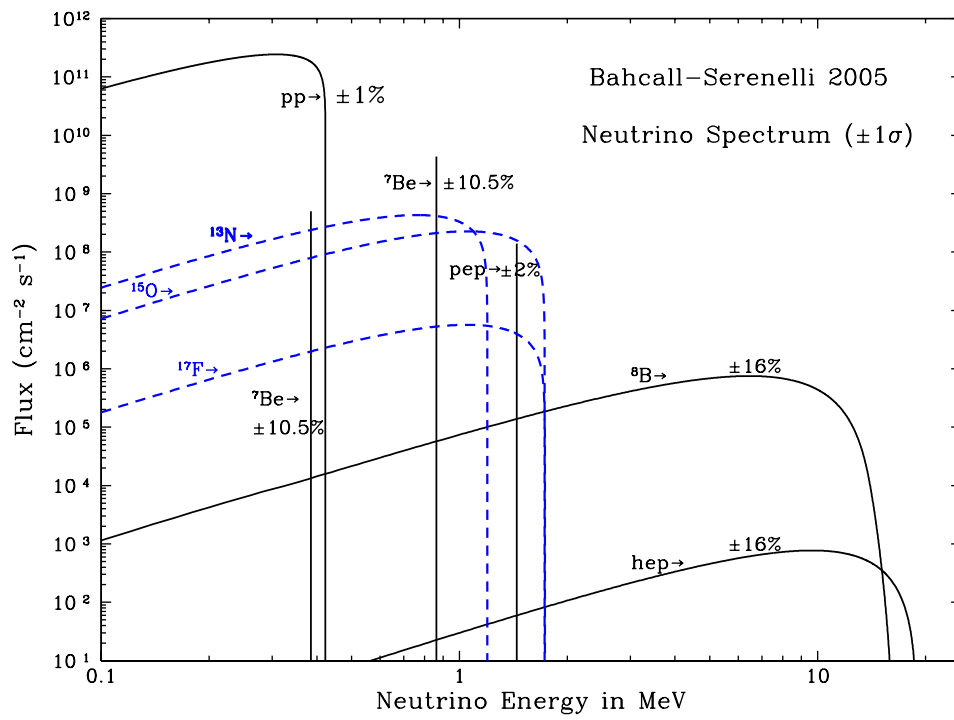
Figure 2.1: Neutrino fluxes predicted by the SSM as a function of the neutrino energy. From [16].

Chlorine experiment at Homestake:

The first result announced by Ray Davis took place in 1968 [17]. The detector, placed at Homestake mine (South Dakota), was a tank filled with ~ 615 Tons of C_2Cl_4, in which solar ν_e were captured via ^{37}Cl $(\nu, e^-)^{37}$Ar. The energy threshold for this reaction is 0.814 MeV, so the relevant fluxes are those of neutrinos coming from the ^{7}Be and ^{8}B (Eq. 2.7 and 2.8). The average event rate measured during the more than 20 years of operation is [18]

$$R_{\mathrm{Cl}} = 2.56 \pm 0.16 \pm 0.16 \text{ SNU} \quad \Rightarrow \quad \frac{R_{\mathrm{Cl}}}{\mathrm{SSM}} = 0.30 \pm 0.03 \qquad (2.9)$$

where $1 \text{ SNU} = 10^{-36}$ captures/atom/sec.

Gallium experiments (SAGE and GALLEX/GNO):

SAGE [19] and GALLEX/GNO [20] (GNO experiment is the successor of GALLEX) are operated at Baksan (Russia) and Gran Sasso (Italy) respectively. Both are radiochemical experiments using ^{71}Ga target: solar neutrinos are captured via ^{71}Ga$(\nu, e^-)^{71}$Ge. The threshold of this reaction is 0.233 MeV and this allows to detect neutrinos from 2.6. The averaged event rates measured by SAGE and GALLEX+GNO are [21]:

$$R_{\mathrm{GALLEX+GNO+SAGE}} = 68.1 \pm 3.75 \text{ SNU} \quad \Rightarrow \quad \frac{R_{\mathrm{Ga}}}{\mathrm{SSM}} = 0.52 \pm 0.03 \,. \qquad (2.10)$$

Water Cherenkov detector (Kamiokande and SK):

Super-Kamiokande [22] (SK) is the evolution of the Kamiokande [23] detector. It is a tank filled with 50 kilotons of water that allows to detect in real time electrons produced by the elastic scattering (ES) of the solar neutrinos, $\nu_a + e^- \to \nu_a + e^-$, thanks to the emission of Cherenkov light. While the detection process in radiochemical experiments is purely a charge current (CC) interaction (W-exchange), the detection ES process goes through both CC and neutral current (NC) (Z-exchange) interactions. Consequently, the ES detection process is sensitive to all active neutrino flavors. The detection threshold in SK is 5 MeV, and therefore it is sensitive to neutrino flux coming from Eq. 2.8. The measured flux is:

$$\Phi_{\mathrm{SK}} = (2.35 \pm 0.02 \pm 0.08) \times 10^6 \text{ cm}^{-2}\text{s}^{-1} \Rightarrow$$
$$\Rightarrow \frac{\Phi_{\mathrm{SK}}}{\Phi_{\mathrm{SSM}}} = 0.413 \pm 0.014 \,. \qquad (2.11)$$

The Sudbury Neutrino Observatory (SNO):

The SNO detector [24, 25, 26] is a great sphere surrounded by photomultipliers, which contains approximately 1000 Tons of heavy water, D_2O, and is located at the Creighton mine (Canada). SNO is sensitive to all flavors of active neutrinos and not just to ν_e. This is possible because energetic neutrinos can interact in the D_2O of SNO via three different reactions. Electron neutrinos may interact via the CC reaction $\nu_e + d \rightarrow p + p + e^-$, and can be detected above an energy threshold of a few MeV (presently $T_e > 5$ MeV). All active neutrinos ($\nu_a = \nu_e$, ν_μ, ν_τ) interact via the NC reaction $\nu_a + d \rightarrow n + p + \nu_a$ with an energy threshold of 2.225 MeV. Finally, the non-sterile neutrinos can also interact via ES, $\nu_a + e^- \rightarrow \nu_a + e^-$. SNO can test if the deficit of solar ν_e is due to changes in the flavor composition of the solar neutrino beam, since the ratio CC/NC compares the number of ν_e interactions with those from all active flavors. This comparison is independent of the overall flux normalization. SNO latest solar flux predictions are:

$$\Phi_{\text{SNO}}^{\text{CC}} = (1.68\,^{+0.06}_{-0.06}\,^{+0.08}_{-0.09}) \times 10^6 \ \text{cm}^{-2}\text{s}^{-1} \Rightarrow \frac{\Phi_{\text{SNO}}^{\text{CC}}}{\Phi_{\text{SSM}}} = 0.29 \pm 0.02\,,$$

$$\Phi_{\text{SNO}}^{\text{ES}} = (2.35 \pm 0.22 \pm 0.15) \times 10^6 \ \text{cm}^{-2}\text{s}^{-1} \Rightarrow \frac{\Phi_{\text{SNO}}^{\text{ES}}}{\Phi_{\text{SSM}}} = 0.41 \pm 0.05\,, \qquad (2.12)$$

$$\Phi_{\text{SNO}}^{\text{NC}} = (4.94 \pm 0.21\,^{+0.38}_{-0.34}) \times 10^6 \ \text{cm}^{-2}\text{s}^{-1} \Rightarrow \frac{\Phi_{\text{SNO}}^{\text{NC}}}{\Phi_{\text{SSM}}} = 0.87 \pm 0.08\,.$$

The simplest mechanism for the solar neutrino flavor transition is that of oscillations of ν_e into ν_μ and/or ν_τ, in a two-neutrino scenario. The measurements of the neutral current flux by SNO confirm that the ν_e deficit corresponds to a ν_μ/ν_τ flux appearance. The combined analysis results from SNO, SK, Gallium and Chlorine experiments can be summarized as:

$$\Delta m_{sol}^2 \sim 6 \times 10^{-5} \ \text{eV}^2,$$

$$\theta_{sol} \sim 33^o$$

It is worth noticing that the interpretation of the solar data led to a set of possible solutions of mass square difference and mixing angle, which indeed were far away one from

another. The degenerate solutions were the so-called *MSW small mixing angle* (SMA), *MSW large mixing angle* (LMA), *MSW low mass* (LOW) and *vacuum oscillations* (VAC) [1]. Only with further SK and SNO data analysis, in particular the inclusion of the time and energy dependence of the ^{8}B neutrino fluxes, this situation was solved by pointing the LMA solution as the most likely to explain the solar neutrino problem.

2.1.2 Atmospheric neutrinos

When cosmic rays interacts with the nitrogen and oxygen in the Earth's atmosphere at an average height of 15 kilometers, pions and some kaons are produced. These hadrons decay into electron and muon neutrinos and anti-neutrinos. Atmospheric neutrinos are observed in underground experiments using different techniques and leading to different type of events depending on their energy. They can be detected by the direct observation of their CC interaction inside the detector. Modern experiments (since the 1970's) follow mainly two directions, allowing both of them flavor classification of the events as well as the measurement of the energy and angle of the outgoing lepton:

Water Cherenkov detectors:
Cherenkov light produced in water by charged leptons is registered by photomultipliers. This is the case of Kamiokande and Super-Kamiokande [27, 28]. Both detectors observed ν_μ fluxes smaller than expected by theoretical calculations. Indeed, the event distribution as a function of the zenith angle θ suggested that the deficit increased with the distance between the neutrino production and interaction points. Comparing the observed and the expected distributions, the following statements can be inferred:

1. ν_e distributions are well described by the MC while ν_μ presents a deficit. Consequently, the atmospheric neutrino deficit is mainly due to disappearance of ν_μ and not the appearance of ν_e.

2. The suppression of contained μ-like events is stronger for larger $\cos\theta$, which implies that the deficit grows with the distance traveled by the neutrino from its production point to the detector.

3. disappearance probability is higher for larger energy neutrinos

Iron calorimeters:
An iron calorimeter is composed of a set of alternating layers of iron which act as

a target and some tracking element (such as plastic drift tubes) which allows the reconstruction of the shower produced by the electrons or the tracks produced by muons. Detectors Soudan2 [29] and MACRO [30] have confirmed the same effects observed by SK.

SK, Macro and Soudan experiments have found definitive evidence of atmosphere ν_μ disappearance. The simplest and most direct interpretation of the atmospheric neutrino anomaly is that of muon neutrino oscillations (in a two-neutrino scenario). On the other hand, there is no observation of ν_e oscillation, leading to the conclusion that mixing angle θ_{13} is small. Combined analysis for the oscillation parameter space can be seen in Figure 2.3. Atmospheric neutrinos experiments show that

$$\Delta m^2_{atm} \sim 2 \times 10^{-3} \text{ eV}^2,$$
$$\theta_{atm} \sim 45^o$$

2.1.3   Reactor neutrinos

Another source of neutrino fluxes are nuclear reactors. They produce $\bar{\nu}_e$ beams with $E_\nu \sim$ MeV. This low energy only allows to produce e's in the neutrino CC interaction that takes place in the detector. In case $\bar{\nu}_e$ oscillates, the remaining neutrino cannot interact via CC and is not detected. Therefore, the oscillation signature in experiments using reactor neutrinos is a disappearance effect, or in other words a deficit in the expected reactor flux. These kind of experiments have the advantage that smaller values of Δm^2 can be accessed due to the lower neutrino beam energy. As previously said, one can choose the distance L between the neutrino source and the detector, and this allows to set the Δm^2 range to be explored. We can distinguish between SBL (CHOOZ [31]) and LBL (KamLAND [32]) experiments:

CHOOZ:
it searched for disappearance of $\bar{\nu}_e$'s coming from a nuclear plant in France, using a detector located at $L \simeq 1$ km from the reactors. The $\bar{\nu}_e$ interaction signature is the delayed coincidence between the prompt e^+ signal and the signal due to the neutron capture in the Gd-loaded scintillator. The ratio between the measured and expected

fluxes averaged over the neutrino energy spectrum is given by

$$R_{\text{CHOOZ}} = 1.01 \pm 2.8\%(\text{stat}) \pm 2.7\%(\text{syst}). \tag{2.13}$$

Thus no evidence was found for a deficit in the flux. Furthermore CHOOZ also presented their results in the form of the antineutrino energy spectrum which showed no distortion. There are other short baseline reactor experiments which did not find a signal of oscillation: Gosgen [33], Krasnoyarsk [34], Bugey [35] and Palo Verde [36]. We recall that the common point to all of them was the short distance L (few km at most from nuclear reactor to neutrino detector). They are sensitive to $\Delta m^2 \gtrsim 7 \times 10^{-3}$ eV^2, far away from the values obtained in the solar neutrino experiments.

KamLAND:

it uses a longer baseline: detector (1 kiloton of liquid scintillator) is placed inside Kamioka mine (Japan), at an average distance of 150-210 km from several nuclear power stations. Such a distance between neutrino source and detector allows to be sensitive to smaller values of Δm^2. It can test oscillations with $\Delta m^2 \gtrsim 10^{-5}$ eV^2, so KamLAND is operating in the same range as solar neutrino experiment. The ratio of the number of observed events to the number of events expected without oscillations is:

$$R_{\text{KamLAND}} = 0.611 \pm 0.094 \tag{2.14}$$

for $E_{\bar{\nu}_e} > 3.4$ MeV [32]. This deficit is inconsistent with the expected rate for massless $\bar{\nu}_e$'s at the 99.95% confidence level. Kamland analysis publised at [37] also presents energy dependence of the events in the form of the prompt energy ($E_{\text{prompt}} \simeq E_{\bar{\nu}_e} + m_p - m_n$) spectrum, showing clearly an energy dependent deficit.

From KamLAND analysis one gets $\Delta m^2_{sol} \sim 7 \times 10^5$ eV^2. However, its results can be combined with the solar data achieving the allowed range for oscillation parameters shown in Figure 2.2. This combined analysis yields:

$$\Delta m^2_{sol} \sim 7.5 \times 10^{-5} \text{ eV}^2,$$

$$\theta_{sol} \sim 34°$$

It is important to notice that CHOOZ provides an interesting result regarding the $3 - \nu$ scenario in which the solar and atmospheric sectors interferes via the mixing angle θ_{13}. The fact that $\bar{\nu}_e$ does not disappear in this experiment leads to the following conclusion:

$$\theta_{13} \lesssim 13°, \quad \text{for} \quad \Delta\text{m}^2_{\text{atm}} \sim 2 \times 10^{-3} \text{ eV}^2$$

2.1.4   Accelerator neutrinos

The neutrino oscillation experiments K2K and MINOS both use the accelerator-based neutrino beam method to be described in Section 2.4. The bottom line is the generation of a very pure ($>$90%) beam of ν_μ with a broad energy distribution peaked in the range $E_\nu \sim$ 1-10 GeV, depending on the exact experimental configuration. Both experiments look for ν_μ disappearance using a two detector approach. A near detector located $\sim$1 km from the neutrino source is used to normalize the expected event rate in the absence of oscillations at a far detector several hundred kilometers distant. An energy dependent deficit in the predicted ν_μ rate is thus evidence for the same $\nu_\mu \rightarrow \nu_\tau$ oscillations as seen in atmospheric neutrinos.

K2K

K2K used the 12 GeV proton synchrotron at KEK to produce a neutrino beam peaked at 1.3 GeV directed at the Super-Kamiokande detector 250 km away which served as a far detector. For the ν_μ disappearance search, K2K observed 112 fully-contained events in Super-K while $158.1^{+9.2}_{-8.6}$ events were predicted based on data in their near detectors [39]. Using a smaller sample (58) of charged-current quasi-elastic events, they were able to observe an energy dependence to the discrepancy consistent with an oscillation hypothesis.

MINOS

The most precise measurement to date of the Δm^2 that dictates the $\nu_\mu \rightarrow \nu_\tau$ oscillation comes from the MINOS experiment at Fermilab [40]. MINOS uses the NuMI (Neutrinos from the Main Injector) neutrino beam produced by 120 GeV protons from the Main Injector. Two functionally identical detectors comprised of alternating iron and scintillator planes are used: a 1 kton near detector at Fermilab and a 5.4 kton far detector located 735 km away in the Soudan Mine in northern Minnesota. In the config-
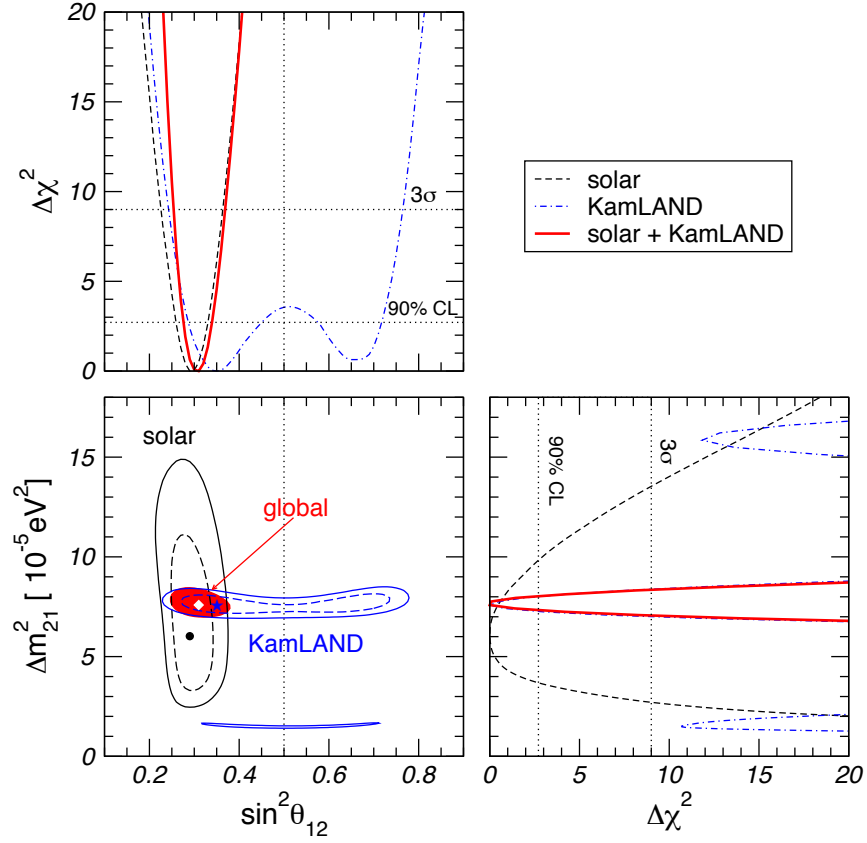
Figure 2.2: Determination of the leading solar oscillation parameters from the interplay of data from artificial and natural neutrino sources. χ^2-profiles and allowed regions at 90% and 99.73% CL (2 dof) are shown for solar and KamLAND, as well as the 99.73% CL region for the combined analysis. The dot, star and diamond indicate the best fit points of solar data, KamLAND and global data, respectively. Minimization is done with respect to Δm_{31}, θ_{23} and θ_{13}, including always atmospheric, MINOS, K2K and CHOOZ data. Figure from [38].

uration used in the oscillation analysis, the ν_μ beam peaks near 3 GeV, making MINOS most sensitive to oscillations of order $\Delta m^2 = 1/(1.267 \times 735km/3GeV) \sim 3 \times 10^{-3} eV^2$.

Their data, recorded between May 2005 and July 2007 correspond to a total of 3.36×10^{20} protons on target [41]. The disappearance of ν_μ is clear, and the oscillation hypothesis fits the spectral distortion well.

Current MINOS data largely supersedes the pioneering K2K measurement which by now gives only a very minor contribution to the Δm^2_{23} measurement. Long-baseline accelerator data and atmospheric neutrino measurements from Super-Kamiokande are combined. Fig. 2.3 illustrates how the determination of the leading atmospheric oscillation parameters θ_{23} and $|\Delta m_{23}|$ emerges from the complementarity of atmospheric and accelerator neutrino data. The best fit points and 1σ errors are:

$$\Delta m^2_{23} \sim \Delta m^2_{\text{MINOS}} = 2.40^{+0.12}_{-0.11} \times 10^{-3} \ eV^2$$
$$\sin^2\theta_{23} \sim \sin^2\theta_{atm} = 0.50^{+0.07}_{-0.06} \tag{2.15}$$

MINOS also searched for $\nu_\mu \to \nu_e$ transitions and their results have been published in [42]. They are based on a 3.14×10^{20} protons-on-target exposure. 35 events have been observed in the far detector with a background of $27 \pm 5(\text{stat}) \pm 2(\text{syst})$ events predicted by the measurements in the near detector. This corresponds to an excess of about 1.5σ which can be interpreted as a weak hint for ν_e appearance due to a non-zero θ_{13}.

Note that the atmospheric and accelerator experiments cannot determine the sign of Δm^2_{23}, but only it's absolute value. This means we do not yet know the hierarchy of the mass states which we call ν_1, ν_2 and ν_3 (see Section 2.3)

Apart from the long baseline experiments, there is also another set of experiments working with accelerator beams but with shorter baselines (hundreds of meters). They are not sensitive to the low values of Δm^2 estimated in atmospheric neutrinos experiments, and have not seen oscillation signal. The only exception is the Liquid Scintillator Neutrino Detector (LSND) [43] running at Los Alamos, where an excess of events compatible with $\bar\nu_\mu \to \bar\nu_e$ oscillations was observed. However, KARMEN [44] and MiniBooNE [45] experiments have completely tested the corresponding phase space of the oscillation parameter with negative results.
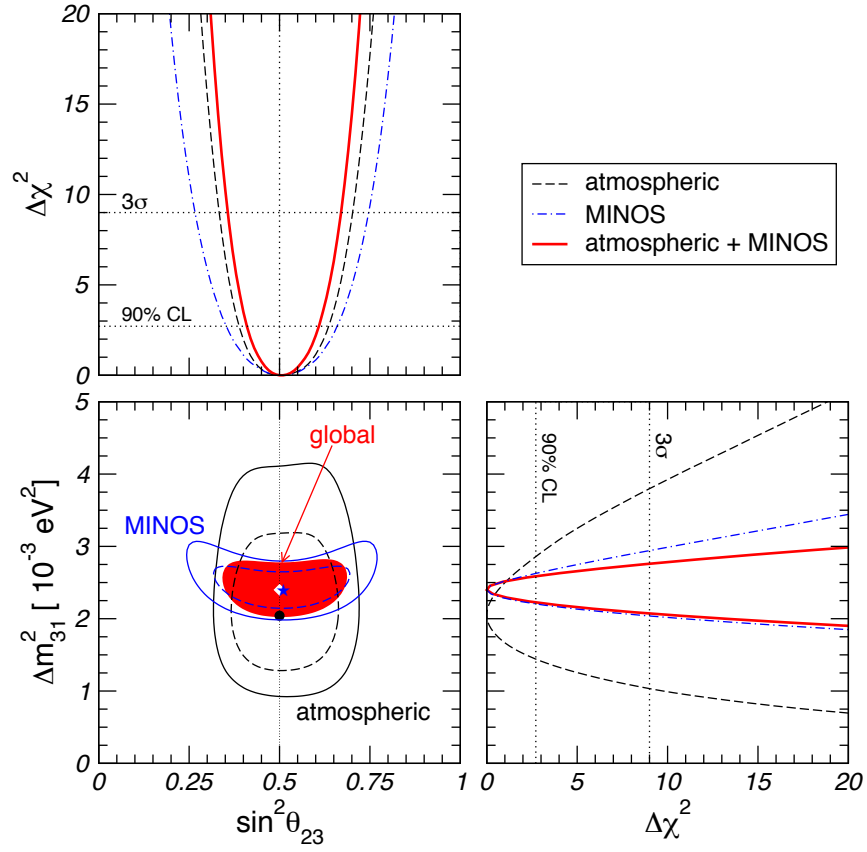
Figure 2.3: Determination of the leading atmospheric oscillation parameters from the interplay of data from artificial and natural neutrino sources. χ^2-profiles and allowed regions at 90% and 99.73% CL (2 dof) are shown for atmospheric and MINOS, as well as the 99.73% CL region for the combined analysis (including also K2K). The dot, star and diamond indicate the best fit points of atmospheric data, MINOS and global data, respectively. Minimization is done with respect to Δm_{21}, θ_{12} and θ_{13}, including always solar, KamLAND, and CHOOZ data. Figure from [38].

2.2 Summary of experimental results

The simplest explanation of the solar neutrino data described in Section 2.1.1 is the oscillations of ν_e into an active (ν_μ and/or ν_τ). Moreover, the simplest and most direct interpretation of the atmospheric neutrino data described in Section 2.1.2 is that of muon neutrino oscillations.

From the results previously described it is obvious that the minimum joint description of solar and atmospheric evidences requires that all three known neutrinos take part in the oscillations. Recall that we have two different Δm^2, from solar and atmospheric experiments:

$$\Delta m_{21}^2 = \Delta m_{sol}^2 \ll \Delta m_{\text{atm}}^2 = |\Delta m_{31}^2| \simeq |\Delta m_{32}^2|. \tag{2.16}$$

In this case, the mixing parameters are encoded in the 3×3 lepton mixing PMNS matrix. Moreover, one can add or not a term containing Majorana phases since they are not observable.

As soon as one considers the 3 neutrino scheme, the interference between solar and atmospheric sectors (Eq. 2.3) has to be taken into account. Regarding the interference parameters (θ_{13} and δ_{CP}), one has to notice that we still have almost no information. Recent global data analysis [38], shows a possible hint for a non-zero θ_{13}. Combining data from the MINOS appearance data and the atmospheric + long-baseline + CHOOZ analysis gives a nonzero best fit value of θ_{13} (see Figure 2.4). Furthermore, if there is a non-vanishing δ_{CP}, the feasibility of a measurement depends on the actual value of θ_{13}, since it enters the PMNS matrix only through the combination with $\sin \theta_{13}$ (see Eq. 1.25).

From the global combined analysis of the oscillation experimental data, the derived ranges for the six oscillation parameters at 1σ (3σ) are [38]:

$$
\begin{aligned}
\Delta m_{21}^2 &= 7.59 \,_{-0.18}^{+0.23} \left(_{-0.56}^{+0.88}\right) \times 10^{-5} \text{ eV}^2, \\
|\Delta m_{31}^2| &= 2.4 \,_{-0.11}^{+0.12} \left(_{-0.33}^{+0.35}\right) \times 10^{-3} \text{ eV}^2, \\
\sin^2 \theta_{12} &= 0.318 \,_{-0.016}^{+0.019} \left(_{-0.048}^{+0.062}\right), \\
\sin^2 \theta_{23} &= 0.50 \,_{-0.06}^{+0.07} \left(_{-0.14}^{+0.17}\right), \\
\sin^2 \theta_{13} &= 0.013 \,_{-0.009}^{+0.013} \left(\leq 0.053\right), \\
\delta_{\text{CP}} &\in [0, 360].
\end{aligned}
\tag{2.17}
$$
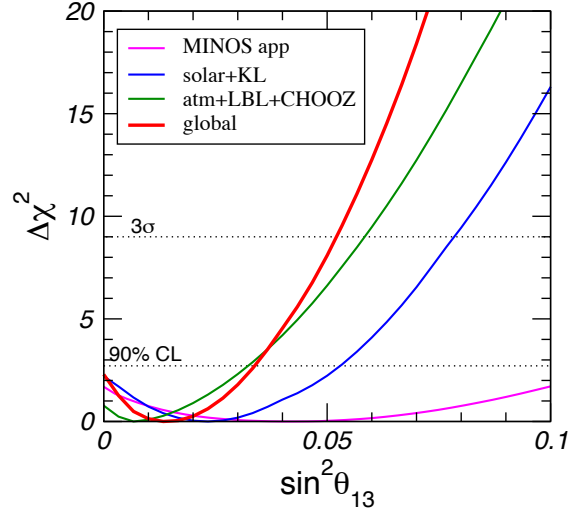
Figure 2.4: The constraint on $\sin^2\theta_{13}$ from MINOS ν_e appearance data, solar + KamLAND data, atmospheric + CHOOZ + K2K + MINOS (disappearance as well as appearance), and the combined global data. Taken from [38]

Oscillation experiments cannot determine the absolute magnitude of the masses, or differentiate between different mass patterns. In particular, if ν_i ($i = 1, 2, 3$) are the mass eigenstates, such that $m_1 < m_2 < m_3$, one could have:

$$\Delta m_{\text{sol}} = m_2 - m_1, \quad \Delta m_{\text{atm}} = m_3 - m_2$$
$$\Delta m_{\text{atm}} = m_1 - m_3, \quad \Delta m_{\text{sol}} = m_2 - m_1 \tag{2.18}$$

The first situation corresponds to the neutrino pattern known as *normal* hierarchy (the gap between the two lightest states corresponds to the small mass difference measured by solar experiments) while the second is known as *inverted* hierarchy (the gap between the two lightest states corresponds to the large mass difference measured by atmospheric experiments). This is shown in Figure 2.5.

Finally, kinematical tests and cosmological data provide upper limits to the absolute neutrinos mass scale. Results can be summarized as follows:
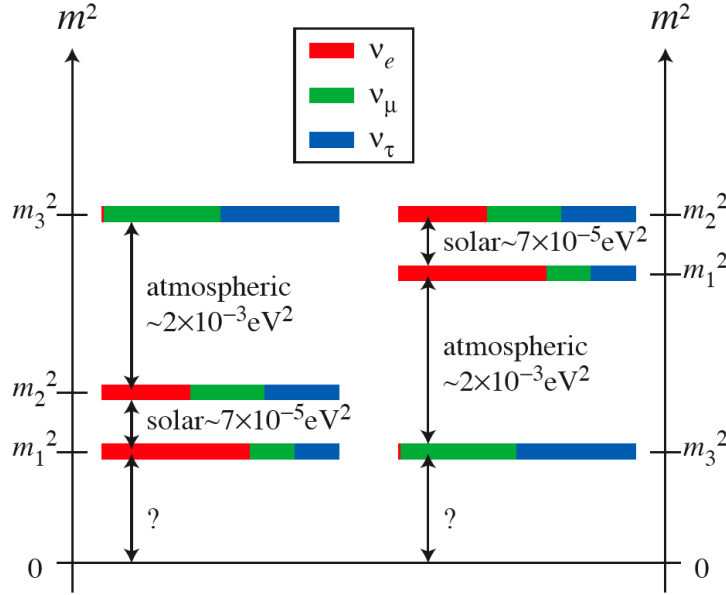
Figure 2.5: The two possible configurations of neutrino masses, normal (left) and inverted (right) hierarchies, as suggested by oscillation experiments. The flavour composition of the mass states is shown as well.

$$m_{\nu_e} < 2.2 \text{ eV} \qquad \text{from} \quad {}^3\text{H} \to {}^3\text{He} + e^- + \bar{\nu}_e$$

$$m_{\nu_\mu} < 190 \text{ keV} \qquad \text{from} \quad \pi^- \to \mu^- + \bar{\nu}_\mu$$

$$m_{\nu_\mu} < 18.2 \text{ MeV} \qquad \text{from} \quad \tau^- \to n\pi + \nu_\tau$$

$$\sum m_\nu < 0.3 - 3.0 \text{ eV} \qquad \text{from} \quad \Omega_\nu h^2 = \sum_i m_i/(94 \text{ eV})$$

2.3   Open issues in neutrino physics

We summarize now the open issues concerning neutrino physics and the ways in which they can be solved. The next generation of accelerator neutrino experiments like T2K [46], NOνA [47] and reactor neutrino experiments like Double-Chooz [48], Daya-Bay [49] and RENO [50] will provide better accuracy for the oscillation parameters and improved sensitivity to the mixing angle θ_{13}. In order to observe CP violation (measurement of the phase δ in PMNS matrix) and to resolve neutrino mass pattern, a new generation of experiment will need to be projected: the so-called Beta Beams [51], Neutrino Factories

[52] or very long baselines experiments are the possibilities under study. Moreover, new $\beta\beta$ experiments will keep on searching for the $\beta\beta^{0\nu}$ process to test the Majorana nature of neutrinos. From the theoretical point of view, the models explaining neutrino masses will need to be revisited as new experimental results show up. More specifically, the following is the list of the open issues in experimental neutrino physics:

1. **Precision measurements of the oscillation parameters**
   Now that oscillation of both solar and atmospheric has been confirmed, the goal regarding oscillation experiments is to measure the known oscillation parameters (θ_{12}, θ_{23}, Δm_{21}^2, $|\Delta m_{31}^2|$) with better accuracy. This task is currently performed by experiments like T2K [46] or OPERA [53]. T2K has now accumulated one year of data and the first results on the ν_μ disappearance and ν_e appearance analyses are expected in 2011. The first candidate ν_τ CC interaction has been observed in the OPERA detector at LNGS [54]. This does not allow yet claiming the observation of $\nu_\mu \to \nu_\tau$ oscillation. However, if OPERA was to succeed measuring the appearance of ν_τ it will prove unambiguously that $\nu_\mu \to \nu_\tau$ oscillation is the dominant transition channel at the atmospheric scale.

2. **Measurements of the mixing angle θ_{13}**
   θ_{13} is still unknown, although we know it is really small or even vanishing. Its measurement is a major issue since this parameter will open the doors for an observation of the CP violation characterized by the phase δ: we recall that δ only appears in the PMNS matrix in combination with $\sin\theta_{13}$. Long baseline experiments such as T2K [46] (using SK as far detector) and NOνA [47] can determine θ_{13} by searching for ν_e appearance in man-made off-axis ν_μ beam. The main difference with reactor experiments is that θ_{13} now depends on δ_{CP}. T2K and NOνA look for ν_e appearance by comparing neutrino fluxes measured in a near detector to fluxes measured in a far detector, placed at the end of the baseline. The baseline is 295 km for T2K and 810 km for NOνA. Both use the so-called off-axis technique for their detectors to produce a sharp peak in the energy spectrum of neutrinos at the critical energy. This optimize greatly the measure of the oscillation probability. The Neutrino beam energy will be 0.7 GeV for T2K and 2.3 GeV for NOνA. Both experiments expect to measure θ_{13} if it is greater of about 2.5°. T2K is currently taking data and NOνA is expected to start in 2013. Moreover, Double Chooz, Daya-Bay and RENO will be able to analyze the

survival probability of reactor antineutrinos in a short baseline:

$$P_{ee} \simeq 1 - \sin^2 2\theta_{13} \sin^2 \left(\frac{\Delta m_{31}^2 L}{4E} \right) + ... \tag{2.19}$$

At a future stage, long baseline accelerator experiments will use Super-beams, with major intensity upgrades with respect to current beams, thus reaching better sensitivities to θ_{13}. The ultimate accelerator facility for neutrino oscillation experiments will be a neutrino factory, where ν_e and $\bar{\nu}_\mu$ ($\bar{\nu}_e$ and ν_μ) beams of high intensity will be obtained from the decay of stored μ^+ (μ^-), along with new detector technologies.

3. **Mass hierarchy**

The current knowledge of the oscillation parameters leads to two possible orderings of the neutrino mass eigenstates: the so-called normal and inverse hierarchies. These two mass patters can be distinguished by means of matter effects in long-baseline experiments, which enhance the probability $P(\nu_\mu \to \nu_e)$ and suppress $P(\bar{\nu}_\mu \to \bar{\nu}_e)$ or vice versa depending on the sign of Δm_{31}^2. Long baselines are needed in order to observe such matter effects.

4. **CP violation**

If there is intrinsic CP violation in the neutrino sector, then $P(\nu_\mu \to \nu_e) \neq P(\bar{\nu}_\mu \to \bar{\nu}_e)$, depending the difference in these CP-conjugate vacuum probabilities on the oscillation parameters:

$$\Delta P \propto \left(\frac{\Delta m_{21}^2}{\Delta m_{31}^2} \right) \sin \delta \sin^2 \theta_{13}, \quad \frac{\Delta P}{P} \propto \frac{X_{21} \sin \delta}{\theta_{13}} \tag{2.20}$$

Thus, as previously pointed out, the feasibility of a measurement of the CP phase δ depends on the value of the mixing angle θ_{13}. Moreover, actual CP violation has to be distinguished from the faked one coming from matter effects by means of the proper choice of the baseline length.

5. **Unitarity of the 3x3 mixing matrix**

In order to test the unitarity of the neutrino mixing matrix and thereby determine is there is room for the existence of sterile neutrinos, one needs to measure all its elements. Again, a neutrino factory could measure the needed six oscillation probabilities ($\nu_\mu \to \nu_\nu$, $\nu_\mu \to \nu_e$, $\nu_\mu \to \nu_\tau$, $\bar{\nu}_e \to \bar{\nu}_e$, $\bar{\nu}_e \to \bar{\nu}_\mu$, $\bar{\nu}_e \to \bar{\nu}_\tau$) through the detection of the six corresponding charged leptons.

6. **Dirac or Majorana masses**

   The only way to discover the actual nature of neutrino masses is by the measurement of the $\beta\beta^{0\nu}$ decay, since it occurs only if neutrinos are Majorana particles. In addition, the observation of such a process would provide a measurement of the neutrino effective mass $\langle m_{\beta\beta} \rangle$, offering a valuable information to constrain neutrino absolute mass scale. There are several projects for the $\beta\beta^{0\nu}$ search using different experimental approaches. No matter which technology is used, $\beta\beta^{0\nu}$ experiments face the same kind of problems: the background has to be reduced almost to zero, meanwhile the amount of isotope used has to be really large (hundreds of kg) if one wants to test the inverse hierarchy.

The fact that neutrinos are massive particles is the first discovery beyond the Standard Model. Although first round of oscillation experiments have provided a measurement of the parameters involved in the so-called solar and atmospheric sectors, the projected experiments for the near future (few years) have great potential for another breakthrough in the measurement of the mixing angle θ_{13} that connects both sectors. Moreove, a larger time scale is needed in order to test the CP-violation in oscillation experiments, as well as to reach sensitivity to the normal hierarchy region in $\beta\beta$ experiments.

2.4 Accelerator-based neutrino beams

2.4.1 Overview

Conventional accelerator-based neutrino beams come from the decay of light hadrons produced on a fixed target, when a primary proton beam collides with it. Neutrinos come mostly from pion decay, although kaons give also a contribution :

$$
\begin{aligned}
p + \text{target} \rightarrow & \quad \pi^{\pm} + X \\
\pi^{\pm} \rightarrow & \quad \mu^{\pm} + \nu_{\mu}(\bar{\nu}_{\mu}) \\
& \quad \mu^{\pm} \rightarrow e^{\pm} + \nu_e(\bar{\nu}_e) + \bar{\nu}_{\mu}(\nu_{\mu})
\end{aligned}
\tag{2.21}
$$

A major enhancement of neutrino fluxes has been achieved through the addition of magnetic focusing systems, called horns, in the neutrino beam design. The neutrinos themselves, of course, cannot be focused by magnetic fields, but only their charged π and K parents. However, the daughter neutrinos are highly boosted in the laboratory frame for typical parent meson energies at the order of 1 GeV so the neutrino direction is highly

correlated with the meson direction in the lab and focusing the parent mesons acts to focus the neutrino beam.

The beam contains both μ- and e-neutrinos and antineutrinos. The final composition and energy spectrum of the neutrino beam is determined by selecting the sign of the decaying π and by stopping the produced μ in the beam line. The beam intensity depends on the energy of the primary proton beam. There is an additional contribution to the electron neutrino and antineutrino flux from kaon decay (see next Section).

Accelerator neutrino beams can be used to test oscillation of atmospheric neutrinos taking advantage of the controlled neutrino source. Energy of accelerator neutrinos is about a few GeV, and thus distance between accelerator and neutrino detector has to be of the order of hundred kilometers in order to be sensitive to the same Δm^2 involved in atmospheric neutrino oscillation.

The analysis technique of accelerator neutrino beam experiments relies on the comparison between neutrino flux measured at a far detector, where oscillation is expected to take place according to atmospheric neutrinos experiments, and the predicted flux at the same detector in absence of oscillation. Any discrepancy between the observation and the prediction can be described in terms of neutrino oscillation. Therefore, the key point of these experiments is to be able to predict with high accuracy the un-oscillated flux at the far detector. To get such a prediction, neutrino flux is measured at a near detector (close to the beam source), where neutrinos have not oscillated yet, and then flux is extrapolated somehow to the far detector.

2.4.2   Relevance of hadron production measurements for accelerator-based neutrino experiments

Limitations in modeling hadron production using Monte Carlo simulations

To better motivate the measurement to be presented below we now look at the impact of the hadronic interaction models used in the simulation of accelerator-based neutrino beams. A typical simulation of an accelerator neutrino beam begins with inclusive, double-differential production cross-sections for p, n, π^+, $\pi-$, K^+, K^- and K^0 produced in the collisions of incident protons on a nuclear target. The major source of uncertainty in the accurate prediction of neutrino fluxes is the production of these primary hadrons. A secondary effect arises from the reinteractions and absorption that can take place in thicker

nuclear targets. Further, the use of focusing systems means that a larger region of π and K phase space is relevant to the flux predictions.

Figure 2.6 shows the resulting neutrino fluxes using the MiniBooNE Geant4 beam Monte Carlo [55]. The left panel shows the resulting ν_μ flux predictions in neutrinos per proton on target per cm^2 of detector surface area for four different primary hadronic interaction models used in the simulation[1]. All other components of the MiniBooNE beam Monte Carlo are held fixed for these comparisons.

One clearly sees that a naive choice of available hadronic interaction models is not acceptable. Just the four models shown would imply a flux uncertainty of order 50-100%. Production data is clearly needed to motivate a choice between available models or to facilitate the generation of a new one.

The best way to reduce primary production uncertainties is by making dedicated hadron production measurements with an identically matched beam and target configuration. That was one of the primary design of the HARP experiment.

HARP data have been used to reduce these uncertainties in two major neutrinos experiment:

K2K

The calculation of the flux and neutrino flavours composition of a neutrino beam requires a precise measurement of the interaction cross-section between the beam particles and the target material. In the case of the K2K and MiniBooNE experiments, the dominant component of the beam (muon neutrinos) comes from the decay of positive pions produced in the collisions between the incident protons and the target. To compute the ν_μ flux one needs a 4π parametrization of the differential cross section which, in order to be reliable, must be based on a wide-acceptance and precise measurement. In the K2K analysis, the determination of the far/near ratio was the leading energy-dependent systematic error. To compute this quantity a Monte Carlo program simulating all relevant beam-line geometry and materials, and all relevant physics processes, is used. In this simulation, the neutrino flux prediction uncertainty is dominated by the uncertainties in the forward π^+ production from the interactions of the 12.9 GeV/c protons in the aluminium target material. By using

---

[1]MARS (v15) [56], "Low Energy Parameterization Driven Model" (G4 LHEP) [57], "Bertini Intranuclear Cascade Model" (G4 Bertini) [58], "Binary Cascade Model" (G4 Binary) [59]
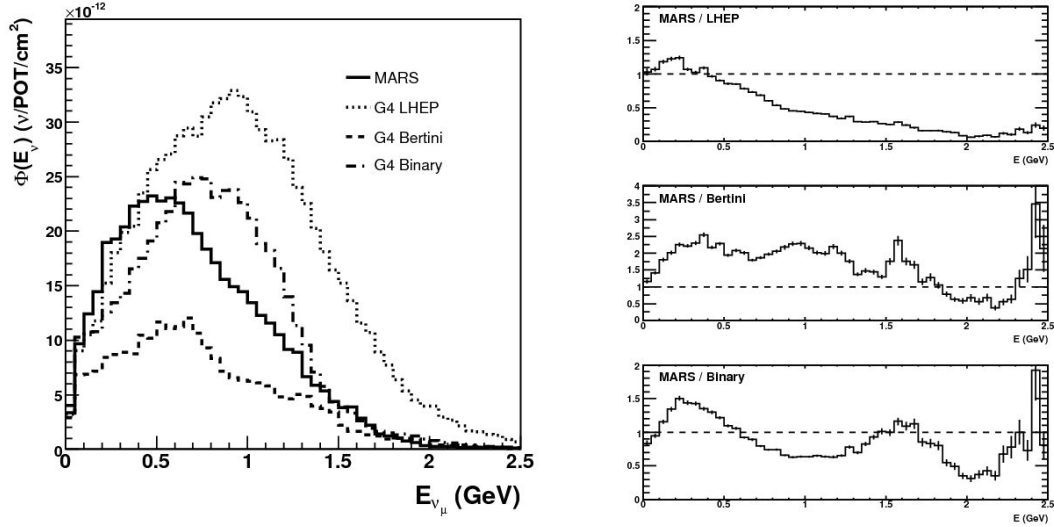
Figure 2.6: Comparison of generated ν_μ fluxes at the MiniBooNE detector for four different hadronic interaction Monte Carlos used for the production of hadrons in primary interactions of p+Be at 8.9 GeV/c. Plot taken from [60]

the HARP results on pion production measurements obtained for the same proton beam momentum (12.9 GeV/c) and nuclear target material (aluminum) as those used to produce the K2K neutrino beam, the total F/N error is reduced by a factor 2 across all energies with respect to the previous results based on the simulation. The result of the pion production measurements of HARP experiment [61] is incorporated into the K2K beam MC simulation to estimate the neutrino spectra at ND and SK and the energy dependence of the F/N flux ratio in the absence of neutrino oscillations. The F/N flux ratio, Φ^{SK}/Φ^{ND}, predicted by the HARP π^+ production measurement for primary hadronic interactions with the systematic error evaluation discussed above, in the absence of neutrino oscillations, is shown in Figure 2.7 as a function of neutrino energy. The flux ratio uncertainty as a function of the neutrino energy binning used in the K2K analysis is at the 2-3% level below 1 GeV neutrino energy, while it is of the order of 4-9% above 1 GeV. The dominant contribution to the uncertainty in F/N comes from the HARP π^+ measurement itself. In particular, the uncertainty in the flux ratio prediction integrated over all neutrino energies is 2.0%, where the contribution of the HARP π^+ production uncertainty is 1.4%. The dotted histograms in Figure 2.7 show the central value predicted by using the Cho-CERN compilation for primary hadronic interactions, which was used in K2K prior to the availability of HARP data. In this case,
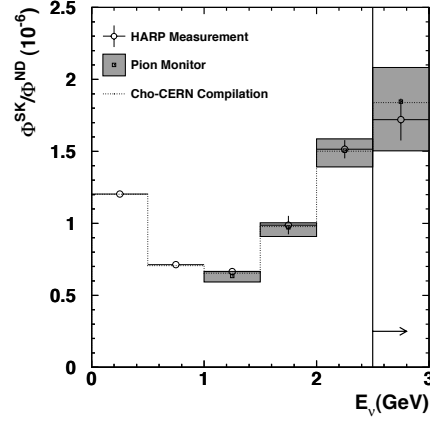
Figure 2.7: Prediction for the K2K muon neutrino F/N flux ratio in absence of oscillations. The empty circles with error bars show the central values and systematic errors on the muon neutrino flux predictions from the HARP π^+ production measurement discussed in the text, the empty squares with shaded error boxes show the central values and errors from the pion monitor measurement, and the dotted histograms show the central values from the Cho-CERN compilation of older (non-HARP) π^+ production data. Plot taken from [39].

the same Sanford-Wang [62] functional form of π^+ production is employed to describe a CERN compilation of π^+ production measurements in proton-beryllium interactions, which is mostly based on Cho et al. data [63]. A nuclear correction to account for the different pion production kinematics in different nuclear target materials is applied. We find that the predictions of F/N flux ratio by HARP and Cho-CERN are consistent with each other for all neutrino energies. Note that the difference between Cho-CERN and HARP central values represents a difference in hadron production treatment only. Among the available parametrization, K2K uses in neutrino oscillation analysis the one predicted by the HARP measurements since the HARP pion production measurement was done in the same conditions as K2K experiment: the proton beam momentum and the relevant phase space of pions responsible for the neutrinos in K2K are the same. In particular, the measured momentum region of the HARP experiment reaches below 2 GeV/c down to 0.75 GeV/c where the K2K Monte Carlo is insensitive.

MiniBooNE

MiniBooNE, at Fermilab was designed to address the oscillation signal reported by the LSND collaboration. MiniBooNE searched for the appearance of electron neutrinos

in a beam that is predominantly muon flavour with an L/E similar to LSND but with substantially differing systematics. One important systematic arises from the prediction of the fluxes of different neutrino flavours at the MiniBooNE detector. The MiniBooNE neutrino beam is produced from the decay of π and K mesons as results of collisions of 8.9 GeV/c protons from the Fermilab Booster on a 71 cm beryllium target.

Early versions of the MiniBooNE flux predictions were based upon the SW model fit to the $\pi^{\pm}$ production cross-sections at $p_B = 6.4$ GeV/c and 12.3 GeV/c measured by the E910 experiment at Brookhaven National Laboratory [64]. A model such as SW was absolutely necessary for interpolating the differential cross-sections to $p_B = 8.9$ GeV/c, but model uncertainties are large and difficult to quantify. The HARP data, therefore, being at exactly the Booster momentum, are a critical addition to the development of the pion production model, reducing the model uncertainties from extrapolation to 8.9 GeV/c. The result is an absolute neutrino flux prediction with uncertainties larger than those of the underlying hadron production data used to predict it. However it is critical to note that the analysis methods used in the ν_e appearance search make it largely insensitive to normalization errors on pion production. It is for absolute neutrino cross-section measurements and ν_{μ} disappearance searches to be made at MiniBooNE in the future that the flux errors from pion production have the greatest impact. Using the spline method [65], absolute flux predictions to better than 10% should be achievable where the flux is directly constrained by production data at 8.9 GeV/c from HARP.

Figure 2.8 illustrate the regions of muon and electron neutrino flux that are directly constrained by the HARP cross-section data for neutrino modes. It is worth noting that any tests one can perform to quantify the coverage are slightly circular - data is used to generate a model which is used in a simulation of the beamline which is, in turn, used to quantify the impact of the data. Despite small model dependencies, however, such an exercise remains important for defining the regions of meson production which are shown to be important to the flux prediction yet remain unconstrained by data. In each panel of Figures 2.8 the total ν_{μ} or ν_e flux prediction is given by the solid black histogram on the right plot. The other curves and the left panel illustrate the direct impact of the HARP data on the MiniBooNE flux prediction. For example, in the top panel the blue curve on the right shows the high fraction (90.3%) of total ν_{μ} which come from the decays of π^+ which were created in primary interactions in the target. The kinematic distribution of these π^+ are shown by the black histogram in the 2D panel on the left. The red box marks the
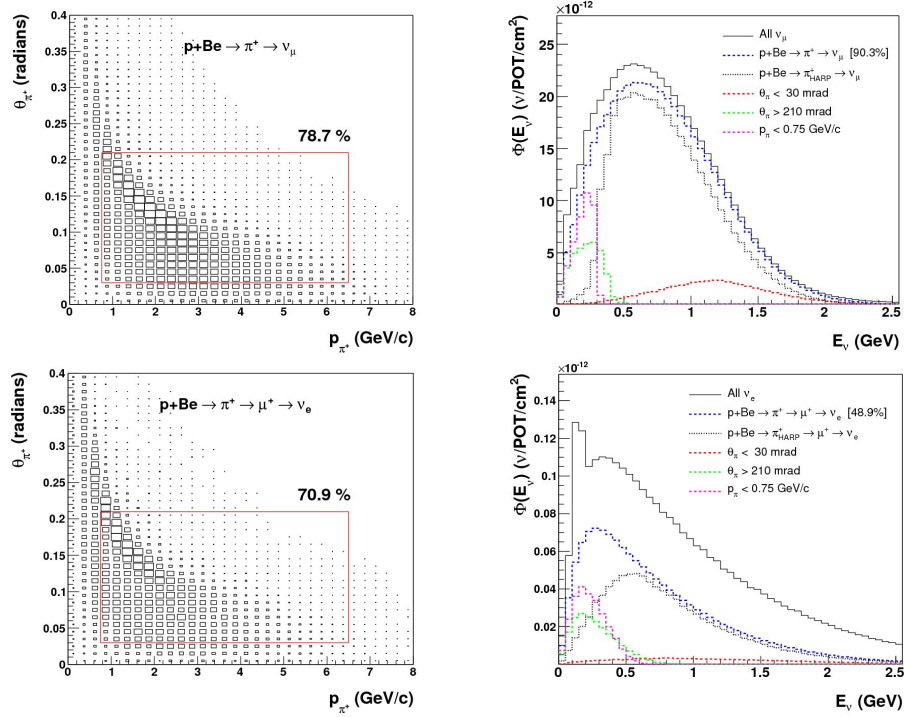
Figure 2.8: Relevance of the HARP forward production data for the MiniBooNE ν_μ and ν_e flux predictions in neutrino mode. See the text for details. Plots taken from [60].

boundary of the HARP measurement and thus the region of the π^+ parameterization that is directly constrained by data. Moving back to the right panel, the dashed black curve, labeled $p + Be \rightarrow \pi^+_{\mathrm{HARP}} \rightarrow \nu_\mu$, shows the ν_μ whose parent π^+ is directly constrained by the HARP data (originates from inside the red box). Almost 80% of the π^+ which contribute to the ν_μ flux are being directly constrained by the measurement. The remaining three curves (red, green, magenta) show the flux contributions from primary π^+ which are not being directly constrained by HARP data.

2.4.3 Relevance of Kaon measurements

As explained above, the interaction of primary beam protons with the target also produce charged kaons. Strange particle production in the forward direction must be well known when trying to determine the ν_e background in a ν_μ beam, since K_{e3} decays of $K^\pm$ and K^0_L constitute an irreducible background in the search of the $\nu_\mu \rightarrow \nu_e$ oscillations.

This applies particularly to the MiniBooNE where G4 simulations showed that
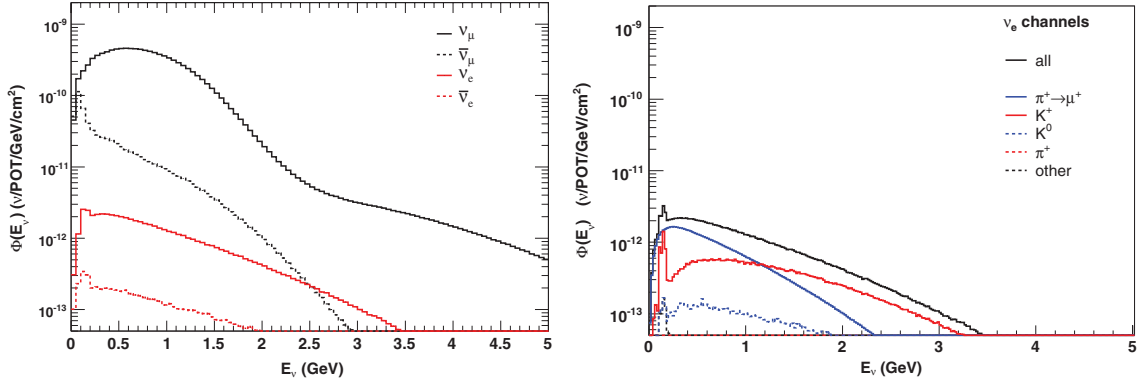
Figure 2.9: Left: Total predicted flux at the MiniBooNE detector by neutrino species with horn in neutrino mode. Right: predicted ν_e flux at the MiniBooNE detector by parent meson species with horn in neutrino mode. The black line is the total predicted flux, while all the subcomponents apart from the dashed black are from nucleon-induced meson production of the indicated decay chains. The dashed black histogram includes all other contributions, primarily from meson decay chains initiated by meson-nucleus interactions. Plots taken from [66].

kaon decays contribute to more than 40% of the total intrinsic ν_e background of the beam. The top panel of Figure 2.9 shows the total predicted flux of each neutrino species at the MiniBooNE detector with the horn set in neutrino mode. This shows quantitatively the irreducible background one can expect in the neutrino beam. The channels through which ν_e are produced (horn in neutrino mode) are shown in the bottom panel of Figure 2.9. For the ν_e flux, the two dominant components are the $\pi^+ \to \mu^+ \to \nu_e$ decay chain and three-body $K^+ \to \nu_e$ decay, where the former is dominant at low energies (< 1 GeV) and the latter is dominant at higher energies. The peak in the $K^+ \to \nu_e$ spectrum at low energies is from the decay of K^+ at rest (the peak from two-body decay is much smaller due to helicity suppression). Again, The best way to reduce primary kaon production uncertainties is by making dedicated kaon production measurements with an identically matched beam and target configuration.

Other experiments can also benefit from the direct measurement of charged kaons cross-sections such as SciBooNE, K2K and T2K. This particular HARP data set will also be useful for the determination of the quality of the possible low energy conventional neutrino beam such as the CERN SPL.

The absolute differential production cross-sections for positive kaons produced from

the collisions of 12.9 GeV/c protons with a 5% interaction length aluminum target have been measured int the HARP experiment. The HARP detector is described in Chapter 3 followed by a presentation of the analysis method and results in Chapter 4.

Chapter 3

The HARP Experiment

The HARP experiment at the CERN PS [67, 68] took data in 2001-2002. It was designed to make measurements of hadron yields from a large range of nuclear targets and for incident particle momenta from 1.5 GeV/c to 15 GeV/c. The main motivations are the measurement of pion yields for the design of the proton driver of a future neutrino factory, the calculations of the atmospheric neutrino flux, to provide a large set of data to improve hadronic models in Monte Carlo simulation models and the measurement of particle yields as input for the flux calculation of accelerator neutrino experiments. In this chapter, I describe the experimental apparatus and present the calibration and performance of the sub-detectors relevant to our analysis.

3.1 Motivations

The first proposed [67] goal of the HARP experiment is to contribute to optimization studies in the design of a future Neutrino Factory [52]. The front end of a Neutrino Factory would include a high intensity proton beam focused onto a high Z nuclear target for the large production of secondary charged pions. These pions are allowed to decay and the resulting muons must be cooled and guided into an accelerator channel. An optimized design of this system (including the choice of incident proton beam momentum and target material) requires precise knowledge of the phase space distribution of the charged pions created in proton-target collisions [69].

Second, HARP has collected data with a solid carbon target (carbon has the atomic mass nearest to that of nitrogen and oxygen), as well as with nitrogen and oxygen cryogenic

targets as these results have a direct relevance for the precise prediction of atmospheric neutrino fluxes (p-C interactions) and extended air shower modeling (π-C interactions). The largest systematic in the determination of oscillation parameters from atmospheric neutrino data arises from an incomplete model of the interactions of protons and pions with nitrogen and oxygen in the Earth's atmosphere [27].

Third, the data recorded by HARP can have a broad impact on the improvement of models used in the simulation of hadronic interactions in this energy range. There are several hadronic interaction simulation packages which claim some validity in the energy range represented by the HARP data set, including MARS15 [56], the Binary cascade model [59], the Bertini intra-nuclear cascade model [58], the Quark-Gluon String CHIPS (QGSC) model and the Quark-Gluon String Precompound (QGSP) model. Differences between the models' predictions can be resolved and deficiencies in the models can be revealed by a detailed comparison of their predictions to a data set like that available from HARP.

Finally, measurements made at HARP can have a direct impact on the detailed understanding of the neutrino fluxes of several accelerator-based neutrino experiments, including the K2K [39] experiment in Japan and MiniBooNE [70] and SciBooNE [71] at Fermilab. The K2K muon neutrino beam is created by decaying pions produced in collisions of 12.9 GeV/c protons from the KEK PS with an aluminum target. The Booster Neutrino Beam, used by MiniBooNE and SciBooNE, begins when 8.9 GeV/c protons from the Fermilab Booster are impinged upon a beryllium target. HARP recorded millions of events with these exact beam energies and target materials using both thin and thick targets.

3.2 Glossary of particles and kinematic variables at HARP

- *Primary beam particles* from the T9 beam are guided in from the left in both figures and collided with a nuclear target sitting inside the volume of the TPC.

- *Secondary particles* are created in primary interactions of beam particles with target nuclei. We are only interested in these particles when measuring production cross-sections. Hadrons created in interactions other than primary beam particles with target nuclei are a background to the measurement.

- *Tertiary particles* are those created when secondary particles decay or inelastically interact downstream of the target in air or detector materials and are not to be included

in the measured cross-section.

- In the HARP coordinate system the center of the target is located at $(x, y, z) = (0,0,0)$.

- The z-axis is oriented along the primary beam direction, $+x$ is to the left and $+y$ is up, as shown in Figure 3.1.

- Given azimuthal symmetry in hadron production, all physics results are presented in polar coordinates (p, θ) where p is the total momentum of the particle and θ is the angle with respect to the primary beam direction (approximately equal to the z-axis).

- Given the rectangular geometry of the dipole and drift chambers, $\theta_x = \tan^{-1}(p_x/p_z)$ and $\theta_x = \tan^{-1}(p_y/p_z)$ are useful variables for viewing the detector in x, y-plane coordinates.
  They are related to the standard polar angle by $\theta = \tan^{-1}(\sqrt{\tan^2 \theta_x + tan^2\theta_y})$.

3.3   The HARP detector

The experimental layout consists of four main functional parts: the beamline along with the detection and identification of incoming beam particles, the trigger detectors, the large-angle spectrometer housing the target and the forward spectrometer.

The beamline selects secondary particles with positive or negative charge emerging from a primary target in the extracted proton beam from the PS accelerator. It covers the momentum range between 1.5 and 15 GeV/c . Particle identification in the beamline is provided by two gas Cherenkov detectors (Beam Cherenkov A and B: BCA, BCB) and a pair of time-of-flight counters (TOF-A, TOF-B). Four multi-wire proportional chambers (MWPC) measure the position and direction of the beam particles upstream of the target. Several scintillation counters serve to trigger on single incoming beam particles.

The global layout of the HARP experiment is shown in Figure 3.1. It covers a total length of 13.5 m along the beam direction. The large-angle spectrometer, composed of the TPC and a set of multi-gap resistive plate chambers (RPC), is housed in a solenoid magnet. The TPC provides track, momentum and vertex measurements for all outgoing charged particles in the angular range from 20° to 160° with respect to the beam axis. In addition, it provides particle identification by recording the particle's energy loss in the gas
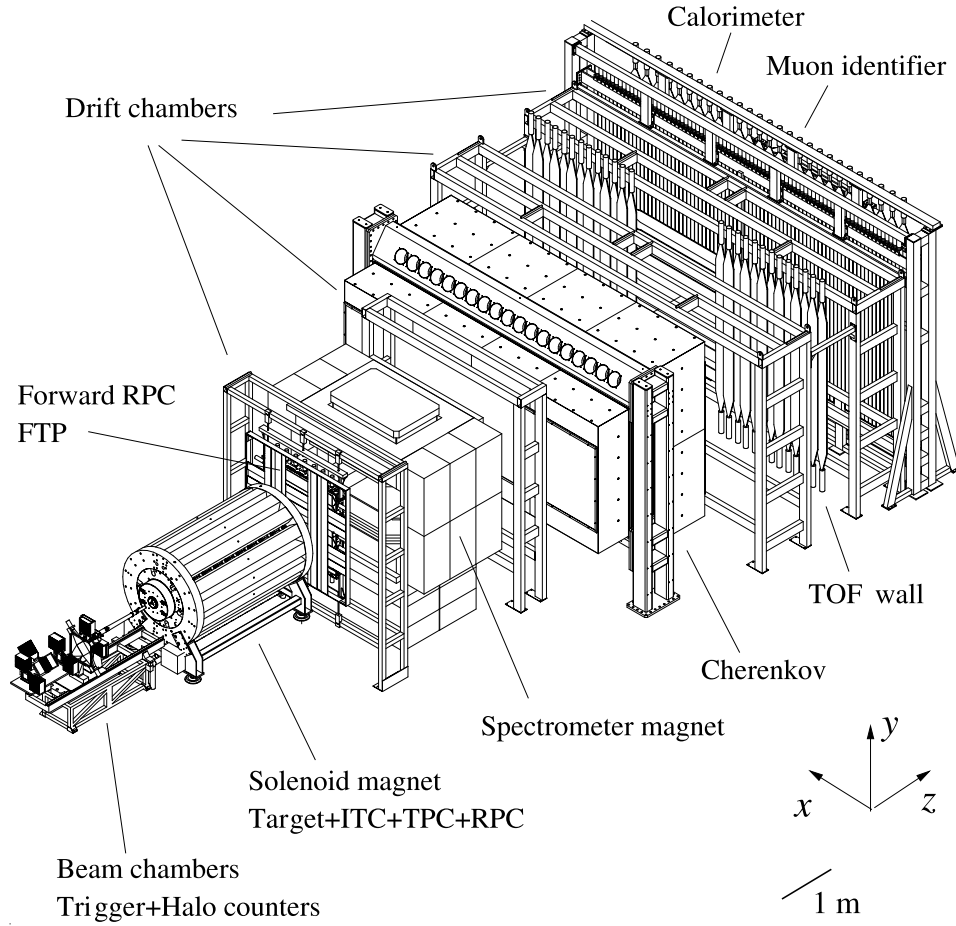
Figure 3.1: Overall layout of the HARP detector. The different sub-detectors are shown. The target is inserted inside the TPC. The convention used for the coordinate system is drawn in the figure.

(dE/dx). Its particle identification capabilities are complemented by a set of multi-gap RPC serving as time-of-flight detectors and surrounding the TPC.

The forward spectrometer measures particles produced in the forward direction at angles up to $\sim 14.3°$. A double plane of scintillation counters (forward trigger plane, FTP) placed downstream of the solenoid magnet provides the forward interaction trigger. The tracks and momenta of the outgoing particles are measured in a dipole magnet and two sets of multi-wire drift chambers (NDC). Several additional sets of drift chambers are placed further downstream to follow the particle tracks between the various particle identification detectors. Discrimination between forward going protons and pions is provided by a threshold Cherenkov counter and a time-of-flight detector. The Cherenkov counter provides particle identification at high momenta and the (TOFW) detector at low momenta. Electrons are identified and their energy is measured in a electromagnetic calorimeter (ECAL). The calorimeter also provides further particle identification for hadrons. The origin of the HARP coordinate system is placed in the centre of the target. The z-coordinate points in the direction of the beam, the y-coordinate upward, and the x-coordinate to the left when looking in the direction of the beam.

3.4   Targets

HARP collected data on a large range of target nuclei. Both solid and cryogenic targets were used to cover a range from small to high atomic weight, to attempt to understand the cross section scaling dependence with respect to the Z of the different materials. Moreover, to study the effect of secondary interactions, targets of different thicknesses have been analysed.

Seven elements (Be, C, Al, Cu, Sn, Ta, Pb) were chosen to provide solid targets, covering the atomic number range from 4 to 82. In order to observe the produced particles with the minimum amount of scattering or reinteraction, most measurements were made with thin disc targets (2% and 5% of one interaction length, λ_I). Because of the size of the beam, the targets are all 30 mm in diameter. Particles produced at $90°$ with respect to the beam axis would therefore see a significant amount of material. To ensure that corrections for secondary interactions are satisfactorily modelled and corrected, data have been also collected with thick targets, a full interaction length long. Finally, data have also been

collected with replica targets from two accelerator neutrino experiments, MiniBooNE [70][1] and K2K [39][2], with the intention of reducing the systematic uncertainties on the calculated neutrino fluxes of the experiment. Data have also been taken with cryogenic targets of H2, D2, N2 and O2. Data taken with H2 and D2 targets are fundamental to distinguish nucleon-induced contributions to the cross-sections from nuclear effects. Data collection with O2 and N2 targets yields direct information for the precise prediction of atmospheric neutrino fluxes. The cryogenic targets required a particular housing due to the fact that they were in liquid or gaseous form. They are contained in an envelope with a diameter of 35 mm and made from a 125 μm thick mylar foil. The entrance window has a diameter of 20 mm, thus defining the effective diameter of this target. The target cylinder is connected to the target support by a copper ring with an external radius of 18 mm and internal radius of 10 mm. The target is surrounded by aluminised mylar superinsulation layers and placed inside a cylindrical aluminum cryostat, 60 mm in diameter and 0.6 mm wall thickness, of similar shape to the solid target arm. The endcap of this tube (thickness of 250 μm) is positioned to avoid being crossed by large angle particles and to avoid multiple scattering and re-interactions. The Hydrogen 180 mm target has the same geometry of the short cryogenic target but the mylar tube that contains the Hydrogen has a length of 180 mm. Also the aluminium cryostat is the same in the two cases.

3.5   Beam instrumentation

The beam instrumentation upstream of the target includes a pair of gas threshold Cherenkov counters (BCA and BCB), two scintillation halo counters (HALO-A and HALO-B), a beam time-of-flight system (TOF-A and TOF-B), a set of four multi-wire proportional chambers (MWPC) and two special scintillation counters (BS and TDS). Their role is twofold: to provide the detection, tracking and identification of incoming beam particles (BC, TOF and MWPC) and to generate primary signals for the trigger decision (TOF-B, BS, TDS, HALO counters and optionally BCs). A schematic view of the relative positions

---

[1]The MiniBooNE replica targets are made of Beryllium and have a three-wing shape, with the wings pointing at $120°$ of each other, like the bisector of an equilateral triangle. They are 406 and 163 mm long, with a 29 mm diameter.

[2]The K2K replica targets are made of an alloy containing 98% Aluminum and are 650 and 200 mm long, with a 29.9 mm diameter.
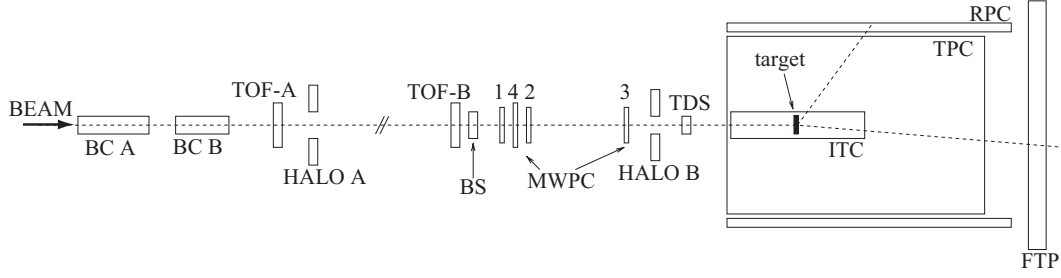
Figure 3.2: Schematic drawing of the HARP beamline showing the relative locations of the tracking (MWPC), triggering (BS,TDS,HALO-A,HALO-B) and particle identification (BCA,BCB,TOFA,TOFB) detectors. The locations of the target and ITC trigger inside the TPC volume and the FTP downstream of the TPC are also shown.

of all beam and trigger detectors is shown in Figure 3.2.

The task of beam particle identification is shared between the beam Cherenkov counters and the beam time-of-flight system. Below 3 GeV/c, the beam Cherenkovs are used to tag electrons or positrons. The TOFs are capable of resolving the more massive beam particles such as pions and protons. At 5 GeV/c the π/p-separation is done jointly by the beam TOF and one of the Cherenkovs (usually BCB), while the other Cherenkov (BCA) is used to tag $e^{\pm}$. At higher momenta the $e^{\pm}$-contamination drops to below 1% and at the same time the beam TOF system becomes unable to clearly separate pions and protons efficiently. The task of π/K/p-separation is performed by the beam Cherenkov detectors as shown in Figure 3.3.

The tracking of beam particles is performed by the beam MWPCs located near the target. These chambers are accurately aligned with respect to the nominal HARP coordinate system.

The measured tagging efficiency of both counters for pions and $e^{\pm}$ is close to 100%. The limited K-tagging capability at $\geq$12 GeV/c (Figure 3.3) is sufficient given the relatively small fraction of kaons in the beam (<1%)[3].

The beam time-of-flight system with a 21.4 m-long base is used for beam particle identification up to 5 GeV/c. In addition, the beam momentum can be accurately determined

---

[3]The K-tagging option was used mainly during exposures with K2K replica targets at 12.9 GeV/c, for which a very pure proton beam was requested.
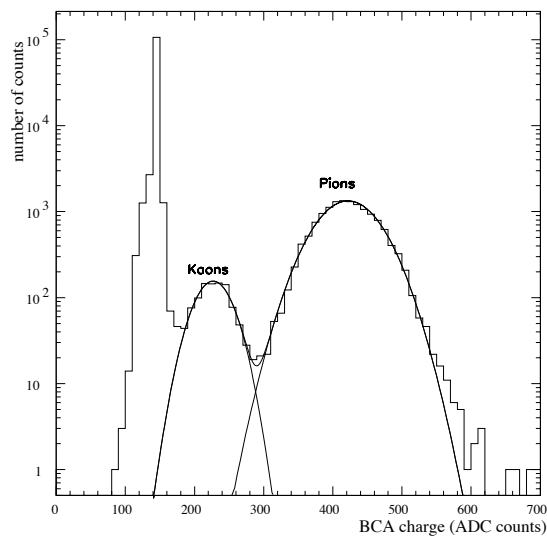
Figure 3.3: The pulse-height spectrum from the BCA Cherenkov counter for the positive 12.9 GeV/c beam.

by comparing the measured velocities of pions, protons and deuterons of the same beam, as illustrated by Figure 3.4. Two identical scintillation hodoscopes, TOF-A and TOF-B [72] provide the average time-of-flight resolution of ≈ 100 ps.

Four beam MWPCs are used for the off-line reconstruction of the beam particles, as well as for real-time beam tuning and beam-quality monitoring. They measure the beam particle position and the angle at the target with an accuracy of <1 mm and <0.2 mrad per projection. They are located close to the target in order to reduce multiple scattering effects between the track measurement and the target. The HV settings are chosen so as to maintain the efficiency above 99% for each chamber.

A beam muon identifier is placed at the downstream end of the HARP detector. Beam muons need to be identified since they would lead to a wrong interaction cross-section when accounted for as pions. At high momenta the most effective way to tag them is through non-showering in a sufficiently deep, longitudinally segmented calorimeter. At low beam momenta, beam muons, which generally result from kaon and pion decays along the beamline, are hardly discriminated from pions but are strongly bent by the magnetic dipole field of the spectrometer
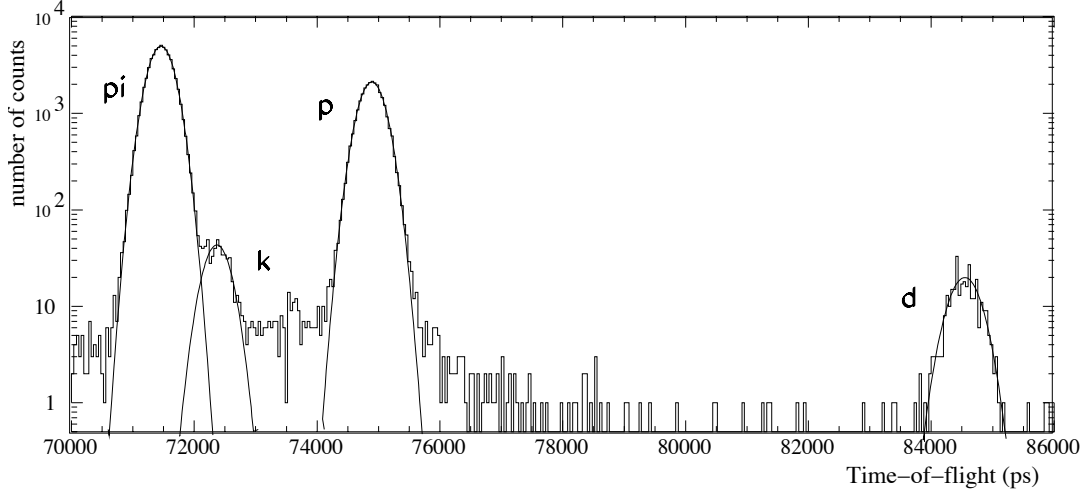
Figure 3.4: Example for beam particle identification with time-of-flight at nominal beam momentum of 3 GeV/c. Electrons have been rejected with the Cherenkov counters.

3.6 Trigger detectors

The detectors used in the trigger can be divided into two groups: beam particles are detected upstream of the target, whereas the detection of secondaries emerging from the target relies on downstream detectors and detectors surrounding the target. A schematic view of the relative position of all trigger and beam equipment is shown in Figure 3.2.

Two HALO counters (HALO- A and HALO-B) are scintillator slabs with a central hole and are used to veto events where the beam particle is accompanied by a second particle in the halo of the beam. The hole diameter of 3 cm is consistent with the target diameter.

The beam scintillator (BS) starts the decision logic of the trigger system. It is located a few centimeters downstream of TOF-B. In coincidence with a TOF-B hit it represents the lowest-level trigger (strobe). As a consequence, the timing of all trigger signals is given by the original BS signal, *i.e.* BS provides the timing reference for all ADC gates, TDC start and stop signals.

The Target Defining Scintillator (TDS) is a scintillator disc of 20 mm diameter and 5 mm thickness which is viewed by four photo-multiplier tubes. The TDS is designed to have a very high efficiency and to define a subset of beam particles which are guaranteed to hit the target. Therefore it is located as near as possible to the entrance of the TPC and with 20 mm its diameter is somewhat smaller than that of the target which is 30 mm. The TDS gives a signal if at least one PMT was hit. An efficiency of well above 99.9% is assured.
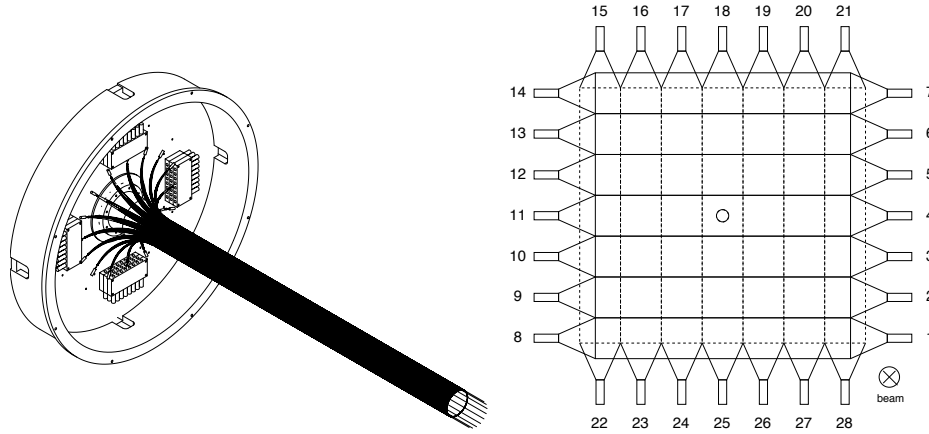
Figure 3.5: HARP downstream trigger counters. The left panel shows the Inner Trigger Counter (ITC) which surrounds the target volume inside of the TPC. The right panel is a schematic drawing of the 14 scintillator slabs of the Forward Trigger Plane (FTP) which sit downstream of the TPC and triggers on forward going particles.

The TDS has a sufficiently good time resolution ($\sim$ 130 ps) and stability to be used as an additional detector for the beam TOF system.

There are two downstream trigger counters (see Figure 3.5), one for the large angle spectrometer and one for the forward angle system.

The Inner Trigger Cylinder (ITC) provides a trigger for large angle secondaries emerging from the target. It is mounted inside the inner field cage of the TPC (see the following section) and consists of an aluminium/carbon tube with a length of 1300 mm and an inner and outer diameter of 76 mm and 92 mm, respectively. Six layers of scintillating fibres (each of diameter 1 mm) are glued on the tube (see left panel of Figure 3.5). Triggering on a logical OR condition of all 24 channels provides a combined efficiency for a single track detection of well above 99%.

Downstream of the solenoid, the Forward Trigger Plane (FTP) covers the small angle region complementary to the ITC. It is made of two planes of scintillator slabs as seen on the right panel of Figure 3.5. The planes are at 90° with respect to each other in order to minimize the insensitive areas due to the spacing between the scintillators. A 60 mm diameter hole has been cut out along the beam axis to allow non-interacting beam particles to pass without triggering the FTP. The efficiency of the FTP for single tracks is > 98%.

3.7   The large angle spectrometer

The large-angle spectrometer includes a TPC and a system of RPC counters all inside a solenoidal magnet. The detector has to measure and identify large-angle tracks in the angular region $20° \leq \theta \leq 160°$. Particle identification is obtained mainly via the dE/dx measurement performed by the TPC. Additional particle identification is performed through a time-of-flight measurement in the RPCs.

3.8   The forward spectrometer

The forward spectrometer measures the momentum and trajectory of tracks produced at small angles ($\theta \leq 17°$) via a set of drift chambers. Particle identification is performed by combining informations from a threshold Cherenkov counter (CKOV, at higher momenta), a time-of-flight wall (TOFW, at lower momenta) and an electromagnetic calorimeter (ECAL).

The dipole magnet used for momentum measurement in the forward spectrometer has a non-homogeneous field: the vertical component B_y amounts to 0.5 T in the central region and rapidly approaches zero outside the aperture. Secondary particles leaving the TPC pass through an integral field of $\int B_y dL$ of 0.66 Tm.

3.8.1   Drift chambers

A set of large drift chambers[4] is placed upstream and downstream of the spectrometer magnet (see Figure 3.1) to act as a tracking device for the forward going particles. Five modules of the NOMAD drift chambers (NDC) are used: one directly upstream of the dipole magnet, one directly downstream of the magnet, and three modules further downstream, covering a large lateral surface between the Cherenkov detector and the TOFW.

The dimensions of the NDC modules (3m × 3m) allow for full coverage of the forward solid angle as defined by the aperture of the spectrometer magnet. A charged particle can leave up to 12 hits in each traversed module, which allows a fairly accurate segment reconstruction, though each chamber represents 2% of a radiation length. Three more drift chambers were used as preshower in front of the electromagnetic calorimeter.

---

[4]These chambers have been reused from the NOMAD experiment [73], where they served both as a target for neutrino interactions and as a tracker for the produced charged particles.
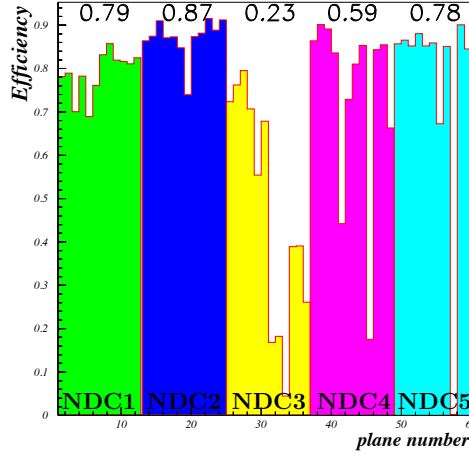
Figure 3.6: Hit efficiencies of the drift chamber planes. Different modules of drift chambers (from NDC1 to NDC5, 12 consecutive planes each) are shown by different colours. The average efficiency for each NDC module is also given.

Each chamber is made of four panels of lightweight composite materials delimiting three 8 mm gas gaps. The very efficient NOMAD gas mixture, Ar (40%) - C_2H_6 (60%), could not be used because of the stricter CERN safety rules, and a classical, non flammable mixture: Ar (90%) - CO_2 (9%) - CH_4 (1%) was chosen instead. The central gap is equipped with sense wires at $0°$ with respect to the vertical axis, the direction of the dipole magnetic field; in the outer gaps the wires are at $+5°$ and $-5°$. This small stereo angle allows for 3-D reconstruction with full precision in the horizontal direction, essential for the momentum measurement via track bending in the spectrometer magnet.

To extract the performance of the chambers (spatial resolution and hit efficiency) an alignment of all wires was done first. We used the samples of cosmic events recorded via a special trigger requiring a coincidence between the forward trigger plane (FTP), the time-of-flight wall (TOFW) and the cosmic wall (CW). The alignment parameters are validated also using beam data taken with a thick target. The resulting residual distribution gives a spatial resolution of about 340 μm, sufficient for the requirements of the HARP experiment.

Reconstructing long tracks allows us to compute hit efficiencies per chamber plane. Figure 3.6 shows their distribution for the five tracking modules (NDC1 to NDC5, 12 consecutive planes each). The average efficiencies for the central modules (NDC1, NDC2 and NDC5) lie between 80% and 85%.

Tracks are reconstructed in two steps. In the first step a segment reconstruction algorithm builds track segments in each module. A special software implementation of the Kalman filter technique [74] is used in the second step for matching of track segments and hit collection, taking into account multiple scattering and the exact field map of the spectrometer magnet. To increase track reconstruction efficiency not only tracks with good upstream and downstream segments, with respect to the dipole magnet, are considered, but also tracks with short upstream segments or even with only some hits upstream imposing a vertex constraint.

Higher level features of the drift chamber system such as the track reconstruction efficiency and the resolution and absolute scale of track momentum measurements will be explained in details in Section 3.9.

3.8.2 Cherenkov detector

In the forward direction, the particle identification capabilities of the TOFW are supplemented by a threshold gas Cherenkov detector located immediately downstream of the NDC module after the dipole bending magnet. The radiator gas chosen is perfluorobutane C_4F_{10}. In addition to its environmentally safe properties, its high refractive index allows the detector to be operated at atmospheric pressure in threshold mode to separate secondary pions from protons and kaons (see Table 3.1 for more details).

Index of refraction	1.001415
π threshold (GeV/c)	2.6
K threshold (GeV/c)	9.3
proton threshold (GeV/c)	17.6

Table 3.1: Physical properties of the perfluorobutane C_4F_{10} radiator

The particles traverse about 2 m of the radiating medium and generate photons that are deflected by about 135° upwards or downwards by two large cylindrical mirrors 6 m long and with a radius of curvature of 2.4 m. The reflecting layers of aluminium with a protective coating of magnesium fluoride were evaporated on appropriately bent 3 mm thick

polycarbonate panels. The average reflectivity of the mirrors was about 90%. A modular structure of assembled honeycomb panels supports the mirrors. The goal of the mechanical design was to obtain a large rigid structure with the minimal mass budget along the path of the dominant flux of particles. A light collection efficiency of about 80% was reached.

In order to identify a particle crossing the active volume a calibration must be performed which assigns the total number of photo-electrons to an individual cluster. Each PMT was equipped with a diode emitting a tiny pulse of light during the inter-spills of the normal data taking. In this way the single photo-electron peaks and the pedestals of each channel can be determined.

Signals in the detector are grouped into clusters, each giving a total number of photo-electrons and a position in the x-y coordinate; since the position is computed as a centre of gravity of the hit PMTs, the y coordinate of a cluster is something abstract, showing how much the signal is shared between the upper and lower rows of photomultipliers, while the x coordinate is directly related to the passage of the charged particle through the gas volume. Using runs at varying energies and selecting the beam particles in a proper way a plot for the light yield versus momentum can be obtained, as shown in Figure 3.7.

The curve adjusted to the data is:

$$N_{phel} = N_0 \cdot (1 - 1/n^2 \cdot (1 + (\frac{m_\pi}{p})^2))$$

where the parameter N_0 is the number of photo electrons in the regime of high momentum ($p \rightarrow \infty$), n is the refractive index of the gas mixture (constant) and m_π is another parameter of the fit (related to the threshold value) which should be close to the mass of the selected species (pions in this particular case). For the selected sample the fit gives $N_0 = 20.9 \pm 0.2$ and $m_\pi = 139 \pm 3$ MeV/c. The result is in agreement with the value of the pion mass.

The performance of the apparatus can be inferred from the data themselves by exploiting the redundancy of the HARP spectrometer. Information from the NDC reconstruction is used to infer the position of the Cherenkov light cone axis on the PMT plane. Combining the information from the NDC tracks, the Cherenkov hits and the energy measured in the calorimeter, one can discriminate between electrons and pions.
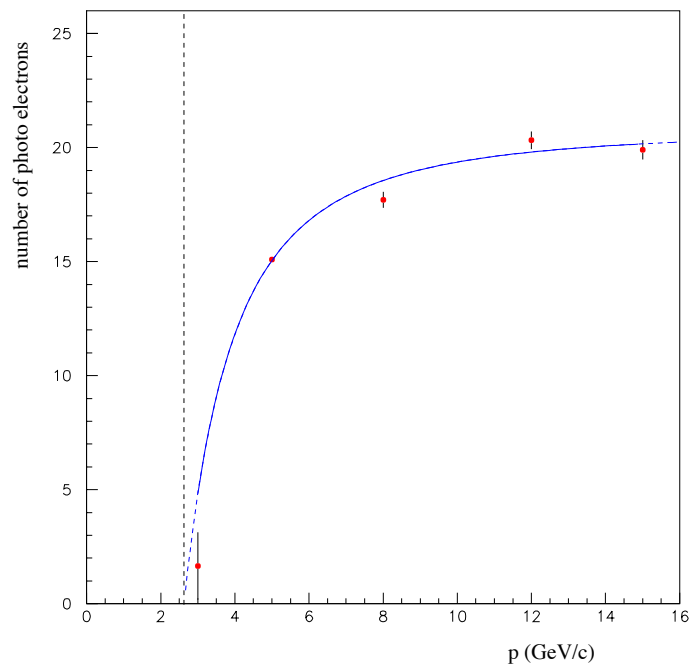
Figure 3.7: Pion light yield as a function of particle momentum: the dots are the experimental points taken at five different beam momenta (3, 5, 8, 12 and 15 GeV/c). The solid curve is a fit to the data with the function described in the text. The dashed vertical line marks the threshold for light production from pions in a gas with refractive index $n = 1.0014$.
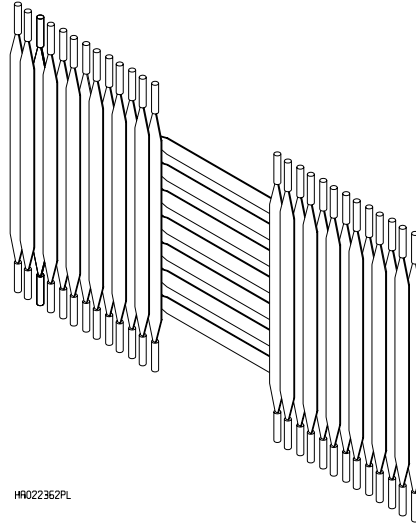
Figure 3.8: Layout of the TOF wall of the HARP experiment. The beam enters the wall from the front-left in the figure. The auxiliary detectors used for the calibration are not shown.

3.8.3   TOF wall detector

The requirements for the forward time-of-flight wall (TOFW) called for a time resolution of $\sigma \simeq 250$ ps to separate pions from protons at 4σ up to 3.5 GeV/c, on the basis of a 10 m flight path, and a good transverse segmentation to avoid particle pile-up on single counters. Particle identification is achieved by combining leading-edge time measurements (from TDC) with pulse-height informations for time-walk corrections (from ADC).

The layout of the HARP TOFW, covering an active area of $\sim 6.5 \times 2.5$ m^2 at a distance of 10 m from the production target, is shown in Figure 3.8; for more details see [75].

The scintillator counters are made of BC-408 bars from Bicron, 2.5 cm thick and 21 cm wide. In each wall the counters are partially overlapped by 2.5 cm to ensure hermetic coverage. Moreover the particles passing through the overlapping areas can be used to cross-calibrate the counters within a given wall. The intrinsic counter time resolution of the HARP TOFW has been measured as $\sigma_0 \sim 160$ ps on average (see [75] for details).

The vertical position in the outside slabs and the horizontal position in the central slabs can be determined from the time difference of the hits in the PMTs at either end of the counter. The position in the other dimension can only be determined to within the width
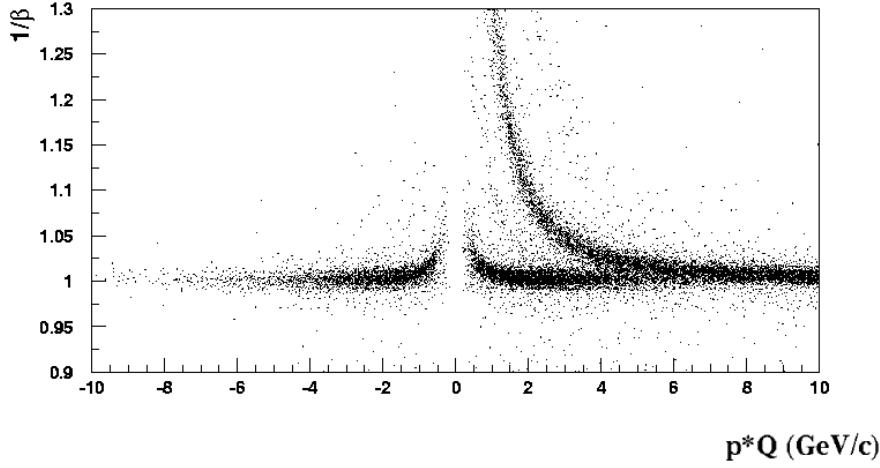
Figure 3.9: $1/\beta$ vs $p*Q$ for secondary particles in 12.9 GeV/c p-Al interactions (thin $5\%\lambda_{int}$ Al target).

of the scintillator slabs, 21 cm. As with the CHE, the x - y position of a hit in the TOFW can be used to associate a time measurement with a reconstructed particle track.

The initial timing calibration (determination of the delay constants of each channel at time $T = T_0$) has been done periodically with cosmic ray runs. In between, the drift of these delays, as a function of the running time T, was traced by the laser calibration system. The precision on the time calibration constants, as determined by the cosmic-rays run and traced by the laser system, was estimated to be $\sim$70 ps.

During data taking, the time-of-flight of particles produced at the target is obtained from the difference between the times measured in the TOFW and in the TOF-B counter, which has an intrinsic time resolution of about 100 ps, or a combination of TOF-A, TOF-B and TDS, with an intrinsic resolution of $\sim$ 70 ps. Therefore the final time resolution on the time-of-flight measurement is $\sim$200 ps, considerably better than the design value of 250 ps.

Figure 3.9 shows in a $1/\beta$ vs $p*Q$ (where Q is the sign of the electric charge) plot clear bands corresponding to positive and negative pions, kaons and protons.

Particle identification in the HARP TOFW relies on the combination of particle momenta, as measured from the drift chambers, and the time of flight between a start signal and a stop signal from the TOFW itself. The previous calibration issues are essential for the quality of the extracted TOF PID and thus the determination of particle masses. After
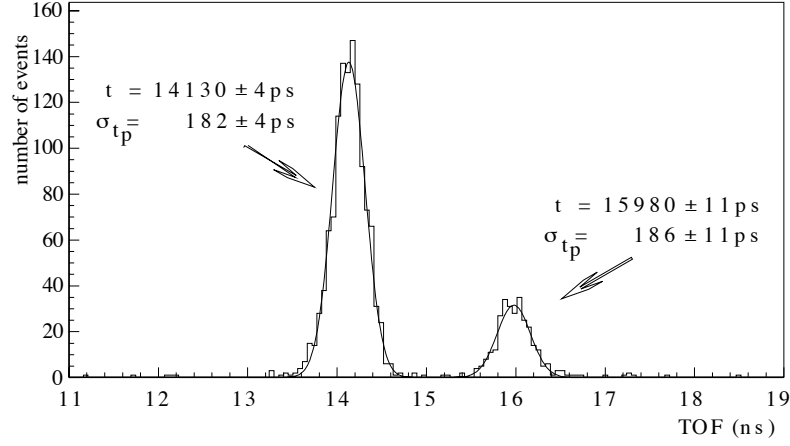
Figure 3.10: Particle identification with the TOFW detector, with 3 GeV/c incident unseparated hadron beam. The pion and proton peaks are clearly visible. The time-of-flight is computed between TOF-B and the TOFW system.

the calibration procedure, π and p are separated at better than 5σ at 3 GeV/c incident momentum, as shown in Figure 3.10.

About 12% of the tracks hit the overlap region of the TOFW detector, between two counters. For these tracks two independent time-measurements are available, improving the resolution. For tracks in this overlap region, kaons and pions are separated at 3σ level up to 3 GeV/c, the full relevant region for MiniBooNE and K2K, while the K/p separation extends up to 5 GeV/c.

3.8.4 Electron identifier

The electron identifier was designed to provide electron-pion separation when charged pions, accompanied by knock-on electrons, are occasionally identified as electrons by the Cherenkov counter.

The two calorimeter planes (EM1 and EM2) consist of 62 and 80 modules, covering a total active width of 4.96 m and 6.4 m respectively. The calorimeter is capable of providing stand-alone particle identification on the basis of the total energy deposition and of the longitudinal shower development, evaluated from the ratio of the energy deposition in the two calorimeter planes. The two-dimensional distribution of total calorimeter energy and ratio of the energy in the first and second plane is shown in Figure 3.11 for 3 GeV/c particles: the electrons are well separated from the pions.
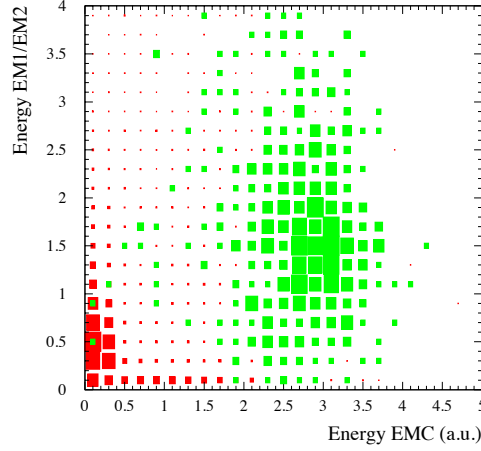
Figure 3.11: Two-dimensional distribution of total calorimeter energy and ratio of the energy in the first and second plane for 3 GeV/c particles. Electrons, identified with the beam Cherenkov, are clustered with a higher value in both paramaters and are shown with the lighter shade, pions are concentrated in the lower left corner and are indicated with the darker shade.

3.9   Performance of the HARP sub-detectors

3.9.1   Secondary track reconstruction

Algorithm

The five drift chambers are used to reconstruct particle trajectory parameters downstream of the target area. The full path is needed to match particles with reconstructed hits in the Cherenkov, TOFW or calorimeter. The directions before and after entering the field area of the dipole magnet are used to determine the particle's momentum. As explained in Section 3.8.2, operating the NDC with the non-flammable mixture Ar-90%, CO_2-9%, CH_2-1%, reduced significantly the the wire hit efficiency ($\sim$80%). A standard reconstruction algorithm which combines triplets of hits (u, x, v)[5] to generate 3D space points was, therefore, not adequate as the 3D point efficiency would go as 0.8^3, or about 50%.

The track reconstruction algorithm starts by building two-dimensional (2D) segments per NDC module. Those are later combined to create 3D track segments (also per

---

[5]The projections are $(0°, +5°, -5°)$

module). The requirements are the following:

- Plane (2D) segment: At least three hits out of four in the same projection (u, x or v) compatible with being aligned. The drift sign associated to each hit is decided during the plane segment reconstruction phase.

- Track (3D) segment: Two or three plane segments of different projections, whose intersection defines a 3D straight line. In the case where only two plane segments are found, an additional hit in the remaining projection is required. This hit must intersect the 3D straight line defined by the other two projections.

Consequently, to form a track segment at least seven hits (from a total of 12 measurement planes) are needed within the same NDC module. Once track segments are formed in the individual modules they are combined (downstream of the dipole magnet) to obtain longer track segments[6]. At this point the Kalman Package [74] is capable of extrapolating these long segments to all PID detectors downstream of the dipole (including the TOFW, CHE and ECAL) for hit matching. All possible combinations of track segments and reconstructed PID hits are attempted and matching-χ^2's calculated.

Finally, downstream segments must be matched with a 3D point or segment upstream of the dipole to determine the track momentum. Two independent upstream constraints on the track have been used to make independent momentum measurements of each reconstructed track:

The first uses the well defined interaction vertex where the secondary particle was created. The x, y coordinates are provided by the MWPC extrapolation of the primary beam particle to the z = 0 plane, or the target center. A matching χ^2 is constructed between the beam particle extrapolation, (x_0, y_0), and the extrapolated position of track segments constructed downstream of the dipole, (x_t, y_t). The algorithm loops over allowed values of the momentum and minimizes this χ^2 to estimate the momentum, p_v, of each secondary. Multiple scattering and inhomogeneities in the dipole magnetic field are fully taken into account by the Kalman Filter implementation. An upper cut on this χ^2 has been applied to reduce contamination by tertiary particles which have not emanated from the primary vertex. This cut will account for about a 1% inefficiency in this algorithm.

---

[6]The Kalman Package does take into account multiple scattering between drift chambers and does not just assume a perfect straight line path

The second upstream constraint is provided by 3D segments reconstructed in the upstream drift chamber, NDC1. The matching algorithm works similarly to the one just described but matches to the NDC1 segment to estimate each particle's momentum, p_{NDC1}. This algorithm suffers a major disadvantage relative to the one using the event vertex described above. The tracking efficiency is now directly proportional to the segment efficiency of NDC1. The segment efficiency in NDC1 is known to be much lower than the other chambers and, further, suffers from charge saturation caused by the bright beam spot even for low event rates. This saturation is difficult to simulate or measure and is a function of event number within a spill from the T9 beamline. For this reason the quantity p_v is used in all physics analysis, but the estimator, p_{NDC1}, can be used to accurately measure the efficiency of the vertex algorithm as will be shown.

Efficiency

The following criteria have been applied to select tracks in the forward spectrometer for all physics analyses:

1. a successful momentum reconstruction, p_v, using a downstream track segment in NDC modules 2, 3, 4 or 5 and the position of the beam particle at the target as an upstream constraint

2. a reconstructed vertex radius (i.e. the distance of the reconstructed track from the z-axis in a plane perpendicular to this axis at z = 0) r ≤ 200 mm

3. number of hits in the road around the track in NDC1 ≥ 4 and average χ^2 for these hits with respect to the track in NDC1 ≤ 30

4. number of hits in the road around the track in NDC2 ≥ 6

Cuts 2-4 are applied to reduce non-target interaction backgrounds. The track reconstruction efficiency is defined as the fraction of the total number of particles that fully traverse the fiducial volume of the HARP spectrometer which are tracked with a measured momentum and direction by the algorithm and pass the above cuts. It is defined as a function of momentum and θ_x and θ_y defined in Section 3.2

$$\varepsilon^{\text{track}}(p, \theta_x, \theta_y) = \frac{N^{\text{track}}(p, \theta_x, \theta_y)}{N^{\text{parts}}(p, \theta_x, \theta_y)} \tag{3.1}$$

where N^{parts} is the number of particles passing through the detector and N^{track} is the number which have had a successful track parameter reconstruction. The goal is to determine the efficiency directly from data to avoid any bias introduced by the Monte Carlo simulation of the spectrometer system. This is enabled by taking advantage of the redundancy of chambers in the downstream region and by the two independent upstream constraints introduced above.

We consider now the calculation of the efficiency for the event vertex algorithm. To measure the efficiency from data one must map the efficiency in a reconstructed quantity, such as the momentum estimator, p_{NDC1}. Additional constraints are applied to ensure that the track is a true secondary particle emanating from the nuclear target: $\chi^2_{\mathrm{match-NDC1}} <$ 10 and reconstructed vertex (in the $z = 0$ plane) less than 15mm[7]. The efficiency is a statistical calculation determined using large samples of tracks, and since p_{NDC1} is Gaussian distributed around the true momentum, p, with $\sigma_p/p < 10\%$, it can be used to approximate the latter for the efficiency calculation. Further, it will be seen that the efficiency is flat at higher momentum, eliminating any tiny bias introduced.

The total tracking efficiency can be expressed as the product of two factors, $\varepsilon^{\mathrm{down}}$, representing the downstream track segment efficiency given that the particle entered the downstream region (without being deflected, absorbed or decaying in the upstream region) and $\varepsilon^{\mathrm{vertex}}$, the efficiency for matching a downstream segment with the event vertex to measure a momentum and direction,

$$\varepsilon^{\mathrm{track}} = \frac{N^{\mathrm{down}}}{N^{\mathrm{parts}}} \cdot \frac{N^{\mathrm{vertex}}}{N^{\mathrm{down}}} = \varepsilon^{\mathrm{down}} \cdot \varepsilon^{\mathrm{vertex}}. \tag{3.2}$$

Further, in the downstream region there are two planes of drift chambers, NDC2 and the *back-plane* made of the combination of NDC3-4-5. A downstream track segment can be made of a segment in NDC2 only, a segment in the back-plane only, or a segment in both which are combined into a longer segment. These independent, but not mutually exclusive probabilities combine to give a total downstream segment efficiency of

$$\varepsilon^{\mathrm{down}} = \varepsilon^{\mathrm{NDC2}} + \varepsilon^{\mathrm{back-plane}} - \varepsilon^{\mathrm{NDC2}} \cdot \varepsilon^{\mathrm{back-plane}}. \tag{3.3}$$

To calculate the segment efficiency of NDC2 one selects tracks from the p_{NDC1} control sample with a segment in the back-plane and then asks if a segment was also reconstructed in NDC2. The efficiency can then be mapped out as a function of the p_{NDC1}

---

[7]all of nuclear targets being analyzed have a radius of 15mm
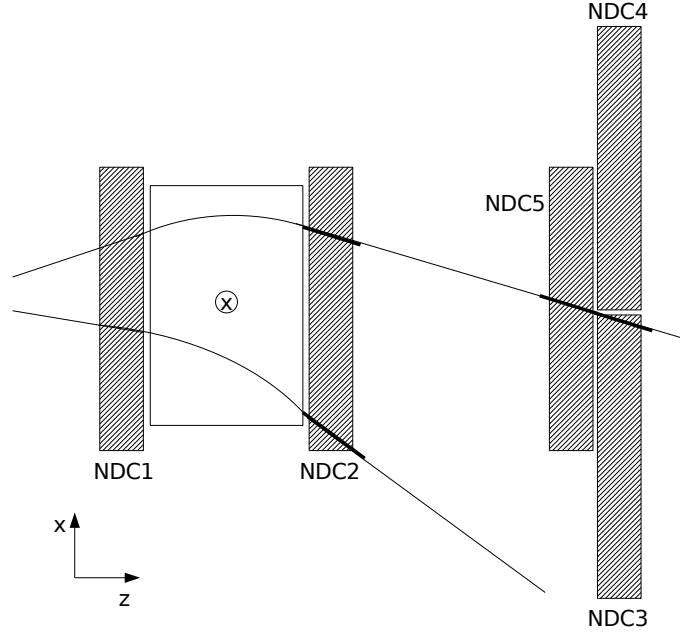
Figure 3.12: Schematic layout of the downstream modules of the drift chambers and the large aperture dipole magnet. Two types of secondary tracks are represented in the diagram (both having negative charge, incidentally). The one at the top of the figure shows how track segments in the back-plane are used to map the segment efficiency of NDC2 and vice versa. The second track illustrates the effect of geometric acceptance for particles at large, positive values of $q \cdot \theta_x$.

reconstructed quantities. This efficiency is the *true* segment efficiency of NDC2 because it is the efficiency of the chamber given that a particle passed through its volume. One knows this because the selected tracks created segments in both NDC1 and the back-plane which surround NDC2 (see Figure 3.12). Figure 3.13 shows the average efficiency calculated by this method for both data and Monte Carlo to be ∼99%.

    To determine the segment efficiency of the back-plane one simply asks the opposite question: for tracks which created a track segment in NDC2, how many also created a segment in the back-plane? A signal in the ECAL, downstream of the back plane of chambers, is also required to ensure the track traversed the back plane of chambers. As seen in Figure 3.13 the efficiency of the back-plane is a few percent lower than was calculated for NDC2, but combining them will result in a total downstream efficiency of nearly 100%. Also clearly visible in Figure 3.13 is the effect of geometric acceptance in the HARP forward spectrometer. The acceptance is both momentum and charge dependent due to the varying
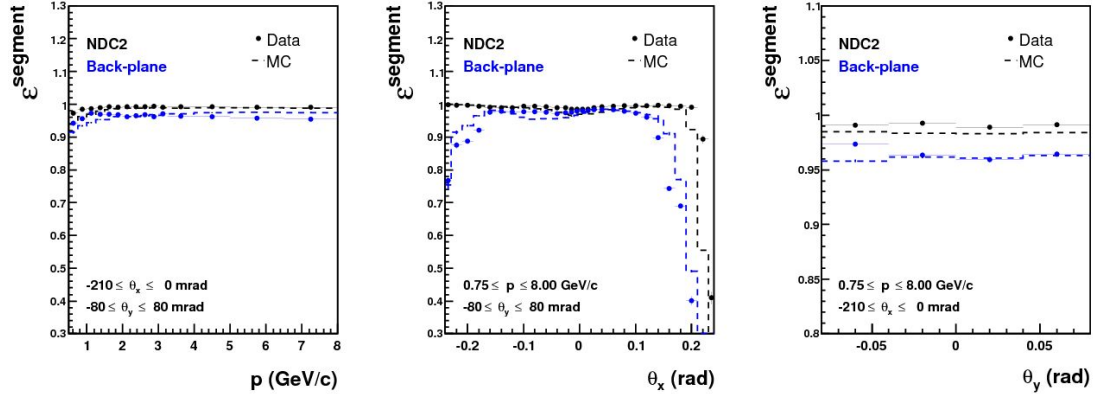
Figure 3.13: Track segment efficiencies for positive particles as a function of particle momentum (left), production angle in the horizontal plane, θ_x (center), and production angle in the vertical plane, θ_x (right). The segment efficiency for NDC2 is shown in black, and that for the back-plane consisting of NDC3-4-5 is shown in blue. Plot taken from [60]

amount and direction of bend in the track path that results from passing through the magnetic field region. The dipole bends particles in the horizontal plane and low momentum tracks at large, positive values of $q \cdot \theta_x$ can be bent beyond the reach of the downstream drift chambers. One expects the effect to extend to smaller values of $q \cdot \theta_x$ for the back-plane because it is further downstream (see Figure 3.12), and this can be seen in the middle panel in Figure 3.13. The small acceptance loss visible at large negative θ_x (for positive particles) are high momentum tracks that are bent only slightly in the magnetic field region and miss the back-plane of chambers on the opposite side. The efficiency for negative particles has been calculated to be almost exactly the mirror image of that for positives as a function of θ_x. By combining the efficiencies of the two downstream planes according to Eq. 3.3, one determines the total downstream segment efficiency, $\varepsilon^{\mathrm{down}}$, shown in the top panel of Figure 3.14. After accounting for geometric acceptance of the spectrometer the downstream segment efficiency is $\sim$100% and does not depend on momentum or opening angle in the vertical plane, θ_y.

The final piece of the track reconstruction efficiency, $\varepsilon^{\mathrm{vertex}}$, is the efficiency of the p_v algorithm given that a downstream track segment was constructed. Again, this can be measured by using a sample of p_{NDC1} tracks. The successful p_{NDC1} momentum reconstruction guarantees the existence of a downstream segment allowing us to determine the ratio $N^{\mathrm{vertex}}/N^{\mathrm{down}}$. The result is shown in Figure 3.14. The average efficiency is $\sim$97%, most
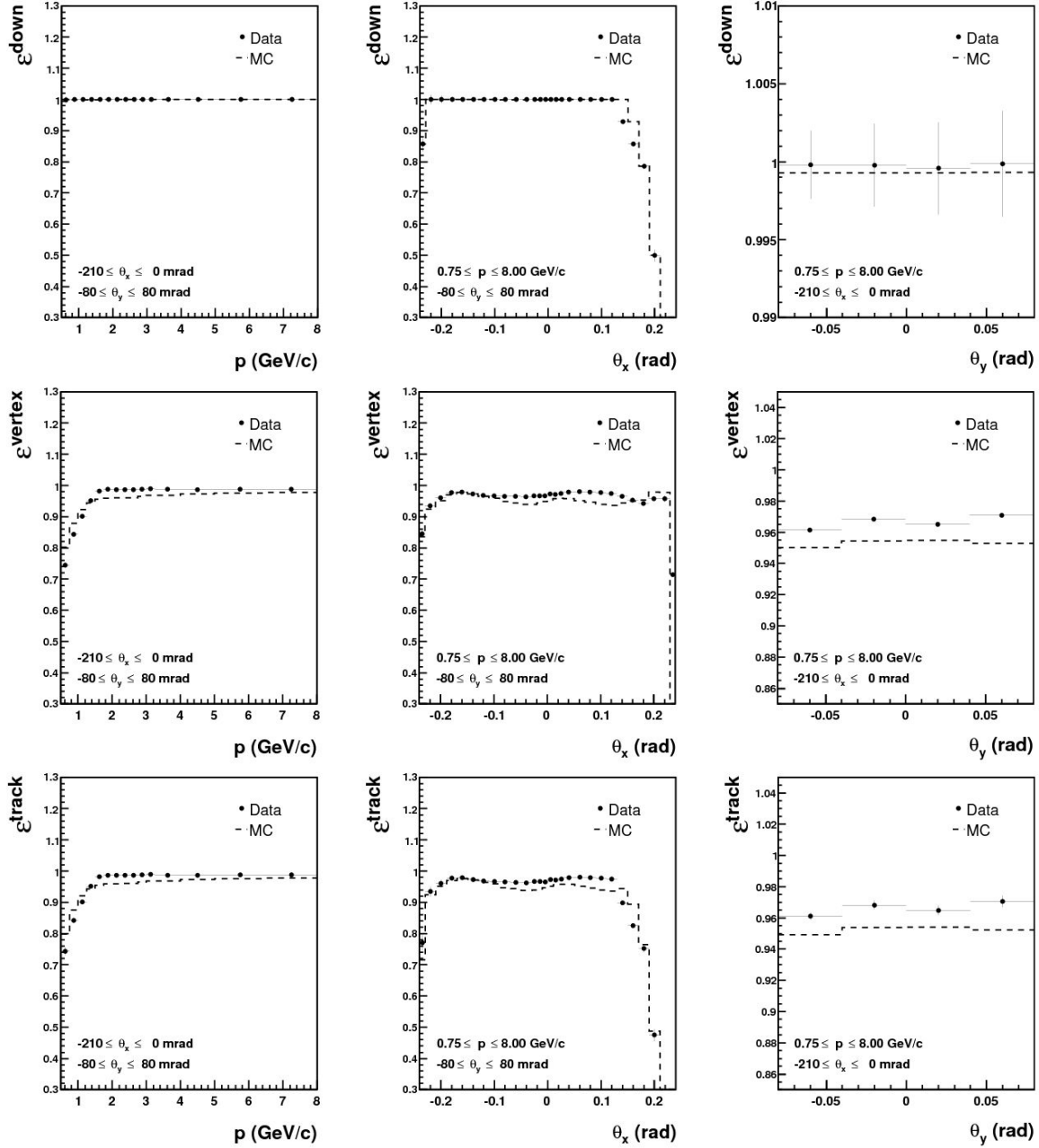
Figure 3.14: The track reconstruction efficiency (bottom row), shown as a function of particle momentum (left), production angle in the horizontal plane, θ_x (center), and production angle in the vertical plane, θ_y (right), is computed by multiplying the downstream segment efficiency (top row) by the vertex matching efficiency (middle row) according to Eq. 3.2. Each are measured from the data and the Monte Carlo. The results from data will be used in the cross-section measurements to be presented. Plot taken from [60].

easily seen in the plot as a function of θ_y. The drop in efficiency below ~ 1.75 GeV/c is due to the second cut listed above, $r \leq 200$ mm. This cut is necessary to remove a substantial non-target background and maintain a good resolution at low momentum. However, because the efficiency can be measured from the data themselves, the only systematic error contribution will come from the statistical uncertainty in the sample used to generate the correction. For this reason, high momentum data sets ranging from 8-15 GeV/c and using aluminum, beryllium, carbon and tantalum targets have all been combined. Studies have shown that small changes in spectrum and secondary multiplicity have negligible effects on the track reconstruction efficiency as a function of p, θ_x and θ_y.

Geometric acceptance correction

To avoid unnecessary complications caused by the momentum dependent acceptance of the spectrometer, most clearly visible in the plot of $\varepsilon^{\text{down}}$ as a function of θ_x, a fiducial volume cut ($-210 \leq \theta_x \leq 0$ mrad for positives and $0 \leq \theta_y \leq 210$ mrad for negatives) will be applied to all cross-section analyses, thus utilizing only the region where the downstream segment efficiency is $\sim 100\%$ and extremely flat. In the vertical direction only tracks with $-80 \leq \theta_y \leq 80$ mrad are selected to avoid drift chamber and magnetic field edge effects. This restricted fiducial volume definition necessitates a correction. Assuming azimuthal symmetry in hadron production this correction is purely analytical. Inside the θ_y acceptance (± 80 mrad) the correction is a simple factor of 2 since tracks with $\theta_x > (<)$ 0 mrad are not used for positive (negative) tracks. For values of θ above the θ_y cutoff the correction is:

$$\varepsilon^{\text{acc}}(p, \theta_x, \theta_y) = \frac{1}{\pi} \cdot \arcsin \left(\frac{\tan(\theta_y^{\text{cut}})}{\tan(\theta)} \right) \tag{3.4}$$

Figure 3.15 shows a sketch depicting the two forms of the geometric acceptance and the origins of the correction formulas. All reconstructed tracks are weighted by $1/\varepsilon^{\text{acc}}(\theta)$ as explained in Section 4.2.2.

Momentum resolution and scale of the pv algorithm

Two important sources of systematic uncertainty are the momentum resolution and the absolute momentum scale of the reconstruction. Each, in general, vary with the value of the true momentum and angle of the track. The Monte Carlo will be used to generate corrections to the measured momenta so a validation of the simulation becomes necessary.
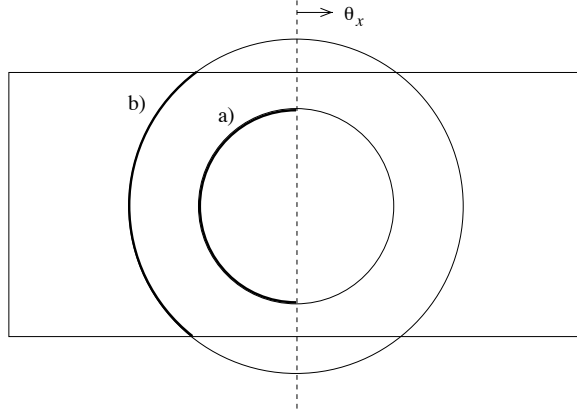
Figure 3.15: Sketch of the forward detector showing the two kinds of acceptance corrections, a) for $\theta < \theta_y^{\mathrm{cut}}$ where $\varepsilon^{\mathrm{acc}} = 0.5$, and b) for $\theta > \theta_y^{\mathrm{cut}}$ where $\varepsilon^{\mathrm{acc}}$ is given by Eq.3.4.

Several methods were developed by HARP collaborators to measure and map the momentum scale and resolution as a function of p and θ. Parameters of the Monte Carlo simulation were then adjusted to attain adequate agreement with data. Detailed descriptions of these methods have been given previously in [76] and will not be repeated here. The challenge is to isolate a set of tracks in the data sample with a known momentum. Briefly, the three methods are based on empty target data sets, samples of elastic scattering events and using the excellent resolution of the time-of-flight system to determine the momentum.

Figure 3.16 shows the resolution as a function of momentum for a set of empty target data sets and Monte Carlo samples. In this case the known momentum is the incoming primary T9 beam momentum. Histograms of secondary tracks were fit to a Gaussian function and the fractional resolution, $\sigma p/p$, is plotted as a function of the beam momentum. Incoming pion and proton beams were used for both data and Monte Carlo. There is good agreement between data and Monte Carlo and between different particle types across the full momentum range from 1.5 GeV/c to 15 GeV/c. Below 5 GeV/c, where most of the total production cross-section of pions and kaons will be for the data sets being analyzed, the resolution is better than 5% and everywhere better than 10%.

A multiplicative momentum scale correction is applied to all reconstructed tracks in the data to remove a θ_x, θ_y dependence seen in the calibration samples. After this correction, no significant momentum mis-calibration is seen beyond the 2% absolute momentum scale uncertainty estimated using the elastic scattering technique [76]. Also shown in Figure 3.16
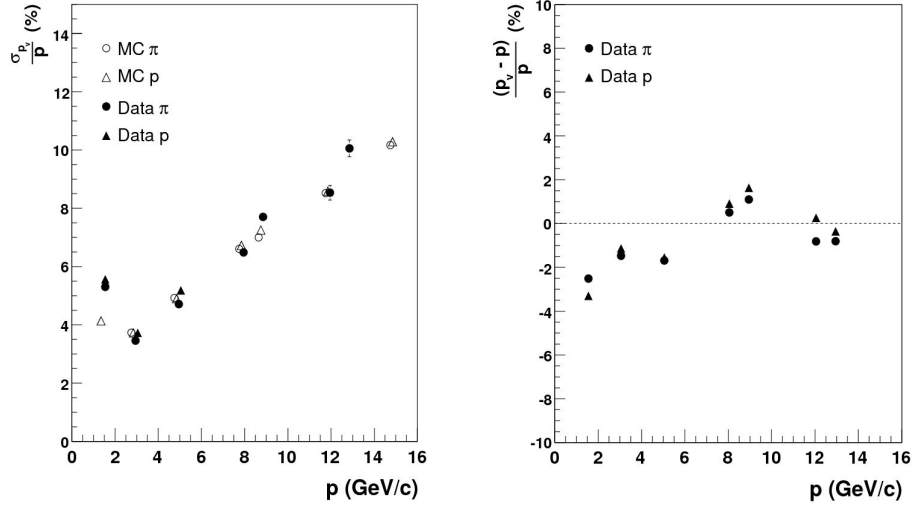
Figure 3.16: The momentum resolution (left) and absolute scale (right) can be measured as a function of momentum by using data sets taken using several well-defined discrete beam momenta and no nuclear target. Plot taken from [60]

is the momentum scale, again computed using empty target data sets. Pion and proton beams are compared and no difference is seen. At most momenta the momentum scale is better than 2%. In the cross-section analysis, the minimum ratio of momentum bin width over momentum bin central value will be 8%, four times this value.

3.9.2 PID detector hit selection and response functions

In this section we describe the quality criteria applied to select PID detector hits and the resulting response functions for pions and protons. Previously, PID detector hits have been associated with reconstructed tracks based only on a geometrical matching criterion. A Kalman filter package is used to extrapolate each track to the plane of each detector, and this position is compared to the reconstructed x, y positions of all reconstructed hits in that detector. The detector hit with the best matching χ^2 was then assigned to that track. In this scheme the reconstruction can associate a single detector hit with multiple tracks and each track likely has additional candidate detector hits which are being ignored. In particular, in [61] it was seen that a fraction of protons had a non-negligible amount of associated photo-electrons due to light from pions or electrons being wrongly associated with proton tracks. Also in [61] the TOFW response function contained a non-gaussian compo-
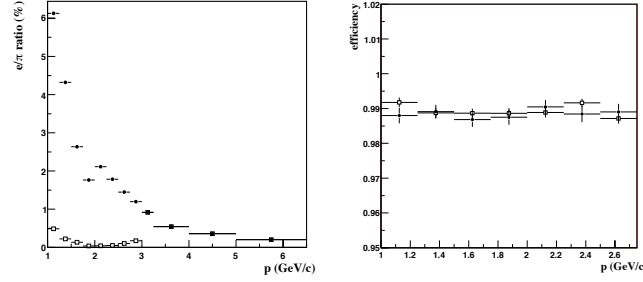
Figure 3.17: The left panel shows the e/π ratio from a Monte Carlo simulation before (solid points) and after (open squares) the application of a 15 photo-electron cut. This cut reduces the electron contamination to 0.5% or less in the region where it is applied. The right panel shows the efficiency for pions (solid points) and protons (open squares) to pass the 15 photo-electron cut below 3 GeV/c, and is $\approx 99\%$ for both.

nent where $\approx 10\%$ of reconstructed β fell greater than 5σ from the mean expectation and could not be used for identification. Additional criteria have been developed for selecting PID detector hits to address these issues and have led to a reduction in PID backgrounds by as much as a factor of 10 in some regions of phase space. This is the source of the drastic improvement in PID systematics since the publication of [61] (3.5% to 0.5%). The PID hit selection is described in detail below.

Cherenkov response

The Cherenkov detector is used to veto electrons below 3 GeV/c and to differentiate pions from protons and kaons above 3 GeV/c. Below 3 GeV/c the Cherenkov signal is used to remove electrons by a simple veto of tracks with greater than 15 photo-electrons. Fig. 3.17 demonstrates the effect of the electron veto cut. The left panel shows the e/π ratio in the Monte Carlo before and after applying the 15 photo-electron cut below 3 GeV/c. The remaining electron contamination is less than 1% everywhere, and less than 0.5% in the region where the veto is applied. One expects a very small efficiency loss for pions and protons due to this cut in photo-electrons and this is also shown in Figure 3.17. Approximately 1% of pions and protons do not pass the electron veto; a correction has been applied in the present analysis.

Above 3 GeV/c the Cherenkov is a powerful discriminator of pions kaons and protons. Monte Carlo simulations indicate that there are a negligible number of electrons
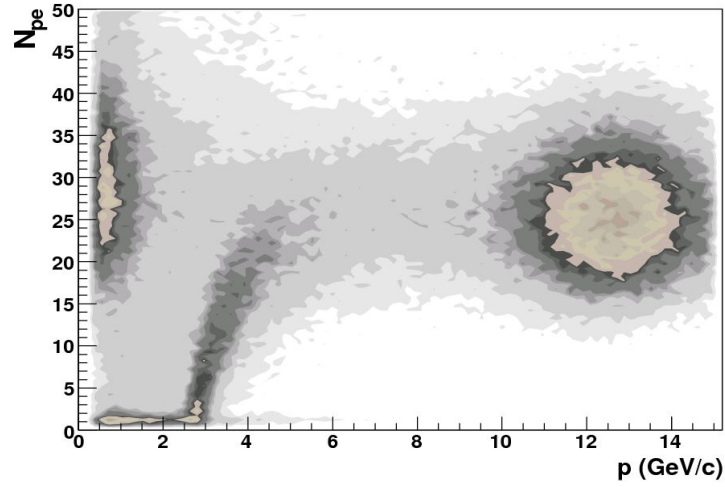
Figure 3.18: Reconstructed number of photo-electrons in the Cherenkov detector as a function of particle momentum for a data set with a 12.9 GeV/c π^+ beam on a thin aluminum target. See the text for an explanation.

above 3 GeV/c and these are thus ignored.

Figure ref 3.18 qualitatively demonstrates this discrimination power using a data set with a 12.9 GeV/c π^+ beam on a thin aluminum target. A minimum bias trigger was used and the non-interacting beam pions are clearly visible at high momentum and large number of photo-electrons (Npe). At p < 2 GeV/c secondary electrons can be seen clustered at ~25-30 Npe and are easily separable from pions at Npe < 2. Finally, the Cherenkov threshold for pions at 2.6 GeV/c is clearly visible. Only a small number of protons are represented in this plot, but would show up as a band below 2 Npe out to 17.6 GeV/c.

Presently the Cherenkov is being used digitally. That is the spectral information of the light output is not being used. Instead we define a signal as an associated hit with greater than 2 photo-electrons. Two or less is considered no signal. Based on this definition we determine the efficiency for pions and protons to have a signal in the Cherenkov as a function of particle momentum.

Fig. 3.19 shows the expected response for pions and protons in the Cherenkov both above and below the pion threshold. Above threshold the Cherenkov is greater than 99% efficient for pions. The small efficiency for protons and pions below threshold of around 1.5% is due to false associations with light generated by other particles in the event.
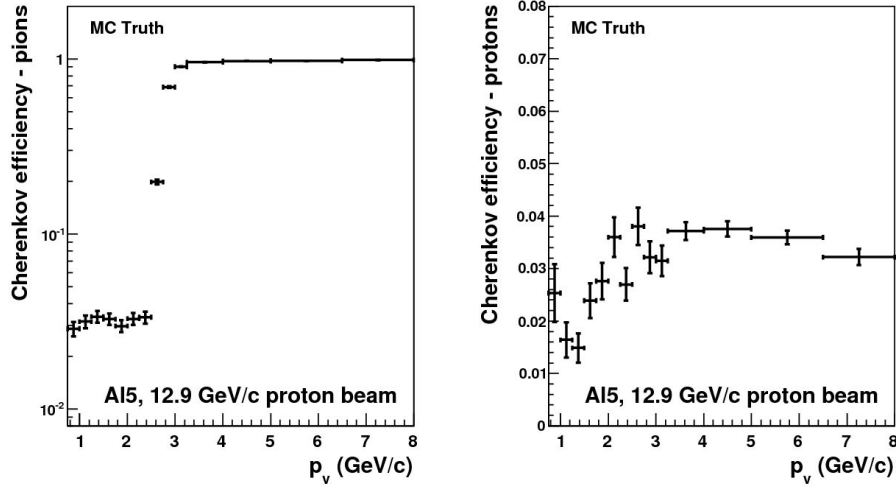
Figure 3.19: Cherenkov response for the aluminum data set for pions (left) and protons (right). The points are the efficiencies for a track to have an associated Cherenkov hit with greater than 2 photo-electrons. The threshold for pions at around 2.6 GeV/c is clearly visible (note the log scale). The small efficiency for protons and below threshold pions of around 1.5% is due to false associations with light generated by other particles in the event.

Time-of-flight response

A time-of-flight measurement is required for particle identification in this analysis. It was discovered, due to the presence of a significant, almost flat background far from the Gaussian peaks in the β distributions, that a more strict set of selection cuts was required to ensure a quality time-of-flight measurement.

Each track can have multiple time-of-flight measurements (TOFW - t_0) associated with it in the reconstruction. It is possible for a single hit to match with multiple tracks if the tracks are close enough together when hitting the wall. It is also possible that electromagnetic showers associated with a particle passing through detector material can create additional hits beyond the primary hit caused by the hadron of interest. To minimize inaccurate time measurements due to these effects, the time-of-flight candidates for each track are time-ordered and the earliest hit passing the following criteria is selected:

- if the track shares the TOFW hit with another track, it must have the better geometric matching χ^2;

- χ^2 of the geometrical matching between the track and TOFW hit ≤ 6;
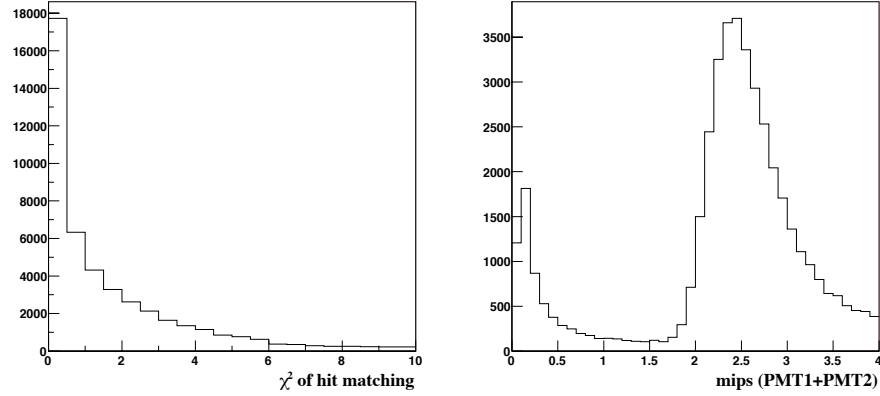
Figure 3.20: TOFW hit reconstructed variables. The left panel shows the distribution of the χ^2 between the extrapolated track position and the reconstructed scintillator hit position. The right panel shows the total reconstructed number of minimum ionizing particles (mips) from the two PMTs on the scintillator volume that was hit. Time-of-flight hits are selected by requiring a $\chi^2 \leq 6$ and number of mips ≥ 1.5 (see the text).

- total reconstructed number of minimum ionizing particles (mips) from the two PMTs in a hit ≥ 1.5.

The χ^2 distribution for track-TOFW hit matching and the total pulse-height distribution for the Berylium data set are shown in Figure 3.20.

Having applied these criteria to time-of-flight measurements we must understand the associated efficiency loss as well as the remaining level of non-Gaussian component to the β spectrum. Each of these have been carefully measured and the needed corrections applied.

The efficiency is measured from the data by using a sample of reconstructed tracks which leave a signal in the calorimeter (downstream of the scintillator wall) and asking how often a time-of-flight measurement passing selection cuts is found. Fig. 3.21 shows the matching efficiency for data and Monte Carlo to be flat in momentum and around 95% in the data.

In the cross-section analysis to be presented we will require a TOF measurement as part of our selection of secondary tracks. Therefore, the efficiency loss due to TOFW hit selection must be combined with the tracking efficiency discussed earlier to form an overall *reconstruction efficiency*:
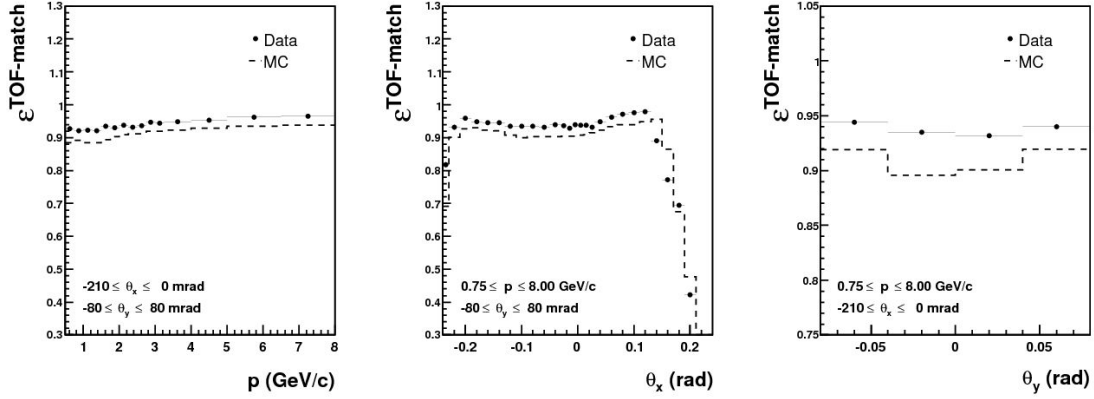
Figure 3.21: TOFW matching efficiency as a function of particle momentum (left) and production angle in the horizontal plane, θ_x (center), θ_y (right), as measured from data and Monte Carlo. The TOFW matching efficiency does not have the momentum dependence of the tracking efficiency, but does exhibit the same effects of geometric acceptance as the drift chambers as seen in the right, θ_x, plot. Note the present analysis is performed using tracks in the range -0.210 rad $\leq \theta_x \leq 0$ rad where the acceptance is flat in momentum.

$$\varepsilon^{\mathrm{recon}} = \varepsilon^{\mathrm{track}} \cdot \varepsilon^{\mathrm{TOFW-match}} \tag{3.5}$$

Figure 3.22 shows the final reconstruction efficiency for positive and negative tracks in the forward spectrometer. The mirror symmetry in the acceptance for tracks of opposite charge is clear in the figures. These efficiencies, measured directly from the data, will be used in the cross-section analysis presented in Chapter 4.
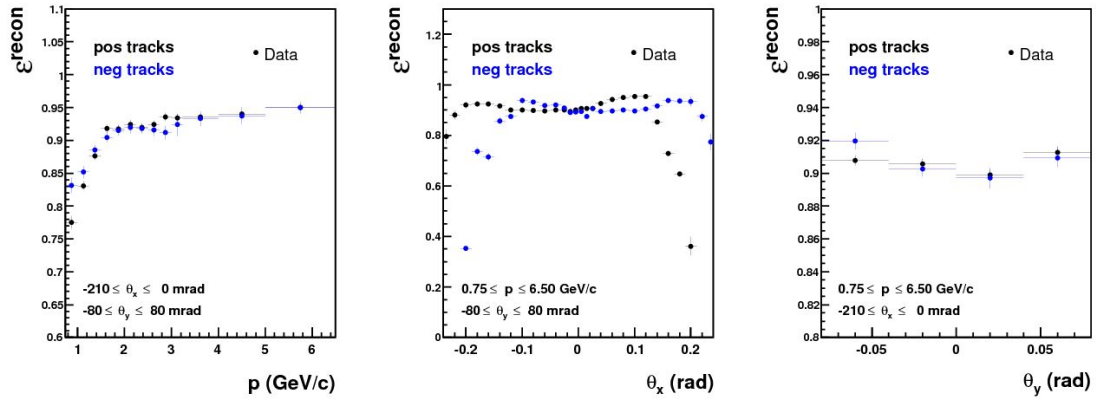
Figure 3.22: Total reconstruction efficiency including track kinematic parameters and time-of-flight measurement for positive (black) and negative (blue) tracks in the forward spectrometer. The effects of geometric acceptance are clearly visible in the plot as a function of θ_x (center). The average reconstruction efficiency for tracks of both charges is around 91%. Plot taken from [60].

Chapter 4

Kaon Cross-Section Measurements

We present the measurement of the absolute differential production cross-sections for positive kaons. To this effect, a new algorithm to measure the cross-sections that differs from the algorithm used in the previously published papers has been developed. The differences between the two 'recipes' comes mainly from the method used for identifying secondary particles (PID). A detailed explanation of the new PID method and its consequences on the general cross-section algorithm are described.

4.1 Particle identification

Particle identification is done using information from the Cherenkov and time-of-flight detectors. The discrimination power of the time-of-flight below 3 GeV/c and the Cherenkov above 3 GeV/c are combined to efficiently separate pions, kaons and protons. The calorimeter has been used only to separate pions and electrons when characterizing the response of other detectors (see Section 3.9.2). The resulting efficiency of pion identification in the analysis region is excellent.

We briefly introduce now the PID algorithm previously used in the published analyses and compare it with the new algorithm developed for the kaon analysis.

4.1.1 Previously used PID algorithm

Particle identification is performed by determining the probability that a given track is a pion or a proton based on the expected response of the detectors to each particle

type and the measured response for the track. Information from both time of flight (TOFW) and Cherenkov (CHE) detectors is combined using Bayes theorem:

$$P\left(\alpha \mid \beta, N_{\mathrm{pe}}, p, \theta\right) = \frac{P\left(\beta, N_{\mathrm{pe}} \mid \alpha, p, \theta\right) \cdot P\left(\alpha \mid p, \theta\right)}{\sum_{i=\pi,p} P\left(\beta, N_{\mathrm{pe}} \mid i, p, \theta\right) \cdot P\left(i \mid p, \theta\right)} \tag{4.1}$$

where $P\left(\alpha \mid \beta, N_{\mathrm{pe}}, p, \theta\right)$ is the probability that a track with reconstructed velocity β , number of associated photo-electrons N_{pe}, and momentum and angle p and θ is a particle of type α. $P\left(i \mid p, \theta\right)$ is the so-called prior probability. In the Bayesian approach, these probabilities are the fractions of particles having type i in the bin (p, θ) and are the quantities to be determined by the analysis. Finally, $P\left(\beta, N_{\mathrm{pe}} \mid \alpha, p, \theta\right)$ is the expected response (β and N_{pe}) of the PID detectors for a particle of type i and momentum and angle p, θ.

Equ. 4.1 can be simplified when assuming:

- No a priori knowledge of the underlying pion/proton spectra. This is equivalent to assume flat prior distributions, $P\left(i \mid p, \theta\right) = 1$ for all p, θ. This allows the priors to be dropped from the equation but makes the PID estimator without full probabilistic interpretation. It can therefore not be used directly when estimating the particle yields. One could iterate the probability distributions to determine the yields. Alternatively one can build the PID estimator for each track independently and an efficiency and migration must be determined for a given cut on the estimator value, $P_{\mathrm{track}} > P_{\mathrm{cut}}$.

- The PDFs that enters the PID estimator are averaged over all angles (no angular dependance is seen on the PDFs).

- Also we consider the response functions of the PID detectors as independent and we can therefore factorize the probability into separate terms for the time-of-flight and Cherenkov.

$$P\left(\alpha \mid \beta, N_{\mathrm{pe}}, p\right) = \frac{P\left(\beta \mid \alpha, p\right) \cdot P\left(N_{\mathrm{pe}} \mid \alpha, p\right)}{P\left(\beta \mid \pi, p\right) \cdot P\left(N_{\mathrm{pe}} \mid \pi, p\right) + P\left(\beta \mid \mathrm{p}, p\right) \cdot P\left(N_{\mathrm{pe}} \mid \mathrm{p}, p\right)} \tag{4.2}$$

where $P\left(\alpha \mid \beta, N_{\mathrm{pe}}, p\right)$ is the PID estimator for a track with reconstructed β , N_{pe} and p to be of type α and $P\left(\beta \mid \pi(\mathrm{p}), p\right)$ and $P\left(N_{\mathrm{pe}} \mid \pi(\mathrm{p}), p\right)$ are the response functions for the TOFW and CHE, respectively for pions(protons). The TOFW response function is
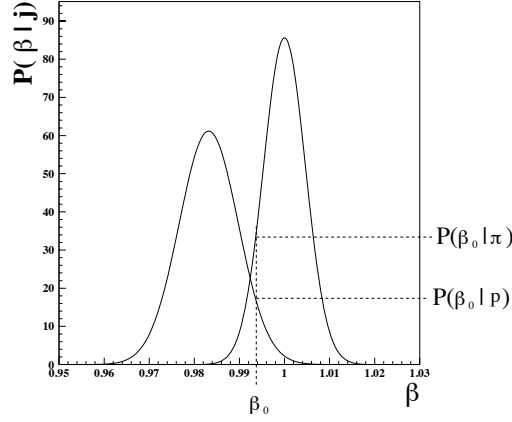
Figure 4.1: Ideal β distributions for 5 GeV/c pions and protons normalized to unity. These correspond to the TOFW PDF's used in the PID estimator. The combined pion probability using the TOFW alone for a measurement β_0 would be $P\left(\pi \mid \beta_0, p = 5\text{GeV/c}\right) = P\left(\beta_0 \mid \pi\right) / \left[P\left(\beta_0 \mid \pi\right) + P\left(\beta_0 \mid p\right)\right] \simeq 34/[34 + 18] = 0.65$. Plot taken from [77].

shown in Fig. 4.1. A detailed description of the method can be be found in [77]. The PID estimator is evaluated for each reconstructed track under the pion and proton hypotheses, once the the e-veto cut has bee applied to reject electrons. A selection cut for both particles of $P \geq 0.6$ was used to build raw yields of pions and protons. This cut yields a very high purity and eliminates the possibility of identifying a single track as both pion and proton (the estimators have been normalised).

4.1.2   Current PID algorithm: fitting beta spectra

The PID response functions descrived above were well suited to differentiate between pions and protons. The underlying kaon background was estimated from the data, and subtracted from the dominant yields of pions and protons. However the PID cut method can not be applied to the current Kaon analysis for two main reasons: the kaon signal at the TOFW is very small and the kaon and pion peaks are close to each other. In that case, one would have to apply a very tight cut on the PID estimator, which would result in an inefficient kaon identification.

Instead, the measured hadron yield is obtained by fitting simultaneously the inclusive β spectrum to a model accounting for pions, kaons and protons in each bin of reconstructed momentum and angle. The β variable is defined as d/tc, where d and t are

the track length and the time of flight measured between the reconstructed vertex and the TOFW, respectively.

The main advantage of this method is that no PID cuts need to be applied, conserving the full statistical power for each particle species, what is crucial for detecting the small kaon signal. Moreover, PID corrections (efficiencies and migration) are not needed anymore since the total true particle yield for each hadron type (and its error) is directly obtained from the fit. The full method is described in the next section.

4.2 Cross section measurement strategy

The goal of this analysis is to measure the inclusive yield of secondary positive kaons produced from the collisions of 12.9 GeV/c protons with a 5% interaction length aluminum target:

$$p + A \rightarrow K^+ + X$$

The absolutely normalized double differential cross-section can be expressed in bins of kinematic variables in the laboratory frame, (p, θ), as

$$\frac{\mathrm{d}^2\sigma^{K^+}}{\mathrm{d}p\,\mathrm{d}\Omega}(p, \theta) = \frac{1}{N_{\mathrm{p.o.t.}}} \cdot \frac{A}{N_A\,\rho\,t} \cdot \frac{1}{\Delta p\,\Delta\Omega} \cdot N^{K^+}(p, \theta) \tag{4.3}$$

where :

- $\frac{\mathrm{d}^2\sigma^{K^+}}{\mathrm{d}p\,\mathrm{d}\Omega}$ is the cross-section in $cm^2/(GeV/c)/sr$ for each (p, θ) covered in the analysis.

- $\frac{A}{N_A\rho}$ is the inverse of the number of target nuclei per unit area. A is the atomic mass of the target material, N_A is Avogadro's number and ρ is the density of the target.

- t is the thickness of the nuclear target along the the beam direction.

- $\frac{1}{N_{\mathrm{pot}}}$ is the number of incident protons on target, after selection cuts.

- Δp and $\Delta\Omega^1$ are the bin sizes in momentum and solid angle, respectively.

- $N^{K^+}(p, \theta)$ is the number of kaons in bins of momentum and polar angle in the laboratory frame.

---

[1] $\Delta\Omega = 2\pi(\cos(\theta_{\mathrm{min}}) - \cos(\theta_{\mathrm{max}}))$

Migration from a true particle type α to a different reconstructed particle type α' may occur. Thus, Eq. 4.3 must be generalised to account for this effect. The inclusive cross-section for a particle of type α is:

$$\frac{\mathrm{d}^2\sigma^\alpha}{\mathrm{d}p\mathrm{d}\Omega}(p,\theta) = \frac{1}{N_{\mathrm{p.o.t.}}} \cdot \frac{A}{N_A \rho t} \cdot \frac{1}{\Delta p\,\Delta\Omega} \cdot M^{-1}_{p\theta\alpha p'\theta'\alpha'} \cdot N^{\alpha'}(p',\theta') \tag{4.4}$$

where the reconstructed quantities are marked with a prime and $M_{p\theta\alpha p'\theta'\alpha'}$ is the correction matrix, which fully describes the signal efficiency, background subtraction and the migrations between bins of true and reconstructed quantities: laboratory frame momentum p, laboratory frame angle θ and particle type α. In practice, the matrix M can be factorised into a set of individual corrections. The reasons to do so are the following:

- Not all corrections are functions of all three variables (p, θ, α). For example, the tracking efficiency and momentum resolution are the same for all particle types.

- Using techniques described in Section 3.9.1 the tracking efficiency can be determined from the data themselves and do not rely on simulation. Other corrections require using the Monte Carlo simulation.

- Measuring and applying the corrections separately eases the assessment of systematic errors.

The corrections can be separated into three basic categories: signal efficiencies, background subtraction, and bin-to-bin migrations between true and reconstructed quantities. The various corrections can be functions of either reconstructed or true quantities and must therefore be applied at the appropriate stage of the analysis.

Two methods have been developed to compute the production cross-sections. They are mostly similar but differ in the way the particle identification is done. Therefore, the set of corrections will also vary depending on the method used. We will first present the method used previously by the HARP collaboration and then introduce the new method developed for our analysis.

4.2.1   Previously used cross-section recipe

In the previously published HARP analyses, the correction matrix, $M^{-1}_{ij\alpha i'j'\alpha'}$ has been factorised into the following components:

- $\varepsilon^{\mathrm{recon}}(p', \theta'_x, \theta'_y)$ is the efficiency for the reconstruction of an 'analysis track'. An 'analysis track' is defined to include a momentum measurement from the event vertex constraint as well as a matched time-of-flight hit passing the selection the criteria outlined in Section 3.9.2. The reconstruction efficiency is measured directly from the data.

- $\varepsilon^{\mathrm{acc}}(\theta')$ is the correction for the geometric acceptance of the spectrometer and is a purely analytical function based on the assumption of azimuthal symmetry in hadron production and the fiducial volume cuts used in the analysis. See Section 3.9.1 for a detailed explanation of this correction.

- $M_{p \cdot p'}$ is a matrix describing the migration between bins of generated and measured momentum. This matrix is generated from the Monte Carlo (see Section 4.9).

- $M^{-1}_{\theta \cdot \theta'}(p)$ is a unitary matrix, implying that angular migrations, which are small, are being neglected.

- $\eta^{\mathrm{absorb}}(p, \theta_x, \theta_y, \alpha)$ is the absorption plus decay rate of secondary particles before reaching the time-of-flight wall, which is required for particle identification. The absorption correction accounts for the fraction of particles which never make it to the downstream detectors. The absorption rate cannot be measured from data and must be determined from a Monte Carlo simulation. This correction is obtained as a function of the true kinematic variables of the lost particle.

- $(1 - \eta^{\mathrm{tert}}(p', \theta'_x, \theta'_y, \alpha'))$ corrects by the fraction $\eta^{\mathrm{tert}} = \frac{N^{\mathrm{rec\ \text{-}\ tert}}}{N^{\mathrm{rec}}}$ of total tracks passing selection cuts, N^{rec}, which are actually tertiary particles, $N^{\mathrm{rec\ \text{-}\ tert}}$, that is particles produced by the reinteraction of secondary particles. The Monte-Carlo is used to estimate this rate, but the tertiary correction is generated as a function of the reconstructed quantities.

- $M_{\alpha\ \alpha'}(p)$ is a matrix accounting for PID efficiency and migration among particle types.

- $\varepsilon^{\mathrm{e\text{-}veto}}(p, \alpha)$ is the efficiency for particles of type α passing the electron veto cut used to remove electrons from the analysis track sample.

Eq. 4.4 can be rewritten after expanding $M^{-1}_{ij\alpha i'j'\alpha'}$ into individual corrections:

$$
\begin{aligned}
\frac{\mathrm{d}^2\sigma^\alpha}{\mathrm{d}p\mathrm{d}\Omega}(p,\theta) = {}& \frac{1}{N_{\text{p.o.t.}}} \cdot \frac{A}{N_A \rho t} \cdot \frac{1}{\Delta p\,\Delta\Omega} \\
& \times \frac{1}{\varepsilon^{\text{e-veto}}(p,\alpha)} \\
& \cdot \frac{1}{1-\eta^{\text{absorb}}(p,\theta_x,\theta_y,\alpha)} \\
& \cdot M^{-1}_{\alpha\ \alpha'}(p) \cdot M^{-1}_{p\,p'} \cdot (1-\eta^{\text{tert}}(p',\theta'_x,\theta'_y,\alpha')) \\
& \cdot \frac{1}{\varepsilon^{\text{acc}}(\theta')} \cdot \frac{1}{\varepsilon^{\text{recon}}(p',\theta'_x,\theta'_y)} \\
& \cdot N^{\alpha'}(p',\theta')
\end{aligned}
\tag{4.5}
$$

where the order in which corrections are applied has been mantained.

At last, one has to subtract the background that arises from beam protons interacting in materials other than the nuclear target (parts of the detector, air, etc.). These events can be subtracted by using data collected without the nuclear target in place where tracks have been selected and identified using the identical algorithm and set of cuts. This is called the empty target subtraction:

$$
N^{\alpha'}(p',\theta') \to \left[N^{\alpha'}_{\text{target}}(p',\theta') - N^{\alpha'}_{\text{empty}}(p',\theta') \right]
$$

4.2.2 Cross-section recipe for the Kaon analysis

As described in Section 4.1.2, PID cuts are not applied in the current analysis. Instead, PID is now done fitting the β distribution to the appropriate model, and the resulting raw yields $N^\alpha_{p',\theta'}$ are expressed in the true particle type variable α. This implies that the PID matrix, $M^{-1}_{\alpha\ \alpha'}(p)$, in Eq. 4.5 is just the identity. This is the main difference between the two analysis methods. There are however other subtleties that need to be described.

Corrections are applied in a two-step procedure. As it will be explained later in more detail four corrections are applied before the β spectrum fit and two after it. Pre-fit corrections can be applied on a track-by-track basis when filling the β spectrum. In other words, each track that passes all selection cuts and that enters in the corresponding β histogram for a given kinematic bin (p,θ) will not have a weight of 1 but the corresponding to the four pre-fit corrections. The main advantage of this solution is that the full kinematics

of each track (p, θ_x, θ_y) is available when applying the correction and not only p and θ, which will be the only available information otherwise. The reasons to decide whether a correction should be applied before or after the fit are threefold: i) if the correction depends on true kinematic variables it has to be applied after the fit, ii) if we want to keep the θ_x and θ_y dependencies the correction must be applied before the fit, iii) if the correction depends on β it has to be applied before the fit. We briefly descrive now how the corrections are applied:

- Two corrections depend on β : tertiary particles and empty target. Keeping the β dependence is very important since these two backgrounds may cause distortions to the β distributions that are not taken into account by our fitting model. Thus, they need to be subtracted before fitting. On the other hand, although these corrections depend on θ_x and θ_y, the way they are computed (see Section 4.6) does not allow to take into account all these dependencies due to lack of statistics. Instead they are approximated to be a function of θ. The transformation to polar coordinates (p, θ) is done integrating over all θ_x and θ_y that result in the same θ.

- The reconstruction efficiency, being a function of the reconstructed θ_x and θ_y, is applied before the fit.

- The acceptance correction only depends on the polar angle θ, whose true-to-reconstructed migration is negligible. Thus, this correction could be applied before or after the fit. We decided to apply it before the fit.

- The kinematic migration correction, which depend on both true and reconstructed quantities is applied after the fit and before the absorption correction.

- Finally, the absorption correction is obviously a function of the true kinematic variables, since by definition it accounts for particles that are not fully reconstructed. Thus, it has to be aplied after the fit. As a post-fit correction, θ_x and θ_y information is not available, and it has to be approximated to be a function of θ.

The method used to compute each correction is described in Sections 4.6 and 4.9. The above procedure can be summarised as follows. In the first step the reconstruction efficiency, acceptance correction and tertiary correction weights are applied on a track-by-track basis:

$$N_{p',\theta'}^{target}(\beta) = W_{p',\theta'_x,\theta'_y}^{\mathrm{rec}} \cdot W_{\theta'}^{\mathrm{acc}} \cdot W_{p',\theta'}^{\mathrm{tert}}(\beta) \cdot N_{p',\theta'_x,\theta'_y}^{\mathrm{raw}}(\beta) \tag{4.6}$$

In the second step, empty target data properly normalised is subtracted from the target data, and the partially corrected yield, $N^{\alpha}_{p',\theta'}$, is found after the fit:

$$N_{p',\theta'}(\beta) = N^{target}_{p',\theta'}(\beta) - N^{empty}_{p',\theta'}(\beta) \xrightarrow{\text{Fit}} N^{\alpha}_{p',\theta'} \qquad (4.7)$$

In the third step, pos-fit corrections (momentum migration and absorption correction) and normalisation factors are applied to obtain the cross-section:

$$\frac{\mathrm{d}^2\sigma_{\alpha}}{\mathrm{d}p\,\mathrm{d}\Omega} = \frac{1}{N_{\text{p.o.t.}}} \cdot \frac{A}{N_A\,\rho\,t} \cdot \frac{1}{\Delta p\,\Delta\Omega} \cdot (\varepsilon^{\text{absorb}}_{p,\theta,\alpha})^{-1} \cdot M^{-1}_{p\theta p'\theta'} \cdot N^{\alpha}_{p',\theta'} \qquad (4.8)$$

4.3   Event selection

Beam protons are selected by vetoing particles which give a signal in any of the beam Cherenkov detectors (see Section 3.5). Only events with a single reconstructed beam track in the four beam multi-wire proportional chambers (MWPCs) and no signal in the beam halo counters are accepted. This MWPC track is used to determine the impact position and angle of the beam particle on the target. A time measurement in one of three beam timing detectors consistent with a beam particle is also required for determining the arrival time of the proton at the target, t_0. This t_0 is necessary for calculating the time-of-flight of secondary particles. The criteria to select beam protons are:

- ADC counts less than 120 in both beam Cherenkov A and beam Cherenkov B.

- Time measurement(s) in TOFA, TOFB and/or TDS which are needed to for calculating the arrival time of the beam proton at the target, t_0. t_0 is necessary to calculate the time-of-flight of secondary particles.

- Leave a single track in the MWPCs. Only beam particle with extrapolated position at the target within a radius of 10mm and an extrapolated angle at the target less than 5 mrad from the nominal beam direction

- Leave no signal in the beam halo counters.

At the time of data taking, for data taken with a nuclear target, a downstream trigger in the forward trigger plane (FTP) was required to record the event. The FTP is a double plane of scintillation counters covering the full aperture of the spectrometer magnet except a 60 mm central hole for allowing non-interacting beam particles to pass - which for

Beam momentum	12.9 GeV/c	
Target	**Al 5%**	**Empty**
protons on target	16,258,688	4,174,336
total events processed	4,252,252	674,027
events with accepted beam proton	3,082,365	478,747
beam proton events with FTP trigger	1,889,865	197,181
total good tracks in fiducial volume (pos)	120,837	7,066

Table 4.1: Total number of events and number of protons on target as calculated from the pre-scaled trigger count for the 12.9 GeV/c data set with and without aluminum nuclear target.

a 5% interaction length target would otherwise comprise most of the recorded data. The efficiency of the FTP is measured to be $> 99.8\%$. Using the FTP as an interaction trigger necessitates an additional set of unbiased, pre-scaled triggers for absolute normalization of the cross-section. Beam protons in the pre-scale trigger sample (1/64 of the total trigger rate) are subject to exactly the same selection criteria as FTP trigger events allowing the efficiencies of the selections to cancel and adding no additional systematic uncertainty to the absolute normalization of the result. These unbiased events are used to determine the $N_{p.o.t.}$ used in the cross-section formula (Eq. 4.3). The number of protons-on-target is known to better than 1%.

Applying the above selection cuts to the 12.9 GeV/c aluminum 5% λ_I target data set and the 12.9 GeV/c empty target data set results in the total statistics listed in Table 4.1.

4.4   Secondary track selection

In the forward spectrometer, secondary tracks have been selected using the following criteria:

- A successful momentum reconstruction using track segments in NDC modules downstream the magnet and the position of the beam particle at the target as an upstream constraint.

- Number of hits in the road around the track in NDC1 $\geq$ 4 and average χ^2 for these hits with respect to the track in NDC1 $\leq$ 30. This reduces non target interaction background.

- Number of hits in the road around the track in NDC2 $\geq$ 6. This reduces non target interaction background.

- A matched TOFW hit passing quality cuts described in Section 3.9.2.

- Number of photoelectrons in the cherenkov detector has to be smaller than 15 for tracks below 2.5 GeV/c. This cut is applied to reject electrons.

- Reconstructed angles are within the fiducial volume to be used for this analysis, -210 mrad $\leq \theta_x \leq$ 0 mrad for positive particles and -80 mrad $\leq \theta_y \leq$ 80 mrad (see Section 3.9.1).

4.5   Filling the β spectra

Positive particle β spectra are filled for each (p, θ) bin by selecting events passing the analysis cuts described in Sections 4.3 and 4.4. The kinematic range chosen for the analysis is defined by:

$$p = [0.75, 1.0, 1.25, 1.5, 1.75, 2.0, 2.25, 2.5, 2.75, 3.0, 3.25, 4.0, 5.0] \text{ GeV/c}$$
$$\theta = [0.03, 0.06, 0.09, 0.12, 0.16, 0.21] \text{ rad} \tag{4.9}$$

Fig. 4.2 shows an example of β distributions for positive particles, before applying any correction.

The corrections are applied in a two-step procedure given by Eq. 4.6 and 4.8. All pre-fit corrections are applied either as a weight *while* filling the β spectra or directly on the weighted spectrum, before fitting. Particle yields are extracted by fitting pre-corrected β distributions simultaneously to pion, kaon and protons hypothesis. Finally, one applies the momentum migration correction on the measured yields (conversion into true kinematic variables) and corrects for the absorption and decay.
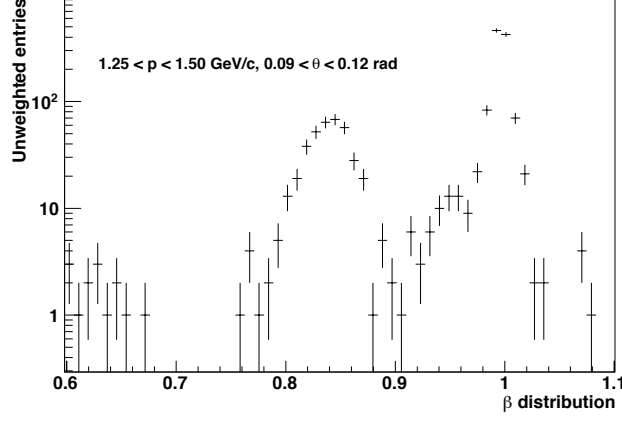
Figure 4.2: Unweighted β distributions for positive particles at a given (p, θ) bin. The error bars are given by the square root of the bin content.

Below 2.5 GeV/c the proton, pion and kaon peaks are well separated and are fitted simultaneously. Above 2.5 GeV/c the Cherenkov is used to reject pions and better expose the proton and kaon peaks.

4.6 Pre-fit particle yield corrections

Pre-fit corrections are applied before fitting the β spectra either as a weight *while* filling the spectra (reconstruction efficiency, acceptance correction, tertiary particles subtraction) or by direct subtraction (empty target).

4.6.1 Reconstruction efficiency

$\varepsilon^{\text{recon}}(p', \theta'_x, \theta'_y)$ is the efficiency for the reconstruction of an analysis track. An analysis track is defined to include a momentum measurement from the event vertex constraint as well as a matched time-of-flight hit. This efficiency is measured directly from the data to avoid any bias introduced from the Monte Carlo simulation. It is a function of the reconstructed quantities p', θ'_x, θ'_y and is applied, as a weight, $W^{\text{recEff}}_{p', \theta'_x, \theta'_y}$, when filling the β spectra. See 3.9.1 for a detailed explanation and computation method.

4.6.2 Acceptance correction

$\varepsilon^{\mathrm{acc}}(\theta')$ is the correction for the geometric acceptance of the spectrometer and is a purely analytical function based on the assumption of azimuthal symmetry in hadron production and the fiducial volume cuts used in the analysis and is explained in detail in Section 3.9.1. The fiducial volume is chosen as the region where the reconstructed efficiency is $\sim 100\%$. This correction is a function of the reconstructed angle θ' and is applied as a weight, $W_{\theta'}^{\mathrm{acc}}$, when filling the β spectra.

4.6.3 Tertiary particle subtraction

The tertiary correction refers to the subtraction of reconstructed tracks which are actually reconstructions of tertiary particles, i.e. particles produced in inelastic interactions or decays of true secondary particles and not in primary interactions of beam protons with target nuclei. The tertiary subtraction includes muons created in decays which are falsely identified as pions nearly 100% of the time due to their high β.

The reconstruction of the particle velocity, β, assumes that the particle has been produced at the target. Tertiary particles included in our β spectrum will add distortions than can not be reproduced by our three-particle β model. Therefore, all tracks corresponding to a tertiary particle must be subtracted from the spectra before the fit.

$(1 - \eta^{\mathrm{tert}}(p', \theta', \beta))$ corrects by the fraction $\eta^{\mathrm{tert}} = \frac{N^{\mathrm{rec\,\text{-}\,tert}}}{N^{\mathrm{rec}}}$ of total tracks passing reconstruction cuts, N^{rec}, which are actually tertiary particles, $N^{\mathrm{rec\,\text{-}\,tert}}$. Both $N^{\mathrm{rec\,\text{-}\,tert}}$ and N^{rec} are obtained by fitting the corresponding β distributions in bins of reconstructed momentum and angle using the same event selection and fitting algorithm as described in Section 4.7. The tertiary correction is the ratio of the resulting fit functions. This produces a tertiary weight function, $W_{p',\theta'}^{\mathrm{tert}}(\beta)$, for each (p', θ') bin. Fig. 4.3 shows the fitted β spectra for both $N^{\mathrm{rec\,\text{-}\,tert}}$ and N^{rec} and the resulting weight function.

The tertiary correction is applied as a weight, $W_{p',\theta'}^{\mathrm{tert}}(\beta)$, while filling the β spectra. Note that the correction does not depend on the particle type and is computed globally for all inclusive positive particles.

The tertiary correction is computed in terms of reconstructed kinematic variables while selecting tertiaries with true variables in the Monte Carlo. The efficiency of the matching between true and reconstructed variables within the simulation has to be computed to get a sense of the bias introduced by the matching procedure. In our analysis we assume
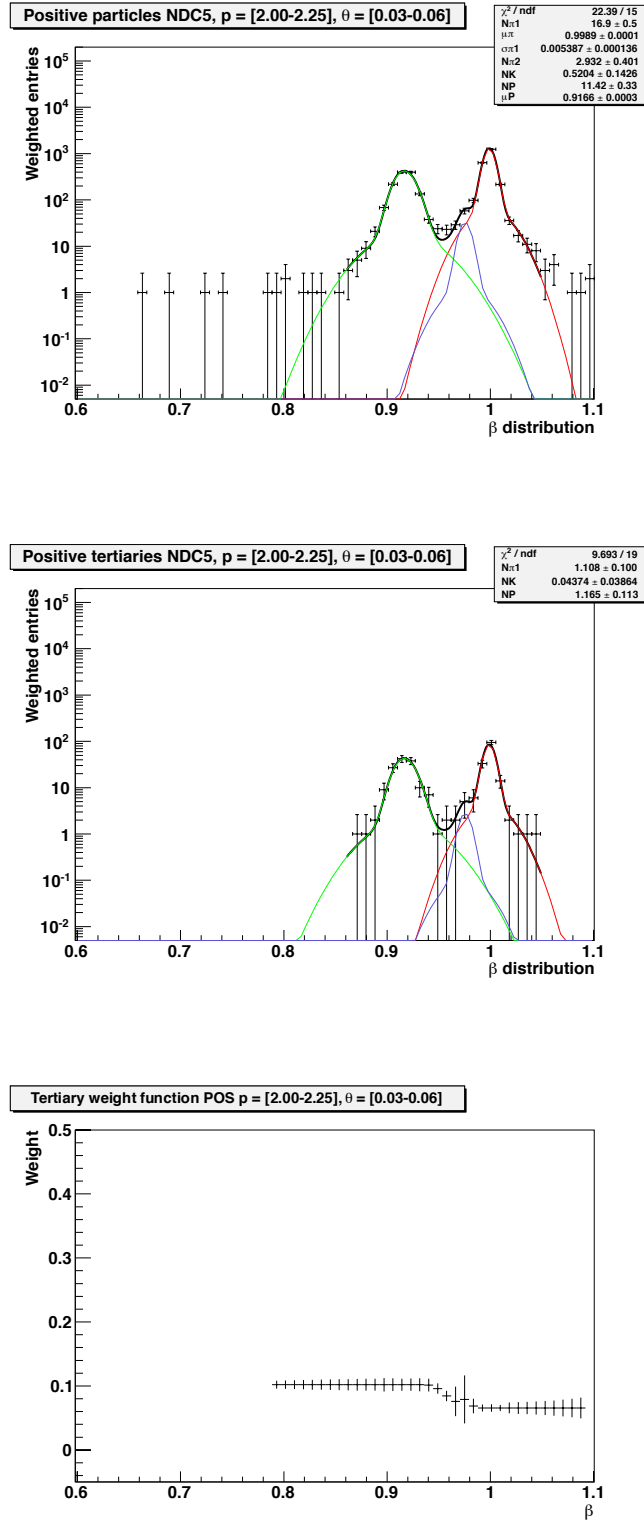
Figure 4.3: The tertiary weight function (bottom) is obtained by fitting the β distributions of the particles that reach the drift-chambers back-plane, following a two-step procedure: first, the β distribution of inclusive particles (top) and second, the β distribution of the tertiary particles (middle). See text for details.

this effect to be small and we consider it to be contained in the global systematic uncertainty added on the cross-sections, as explained in Section 4.10.2.

4.6.4   Electron veto efficiency

The Cherenkov detector is used to veto electrons below the pion threshold (see Section 3.9.2 for a full description of the method). Tracks below 2.5 GeV/c with $N_{\mathrm{pe}} > 15$ are rejected as electrons. Using Monte Carlo simulation one can show that the electron contamination is less than 1% everywhere and is 0.5% or less in the region where the veto is applied. One expects a small efficiency loss for pions, kaons and protons due to this cut in photo-electrons. Approximatively 1% of pions and protons do not pass the electron veto and this has to be taken into account. A 1% global correction has been applied on the final yields.

4.6.5   Empty target subtraction

The empty target data subtraction removes the background coming from beam protons interacting in materials other than the nuclear target (parts of the detector, air, etc.). These events can be subtracted by using data collected without the nuclear target in place. Events and tracks have been selected and reconstructed using the identical set of cuts and algorithm as the nuclear target data set.

β distributions of secondary particles created outside the nuclear target are filled in bins of (p', θ') and are subtracted directly from the corresponding β distributions generated from the target data set. The empty target data set has been corrected with the same pre-fit corrections as the target data set while filling the empty target β spectra, with the exception of the tertiary correction. Tertiary particles produced in *both* the aluminum and empty target data sets need to be subtracted from the β spectra before fitting.

The empty target data set contains about four times less statistics than the aluminum data set. The empty target β distribution is therefore weighted to the ratio of events, $N^{\mathrm{target}}/N^{\mathrm{empty}}$ before the subtraction. However, the subtraction of the the empty target distribution bins that have a small number of entries (pure statistical fluctuations), once weighted, can impact greatly the aluminum target distribution. One way to smooth the empty target distribution is to fill them using a wider binning in β (75 bins instead of 150). The empty correction is therefore averaged over two consecutive bins when subtracted from
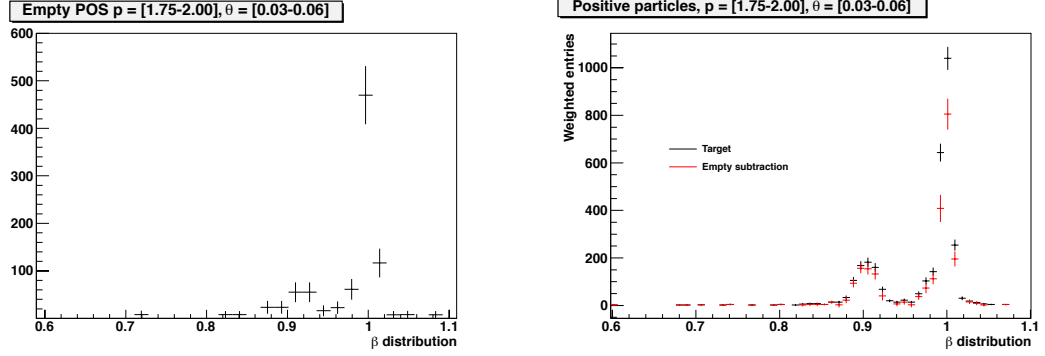
Figure 4.4: Direct application of the empty target correction on the β spectra before fitting shown for a random (p', θ') bin. The top panel shows the β distribution of particles coming from protons interacting in materials other than the nuclear target. The bottom panel show both the original β spectrum of particles coming from 12.9 GeV/c protons interacting with the aluminum target (black points) and the resulting spectrum after the empty target correction subtraction (red points).

the target β distributions. Fig. 4.4 shows both the empty target β distribution and the resulting target β distribution after subtraction, for a given (p', θ') bin.

4.6.6 Weighted β distributions

All pre-fit corrections except empty target subtraction are applied as a weight while filling the β spectra. Fig. 4.5 shows an example of the comparison between unweighted and weighted β distributions.

Fig. 4.6 shows the distribution of the total weight values computed for each β bin. Also shown is the relative contribution of all three individual weights to the total weight. One simply multiplies the values of the three correction weights to obtain the total weight value. Some bins are empty and their corresponding weight is null.
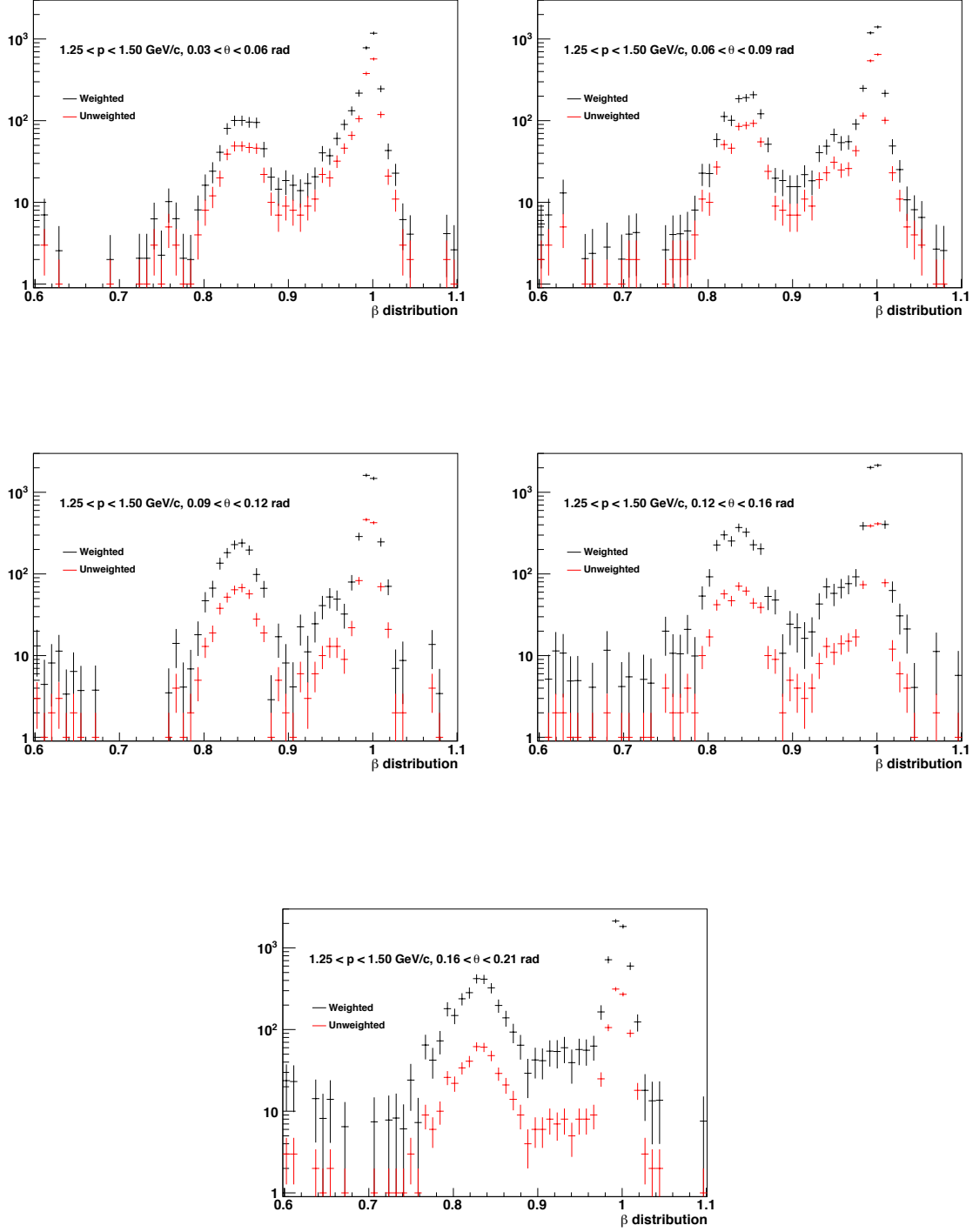
Figure 4.5: Comparison between unweighted and corrected β distributions applying pre-fit correction weights shown for $p' = 1.25$ GeV/c at all angular bins. Error on the unweighted distributions are statistical only and are given by the square root of the number of entries. The errors on the weighted distributions are computed according to Eq. 4.31.
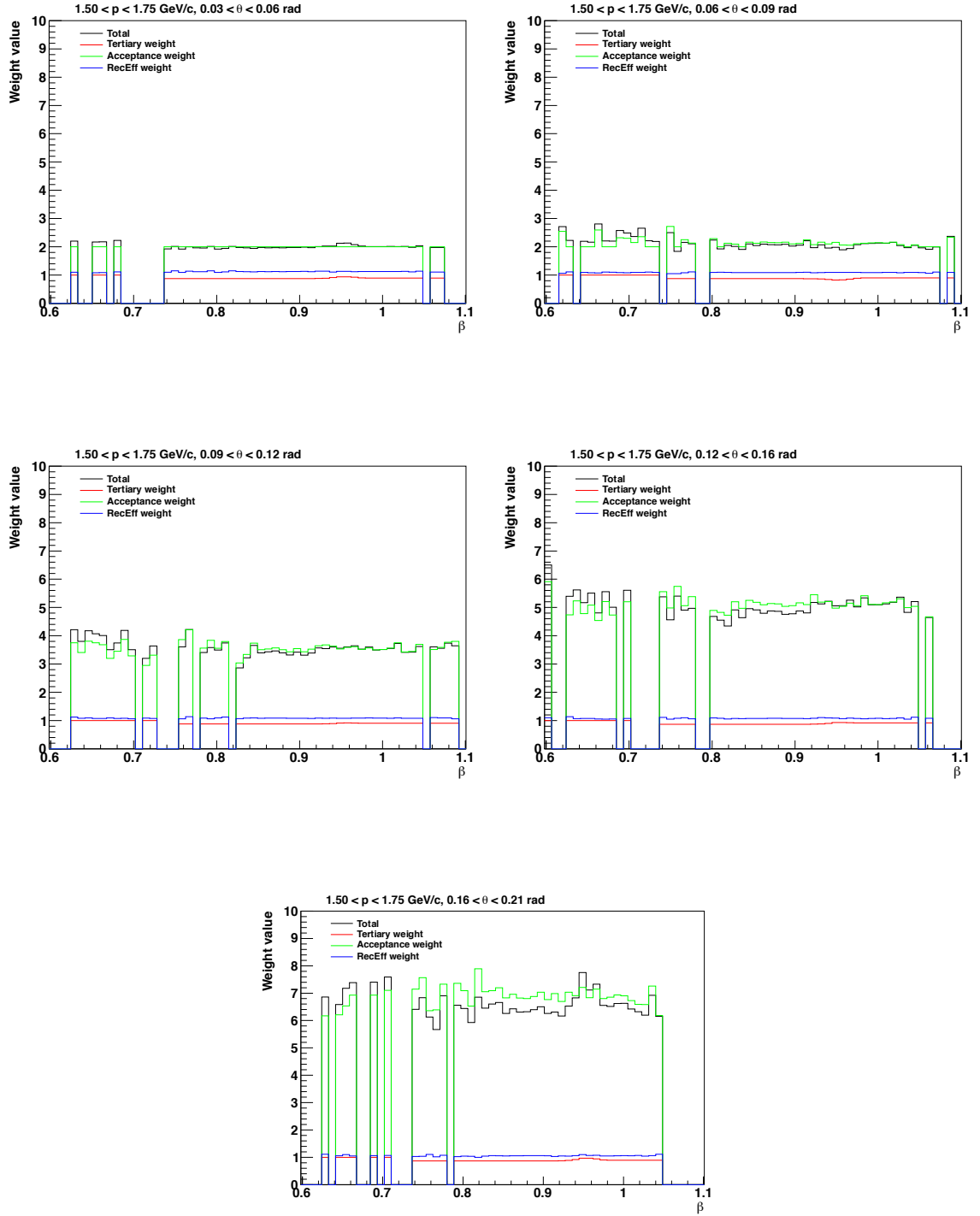
Figure 4.6: Total weight value and the relative contributions of all three pre-fit corrections.

4.7   Modelling the β spectra

Positive particles β distributions are fitted to a three-particle hypothesis probability density function (PDF) for each bin of reconstructed momentum and angle. The PDF is built for each particle species taking into account the following effects of the β and momentum reconstructions:

1. The intrinsic TOFW resolution, σ_β, which is the same for all particles.

2. The momentum resolution of the forward spectrometer, σ_p.

3. The width of the reconstructed momentum bins, $[p_0^{\mathrm{rec}}, p_1^{\mathrm{rec}}]$.

4. The variation of the particle yields within the bin $[p_0^{\mathrm{rec}}, p_1^{\mathrm{rec}}]$.

The PDF function used to model the particle β distributions, evaluated at a reconstructed β value β^{rec} in the $[p_0^{\mathrm{rec}}, p_1^{\mathrm{rec}}]$ momentum bin and for a particle α is ideally:

$$
P\left(\beta^{\mathrm{rec}} \mid p_0^{\mathrm{rec}}, p_1^{\mathrm{rec}} \mid A_\alpha, \sigma_\beta, \sigma_p\right)
$$
$$
= \int_{p_0^{\mathrm{rec}}}^{p_1^{\mathrm{rec}}} \mathrm{d}p^{\mathrm{rec}} A_\alpha(p^{\mathrm{rec}}) \int_{-\infty}^{+\infty} \mathrm{d}p^{\mathrm{true}} \ G(p^{\mathrm{true}} \mid p^{\mathrm{rec}}, \sigma_p) \cdot G(\beta^{\mathrm{rec}} \mid \beta^{\mathrm{true}}, \sigma_\beta) \qquad (4.10)
$$

where σ_p and σ_β are respectively the momentum and β resolutions, and β^{true} is the expected β value for a particle of type α and true momentum p^{true}. A_α is a normalisation factor which depends on momentum. Eq. 4.10 is the convolution of two gaussians that represent the spectrometer's momentum and β resolutions. For each value of the reconstructed momentum p^{rec} there is an infinite number of true momentum values contributing, gaussianly distributed around the value of p^{rec} and with standard deviation σ_p. Each true value of the momentum corresponds to a true β value, which due to finite TOFW resolution is distributed among an infinite number of reconstructed β values, distributed gaussianly around β^{true} with standard deviation σ_β. We can approximate

$$
\int_{-\infty}^{+\infty} \mathrm{d}p^{\mathrm{true}} \ G(p^{\mathrm{true}} \mid p^{\mathrm{rec}}, \sigma_p) \cdot G(\beta^{\mathrm{rec}} \mid \beta^{\mathrm{true}}, \sigma_\beta) \simeq \mathrm{G}\left(\beta^{\mathrm{rec}} \mid \mu_\alpha - \Delta\beta, \sigma_\beta^\alpha\right) \qquad (4.11)
$$

where μ_α is the gaussian mean for the central momentum value of the bin, $\bar{p} = (p_0^{\mathrm{rec}} + p_1^{\mathrm{rec}})/2$, and $\Delta\beta$ is defined as:

$$
\Delta\beta = \beta' - \beta(\bar{p}) \qquad (4.12)
$$
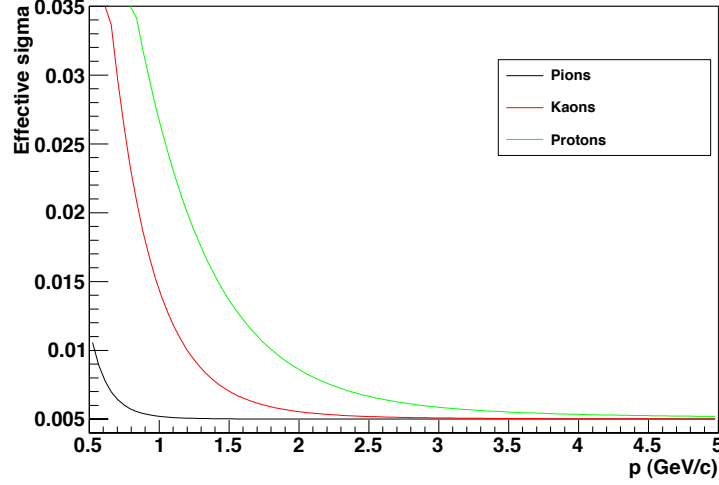
Figure 4.7: Theoretical effective resolution for pions, kaons and protons.

being β' and $\beta(\bar{p})$ the expected velocities for a particle of type α, and momenta p^{rec} and $\bar{p}$ respectively, where this expected value is found using the standard definition:

$$\beta = \frac{p}{\sqrt{p^2 + m^2}} \tag{4.13}$$

Eq. 4.11 corresponds to a single gaussian with *effective* mean $\mu_\alpha - \Delta\beta$ and *effective* resolution σ_β^α, given by

$$\sigma_\beta^\alpha(p^{\text{rec}}) = \sqrt{\sigma_\beta^2 + \left(\frac{\mathrm{d}\beta}{\mathrm{d}p}(p^{\text{rec}}, \mathrm{m}_\alpha) \cdot \sigma_p(p^{\text{rec}})\right)^2} \tag{4.14}$$

where the second term accounts for the variations of β associated to the finite momentum resolution. The effective resolution for pions, kaons and protons is shown in Fig. 4.7.

The integration variable can be changed in Eq. 4.10 from p^{rec} to β', as defined previously. Then, Eq. 4.10 can be rewritten as:

$$P\left(\beta^{\text{rec}} \mid \beta_0', \beta_1' \mid A_\alpha, \mu_\alpha, \sigma_\beta, \sigma_P\right) = \int_{\beta_0'}^{\beta_1'} \mathrm{d}\beta' \ A_\alpha(\beta') \ \mathrm{G}\left(\beta^{\text{rec}} \mid \mu_\alpha - \Delta\beta, \sigma_\beta^\alpha\right). \tag{4.15}$$
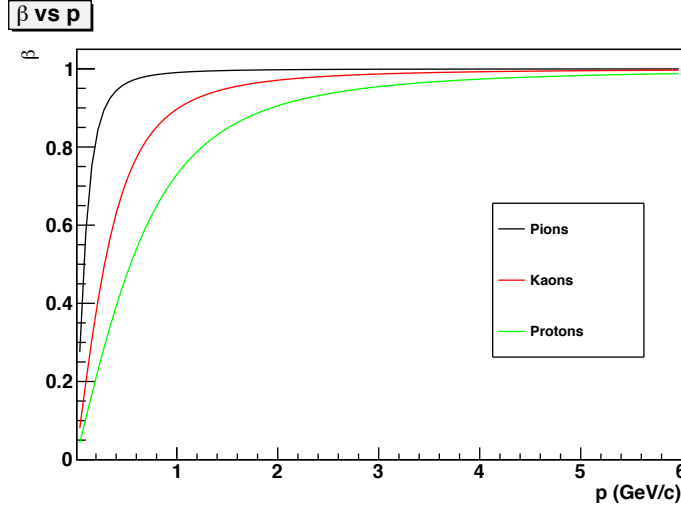
Figure 4.8: Theoretical β vs momentum for pions, kaons and protons. Pions reach relativistic speeds at low momentum.

The lower and upper integration limits, β_0' and β_1' correspond to the momentum bin's lower and upper values, p_0^{rec} and p_1^{rec}. Eq. 4.15 models the smearing effect due to both the TOFW and momentum resolutions around each value of β^{rec}. It can be seen as the superposition (the integral over β) of several Gaussians with different widths (due to the variable σ_β^α) and different normalisation (due to the non-flat particle yield within the reconstructed momentum bin).

PDF for pions

The effective resolution for pions is the intrinsic TOFW resolution as pions are reaching the TOFW at relativistic speed already at low momentum. Looking at Fig. 4.8, one can see that pions with momentum above 0.75 GeV/c give essentially the same β. This has two consequences to the general formulae presented above. First, Eq. 4.14 becomes simply $\sigma_\beta^\pi = \sigma_\beta$ as the second term, $\frac{\mathrm{d}\beta}{\mathrm{d}p}$, is suppressed. Second, $\beta_0' = \beta_1'$ in Eq. 4.15, which ideally becomes a single gaussian:

$$P\left(\beta^{\text{rec}} \mid A_\pi, \mu_\pi, \sigma_\beta\right) = A_\pi \cdot \mathrm{G}\left(\beta^{\text{rec}} \mid \mu_\pi, \sigma_\beta\right) \tag{4.16}$$

since $\beta_0' = \beta_1'$ implies $\Delta\beta = 0$. However, a second gaussian function with the same mean has been added to approximate the contribution of β-outliers to the main peak:

$$P\left(\beta^{\mathrm{rec}} \mid A_1^\pi, A_2^\pi, \mu_\pi, \sigma_1^\pi, \sigma_2^\pi\right) = \frac{A_1^\pi}{\sqrt{2\pi}\sigma_1^\pi} \cdot \exp\left[-\frac{1}{2}\left(\frac{\beta^{\mathrm{rec}} - \mu_\pi}{\sigma_1^\pi}\right)^2\right]$$
$$+ \frac{A_2^\pi}{\sqrt{2\pi}\sigma_2^\pi} \cdot \exp\left[-\frac{1}{2}\left(\frac{\beta^{\mathrm{rec}} - \mu_\pi}{\sigma_2^\pi}\right)^2\right] \qquad (4.17)$$

where σ_1^π is just the intrinsic TOFW resolution, σ_β, and σ_2^π is defined as

$$\sigma_1^\pi = R_\sigma^\pi \cdot \sigma_2^\pi \qquad (4.18)$$

being R_σ^π a parameter to be determined experimentally.

PDF for kaons and protons

Kaons and protons do not reach the TOFW at relativistic speeds and one can no longer simplify the general formulae as it was done for pions. For kaons and protons, both the intrinsic TOFW and momentum resolutions contribute to the width of the β distributions and the general convolution formula (Eq. 4.15) has to be applied. As explained previously the non-flat distribution of particle yields within a reconstructed momentum bin should be taken into account, at least at low momentum, where the β value may change significantly from the lower to the upper bin limits. The shape of the particle yield within the momentum bin can be approximated by a straight line

$$A_\alpha(\beta') = A_1^\alpha + (\beta' - \beta_0') \cdot S_\alpha \qquad (4.19)$$

where A_1^α is the normalisation for $\beta' = \beta_0'$ and S_α is the slope parameter. The resolution function of Eq. 4.15 is again a sum of two Gaussians with shared mean but different widths and normalisation. As in the pion case the second Gaussian accounts for β outliers. Thus, Eq. 4.15 becomes:

$$P\left(\beta^{\mathrm{rec}} \mid A_1^\alpha, A_2^\alpha, \mu_\alpha, \sigma_1^\alpha, \sigma_2^\alpha, S_\alpha\right) = \int_{\beta_0'}^{\beta_1'} \mathrm{d}\beta'$$
$$\frac{A_1^\alpha + (\beta' - \beta_0') \cdot S_\alpha}{\sqrt{2\pi}\sigma_1^\alpha} \cdot \exp\left[-\frac{1}{2}\left(\frac{\beta^{\mathrm{rec}} - (\mu_\alpha - \Delta\beta)}{\sigma_1^\alpha}\right)^2\right]$$
$$+ \frac{A_2^\alpha + (\beta' - \beta_0') \cdot S_\alpha}{\sqrt{2\pi}\sigma_2^\alpha} \cdot \exp\left[-\frac{1}{2}\left(\frac{\beta^{\mathrm{rec}} - (\mu_\alpha - \Delta\beta)}{\sigma_2^\alpha}\right)^2\right] \qquad (4.20)$$

with:

$$A_1^\alpha = R_A^\alpha \cdot A_\alpha$$

$$A_2^\alpha = (1 - R_A^\alpha) \cdot A_\alpha$$

$$\sigma_1^\alpha = \sigma_\beta^\alpha(p) = R_\sigma^\alpha \cdot \sigma_2^\alpha \tag{4.21}$$

where R_A^α and R_σ^α are the ratios between the two gaussian normalizations and widths, respectively. Their values and the method to define them are presented in Section 4.8. Some parameters may not be fitted depending on the type of particle.

The fit results when using the modified effective resolution formula and adding the slope parameter are shown in Fig. 4.9 and Fig. 4.10, respectively. One can see a clear improvement using the momentum-dependant effective resolution.

The shape of the β distribution is also sensitive to the particle distribution within a bin of momentum. This is especially true for protons at low momenta where small variations in momentum generate a wide range of β values and is negligible for kaons (see Fig. 4.8). The slope parameter takes care of this effect and improves proton fits at low momenta. The method to obtain the slope parameter values is explained in Section 4.8.

4.8   The fit algorithm

The total number of particles in a given reconstructed (p', θ') bin is obtained by fitting simultaneously the pre-corrected β distribution to the sum of the pion, kaon and proton PDFs (Eqs. 4.16 and 4.20) and integrating the resulting best fit functions over the β interval considered for the fit $[\beta_{\min}^{\mathrm{rec}}, \beta_{\max}^{\mathrm{rec}}]$:

$$N_\pi = \int_{\beta_{\min}^{\mathrm{rec}}}^{\beta_{\max}^{\mathrm{rec}}} \mathrm{d}\beta^{\mathrm{rec}} \; \mathrm{P}\left(\beta^{\mathrm{rec}} \mid A_1^\pi, A_2^\pi, \mu_\pi, \sigma_1^\pi, \sigma_2^\pi\right) \tag{4.22}$$

$$N_{k,p} = \int_{\beta_{\min}^{\mathrm{rec}}}^{\beta_{\max}^{\mathrm{rec}}} \mathrm{d}\beta^{\mathrm{rec}} \; \mathrm{P}\left(\beta^{\mathrm{rec}} \mid A_1^\alpha, A_2^\alpha, \mu_\alpha, \sigma_1^\alpha, \sigma_2^\alpha, S_\alpha\right) \tag{4.23}$$

Ideally, all parameters from Eq. 4.17 and 4.20 are let free and the PDFs are fitted over the whole β interval $[\beta_{\min}^{\mathrm{rec}}, \beta_{\max}^{\mathrm{rec}}] = [0 - 1.3]$. The number of free parameters for the total PDF is 15, since the main gaussian width (σ_1^π, σ_1^K, σ_1^p) depends only on the intrinsic TOFW resolution σ_β, which is common for all particle types[2]. Leaving all parameters free

---

[2]In Eq. 4.14, the momentum resolution and the derivative of β with respect to momentum are well known functions

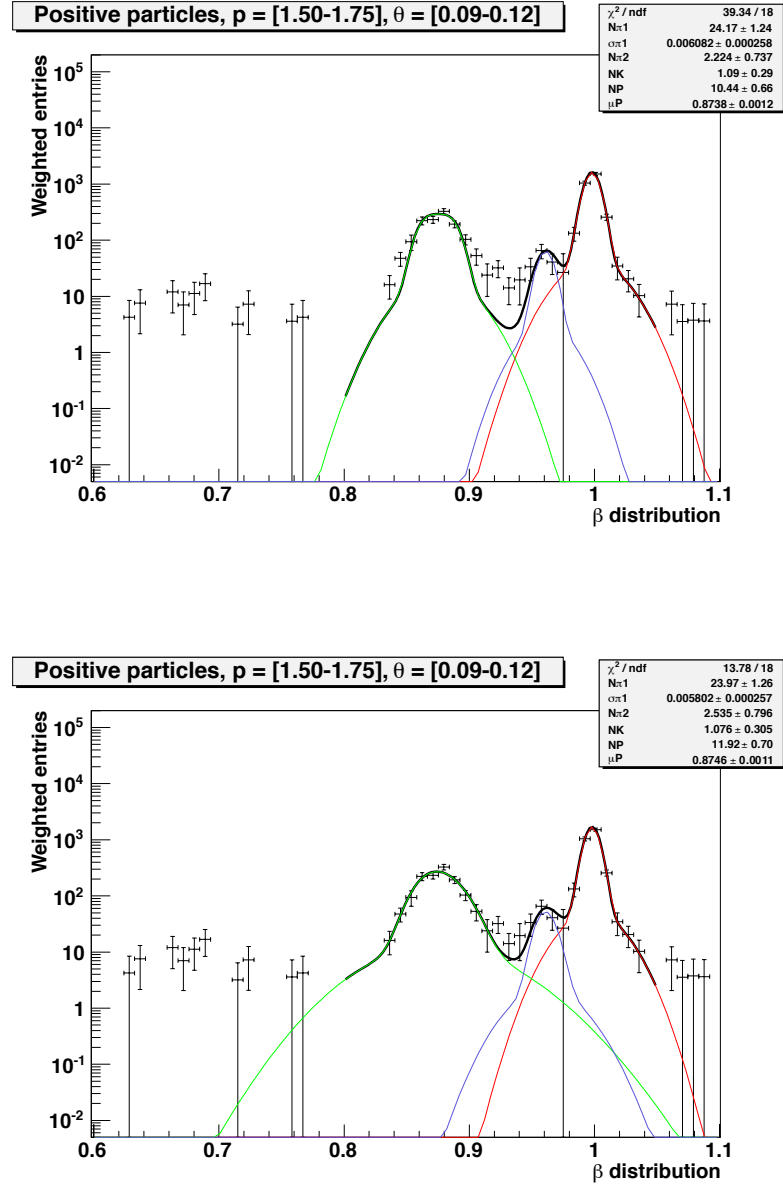Figure 4.9: Top: Pdf as defined by Eq. 4.17 for pions and 4.20 for kaons and protons without using the effective resolution formula. Bottom: Protons and Kaons PDF's using the effective resolution given by Eq. 4.14.
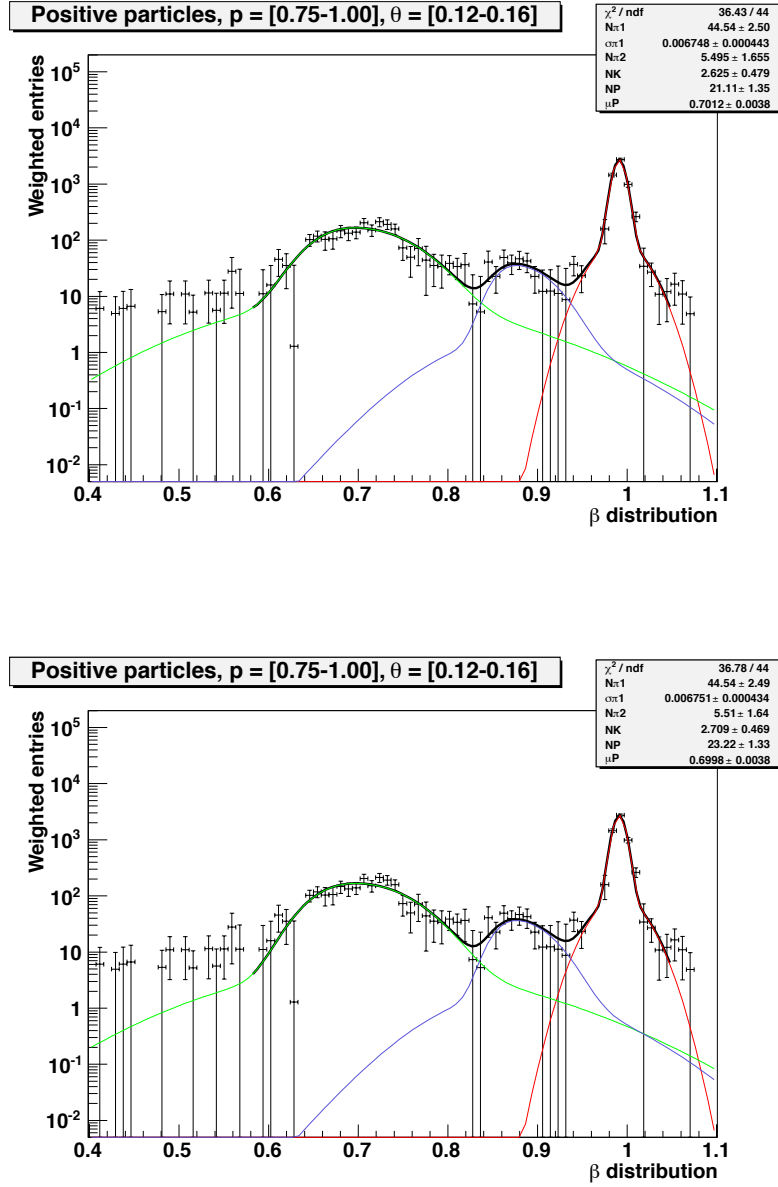
Figure 4.10: Protons and Kaons PDF's computed without using the slope parameter (top) and using the slope parameter (bottom) given by Eq. 4.20. Note the difference in the the number of protons measured.

would result in a highly unstable fit, which would have a big impact on the number of kaons obtained. Is therefore mandatory to fix some of the parameters using some reasonable physics assumptions.

It is crucial to fix all kaon parameters except a single normalisation parameter, since the statistical power of the kaon peak is not sufficient to evaluate most of them. The kaon mean parameter, μ_K can be evaluated interpolating proton and pion means:

$$\mu_K = \mu_\pi - \frac{\overline{\beta}_\pi - \overline{\beta}_K}{\overline{\beta}_\pi - \overline{\beta}_p} \cdot (\mu_\pi - \mu_p) \qquad (4.24)$$

where μ_π and μ_p are the means of the pion and proton PDFs that are being fitted simultaneously. $\overline{\beta}_\pi$, $\overline{\beta}_K$ and $\overline{\beta}_p$ are the expected beta values for kaons, pions and protons evaluated at the center of the momentum bin using Eq. 4.13. As mentioned above, the effective width of the main gaussian depends only on the intrinsic TOFW resolution, σ_β. As we will see, although σ_β enters in all three PDFs its value will be mainly obtained from the width of the pion peak. The ratios between the gaussian normalisations, R_A^K, and the widths, R_σ^K are fixed to the ones observed for pions. This is a reasonable assumption, since the effect of the second kaon gaussian is almost irrelevant due to the small size of the kaon peak compared to the ones of pions and protons. Finally, the kaon slope parameter S_α of Eq. 4.20 can be neglected, since no impact has been observed.

As mentioned above the proton mean parameter, μ_p is let free, while its effective width for the main gaussian depends only on σ_β. As in the Kaon PDF the ratios between the gaussian normalisations, R_A^p, and the widths, R_σ^p are fixed to the ones observed for pions. Obviously, in this case the second proton gaussian should have a considerable impact in the kaon normalisation. This will be treated as a systematic error. The slope parameter cannot be neglected for protons. It is fixed to the value obtained by following this iterative method: one measures the proton yields by fitting β spectra to Eq. 4.20 with $S_p = 0$. Fitting the proton yields distribution allows us to extract the variation of the proton distribution within each bin of momentum. This variation gives directly the value of the slope parameter. The β spectra are then fitted again, with the slope parameter fixed to the value obtained in the previous step. A new set of proton yields is extracted which, in turn, gives a new value for the slope parameter. Three iterations suffice to stabilize the value of the slope parameter, which is then fixed throughout the analysis.

In principle all pion parameters are let free. However those parameters have to be carefully studied as any slight bias on the pion mean or width may have a significant impact
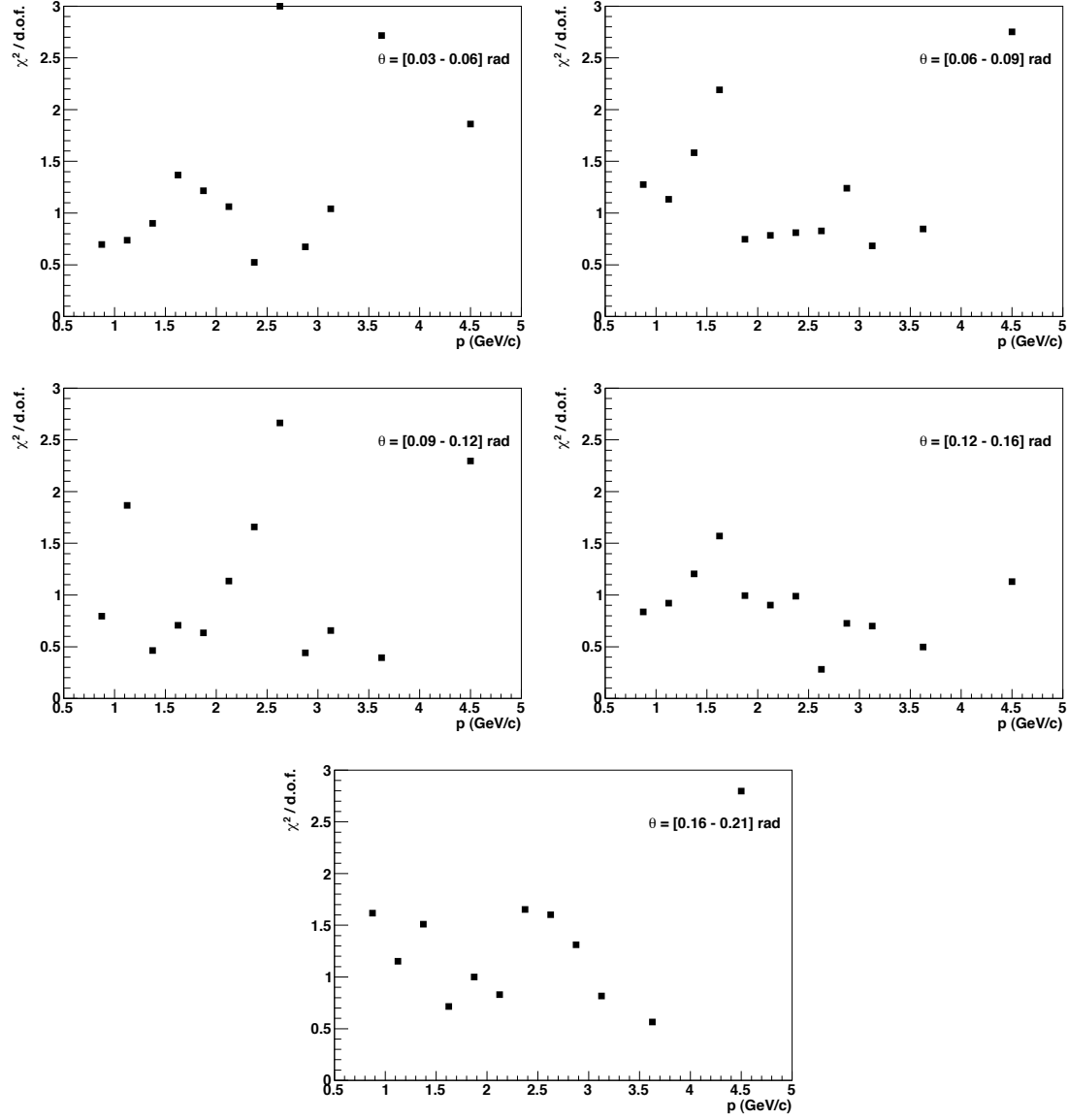
Figure 4.11: $\chi^2/d.o.f.$ vs. momentum obtained by fitting β spectra, letting all parameters in Eq. 4.17 and 4.20 free.

on the kaon measurements. This is especially true when both distributions start to overlap. This will be discussed extensively in the next section.

Finally, the PDFs are fitted over a subinterval of β. The interval is chosen to avoid fitting outside the region of the pion, kaon and proton peaks where TOF-outliers and non relevant particles dominate. The sub-interval has been defined as $[\mu_p - 5 \cdot \sigma_\beta^p, 1.05]$. $\chi^2/d.o.f.$ values obtained by fitting the β spectra with all fit parameters free are shown in Fig. 4.11.

Understanding pion PDF parameters

One way to assert the quality and stability of the fitting method is to plot the resulting fitted parameters μ_π, σ_1^π, σ_2^π vs. momentum for positive pions, as shown in Fig. 4.12. Limits on the pion width parameters have been set to guarantee physical results and the convergence of the fit algorithm:

$$0.005 \leq \sigma_1^\pi \leq 0.01$$
$$0.005 \leq \sigma_2^\pi \leq 0.05 \tag{4.25}$$

Looking at Fig. 4.12, we see on the middle panel that the main gaussian width of the pion distribution, σ_1^π, asymptotically gives the intrinsic TOFW resolution which is ~ 0.0055. By looking at the σ_1^π distribution in Fig. 4.12, we notice that some curves reach the intrinsic TOFW value while other have a chaotic behaviour. We will explain this effect in a later stage of the analysis once more constraints are added to the fit parameters. On the other hand, the second gaussian width (bottom panel) falls in two categories: it is either distributed around 0.02 or reaches the parameter limit values. Notice that the gaussian functions may sometimes interchange during the fitting process, which explains why σ_1^π (σ_2^π) reaches or is close to 0.01 (0.005). To avoid this problem, the second pion gaussian width has been fixed throughout the analysis to:

$$\sigma_2^\pi = 3.6 \cdot \sigma_1^\pi \tag{4.26}$$

where σ_1^π is the width of the main pion gaussian and 3.6 is obtained by computing the ratio between the observed second gaussian width (~ 0.02) and the TOFW intrinsic resolution (0.0055). The effect of this particular choice of the scale factor between the two gaussian widths will be treated as a systematic error.

Fig. 4.13 shows the values of the fitted parameters μ_π, σ_1^π versus momentum for positive pions with σ_2^π fixed following Eq. 4.26. Both μ_π and σ_1^π distributions have
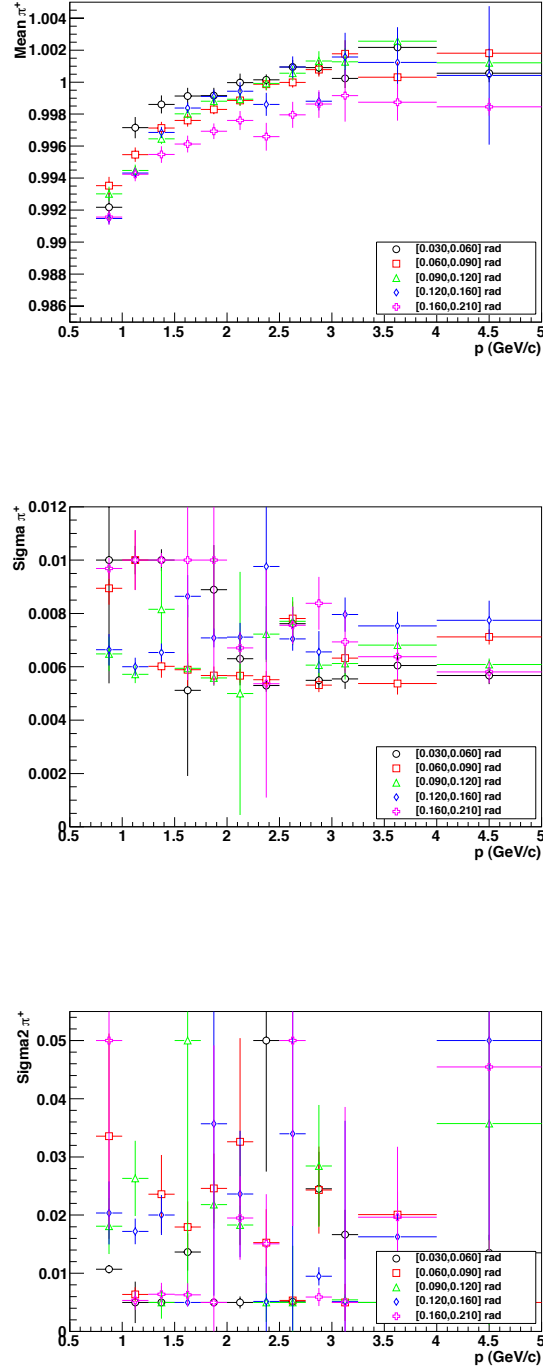
Figure 4.12: Fitted mean and width vs. reconstructed momentum for positive pions. Results are shown for all theta bins. All parameters in Eq. 4.17 are fitted.

Figure 4.13: Fitted mean and width vs. reconstructed momentum for positive pions. Results are shown for all theta bins. The σ_2^π parameter in Eq. 4.17 is fixed to $3.6 \cdot \sigma_1^\pi$.

stabilized at all angles when compared to Fig. 4.12. However, several unexpected effects can be observed. First, σ_1^π shows the expected pattern for the first three angular bins, i.e. the pion width decreases at higher momenta towards the intrinsic resolution of the TOFW (0.0055). This can be seen as the TOFW resolution term dominating in Eq. 4.14[3]. However, points corresponding the last two angular bins do not follow that same pattern (and cannot be explained with the effective resolution formula as it is). σ_1^π tends to increase at high momentum and high angle, as if a missing third term was dominating in the effective resolution formula. Second, μ_π tends to be underestimated in the last angular bin.

This has been interpreted as follows: the TOFW is composed by three modules of scintillator bars (see Section 3.8.3): one central with horizontal slabs and two lateral with vertical slabs, placed at each extremities of the central one (Fig. 3.8). Fig. 4.14 shows the percentage of particles reaching the TOFW lateral modules with vertical slabs ($N^{\text{Vertical}}/N^{\text{Total}}$) as a function of momentum for all angle bins. This distribution has been extracted from the same data set as the one analysed, using the same event and secondary track selection. Notice, that particles in the last angular bin, $[160-210]$ mrad, hit exclusively the lateral modules of the TOFW at momenta greater than 2.25 GeV/c, while particles in the bin $[120-160]$ mrad have a mixture of both modules types that varies with momentum.

---

[3]The momentum resolution term dominates at low momentum for all angular bins
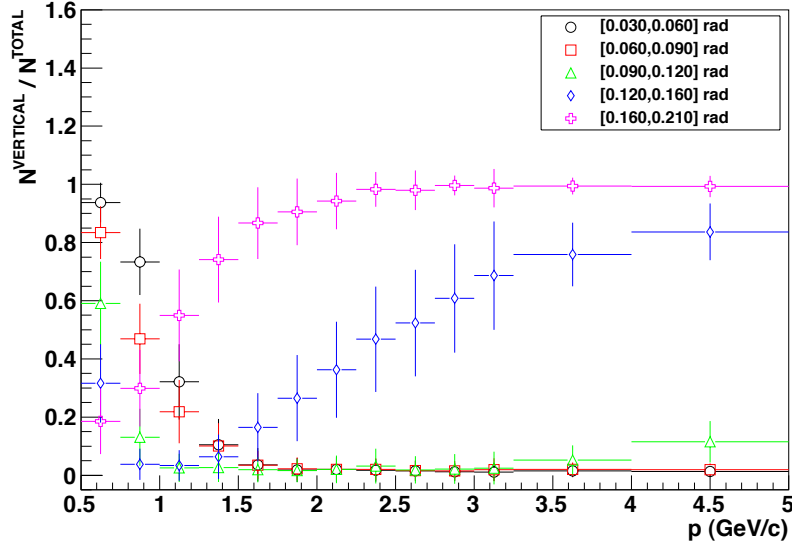
Figure 4.14: Fraction of reconstructed tracks reaching the TOFW lateral modules as a function of momentum shown for all angular bins.

These two angular bins affected by the lateral modules are precisely the ones showing an unexpected behavior at high momentum in the μ_π and σ^π distributions. A bad calibration of the lateral module affecting the two last angular bins could therefore explain the effect. In particular β could be shifted to lower values in the lateral TOFW modules, what would explain why μ_π is underestimated in the last angular bin for almost all momenta, and probably in the last but one angular bin for large momenta. This shift in β between the central and the lateral modules could also explain why σ_1^π tends to be larger when both modules contribute to a given (p', θ') bin.

Another effect that should be taken into account is that the interference of the kaon peak could increase the pion width at large momentum, when both peaks overlap considerably. One way to directly measure the intrinsic resolution of the vertical and horizontal slab TOFW modules, separately, and without the interference of the proton and kaon peaks, is to fit the β distribution obtained by selecting a pure sample of positive pions. This sample is obtained selecting tracks that leave more than 2 photo-electrons in the Cherenkov
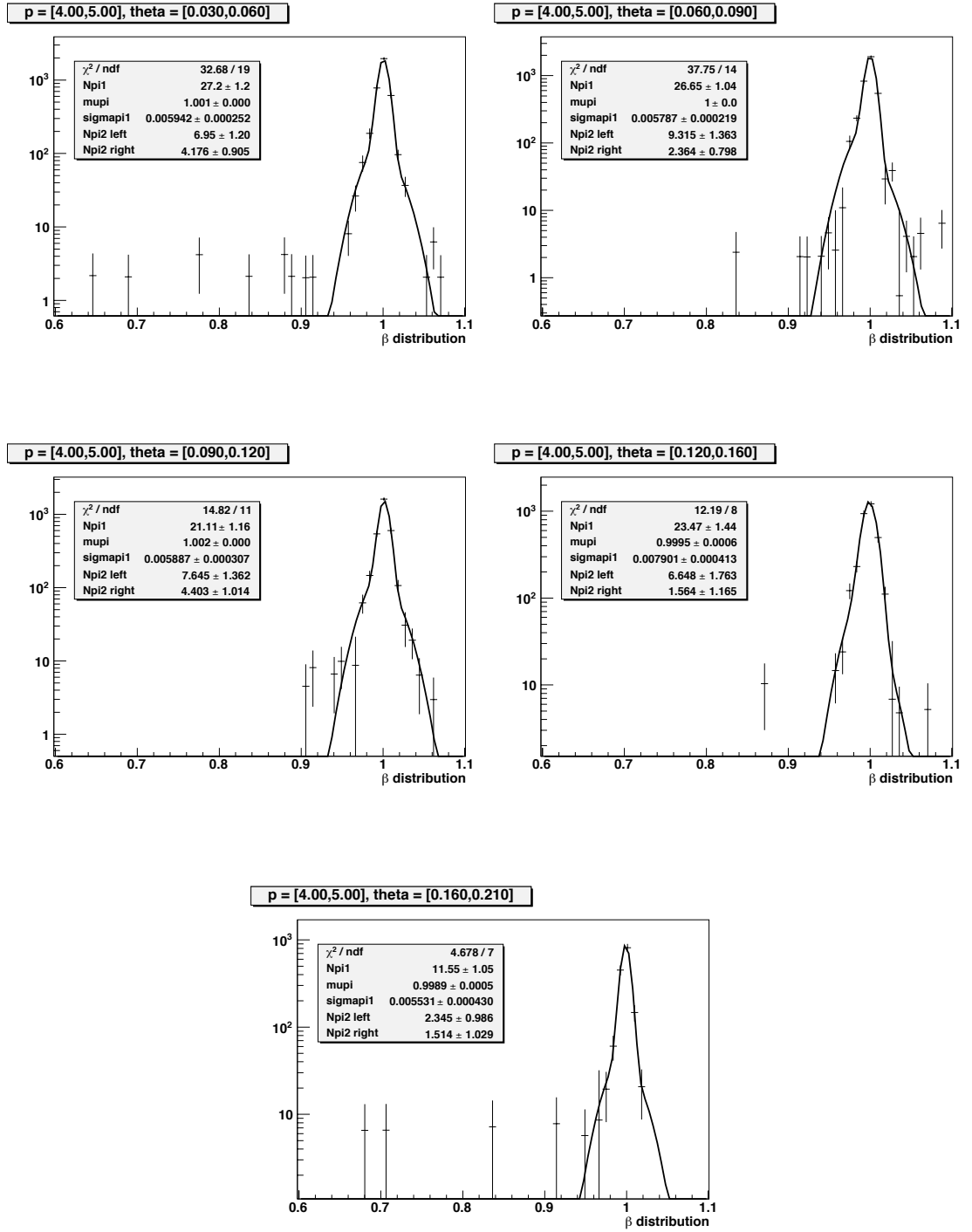
Figure 4.15: β distributions of positive pions. This pure sample has been obtained selecting particles passing only the inverse CKOV cut and is fitted to a double gaussian distribution, similar to Eq. 4.17. The normalization parameters describing the left and right side of the gaussian distribution are fitted independently.
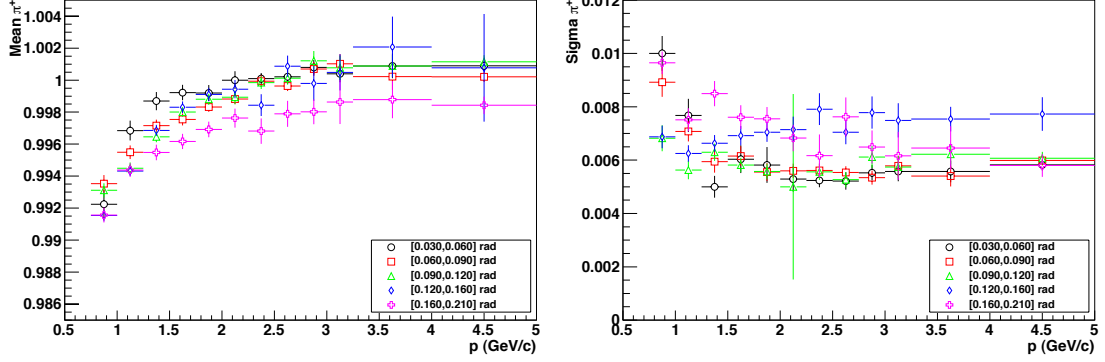
Figure 4.16: Fitted mean and width vs. reconstructed momentum for positive pion. Results are shown for all theta bins. The σ_2^π parameter in Eq. 4.17 has been fixed. μ_π and σ_1^π above 3 GeV/c have been replaced by the values obtained by fitting pure sample π^+ distributions.

detector at momenta p > 2.75 GeV/c. These pure pion β spectra are fitted to the sum of two gaussians, with common means, and with the second gaussian being the factor of the first gaussian defined above. An example of those fits is shown in Fig. 4.15 for the momentum bin 4-5 GeV/c. The fitted widths are compatible with the intrinsic TOFW resolution $\sigma_\beta = 0.0055$ for all angular bins except for the fourth one, with a width of ~ 0.008. This result is again compatible with Fig. 4.14, which shows that particles with momentum above 2.25 GeV/c reach essentially either the vertical or horizontal TOF slabs, with the exception of particles in the fourth angular bin (in blue).

μ_π and σ_1^π values for momenta above 3 GeV/c are replaced by the one obtained by fitting the pure pion sample spectra and is shown in Fig. 4.16. This has the effect to reduce fluctuations and smooth the mean and width curves. However, small fluctuations at high momentum, where the kaon and pion peaks overlap considerably, may introduce important biases in the kaon normalisation parameter. We can further improve the stability of σ_1^π by fitting the experimental points in Fig. 4.16 to the appropriate function. The fit is done at high momentum, where the effect of the momentum resolution is negligible. The fitting function and interval are chosen as follows:

- [0.03-0.09] rad: fit to a constant in the [2.25 - 5] GeV/c interval. No dependence on
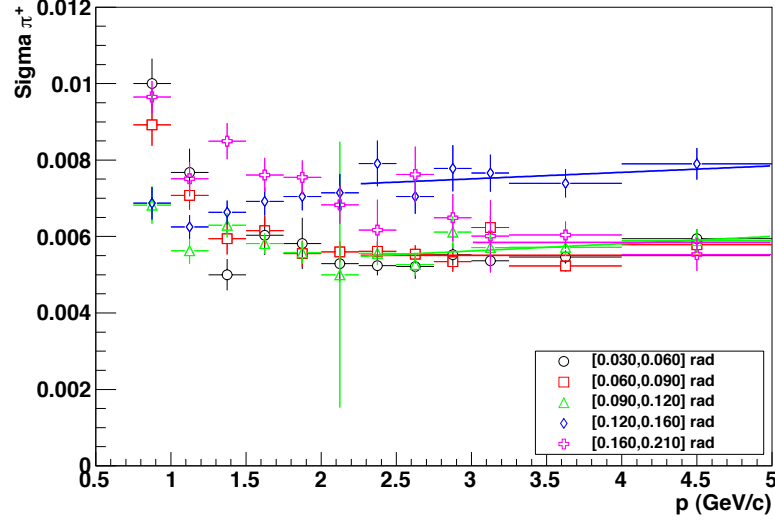
Figure 4.17: Positive pions width vs. momentum. The distributions are fitted to a line with or without slope. See text for details.

momentum is expected above 2.25 GeV/c since all particles reach the central TOFW.

- [0.09-0.16] rad: fit to straight line in the [2.25 - 5] GeV/c interval. We expect some momentum dependence since there is a mixture between the central and lateral TOFW.

- [0.16-0.21] rad: fit to a constant in the [3 - 5] GeV/c interval. No dependence on momentum is expected above 2.25 GeV/c since all particles reach the lateral TOFW.

The fitting interval for the last angular bin is justified by the fluctuations seen at momenta above 2 GeV/c. Moreover, particles in that angular bin reach exclusively the TOFW vertical slabs at momenta above ~ 2.25 GeV/c. Therefore, one can safely extrapolate the pure pion sample fit results down to that momentum value. The resulting fitted σ_1^π distributions are shown in Fig. 4.17.

The β distributions are then fitted with σ_1^π fixed. When plotting the resulting μ_π distributions as a function of momentum, one can see that fixing σ_1^π improved further the fit quality and stability as shown in Fig. 4.18. One can still see that the measured
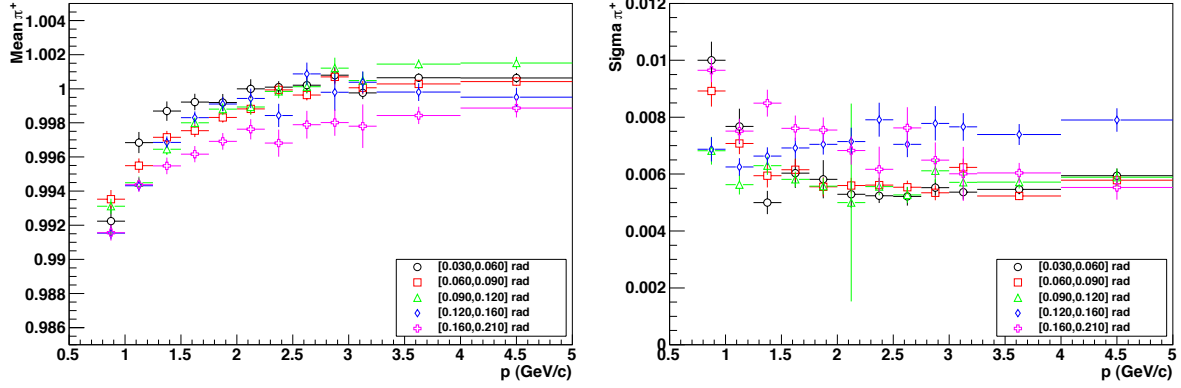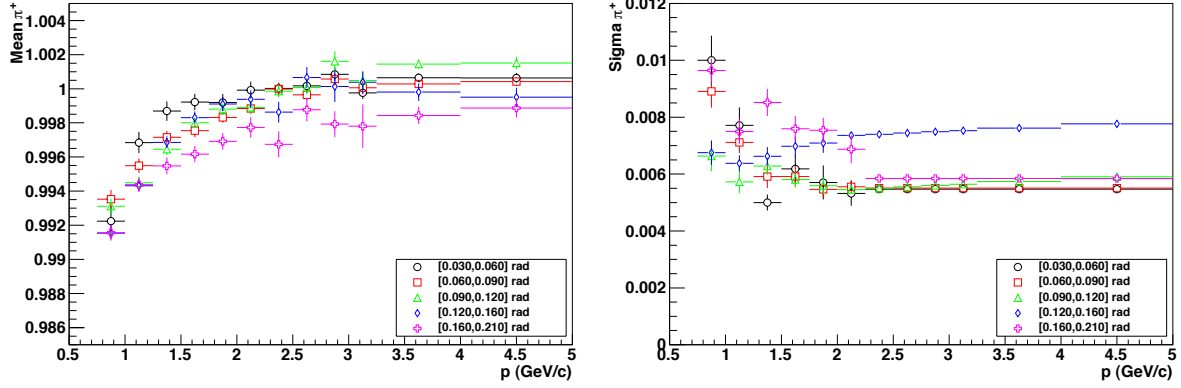
Figure 4.18: Fitted mean and width vs. reconstructed momentum for positive pion. Results are shown for all theta bins. The σ_1^π parameter in Eq. 4.17 is fixed to the fit results shown in Fig. 4.17.

mean is systematically smaller for the last angular bin. In that bin, particles only reach the vertical TOFW slabs and the difference in measured mean could be explained by a biased reconstructed track length or time-of-flight. The same effect can be seen for particles in the fourth angular bin at high momenta. This time particles reach a mix of both vertical and horizontal TOFW slabs. Notice that statistical fluctuations, although small, could influence the kaon peak parameters. Since the momentum dependence of β is a priori known (see Eq. 4.13), the effect of statistical fluctuations can be reduced by fitting the μ_π distributions to the empirical parametrization:

$$a \cdot \frac{(b \cdot p)}{\sqrt{(b \cdot p)^2 + m_\pi^2}} \qquad (4.27)$$

where the parameters a and b account for the miscalibration of the time-of-flight and biases in the measured track length. μ_π parameters are fixed throughout the analysis to the values of the fitted curves as seen in Fig. 4.19.

As explained above, we observe bigger values of σ_1^π for (p',θ') bins which have contribution from both central and lateral TOFW modules at large angles which translate into wider pion peaks in the β distributions. An example of this effect is illustrated in Fig. 4.20 which shows the β distribution and the fitted values of σ_1^π for the 5 different angular bins in the $[1.75 - 2]$ GeV/c momentum bin. The latter corresponds to a region where only
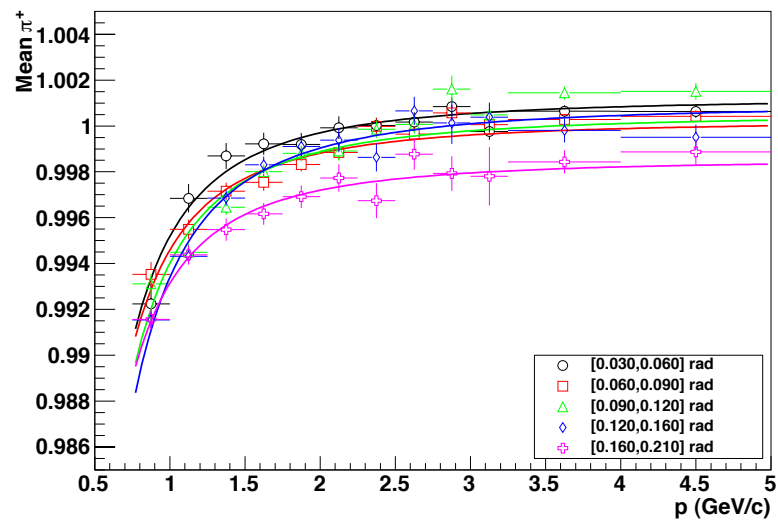
Figure 4.19: Positive pions width vs. momentum. The distributions are fitted to the formula given by Eq. 4.27. See text for details.

the two last angular bins have a mixture of TOFW modules. We observe that indeed only the two last angular bins have σ_1^π considerably larger than σ_β. The same effect is seen on the proton peaks (and therefore also on the kaon peak). This is a real effect which we can explain as the combination of two contributions: the mixture of the two TOFW modules with deficient intercalibration and a worse momentum resolution at large angles.

To model such an effect in the proton and kaon peaks, the static σ_β value (0.0055) in the the effective sigma formula (Eq. 4.14) has been replaced by the fitting parameter σ_1^π, such that variations of the TOFW β resolution with angle and momentum are taken into account. In parallel, we also use a momentum resolution function that depends on the angle θ to further improve the fit algorithm at large angles. An example of a fit using the modified σ_β and σ_p is shown in Fig. 4.21.

Finally, the normalization ratio of the two gaussians in the proton and kaon PDFs has been fixed to the ratio measured for pions. Fig. 4.22 shows the distribution of ratios of the two pion gaussian normalization parameters as a function of momentum. Most ratios are ~ 7, what implies $R_A = 0.88$, according to Eq. 4.21, i.e. the first (second) gaussian will contain 88% (12%) of the total fitted normalization.

This very restrictive set of fixed parameters ensures the stability of the fit method. A systematic error corresponding to each of the parameter being fixed will be considered in Section 4.10.2 to alleviate the impact of these restrictions on the final measured cross-sections.

4.8.1   Cherenkov cut

The Cherenkov detector can be used as a powerful discriminator to remove pions above the 2.75 GeV/c detector threshold and has the effect to better expose the kaon peak in the momentum range where both peaks start to overlap. This improves the fit algorithm reliability and tends to reduce the error on the kaon fit parameters. The Cherenkov cut is applied while filling β distributions and its efficiency is discussed in Section 3.9.2. A two-step fit procedure is used to improve the stability and speed of the fitting algorithm. First, inclusive positive particle β distributions filled *without* applying the Cherenkov cut are fitted following the same procedure and using the same set of fixed parameters as presented in Section 4.8.

Second, β distributions filled applying the Cherenkov cut are fitted for proton,
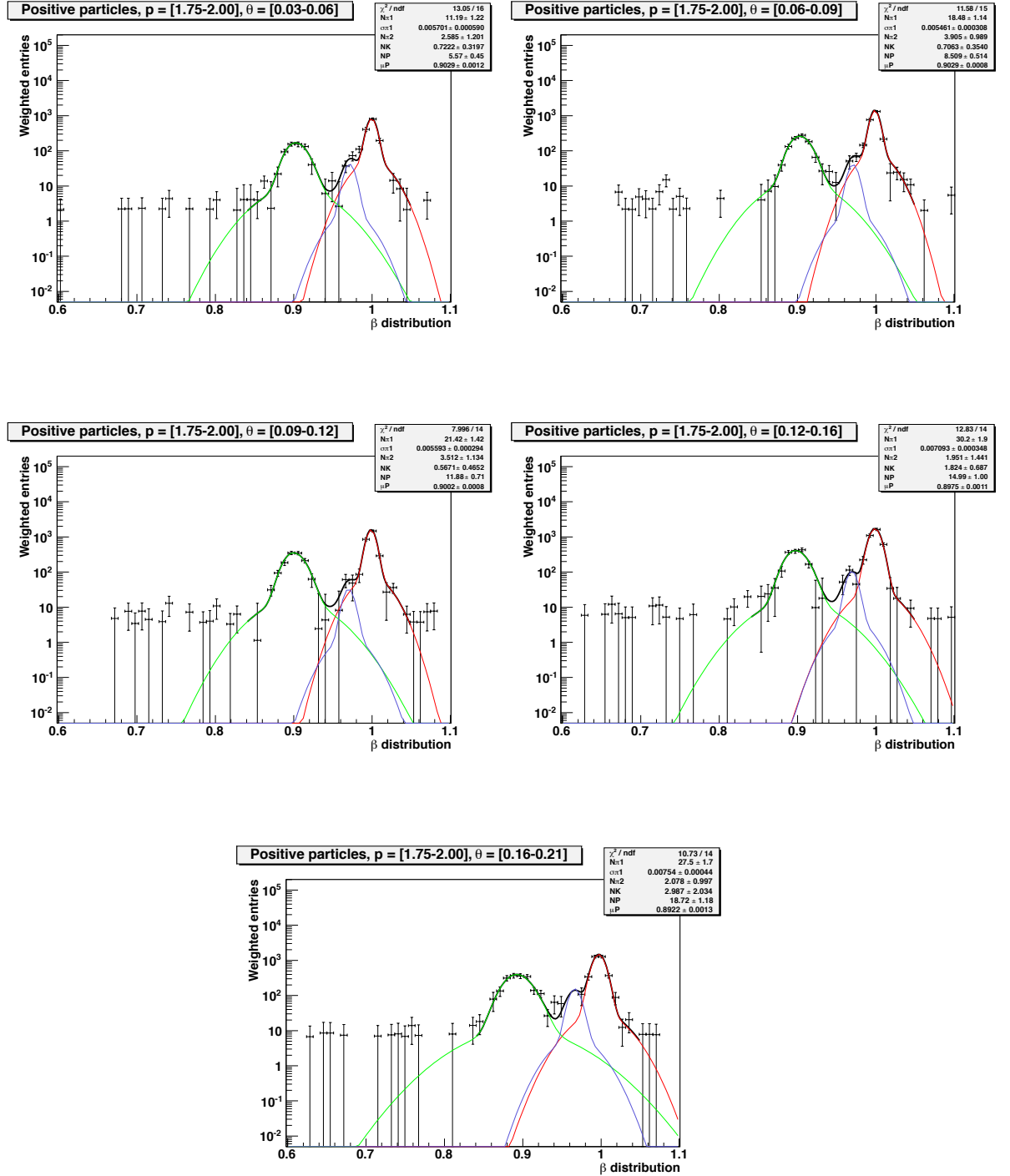
Figure 4.20: Fitted β distributions for the five angular bins at $[1.75 - 2]$ GeV/c momentum bin. Wider pion peaks are observed in the two last angular bins, which translates in higher values of σ_1^π.

χ^2 / ndf	11.86 / 15
Nπ1	25.48 ± 1.75
$\sigma\pi$1	0.007203 ± 0.000452
Nπ2	2.234 ± 1.234
NK	2.511 ± 0.820
NP	14.32 ± 0.99
μP	0.9185 ± 0.0010

χ^2 / ndf	13.93 / 15
Nπ1	25.68 ± 1.75
$\sigma\pi$1	0.007299 ± 0.000476
Nπ2	2.397 ± 1.196
NK	2.024 ± 0.681
NP	13.66 ± 0.94
μP	0.9186 ± 0.0009
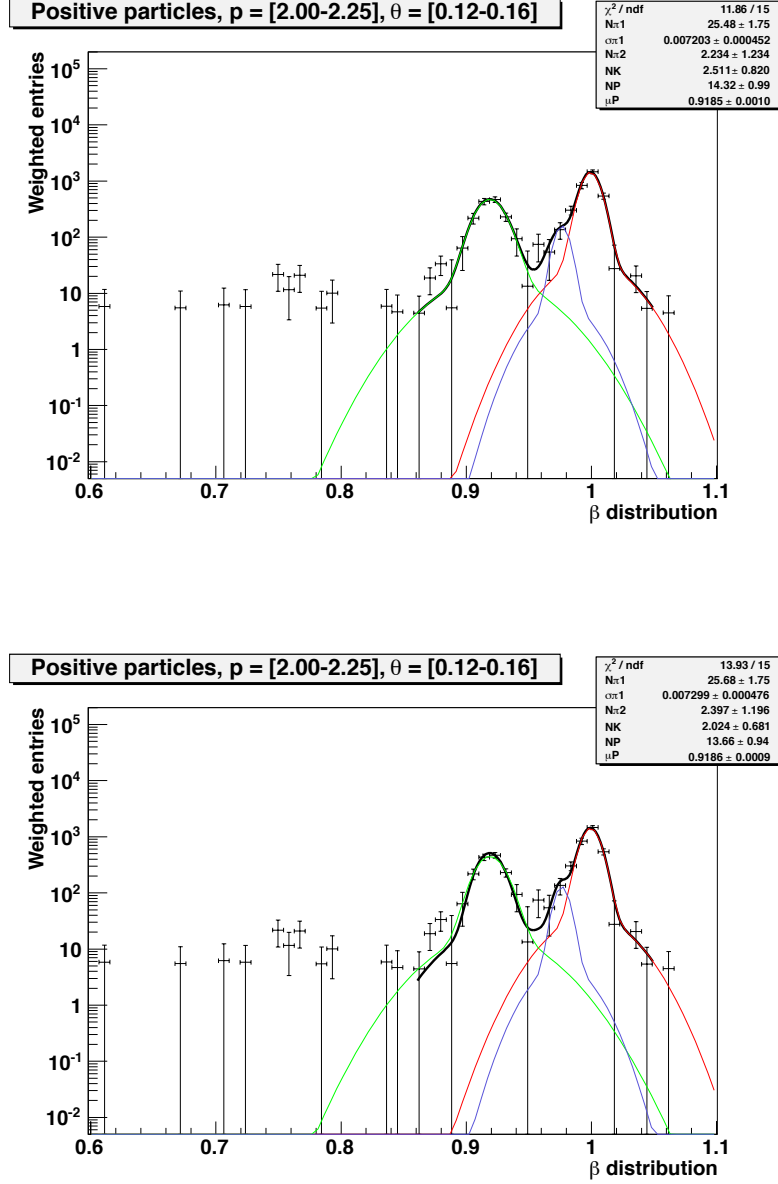
Figure 4.21: Fitted β distributions at $[2 - 2.25]$ GeV/c momentum bin and $[0.12 - 0.16]$ rad angular bin. The static σ_β value (0.0055) in Eq. 4.14 has been replaced by the fitting parameter σ_1^π and the momentum resolution function now depends on the angle θ.
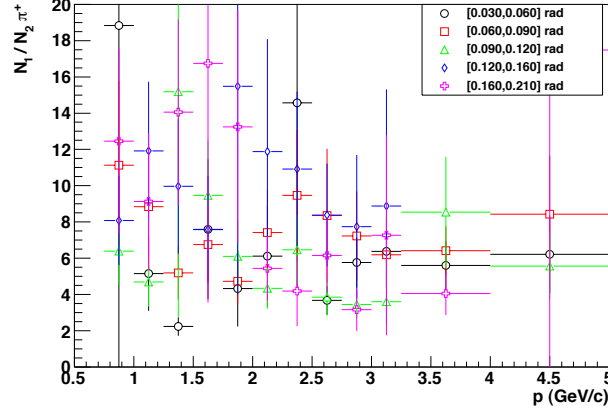
Figure 4.22: Ratios of the pion PDF's two normalization parameters vs. momentum. They are computed by fitting spectra with σ_1^π, σ_2^π and μ_π fixed. See text for details.

kaon and pion normalisation factors only (all the other parameters are fixed to those found in step one). Moreover, in this second step the ratio between the two pion normalization parameters ($A_1^{\pi'}$, $A_2^{\pi'}$), corresponding to the two gaussian functions of the pion PDF, is fixed to the one obtained in the previous step (A_1^π, A_2^π):

$$\frac{A_1^{\pi'}}{A_2^{\pi'}} = \frac{A_1^\pi}{A_2^\pi}$$

This is to ensure the stability of the algorithm when fitting the pion peak after applying the CKOV since the pion parameters are computed more precisely without CKOV cut. Unstable fits may impact greatly the kaon measurement. The remaining parameters to be fitted are therefore A_1^π, A_K and A_p, as defined in Eq. 4.17 and 4.21. Fig. 4.23 shows both the inclusive β distribution and the β distribution after applying the CKOV cut at a momentum above Cherenkov threshold. As expected, the kaon peak is more visible after applying the CKOV cut and the error on the fitted normalization, A_K, decreases considerably.

The fit quality can be probed by looking at the $\chi^2/d.o.f.$ distribution as a function of momentum (Fig. 4.24). The fitting quality is good as the $\chi^2/d.o.f.$ values are stable and close to unity at all momenta and angles.

The CKOV removes pions above the 2.75 GeV/c threshold. Therefore it should impact only the number of fitted pions and leave the kaons and protons unchanged. The
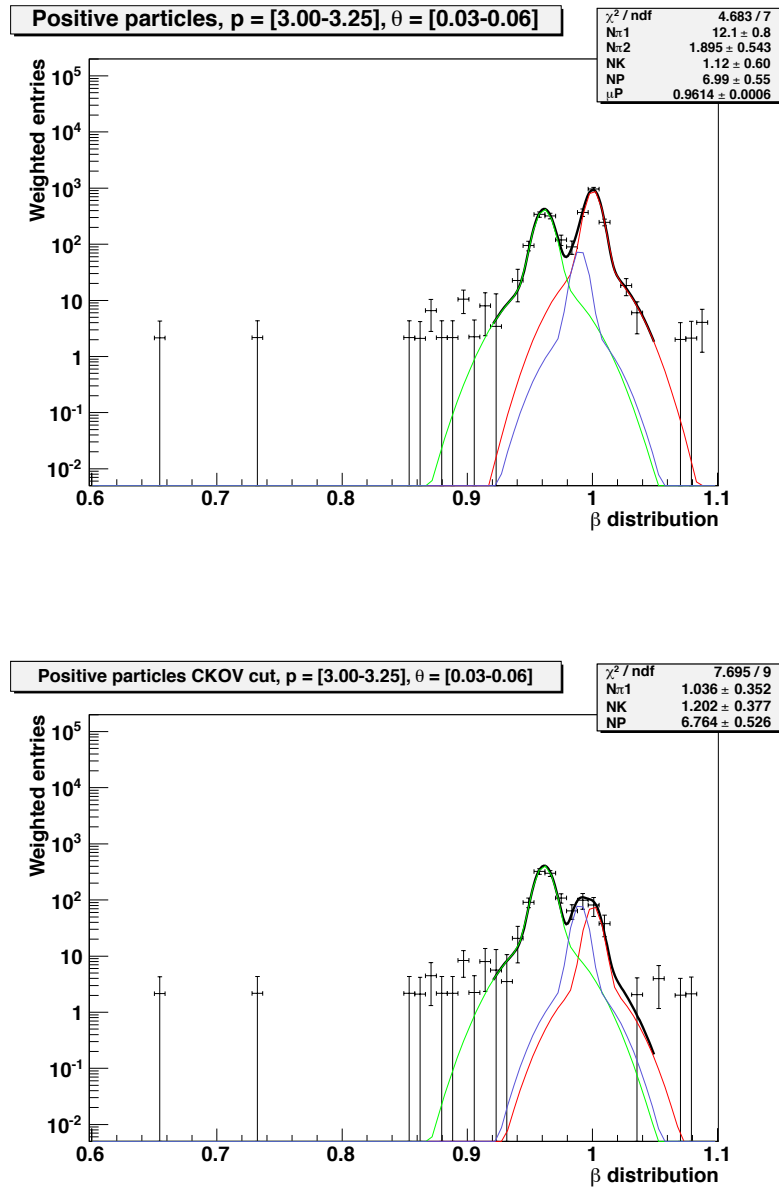
Figure 4.23: 2-step fitting procedure taking advantage of the Cherenkov detector to remove pions above the threshold (2.7 GeV/c) to better expose the kaon peak.
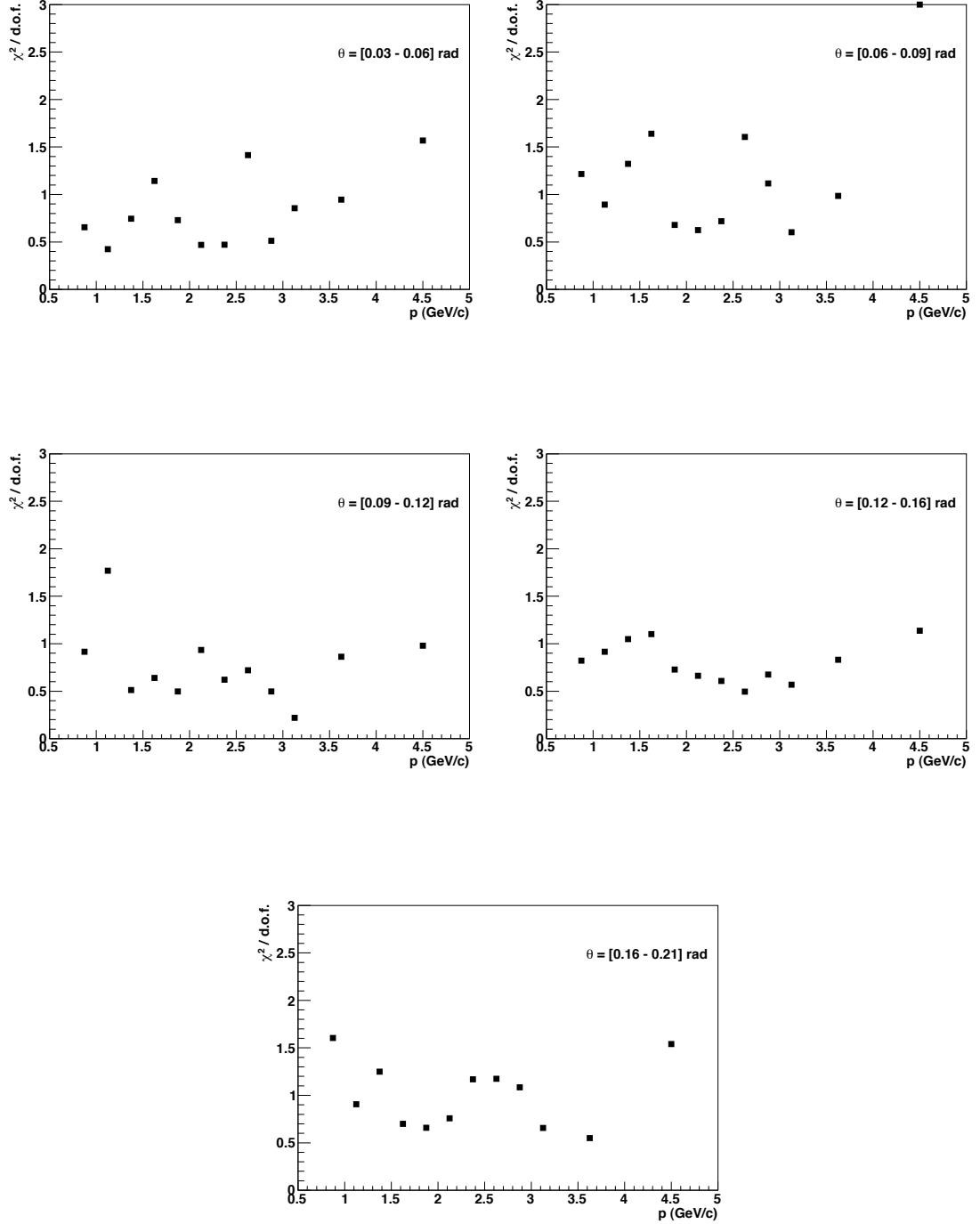
Figure 4.24: $\chi^2/d.o.f.$ as function of momentum. Each angular bin is shown separately. β distributions are filled applying the CKOV cut and are fitted following the 2-step method explained in Section 4.8.1.

ratio between the normalisation parameters with and without CKOV cut is shown in Fig. 4.25 as a function of momentum. The ratio should be ideally ~ 1 for kaons and protons at all momenta and should increase for pions at momenta above 2.75 GeV/c. Ratios for both pions and protons behave as expected. The ratio for kaons is stable up to 3.25 GeV/c and get very unstable beyond. This is explained by the number of kaons without CKOV cut being somehow arbitrary since the kaon peak is basically hidden by the much more prominent pion peak (Fig. 4.25).
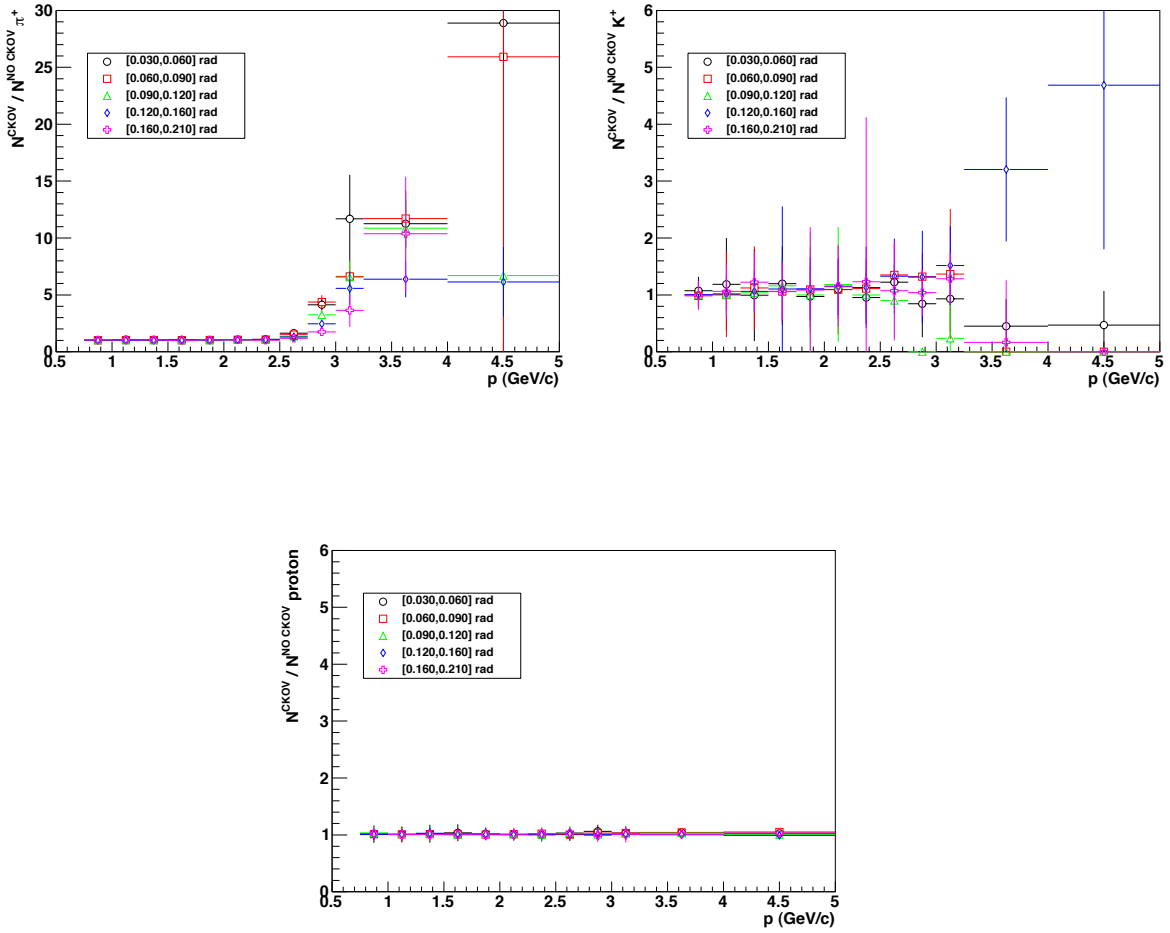
Figure 4.25: Fitted normalization ratio $N^{\mathrm{CKOV}}/N^{\mathrm{NO\ CKOV}}$ for positive particles as a function of momentum. Ratios are shown at all angular bins for pions (top-left), kaons (top-right) and protons (bottom).
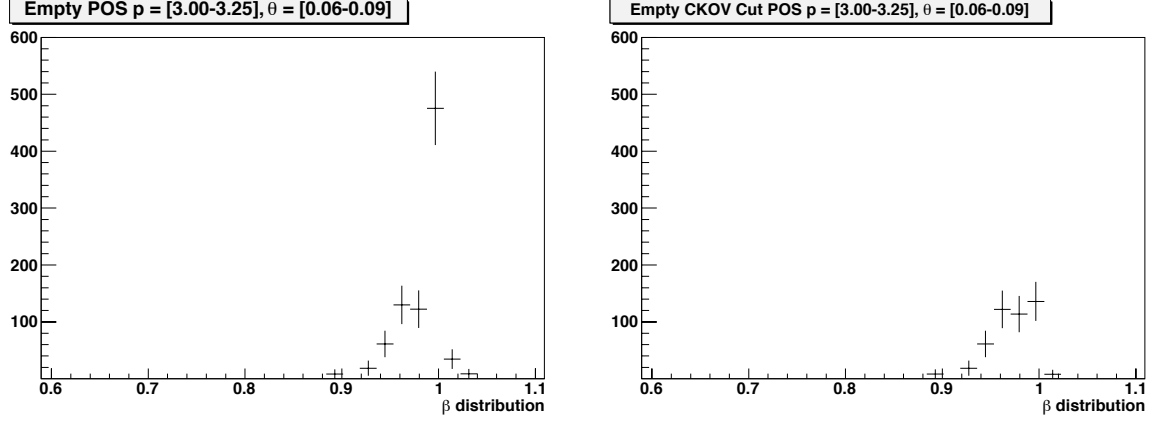
Figure 4.26: Example of β distribution filled with events from the empty target data set without the CKOV cut (left) and with the CKOV cut (right).

Empty target correction with Cherenkov cut

β spectra that have been filled using the Cherenkov cut has to be corrected by the corresponding empty target spectra. The latter, $N_{p',\theta'}^{\text{empty-CKOV}}(\beta)$, are obtained by filling empty target data samples using the same Cherenkov cut as for the aluminum target data samples. One subtracts either $N_{p',\theta'}^{\text{empty}}(\beta)$ or $N_{p',\theta'}^{\text{empty-CKOV}}(\beta)$ from the β distribution $N_{p',\theta'}(\beta)$ depending on reconstructed momentum value (smaller or greater than 2.75 GeV/c, respectively). The full explanation of the empty target subtraction method has been presented in Section 4.6.5.

Fig. 4.26 shows an example of empty target β distributions without and with the CKOV cut applied, at a given (p', θ') bin.

4.8.2 Fit summary

Pion and proton cross-section are extracted following the method presented in Section 4.8, without using the CKOV cut. Kaon cross-section are extracted following the method presented in Section 4.8.1. A summary of the fitting procedure is shown in Table 4.2. Results of these fits for all (p', θ') bins are shown in Appendix C.

Particle	Fit parameters	All Inclusive (AI)	CKOV cut applied
π^+	A_1^π	FIT	FIT
	A_2^π	FIT	Fixed to AI A_1^π/A_2^π ratio
	μ_π	Fixed to Fig. 4.19	Fixed to Fig. 4.19
	σ_1^π	Fixed to Fig. 4.18	Fixed to Fig. 4.18
	σ_2^π	Fixed to $3.6 \cdot \sigma_1^\pi$	Fixed to AI value
K^+	A_K	FIT	FIT
	A_2^K	Fixed to $0.12 \cdot A_K$	Fixed to AI value
	μ_K	Interpolated from μ_π and μ_p	Fixed to AI value
	σ_1^K	Function of σ_1^π	Fixed to AI value
	σ_2^K	Fixed to $3.6 \cdot \sigma_1^K$	Fixed to AI value
	S_K	Fixed to 0	Fixed to 0
p	A_p	FIT	FIT
	A_2^p	Fixed to $0.12 \cdot A_p$	Fixed to AI value
	μ_p	FIT	Fixed to AI value
	σ_1^p	Function of σ_1^π	Fixed to AI value
	σ_2^p	Fixed to $3.6 \cdot \sigma_1^p$	Fixed to AI value
	S_p	Fixed	Fixed

Table 4.2: Fit parameters summary. β spectra filled applying the CKOV cut are fitted with some parameters fixed to the value obtained by fitting the inclusive β spectra. See text for details.

4.9 Particle yield corrections: post-fit

Post-fit correction are applied on the measured particle yields resulting from the fits explained in the previous section. The momentum migration corrects for kinematic migrations and converts the yields into the final true variables (p, θ). The true measured yields are then corrected for absorption and particle decay.

4.9.1 Momentum migration matrix

$M_{p\theta p'\theta'}$ is the inverse of a matrix describing the migration between bins of generated and measured momentum and angle. This matrix is generated using the Monte Carlo simulation. This correction cannot be applied as a weight when filling the β spectra (pre-fit correction) as it will produce non physical spectra, i.e. filling a reconstructed quantity (β) in bins of a true quantity (p). Therefore the correction is applied on the measured secondary hadron yields obtained after fitting the β spectra (post-fit correction).

The migration matrix can be factorized into:

$$M_{pp'} \cdot M_{\theta\theta'}$$

where $M_{\theta\theta'}$ describes angular migrations and is simply a unit matrix as such migrations are small and can be neglected. $M_{pp'}$ is normalized across rows of reconstructed momentum (each track has a 100% probability of coming from some true momentum value) and the weights are used to spread a single reconstructed track over multiple true momentum bins according to the elements of $M_{pp'}$. In this way, the population in each true bin is comprised of tracks from all reconstructed momentum bins. A separate matrix is generated for each angular bin in the analysis since the momentum resolution can be a function of the track's angle:

$$N(p, \theta') = \sum_{p'} M_{pp'}(\theta') \cdot N(p', \theta') \tag{4.28}$$

This approach avoids difficulties associated with inverting a large smearing matrix as well as potential pathologies in the inverted matrix caused by a loss of information at the kinematic boundaries of the matrix itself. The drawback to this method is that one has some sensitivity to the underlying spectrum in the Monte Carlo used to generate the matrix.
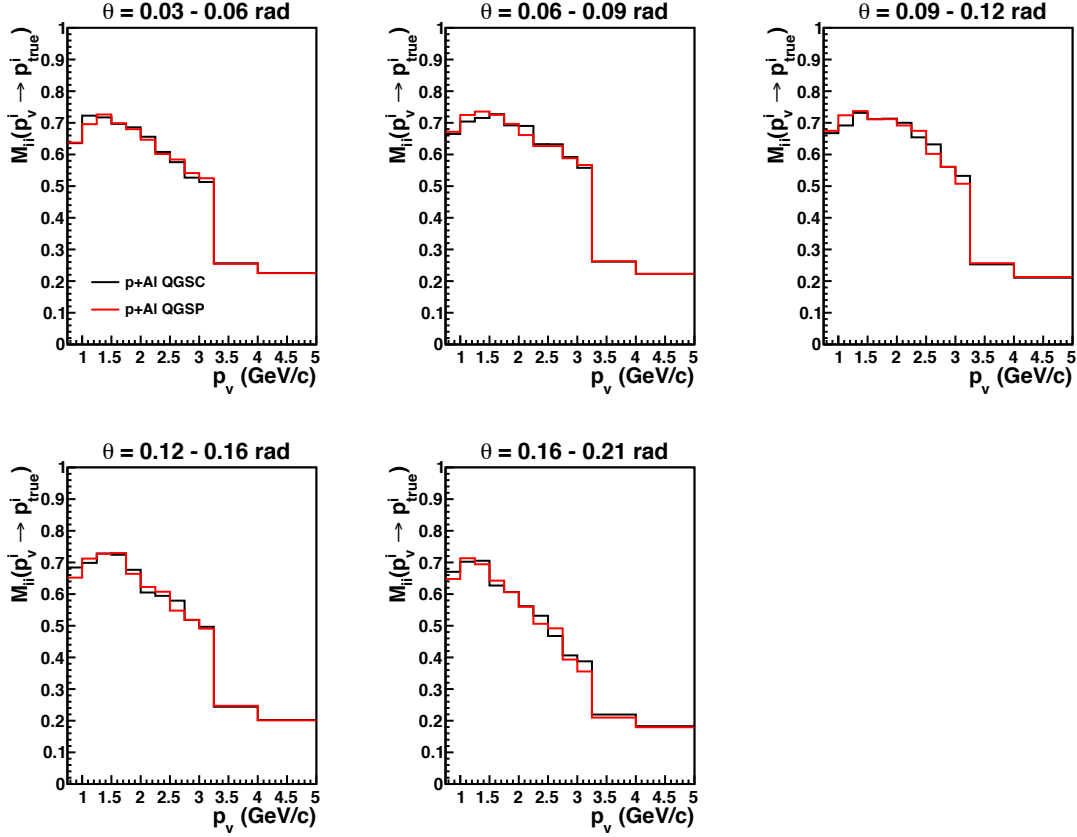
Figure 4.27: Diagonal elements of the momentum migration matrices for the 12.9 GeV/c proton + aluminum data set. Positive particles only. Two hadronic interaction models used in the simulation are shown; The QGSC model (black) and the QGSP model (red).

Three factors contribute to the values of the elements in this matrix: the resolution of the momentum reconstruction, $\sigma_p(p)$, the widths of the momentum bins as a function of momentum, and the underlying true particle spectrum.

Measurements of $\sigma_p(p)$ in [77] from the Monte Carlo and the data show good agreement at zero angle. Other analyses, described in [76], have demonstrated agreement at non-zero angles, thus justifying the use of the simulation to generate the correction.

Using different available hadronic models to build different matrices allows us to quantify this effect on the measured cross-sections. Fig. 4.27 shows the diagonal elements of migration matrices generated for five angular bins for the 12.9 GeV/c proton on aluminum data set. The momentum binning of the analysis was chosen to ensure that the diagonal

migration remained above 50% for most bins. The momentum resolution becomes worse at higher momentum, so above 3.25 GeV/c the momentum bins have been broadened. Two different hadronic models are compared in Fig. 4.27 to give a sense of the variation caused by this effect. Note that in some large angle, high momentum bins the fluctuations are largely statistical due to poor Monte Carlo statistics in these regions.

4.9.2 Secondary particle absorption

$\eta^{\mathrm{absorb}}(p, \theta_x, \theta_y, \alpha)$ is the absorption plus decay rate of secondary particles before reaching the time-of-flight wall. The absorption correction accounts for the fraction of particles which never make it to the downstream detectors, in this case the TOFW. The choice of the downstream detector used to compute this correction has to be consistent with the reconstruction efficiency algorithm. The idea here is to decouple both corrections to get a pure tracking efficiency and a total absorption.

The absorption rate is measured as a function of the true momentum of the lost particle (as this particle may not have a reconstructed momentum). Therefore, this correction is applied after unfolding of the hadron yield. Also, the absorption correction which is originally a function of both θ_x and θ_y[4] has to be expressed in terms of the total polar angle θ, since θ_x and θ_y (in fact the reconstructed ones) are only available when filling the β spectra. This implies averaging over all true angles θ_x and θ_y that contribute to a given θ. By definition, since the absorption correction accounts for not fully reconstructed particles, it cannot be measured from data and must be determined from a Monte Carlo simulation.

Fig. 4.28 and 4.29 show the absorption correction computed for the current analysis. This is an upward adjustment to the measured hadron yield and is implemented as $1/(1 - \eta^{\mathrm{absorb}}(p, \theta_x, \theta_y, \alpha))$ in Eq. 4.8.

4.10   Error estimation

A full error analysis has been performed. Statistical and systematic uncertainties are obtained using a combination of analytical and Monte Carlo techniques and are combined to estimate the accuracy of the cross-section measurements.

---

[4]it depends on the amount and type of physical material a particle passes through. i.e. the geometry of the detector
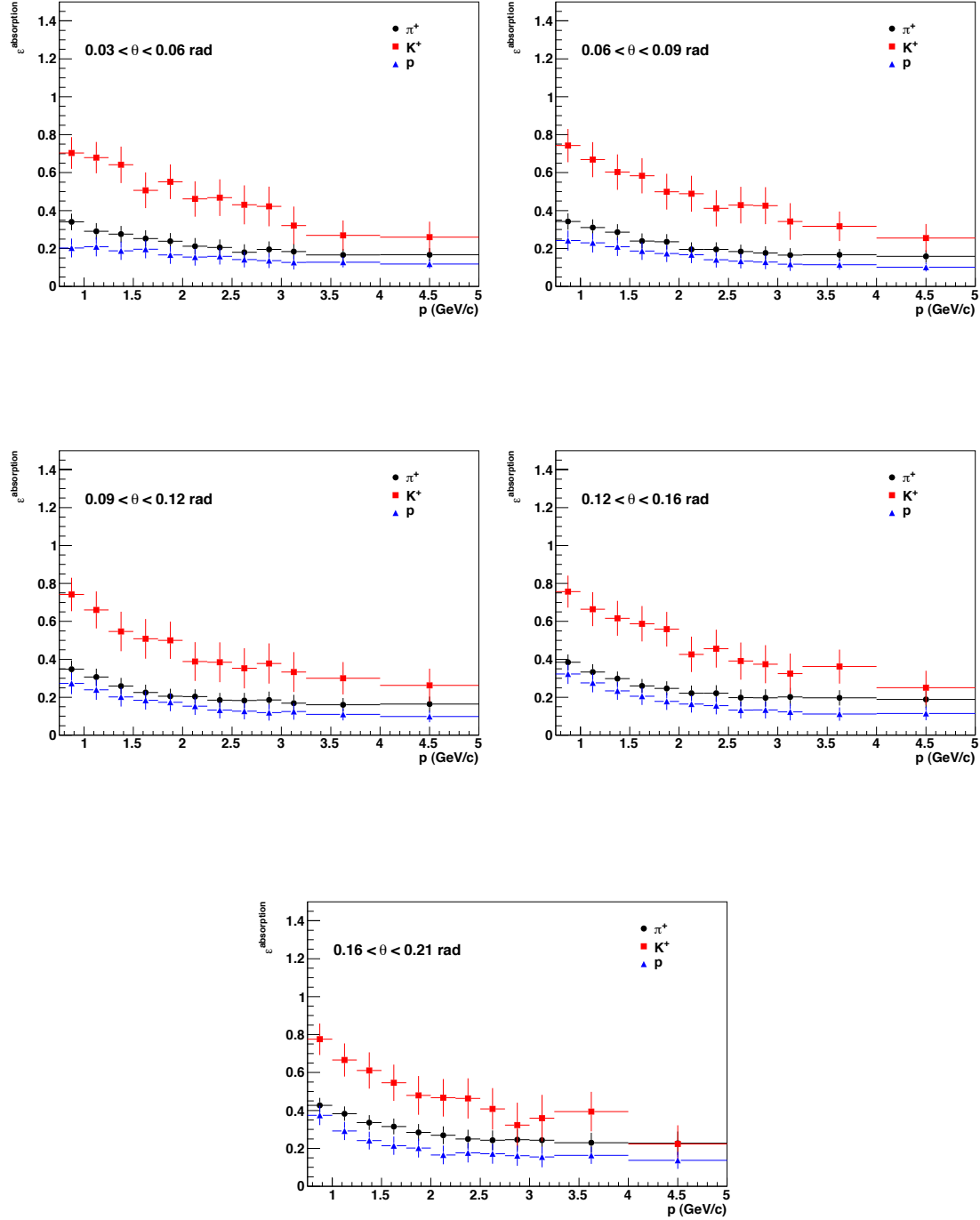
Figure 4.28: Absorption corrections for pions, kaons and protons according to Monte Carlo simulation as a function of particle momentum, shown for the five angular bins of the analysis.
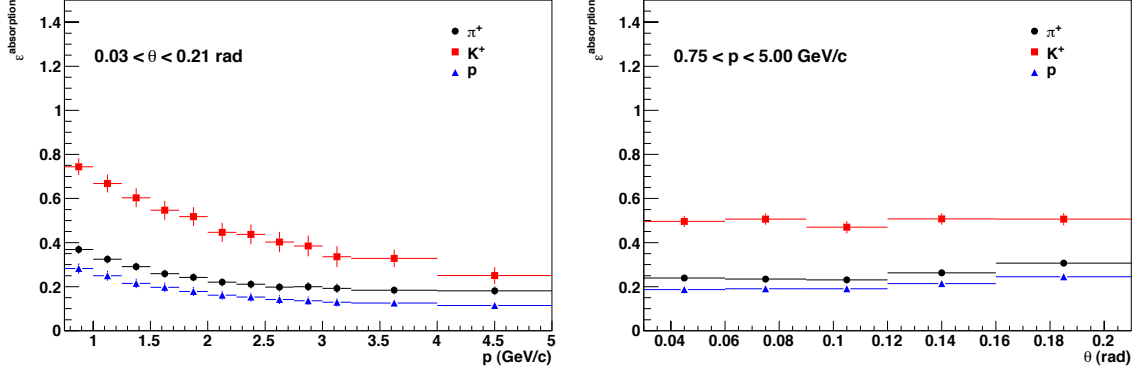
Figure 4.29: Absorption corrections for pions, kaons and protons according to Monte Carlo simulation as a function of particle momentum (left) and production angle (right).

Error bars on the β distribution are obtained by combining the statistical uncertainties of all pre-fit corrections that have been applied in a particular bin and the pure statistical error given by the number of tracks. The fit algorithm uses the standard χ^2 objective function that takes into account the error bars of the distribution and produces a covariant matrix that gives the error on the fitted parameters and their correlations. Statistical errors on the fitted particle yields are computed analytically using the covariance matrix resulting from the fit and the partial derivative of the corresponding PDFs. Finally, statistical uncertainties associated with the post-fit corrections (unfolding, absorption) are propagated to the final cross-section measurements.

The cross-section systematic uncertainties coming from the corrections described in Sections 4.6 and 4.9 are estimated by evaluating the cross-section N_{ana} times for N_{ana} variations of the correction applied. The fully correlated error matrix for each correction is then built from the N_{ana} cross-section results. The total error matrix is just the sum of the individual error matrices.

Final errors on the cross-sections results in a given (p, θ) bin are given by the square root of the corresponding diagonal elements of the total error matrix.

4.10.1   Statistical errors

Statistical errors are analytically propagated throughout the analysis in four steps:

1. Errors on the bin content of the β distributions are obtained by combining the raw yield and pre-fit correction errors.

2. The empty target correction (subtraction of the corresponding empty target β spectrum) is applied before fitting the β distribution.

3. Errors on the fitted particle yields are obtained from the fit covariance matrix and the partial derivation of the corresponding PDF's used during the fitting process.

4. Errors on the true yields are obtained from the combination of the fit and post-fit corrections errors.

First, as explained in Section 4.2.2, pre-fit corrections are applied as a weight on each reconstructed track while filling the β distributions. Hence, at a given (p', θ'), the content of a bin N'_β is given by the sum of the correction weights:

$$N'_\beta = \sum_{k=1}^{N_\beta} W_k(\beta) \tag{4.29}$$

where N_β is the number of reconstructed tracks that passed the analysis cuts for this particular β bin and $W_k(\beta) = W_k^{\mathrm{recEff}}(\beta) \cdot W_k^{\mathrm{acc}}(\beta) \cdot W_k^{\mathrm{tert}}(\beta)$ is the total weight for the kth track contributing to this β bin.

The acceptance correction is a function of θ' and is the same for all (p', β) within a θ' bin. The tertiary correction is a function of (p', θ', β) and gives the same value within a bin β. The reconstruction efficiency correction is a more complex correction that depends on the reconstructed angle θ'_x and θ'_y. However the correction is flat within the fiducial volume selected for this analysis (see Fig. 3.22). Since we fill the β spectra only with events passing the fiducial volume cuts, the reconstruction efficiency correction is the same for all β within a (p', θ') bin. Therefore, all three corrections give the same respective weight in a given (p', θ', β) bin. In other words, all W_k are equal within a given (p', θ', β) bin and therefore Eq. 4.29 can be rewritten as:

$$N'_\beta = N_\beta \cdot W(\beta) \tag{4.30}$$

where $W(\beta)$ is, as before, the combination of all three correction weights. The error on N'_β is simply:

$$
\begin{aligned}
\sigma^2_{N'_\beta} &= (W(\beta) \cdot \sigma_{N_\beta})^2 + (N_\beta \cdot \sigma_{W(\beta)})^2 \\
&= N_\beta \cdot W(\beta)^2 + N_\beta^2 \cdot \sigma^2_{W(\beta)} \\
&= \sum_{k=1}^{N_\beta} W_k(\beta)^2 + N_\beta \cdot \sum_{k=1}^{N_\beta} \sigma^2_{W_k(\beta)}
\end{aligned}
\tag{4.31}
$$

where N_β is the number of entries in the β bin. We assumed the error on the number of entries in a β bin to be gaussian distributed and is given by $\sqrt{N_\beta}$. The uncertainty on the weight $W_k(\beta)$, $\sigma^2_{W_k(\beta)}$, is given by:

$$
\sigma^2_{W_k(\beta)} = \sigma^2_{W_k^{\text{recEff}}(\beta)} + \sigma^2_{W_k^{\text{tert}}(\beta)}
\tag{4.32}
$$

since the acceptance correction is purely analytical (see Eq. 3.4) and has no error.

Second, the empty target correction is applied before fitting, by subtracting directly the empty target β distribution at a given (p', θ') bin from the corresponding all inclusive target β distribution (Eq. 4.7). The uncertainty on the empty target correction is propagated according to:

$$
\sigma^2_{(N'_\beta - N'_\beta \text{ empty})} = \sigma^2_{N'_\beta} + \sigma^2_{N'_\beta \text{ empty}}
\tag{4.33}
$$

Third, the error on the fitted particle yields is obtained directly from the fit covariance matrix and the partial derivation of the different PDF's used in the fit algorithm. The fit objective function is based on a χ^2 algorithm and takes into account the error bars of the histogram being fitted. In our case, it takes into account the combined statistical errors coming from the pre-fit corrections. The fit algorithm produces a covariant matrix that gives the total statistical error on all the fit parameters and the correlations between them.

The fitted particle yields N_α are obtained by integrating the fitted PDFs as described by Eq. 4.22 and 4.23. We build an error matrix which gives the statistical uncertainties on the fitted number of pions, kaons and proton, before applying the absorption and migration corrections:

$$
cov(N_\alpha,\, N_\gamma) = \left(\frac{\partial N_\alpha}{\partial P_i} \right)^T \cdot cov(P_i,\, P_j) \cdot \frac{\partial N_\gamma}{\partial P_j}
\tag{4.34}
$$

where P_i are the fitting parameters, and $cov(P_i, P_j)$ is the covariance matrix resulting from the fits.

The total statistical uncertainties on the fitted number of pions, kaons and protons is given by the diagonal elements $\sqrt{cov(N_\pi,\ N_\pi)}$, $\sqrt{cov(N_K,\ N_K)}$ and $\sqrt{cov(N_p,\ N_p)}$, respectively.

Fourth, the statistical uncertainties on the post-fit corrections (absorption, momentum migration) are propagated to the true particle yields. During the unfolding process, *errors* on the measured yields are distributed over bins of true momentum, p, the same way as with the *values* of the measured yields (Eq. 4.28):

$$\sigma^2_{N_\alpha(p,\theta')} = \sum_{p'} (M_{pp'}(\theta') \cdot \sigma_{N_\alpha(p',\theta')})^2 \tag{4.35}$$

where $\sigma_{N_\alpha(p',\theta')}$ is the statistical uncertainty on the measured yield of the particle-type α, given in step 3. As for the statistical uncertainty of the momentum migration correction itself, it is propagated to the final cross-sections following the method presented in Section 4.10.2.

The absorption correction is applied to the the measured particle yields after the unfolding process. Bin contents of the true measured yield are divided by the absorption correction, $\frac{N_\alpha}{\eta^{\text{absorb}}}$. The uncertainty on the absorption correction is propagated to the measured yield according to:

$$\sigma^2_{\frac{N_\alpha}{\eta^{\text{absorb}}}} = \left(\frac{1}{\eta^{\text{absorb}}} \cdot \sigma_{N_\alpha} \right)^2 + \left(\frac{N_\alpha}{(\eta^{\text{absorb}})^2} \cdot \sigma_{\eta^{\text{absorb}}} \right)^2 \tag{4.36}$$

where σ_{N_α} and $\sigma_{\eta^{\text{absorb}}}$ are the statistical uncertainties on the measured yield (after unfolding) and the absorption correction, respectively.

Measured positive particle yields, with statistical error only, are shown in Appendix B. The fitted yield distributions are then converted into proper cross-section units and the statistical and systematic uncertainties are combined to give the final errors on the yields, as explained in Section 4.10.2. Table 4.3 lists all the corrections applied in the current analysis and how their corresponding statistical uncertainties are computed.

4.10.2   Systematic errors

A systematic error analysis has been performed to estimate the accuracy of the cross-section results following the method from [76]. The contribution to the uncertainty is

Applied	Name	Method
pre-fit	Tertiary subtraction	$N^{\text{tert.}}/N^{\text{total}}$ division with binomial errors
	Reconstruction efficiency	$N^{\text{track}}/N^{\text{parts}}$ division with binomial errors
	Acceptance correction	Analytical function, no error assumed
	Empty target correction	Error propagation, standard subtraction
post-fit	Fitted particle yields	PDFs partial derivatives and covariance matrix
	Momentum migration	P^{rec} error propagation across P^{true} bins
	Absorption correction	Error propagation, standard multiplication

Table 4.3: Statistical error summary. See text for details.

evaluated for each of the corrections applied throughout the analysis. The full correlation between (p, θ) bins is included and results in a full error matrix with N_{bins}^2 elements, where N_{bins} is the number of (p, θ) bins.

For each correction applied on the raw yields, an error is determined on the correction itself. To estimate the impact of a particular correction on the cross-section, $N_{\text{ana}} = 100$ analyses are performed where only this correction is randomly fluctuated according to a gaussian distribution for each analysis with a sigma equal to the error on the correction. This procedure is repeated for each source of systematic error and a fully correlated error matrix is built from the N_{ana} cross-section results:

$$E_{ij}^m = \frac{1}{N_{\text{ana}}} \sum_{n=1}^{N_{\text{ana}}} \left[\frac{\mathrm{d}^2\sigma_{\text{CV}}^\alpha}{\mathrm{d}p\,\mathrm{d}\Omega} - \frac{\mathrm{d}^2\sigma_{m,n}^\alpha}{\mathrm{d}p\,\mathrm{d}\Omega} \right]_i \times \left[\frac{\mathrm{d}^2\sigma_{\text{CV}}^\alpha}{\mathrm{d}p\,\mathrm{d}\Omega} - \frac{\mathrm{d}^2\sigma_{m,n}^\alpha}{\mathrm{d}p\,\mathrm{d}\Omega} \right]_j \tag{4.37}$$

where i and j label bins of (p, θ), E_{ij}^m is the i, j^{th} element of one of the error matrices (labelled m), $\mathrm{d}^2\sigma_{\text{CV}}^\alpha/\mathrm{d}p\,\mathrm{d}\Omega$ is the central value for the double-differential cross-section measurement of particle α and $\mathrm{d}^2\sigma_{m,n}^\alpha/\mathrm{d}p\,\mathrm{d}\Omega$ is the cross-section result from the nth variation of the mth systematic error source.

The different sources of uncertainty are assumed to be independent so that the

total error matrix is the sum of the m matrices:

$$E_{ij} = \sum_m E_{ij}^m \tag{4.38}$$

11 sources of systematic uncertainty has been defined and are contributing to the total error on the measured cross-sections :

1. Tertiary subtraction uncertainty. The tertiary particle reconstruction rate depends on the beam momentum, shape of secondary spectrum and the hadronic production models of hadrons in detector material at a large range of momenta. Most of the material where tertiary particles are produced in the detector is carbon. For that reason the simulation of inelastic interactions of low-energy protons and pions is important when generating this correction. Comparing low momentum HARP p+C, π^++C, π^-+C data to the hadronic models used in the Monte Carlo simulation has verified these models to $\sim 50\%$. This uncertainty is assumed on the calculated tertiary subtraction.

2. Momentum scale uncertainty. The uncertainty on the absolute scale of the momentum reconstruction has been found to be 2% at zero angle using the empty target data samples from 1.5-12.9 GeV/c. Other methods have also been used to evaluate this uncertainty for non-zero angles as described in [76] and the conclusions are the same. To evaluate the impact on the cross-section measurements, N_{ana} measurements were made where the momentum of each track has been scaled by a factor randomly distributed as a Gaussian function centered at 1 with width 0.02.

3. Shared double gaussian normalization uncertainty. Both proton and kaon PDFs are described by the sum of two gaussian distributions with shared mean (Eq. 4.20). The fitted proton and kaon normalization factors are shared in between the two gaussian distributions (Eq. 4.21). R_A^α has been fixed to 0.88 according to the method presented in section 4.8. A conservative 100% systematic uncertainty on this parameter has been chosen.

4. Shared double gaussian width uncertainty. Factor 3.6 between two sigmas which is computed following Eq. 4.26. 0.02 is measured with a $\sim 50\%$ uncertainty and we assume this conservative value as the systematic error on that parameter.

5. Slope Parameter uncertainty. This parameter is computed from the value of the protons fitted yields following the iterative method described in Section 4.7. The error on the yield in a given (p, θ) is typically 10% and we will assume this uncertainty on the parameter.

6. σ^π systematic uncertainty. Results obtained by fitting the σ^π distribution (Fig. 4.17) yields errors of about 10%. We assume this conservative error to account for the approximations done in the fits to σ^π.

7. μ_π uncertainty. Results obtained by fitting the μ_π distribution (Fig. 4.19) yields errors of about 0.05%. This error is momentum dependant and should increase at low momentum. This effect as not been taken into account when running the N_{ana} experiments but a global systematic uncertainty of 0.1% has been applied instead.

8. Empty target subtraction uncertainty. Data samples filled with the same beam momentum but without nuclear target are used to subtract non-interacting background from the target data. Since the nuclear target for the data set analyzed is 5% of a nuclear interaction length, a 5% normalization uncertainty has been estimated for the empty target subtraction.

9. Momentum resolution uncertainty. An error of 10% is assumed on the parameter which corresponds to the uncertainty on the momentum resolution as determined in [76].

10. Absorption correction uncertainty. The absorption correction is estimated for all particles, following the method explained in Section 4.9.2. The Monte Carlo is used to estimate the rate and it depends mostly on the total interaction cross-sections of pions and protons in carbon. The data used to set these cross-sections in the simulation have uncertainties of order 10% and the same systematic uncertainty is assumed for this parameter.

11. Momentum migration uncertainty. The momentum migration correction refers to the migration of reconstructed tracks from their true momentum value to a different momentum value due to the finite resolution of the detector and the reconstruction algorithm used. The correction is described in Section 4.9. The dominant source of systematic uncertainty in the matrix elements is the choice of hadronic generator used

to determine the secondary spectrum. Therefore, to asses the error on the cross-section a matrix is generated for a hadronic interaction model other than the default and compared to the central value cross-section results.

Two additional corrections are added on top of the 11 sources of systematic uncertainties described above:

- Momentum migration statistical uncertainty. The statistical uncertainty in the momentum migration matrix can be large since reconstructed tracks are divided into $N_{\mathrm{bins}}^{\theta} \times N_{\mathrm{bins}}^{p} \times N_{\mathrm{bins}}^{p'}$ bins. To estimate the effects, each row of the matrix is fluctuated according to a multinomial distribution before being normalized and the cross-section is calculated for N_{ana} such variations of the matrix.

- Overall normalization systematic uncertainty. A main source of fully correlated normalization uncertainty comes from the proton beam targeting efficiency. A small fraction ($\sim 1\%$) of the protons which pass all event selection cuts in Section 4.3 are deflected and do no collide with the nuclear target. In addition, there are fully correlated contributions to the reconstruction efficiency calculation estimated at another $\sim 1\%$. Uncertainty on the measured thickness of the nuclear target ($\sim 0.1\%$) and the count of the number of protons on target ($\sim 0.2\%$) are negligible. In total we estimate a fully correlated normalization uncertainty on the measured cross-section of 2%.

Table 4.4 summarizes the different sources of systematic errors and the uncertainty considered for each of them.

We also studied the impact of the choice of the β binning on the final results, which can introduce a binning-related systematic error. In the current analysis we divided the [0, 1.3] β interval into 150 bins.

The problem is the following: unweighted beta distribution histograms (see Fig. 4.30) show that some beta bins contain less than 10 entries at low momentum (mainly within the first momentum bin, $p' = 0.75$ GeV/c). Therefore, one can no longer use the error propagation method explained in Section 4.10.1. In that method, pre-fit correction statistical uncertainties are propagated assuming that the error on the number of entries in each bin of β is gaussian distributed and therefore the square root of the number of entries is used in the error propagation formula (Eq. 4.31). This has for consequence to underestimate the error bars in these specific low statistic bins and could impact the fitting method as error

Correction type	Name	Error considered
pre-fit	Tertiary subtraction	50 %
	Momentum scale	2 %
post-fit	Gaussian norm. ratio R_N	100 %
	Gaussian width ratio R_σ	50 %
	Slope parameter	10 %
	σ_1^π	10 %
	μ_π	0.1 %
	Empty target subtraction	5 %
	Momentum resolution, σ_p	10 %
	Absorption correction	10 %
	Momentum smearing	MC hadronic generator
	Momentum smearing statistical	Multinomial fluctuation
Overall	Overall normalization	2 %

Table 4.4: Summary of systematic error sources and uncertainties considered for each of them. See text for details.

θ (rad)	N_K^{75}	N_K^{150}	Ratio
$0.03 - 0.06$	306 ± 51	332 ± 52	0.92 ± 0.21
$0.06 - 0.09$	203 ± 39	228 ± 40	0.92 ± 0.23
$0.09 - 0.12$	303 ± 49	325 ± 49	0.93 ± 0.20
$0.12 - 0.16$	301 ± 54	317 ± 53	0.95 ± 0.23
$0.16 - 0.21$	486 ± 84	492 ± 80	0.97 ± 0.24

Table 4.5: Fitted positive kaon yield values. The results, their ratios and their corresponding uncertainties are shown for two different β binning setup: 75 and 150 bins in the $[0, 1.3]$ interval.

bars are taken into account by the fitting algorithm and will affect the fit error covariance matrix.

Increasing the size of the beta bins guarantees a minimum number of entries in each bin. Thus, we doubled the size of the bins (75 β bins in total) and measured the fitted positive kaon yields (this is the most sensitive particle species because of its low statistics). Table 4.5 lists the measured kaon yields (for both the 75 and 150 β binning), the resulting N_K^{75}/N_K^{150} ratio and their respective errors. Fig. 4.31 shows the yield ratios vs. the reconstructed angle θ' at $p' = 0.75$ GeV/c. It was fitted to a straight line. Since the fit result is compatible with 1, we conclude that the binning in β does not introduce any significant bias to the fitted yield values. Thus the initial 150 beta binning has been kept throughout the analysis for better consistency.

The measured π^+, proton and K^+ production cross-sections for the 12.9 GeV/c proton + aluminum data are shown in Figs. 4.32, 4.34 and 4.33. All cross-sections and diagonal errors are tabulated in Appendix A.

Finally, we define two dimensionless quantities, δ_{diff}^m and δ_{int}^m:

$$\delta_{\text{diff}}^m \doteq \frac{1}{N_{\text{bins}}} \sum_{i=1}^{N_{\text{bins}}} \frac{\sqrt{E_{ii}^m}}{\left[\mathrm{d}^2 \sigma_{\text{CV}}^\alpha / (\mathrm{d}p \, \mathrm{d}\Omega) \right]_i} \tag{4.39}$$

where N_{bins} is the number of (p, θ) bins. E_{ij} is the total covariance matrix or one of the individual covariance matrices evaluated. δ_{diff}^m can be interpreted as the point-to-point error
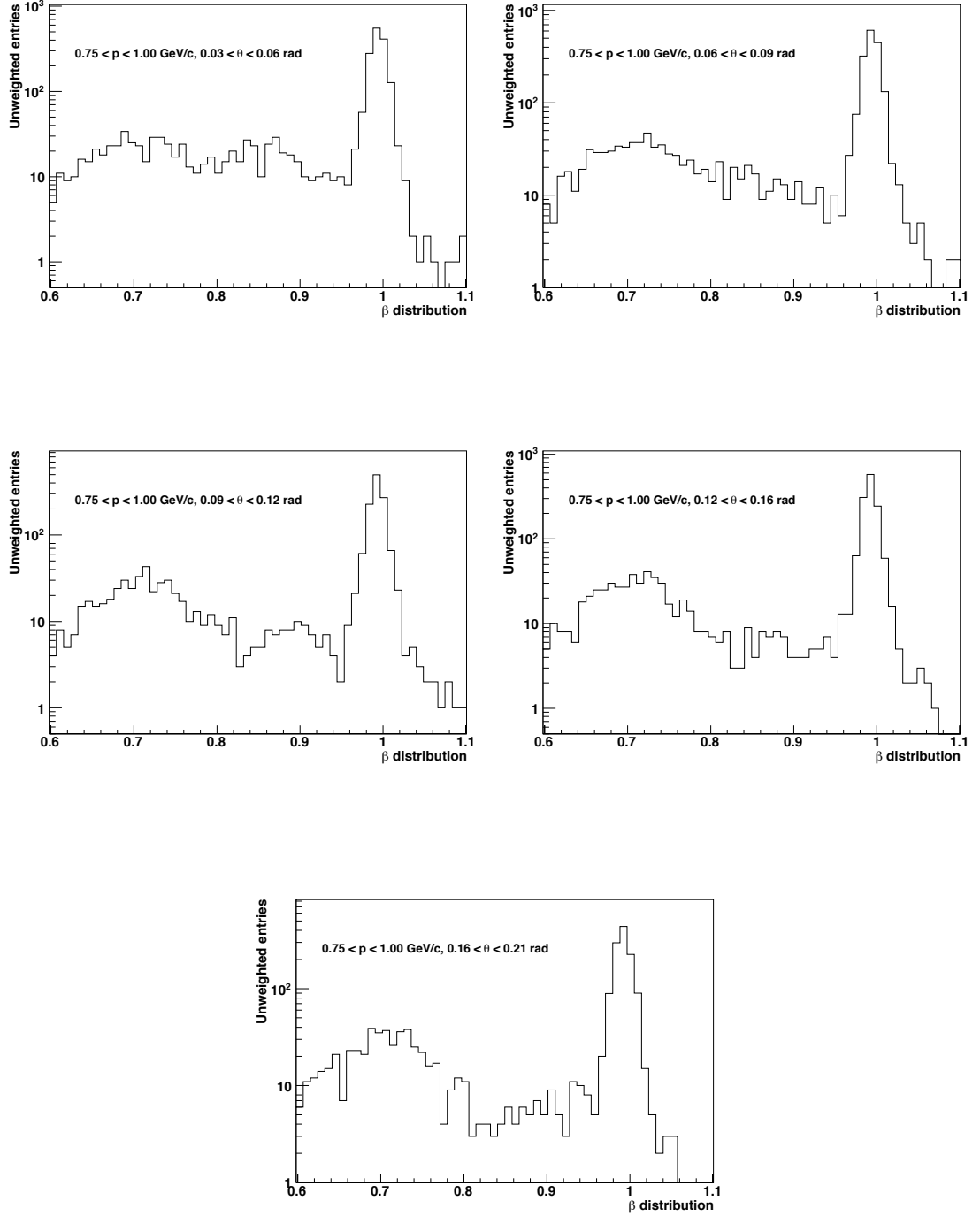
Figure 4.30: Unweighted β distributions of positive particles passing the analysis selection cuts. Shown at $p' = 0.75$ GeV/c for all angular bins.
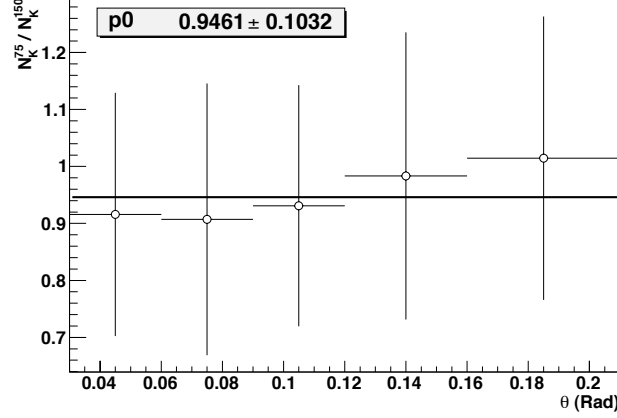
Figure 4.31: Ratio of the fitted positive kaon yields for two different β binning setup vs. reconstructed angle at momentum $p' = 0.75$ GeV/c. The distribution is fitted to a straight line. The result is shown and is compatible to 1.

or weighted error (diagonal errors only), where small bin content contribute less.

$$\delta_{\text{int}}^m \doteq \frac{\sqrt{\sum_{ij}(\mathrm{d}p\,\mathrm{d}\Omega)_i\, E_{ij}^m\,(\mathrm{d}p\,\mathrm{d}\Omega)_j}}{\sum_i(\mathrm{d}^2\sigma_{\text{CV}}^\alpha)_i} \tag{4.40}$$

where $(\mathrm{d}^2\sigma_{\text{CV}}^\alpha)_i$ is the double-differential cross-section in bin i multiplied by the corresponding phase-space factor, $(\mathrm{d}p\,\mathrm{d}\Omega)_i$. δ_{int}^m can be interpreted as the uncertainty on the total integrated cross-section in the kinematic region considered. Both quantities are evaluated for each of the 11 error sources as well as the total. The results are tabulated in Table 4.6. The average total error on the differential cross-section is $\sim$12% for pions, 44% for kaons and $\sim$13% for protons.

The higher error value for kaons can be explained as following: first, kaons have larger statistical errors that comes from their smaller production rates. Second, the momentum scale has a 2% systematic uncertainty as explained above. Applying the 2% systematic uncertainty shifts the reconstructed momenta of all particles. The induced migration in momentum implies a migration in β which is important for protons and almost negligible for pions. In particular, protons migrate to higher or lower momentum bins which results in wider proton distributions in these bins that interfere with the kaon peak and, hence, impact

the kaon measurements. Third, the absorption correction for kaons is on average three times bigger than for pions and protons as seen in Figure 4.28. In this case, it is a large correction applied on a small signal. Finally, the choice of systematic uncertainties on the different fit parameters is very conservative and therefore impacts greatly the kaon total error. At the end, systematic and statistical errors on the kaon measurements are comparable.

Also, the accuracy of the absorption and tertiary corrections could be improved by using the full hadron cross-section data available from HARP to improve the hadronic simulation packages used to generate the corrections. However, this is a sizeable project that goes beyond the scope of this thesis.

4.11 Comparison with previously published HARP production data

The pion and proton cross-sections measured using the method presented in this thesis can be compared with the analyses of the 12.9 GeV/c p-Al data published in [61] and presented in [60]. The most important improvements introduced in both [60] and our analysis compared with the one presented in [61] are:

- An improvement in the χ^2 minimization performed as part of the tracking algorithm has eliminated the anomalous dip in tracking efficiency above 4 GeV/c shown in [61]. The tracking efficiency is now $\geq 97\%$ everywhere above 2 GeV/c. (Section 3.9.1).

- Studies of HARP data other than that described here have enabled a validation of the Monte Carlo simulation of low-energy hadronic interactions in carbon. Specifically, low energy p+C and π+C cross-sections have been compared to distributions from the Binary cascade [59] and Bertini intra-nuclear cascade [58] hadronic interaction models used to simulate the secondary interactions of p, n and $\pi^{\pm}$. The material in the HARP forward spectrometer where tertiary tracks might be produced is predominantly carbon. Consequently, the systematic error on the subtraction of tertiary tracks has been reduced from 100% in [61] to 50%. (Section 4.9.2).

- Analysis techniques were developed for comparing the momentum reconstructions in data and Monte Carlo allowing data to be used to fine-tune the drift chamber simulation parameters. These efforts have reduced the momentum scale uncertainty from

Data Set	12.9 GeV/c proton + aluminum					
secondary particle	π^+		K^+		proton	
momentum range (GeV/c)	0.75 - 5.0 GeV/c		0.75 - 5.0 GeV/c		0.75 - 5.0 GeV/c	
angular range (rad)	0.03 - 0.21 rad		0.03 - 0.21 rad		0.03 - 0.21 rad	
Error Category	$\delta^{\pi^+}_{\mathrm{diff}}(\%)$	$\delta^{\pi^+}_{\mathrm{int}}(\%)$	$\delta^{K^+}_{\mathrm{diff}}(\%)$	$\delta^{K^+}_{\mathrm{int}}(\%)$	$\delta^{p}_{\mathrm{diff}}(\%)$	$\delta^{p}_{\mathrm{int}}(\%)$
Statistical Errors	7.4	1.0	33.6	5.4	7.3	1.0
Track Yield corrections:						
Empty target subtraction	1.2	1.1	3.5	2.3	1.5	0.8
Pion, kaon, proton absorption	3.1	3.4	12.3	16.4	2.1	2.0
Tertiary subtraction	6.0	6.2	6.1	4.5	6.5	5.5
Sub-total	6.9	7.2	14.2	17.2	7	5.9
Momentum reconstruction:						
Momentum resolution, σ_p	0.2	0.1	2.2	0.5	1.3	0.9
Momentum scale	2.2	0.1	11.0	2.1	3.9	2.2
Momentum smearing syst.	1.9	0.1	1.9	0.1	1.8	0.1
Momentum smearing stat.	1.5	< 0.1	1.7	< 0.1	1.5	< 0.1
Sub-total	3.3	0.1	11.5	2.2	4.7	2.4
Fit paramaters:						
Gaussian norm. ratio R_N	1.7	1.5	8.5	7.5	6.5	6.8
Gaussian width ratio R_σ	2.0	1.4	11.4	4.3	2.5	1.9
μ_π	5.0	4.1	13.8	9.8	0.6	0.6
σ_1^π	0.5	0.4	8.8	8.8	1.3	1.7
Slope	0.1	< 0.1	0.3	0.2	0.1	0.1
Sub-total	5.7	4.6	21.7	15.8	7.1	7.2
Overall normalization	2.0	2.0	2.0	2.0	2.0	2.0
Total Systematic	9.7	8.7	28.4	23.5	11.2	9.8
Total Stat + Syst	12.2	8.8	44.0	24.1	13.4	9.9

Table 4.6: Summary of uncertainties affecting the measured π^+, K^+ and proton cross-sections from 12.9 GeV/c proton+aluminum interactions. The average error on the differential cross-section, δ_{diff}, and the error on the total integrated cross-section, δ_{int}, are listed for the error sources described in Section 4.10.2 as well as the total uncertainty.
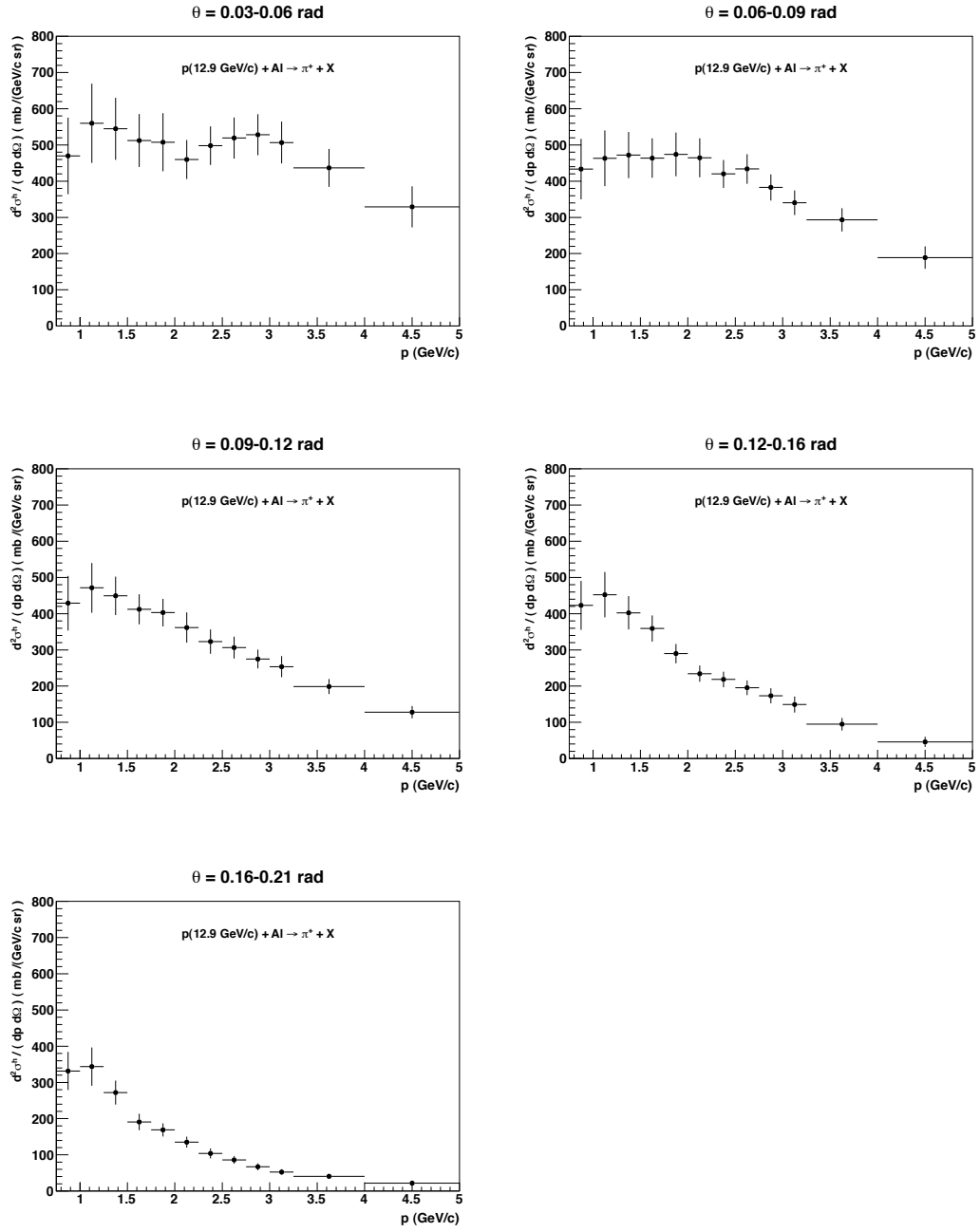
Figure 4.32: Double-differential production cross-sections of π^+ from the interaction of 12.9 GeV/c protons with aluminum. Each panel shows the cross-section as a function of momentum from 0.75 GeV/c to 5.0 GeV/c in a particular angular bin indicated above each plot. The error bars shown are the square-root of the diagonal elements of the total error matrix.
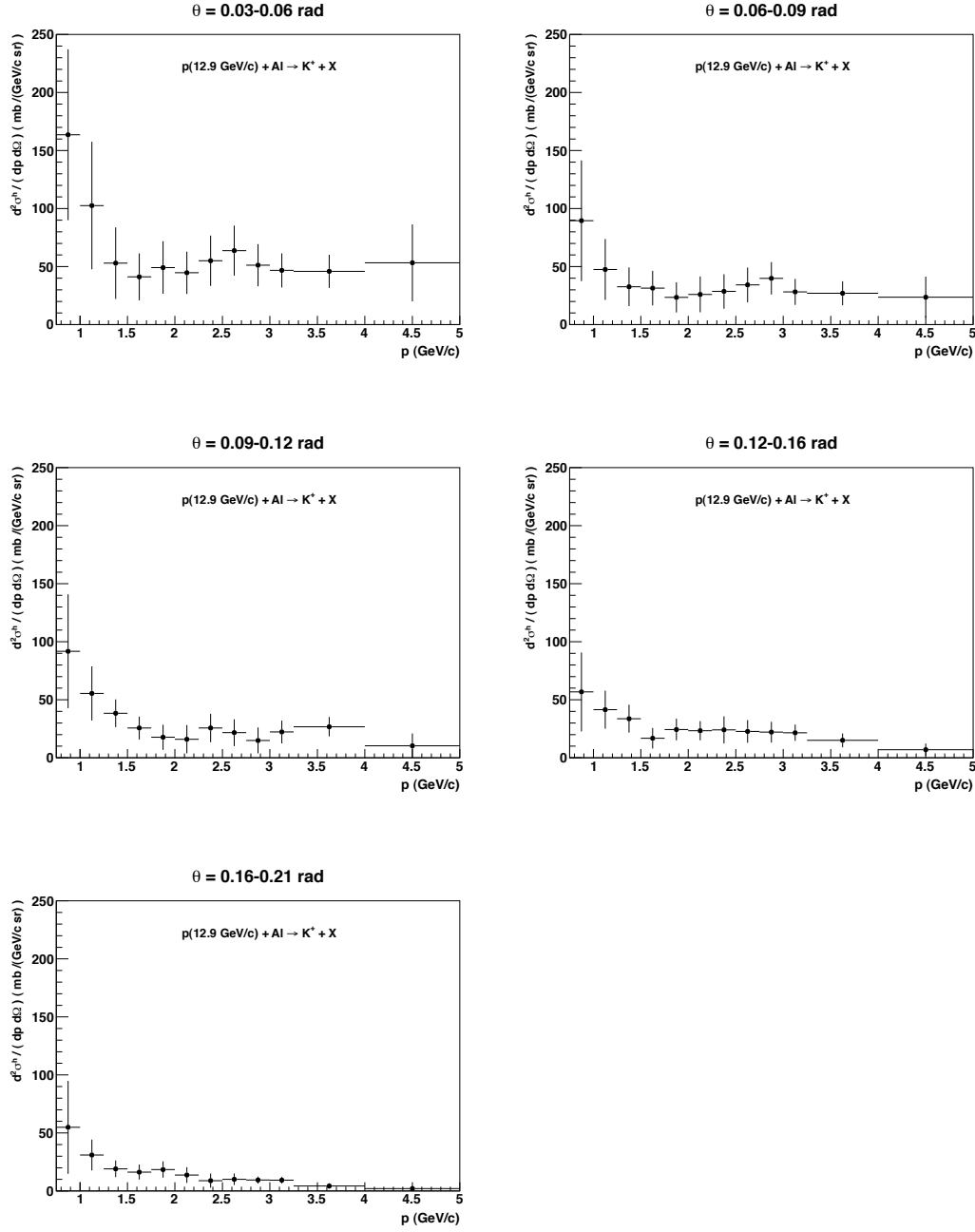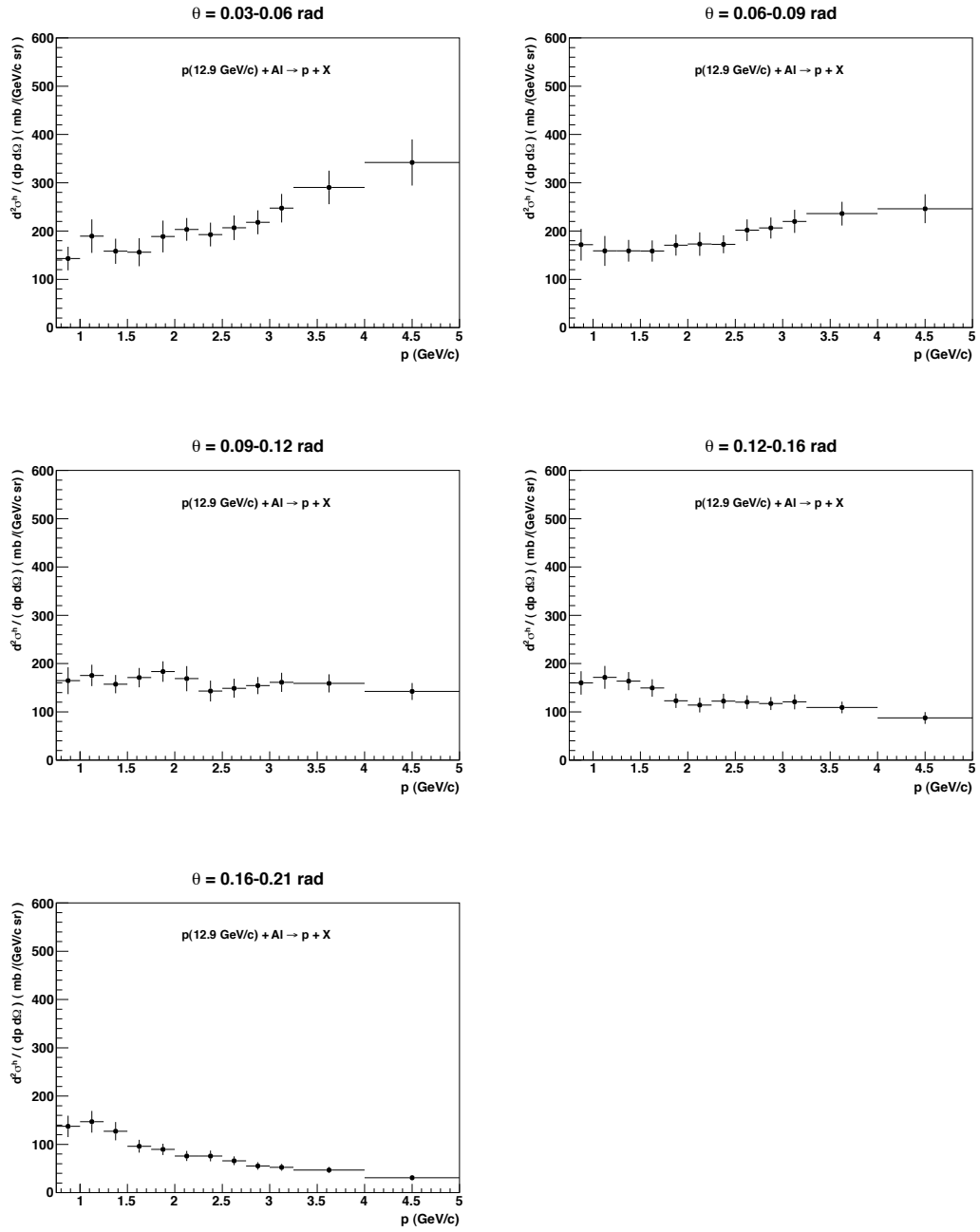
Figure 4.33: Double-differential production cross-sections of K^+ from the interaction of 12.9 GeV/c protons with aluminum. Each panel shows the cross-section as a function of momentum from 0.75 GeV/c to 5.0 GeV/c in a particular angular bin indicated above each plot. The error bars shown are the square-root of the diagonal elements of the total error matrix.

Figure 4.34: Double-differential production cross-sections of protons from the interaction of 12.9 GeV/c protons with aluminum. Each panel shows the cross-section as a function of momentum from 0.75 GeV/c to 5.0 GeV/c in a particular angular bin indicated above each plot. The error bars shown are the square-root of the diagonal elements of the total error matrix.

5% in [61] to 2% in the present analysis and provided a better understanding of the momentum smearing caused by the HARP spectrometer. (Section 3.9.1).

- Improved knowledge of the proton beam targeting efficiency and of fully correlated contributions to track reconstruction and particle identification efficiencies have reduced the overall normalization uncertainty on the pion cross-section measurement from 4% to 2%.

- Significant increases in Monte Carlo production have reduced uncertainties from Monte Carlo statistics and allowed studies to reduce certain systematics to be made.

In the present analysis the cross-sections are presented in 13 momentum bins from 0.75 to 5 GeV/c whereas the p-Al cross-sections were presented in 8 bins. This new binning was selected to attain roughly equal statistical and systematic uncertainties while maximizing the amount of spectral information provided by the measurement. It should be noted that the magnitude of fractional systematic errors arising from the momentum resolution and scale will be affected by the fineness of the binning. In particular, in the present analysis, the momentum scale uncertainty has been reduced from 5% to 2% since [61] yet this does not lead to a smaller systematic contribution on the measured cross-section. This is expected since, simultaneous to the improved reconstruction, most momentum bins have been narrowed by a factor of 2.

A re-analysis of the proton-aluminum data (pion, proton cross-sections) using our analysis method yields results consistent with those presented in both [61] and [60] within the total errors reported there. Consequently, it implies that the analysis method developed for the kaon measurements is robust and that the results presented in this thesis have the required quality.

Bibliography

[1] M. C. Gonzalez-Garcia and M. Maltoni, "Phenomenology with Massive Neutrinos," *Phys. Rept.* **460** (2008) 1–129, `arXiv:0704.1800 [hep-ph]`.

[2] F. Boehm and P. Vogel, "Physics of massive neutrinos,". Cambridge, UK: Univ. Pr. (1992) 249 p.

[3] E. Fermi, "An attempt of a theory of beta radiation. 1," *Z. Phys.* **88** (1934) 161–177.

[4] H. Bethe and R. Peierls, "The 'neutrino'," *Nature* **133** (1934) 532.

[5] F. Reines and C. L. Cowan, "Free anti-neutrino absorption cross-section. 1: Measurement of the free anti-neutrino absorption cross- section by protons," *Phys. Rev.* **113** (1959) 273–279.

[6] T. D. Lee and C.-N. Yang, "Question of Parity Conservation in Weak Interactions," *Phys. Rev.* **104** (1956) 254–258.

[7] C. S. Wu, E. Ambler, R. W. Hayward, D. D. Hoppes, and R. P. Hudson, "EXPERIMENTAL TEST OF PARITY CONSERVATION IN BETA DECAY," *Phys. Rev.* **105** (1957) 1413–1414.

[8] R. P. Feynman and M. Gell-Mann, "Theory of the fermi interaction,"*Phys. Rev.* **109** (Jan, 1958) 193–198.

[9] E. C. G. Sudarshan and R. E. Marshak, "Chirality invariance and the universal fermi interaction,"*Phys. Rev.* **109** (Mar, 1958) 1860–1862.

[10] G. Danby *et al.*, "Observation of High-Energy Neutrino Reactions and the Existence of Two Kinds of Neutrinos," *Phys. Rev. Lett.* **9** (1962) 36–44.

[11] K. Kodama *et al.*, **DONUT** Collaboration, "Observation of tau-neutrino interactions," *Phys. Lett.* **B504** (2001) 218–224, `arXiv:hep-ex/0012035`.

[12] C. Amsler *et al.*, **Particle Data Group** Collaboration, "Review of particle physics," *Phys. Lett.* **B667** (2008) 1–1340.

[13] P. Minkowski, "mu → e gamma at a Rate of One Out of 1-Billion Muon Decays?," *Phys. Lett.* **B67** (1977) 421.

[14] J. N. Bahcall, N. A. Bahcall, and G. Shaviv, "Present status of the theoretical predictions for the Cl- 36 solar neutrino experiment," *Phys. Rev. Lett.* **20** (1968) 1209–1212.

[15] J. N. Bahcall and R. Davis, "Solar neutrinos: A scientific puzzle," *Science* **191** (1976) 264–267.

[16] J. N. Bahcall, A. M. Serenelli, and S. Basu, "New solar opacities, abundances, helioseismology, and neutrino fluxes," *Astrophys. J.* **621** (2005) L85–L88, `arXiv:astro-ph/0412440`.

[17] R. Davis, Jr., D. S. Harmer, and K. C. Hoffman, "Search for neutrinos from the sun," *Phys. Rev. Lett.* **20** (1968) 1205–1209.

[18] B. T. Cleveland *et al.*, "Measurement of the solar electron neutrino flux with the Homestake chlorine detector," *Astrophys. J.* **496** (1998) 505–526.

[19] J. N. Abdurashitov *et al.*, **SAGE** Collaboration, "Measurement of the solar neutrino capture rate by the Russian-American gallium solar neutrino experiment during one half of the 22-year cycle of solar activity," *J. Exp. Theor. Phys.* **95** (2002) 181–193, `arXiv:astro-ph/0204245`.

[20] W. Hampel *et al.*, **GALLEX** Collaboration, "GALLEX solar neutrino observations: Results for GALLEX IV," *Phys. Lett.* **B447** (1999) 127–133.

[21] M. Altmann *et al.*, **GNO** Collaboration, "Complete results for five years of GNO solar neutrino observations," *Phys. Lett.* **B616** (2005) 174–190, `arXiv:hep-ex/0504037`.

[22] M. B. Smy *et al.*, **Super-Kamiokande** Collaboration, "Precise Measurement of the Solar Neutrino Day/Night and Seasonal Variation in Super-Kamiokande-I," *Phys. Rev.* **D69** (2004) 011104, `arXiv:hep-ex/0309011`.

[23] Y. Fukuda *et al.*, **Kamiokande** Collaboration, "Solar neutrino data covering solar cycle 22," *Phys. Rev. Lett.* **77** (1996) 1683–1686.

[24] Q. R. Ahmad *et al.*, **SNO** Collaboration, "Measurement of the charged current interactions produced by B-8 solar neutrinos at the Sudbury Neutrino Observatory," *Phys. Rev. Lett.* **87** (2001) 071301, `arXiv:nucl-ex/0106015`.

[25] Q. R. Ahmad *et al.*, **SNO** Collaboration, "Direct evidence for neutrino flavor transformation from neutral-current interactions in the Sudbury Neutrino Observatory," *Phys. Rev. Lett.* **89** (2002) 011301, `arXiv:nucl-ex/0204008`.

[26] Q. R. Ahmad *et al.*, **SNO** Collaboration, "Measurement of day and night neutrino energy spectra at SNO and constraints on neutrino mixing parameters," *Phys. Rev. Lett.* **89** (2002) 011302, `arXiv:nucl-ex/0204009`.

[27] Y. Ashie *et al.*, **Super-Kamiokande** Collaboration, "A Measurement of Atmospheric Neutrino Oscillation Parameters by Super-Kamiokande I," *Phys. Rev.* **D71** (2005) 112005, `arXiv:hep-ex/0501064`.

[28] Y. Ashie *et al.*, **Super-Kamiokande** Collaboration, "Evidence for an oscillatory signature in atmospheric neutrino oscillation," *Phys. Rev. Lett.* **93** (2004) 101801, `arXiv:hep-ex/0404034`.

[29] M. C. Sanchez *et al.*, **Soudan 2** Collaboration, "Observation of atmospheric neutrino oscillations in Soudan 2," *Phys. Rev.* **D68** (2003) 113004, `arXiv:hep-ex/0307069`.

[30] M. Ambrosio *et al.*, **MACRO** Collaboration, "Matter effects in upward-going muons and sterile neutrino oscillations," *Phys. Lett.* **B517** (2001) 59–66, `arXiv:hep-ex/0106049`.

[31] M. Apollonio *et al.*, **CHOOZ** Collaboration, "Limits on Neutrino Oscillations from the CHOOZ Experiment," *Phys. Lett.* **B466** (1999) 415–430, `arXiv:hep-ex/9907037`.

[32] K. Eguchi *et al.*, **KamLAND** Collaboration, "First results from KamLAND: Evidence for reactor anti- neutrino disappearance," *Phys. Rev. Lett.* **90** (2003) 021802, `arXiv:hep-ex/0212021`.

[33] G. Zacek *et al.*, **CALTECH-SIN-TUM** Collaboration, "Neutrino Oscillation Experiments at the Gosgen Nuclear Power Reactor," *Phys. Rev.* **D34** (1986) 2621–2636.

[34] G. S. Vidyakin *et al.*, "Limitations on the characteristics of neutrino oscillations," *JETP Lett.* **59** (1994) 390–393.

[35] Y. Declais *et al.*, "Search for neutrino oscillations at 15-meters, 40-meters, and 95-meters from a nuclear power reactor at Bugey," *Nucl. Phys.* **B434** (1995) 503–534.

[36] A. Piepke, **Palo Verde** Collaboration, "Final results from the Palo Verde neutrino oscillation experiment," *Prog. Part. Nucl. Phys.* **48** (2002) 113–121.

[37] I. Shimizu, **KamLAND** Collaboration, "Anti-Neutrino Status,". Prepared for TAUP 2007 Conference, `http://www.awa.tohoku.ac.jp/taup2007/slides/workshop14/roomA/02-KamLAND-AntiNeutrino-Status-Shimizu.pdf`.

[38] T. Schwetz, M. A. Tortola, and J. W. F. Valle, "Three-flavour neutrino oscillation update," *New J. Phys.* **10** (2008) 113011, `arXiv:0808.2016 [hep-ph]`.

[39] M. H. Ahn *et al.*, **K2K** Collaboration, "Measurement of Neutrino Oscillation by the K2K Experiment," *Phys. Rev.* **D74** (2006) 072003, `arXiv:hep-ex/0606032`.

[40] E. Ables *et al.*, **MINOS** Collaboration, "P-875: A Long baseline neutrino oscillation experiment at Fermilab,". FERMILAB-PROPOSAL-0875.

[41] P. Adamson *et al.*, **MINOS** Collaboration, "Measurement of Neutrino Oscillations with the MINOS Detectors in the NuMI Beam," *Phys. Rev. Lett.* **101** (2008) 131802, `arXiv:0806.2237 [hep-ex]`.

[42] P. Adamson *et al.*, **MINOS** Collaboration, "Search for muon-neutrino to electron-neutrino transitions in MINOS," *Phys. Rev. Lett.* **103** (2009) 261802, `arXiv:0909.4996 [hep-ex]`.

[43] A. Aguilar *et al.*, **LSND** Collaboration, "Evidence for neutrino oscillations from the observation of anti-nu/e appearance in a anti-nu/mu beam," *Phys. Rev.* **D64** (2001) 112007, `arXiv:hep-ex/0104049`.

[44] B. Armbruster *et al.*, **KARMEN** Collaboration, "Upper limits for neutrino oscillations muon-antineutrino to electron-antineutrino from muon decay at rest," *Phys. Rev.* **D65** (2002) 112001, `arXiv:hep-ex/0203021`.

[45] A. A. Aguilar-Arevalo *et al.*, **The MiniBooNE** Collaboration, "A Search for electron neutrino appearance at the $\Delta m^2 \sim 1\text{eV}^2$ scale," *Phys. Rev. Lett.* **98** (2007) 231801, `arXiv:0704.1500 [hep-ex]`.

[46] Y. Itow *et al.*, **The T2K** Collaboration, "The JHF-Kamioka neutrino project," `arXiv:hep-ex/0106019`.

[47] D. S. Ayres *et al.*, **NOvA** Collaboration, "NOvA proposal to build a 30-kiloton off-axis detector to study neutrino oscillations in the Fermilab NuMI beamline," `arXiv:hep-ex/0503053`.

[48] F. Ardellier *et al.*, **Double Chooz** Collaboration, "Double Chooz: A search for the neutrino mixing angle theta(13)," `arXiv:hep-ex/0606025`.

[49] X. Guo *et al.*, **Daya-Bay** Collaboration, "A precision measurement of the neutrino mixing angle theta(13) using reactor antineutrinos at Daya Bay," `arXiv:hep-ex/0701029`.

[50] J. K. Ahn *et al.*, **RENO** Collaboration, "RENO: An Experiment for Neutrino Oscillation Parameter θ_{13} Using Reactor Neutrinos at Yonggwang," `arXiv:1003.1391 [hep-ex]`.

[51] P. Zucchelli, "A novel concept for a anti-nu/e / nu/e neutrino factory: The beta beam," *Phys. Lett.* **B532** (2002) 166–172.

[52] S. Geer, "Neutrino beams from muon storage rings: Characteristics and physics potential," *Phys. Rev.* **D57** (1998) 6989–6997, `arXiv:hep-ph/9712290`.

[53] A. G. Cocco, **OPERA** Collaboration, "The OPERA experiment at Gran Sasso," *Nucl. Phys. Proc. Suppl.* **85** (2000) 125–128.

[54] N. Agafonova *et al.*, **OPERA** Collaboration, "Observation of a first ν_τ candidate in the OPERA experiment in the CNGS beam," *Phys. Lett.* **B691** (2010) 138–145, `arXiv:1006.1623 [hep-ex]`.

[55] M. Sorel, "Search for Sterile Neutrinos Using the MiniBooNE Beam,". FERMILAB-THESIS-2005-07.

[56] N. V. Mokhov and S. I. Striganov, "MARS15 overview," *AIP Conf. Proc.* **896** (2007) 50–60.

[57] `http://geant4.web.cern.ch/geant4/UserDocumentation/UsersGuides/ PhysicsReferenceManual/html/node110.html`.

[58] A. Heikkinen, N. Stepanov, and J. P. Wellisch, "Bertini intra-nuclear cascade implementation in Geant4," `arXiv:nucl-th/0306008`.

[59] G. Folger, V. N. Ivanchenko, and J. P. Wellisch, "The binary cascade," *The European Physical Journal A - Hadrons and Nuclei* **21** (2004) 407–417. `http://dx.doi.org/10.1140/epja/i2003-10219-7`. 10.1140/epja/i2003-10219-7.

[60] D. W. Schmitz, "A measurement of hadron production cross sections for the simulation of accelerator neutrino beams and a search for ν_μ to ν_e oscillations in the δm^2 about equals $1 - eV^2$ region,". FERMILAB-THESIS-2008-26.

[61] M. G. Catanesi *et al.*, **HARP** Collaboration, "Measurement of the production cross-section of positive pions in p Al collisions at 12.9-GeV/c," *Nucl. Phys.* **B732** (2006) 1–45, `arXiv:hep-ex/0510039`.

[62] J. Sanford and C. Wang, "Empirical formulas for particle pro-duction in p-Be collisions between 10 and 35 GeV/c," *Brookhaven National Laboratory, AGS internal report* (1967) . (unpublished).

[63] Y. Cho, M. Derrick, G. Marmer, T. P. Wangler, J. L. Day, P. Kalbaci, M. L. Marshak, J. K. Randolph, and A. W. Key, "Pion production in proton-beryllium collisions at 12.4 gev/c,"*Phys. Rev. D* **4** (Oct, 1971) 1967–1974.

[64] I. Chemakin *et al.*, **E910** Collaboration, "Pion Production by Protons on a Thin Beryllium Target at 6.4, 12.3, and 17.5 GeV/c Incident Proton Momenta," *Phys. Rev.* **C77** (2008) 015209, `arXiv:0707.2375 [nucl-ex]`.

[65] S. Brice, "Better Propagation of Pion Production Uncertainties.". `http://www-boone. fnal.gov/software_and_analysis/meetings/03_07_08/PipProdErrors.pdf`.

[66] A. A. Aguilar-Arevalo *et al.*, **MiniBooNE** Collaboration, "The Neutrino Flux prediction at MiniBooNE," *Phys. Rev.* **D79** (2009) 072002, `arXiv:0806.1449 [hep-ex]`.

[67] M. G. Catanesi *et al.*, "Proposal to study hadron production for the neutrino factory and for the atmospheric neutrino flux,". CERN-SPSC-99-35.

[68] M. G. Catanesi *et al.*, **HARP** Collaboration, "The HARP detector at the CERN PS," *Nucl. Instrum. Meth.* **A571** (2007) 527–561.

[69] M. G. Catanesi *et al.*, **HARP** Collaboration, "Measurement of the production of charged pions by protons on a tantalum target," *Eur. Phys. J.* **C51** (2007) 787–824, `arXiv:0706.1600 [hep-ex]`.

[70] A. A. Aguilar-Arevalo *et al.*, **MiniBooNE** Collaboration, "The MiniBooNE Detector," *Nucl. Instrum. Meth.* **A599** (2009) 28–46, `arXiv:0806.4201 [hep-ex]`.

[71] A. A. Aguilar-Arevalo *et al.*, **SciBooNE** Collaboration, "Bringing the SciBar detector to the booster neutrino beam," `arXiv:hep-ex/0601022`.

[72] K. Pretzl, "Invited talk at the International Symposium on Strangeness and Quark Matter, Crete,".

[73] J. Altegoer *et al.*, **NOMAD** Collaboration, "The NOMAD experiment at the CERN SPS," *Nucl. Instrum. Meth.* **A404** (1998) 96–128.

[74] P. Billoir, "TRACK FITTING WITH MULTIPLE SCATTERING: A NEW METHOD," *Nucl. Instrum. Meth.* **A225** (1984) 352–366.

[75] M. Baldo-Ceolin *et al.*, "The time-of-flight tofw detector of the harp experiment: construction and performance," *Nucl. Instrum. Meth.* **532** (2004) no. 3, 548 – 561.

[76] M. G. Catanesi *et al.*, "Measurement of the production cross-section of positive pions in the collision of 8.9 GeV/c protons on beryllium," *Eur. Phys. J.* **C52** (2007) 29–53, `arXiv:hep-ex/0702024`.

[77] M. G. Catanesi *et al.*, "Particle identification algorithms for the HARP forward spectrometer," *Nucl. Instrum. Meth.* **A572** (2007) 899–921.

Appendix A

Cross-section data

This appendix contains tables of double-differential production cross-section data measured at the HARP experiment. Proton, π^+ and K^+ production from interactions of 12.9 GeV/c protons with aluminum are presented in bins of laboratory frame momentum, p, and polar angle with respect to the incident proton direction, θ, in the range 0.75 GeV/c $\leq p \leq$ 5.0 GeV/c and 0.03 rad $\leq \theta \leq$ 0.21 rad. For each kinematic bin the central value cross-section and the square-root of the corresponding diagonal element of the covariance matrix are listed.

A.1 Pions, Protons

$\theta_{\min}$ (mrad)	$\theta_{\max}$ (mrad)	$p_{\min}$ (GeV/c)	$p_{\max}$ (GeV/c)	$d^2\sigma^{\pi^+}/(dpd\Omega)$ (mb/(GeV/c sr))			$d^2\sigma^p/(dpd\Omega)$ (mb/(GeV/c sr))		
30	60	0.75	1.00	469.6	$\pm$	106	143.1	$\pm$	25
		1.00	1.25	559.8	$\pm$	109	189.6	$\pm$	35
		1.25	1.50	544.7	$\pm$	86	158.2	$\pm$	26
		1.50	1.75	512.2	$\pm$	73	156.3	$\pm$	29
		1.75	2.00	507.5	$\pm$	80	188.9	$\pm$	33
		2.00	2.25	459.9	$\pm$	54	203.4	$\pm$	23
		2.25	2.50	498.3	$\pm$	53	192.8	$\pm$	25
		2.50	2.75	519.1	$\pm$	57	206.9	$\pm$	26
		2.75	3.00	528.4	$\pm$	57	218.0	$\pm$	25
		3.00	3.25	506.8	$\pm$	58	247.4	$\pm$	30
		3.25	4.00	436.8	$\pm$	53	290.4	$\pm$	35
		4.00	5.00	329.2	$\pm$	57	342.0	$\pm$	48
60	90	0.75	1.00	433.4	$\pm$	83	171.7	$\pm$	33
		1.00	1.25	463.3	$\pm$	77	158.9	$\pm$	31
		1.25	1.50	472.3	$\pm$	64	159.1	$\pm$	22
		1.50	1.75	463.6	$\pm$	55	158.6	$\pm$	22
		1.75	2.00	474.0	$\pm$	60	170.8	$\pm$	22
		2.00	2.25	464.6	$\pm$	54	173.0	$\pm$	24
		2.25	2.50	420.0	$\pm$	38	172.6	$\pm$	18
		2.50	2.75	433.7	$\pm$	41	201.7	$\pm$	23
		2.75	3.00	382.7	$\pm$	36	206.3	$\pm$	22
		3.00	3.25	340.5	$\pm$	34	220.1	$\pm$	24
		3.25	4.00	293.1	$\pm$	32	236.1	$\pm$	25
		4.00	5.00	189.0	$\pm$	31	246.2	$\pm$	30

$\theta_{\min}$ (mrad)	$\theta_{\max}$ (mrad)	$p_{\min}$ (GeV/c)	$p_{\max}$ (GeV/c)	$d^2\sigma^{\pi^+}/(dpd\Omega)$ (mb/(GeV/c sr))			$d^2\sigma^p/(dpd\Omega)$ (mb/(GeV/c sr))		
90	120	0.75	1.00	429.0	$\pm$	75	164.6	$\pm$	28
		1.00	1.25	471.6	$\pm$	69	175.4	$\pm$	22
		1.25	1.50	449.2	$\pm$	53	157.4	$\pm$	19
		1.50	1.75	412.0	$\pm$	42	171.0	$\pm$	20
		1.75	2.00	403.2	$\pm$	38	183.3	$\pm$	21
		2.00	2.25	361.9	$\pm$	42	168.8	$\pm$	26
		2.25	2.50	323.1	$\pm$	34	143.1	$\pm$	22
		2.50	2.75	306.3	$\pm$	30	148.9	$\pm$	20
		2.75	3.00	274.8	$\pm$	26	154.5	$\pm$	18
		3.00	3.25	253.6	$\pm$	29	161.2	$\pm$	20
		3.25	4.00	198.8	$\pm$	21	159.0	$\pm$	19
		4.00	5.00	127.9	$\pm$	17	142.3	$\pm$	18
120	160	0.75	1.00	423.1	$\pm$	67	159.9	$\pm$	24
		1.00	1.25	452.4	$\pm$	63	171.5	$\pm$	24
		1.25	1.50	402.4	$\pm$	46	163.6	$\pm$	19
		1.50	1.75	359.2	$\pm$	36	149.6	$\pm$	18
		1.75	2.00	289.7	$\pm$	27	123.0	$\pm$	15
		2.00	2.25	234.4	$\pm$	22	114.0	$\pm$	15
		2.25	2.50	218.6	$\pm$	21	122.2	$\pm$	15
		2.50	2.75	195.5	$\pm$	20	120.2	$\pm$	14
		2.75	3.00	173.3	$\pm$	21	117.3	$\pm$	13
		3.00	3.25	149.3	$\pm$	22	120.7	$\pm$	15
		3.25	4.00	94.8	$\pm$	17	109.1	$\pm$	12
		4.00	5.00	46.0	$\pm$	14	87.4	$\pm$	12

$\theta_{\min}$ (mrad)	$\theta_{\max}$ (mrad)	$p_{\min}$ (GeV/c)	$p_{\max}$ (GeV/c)	$d^2\sigma^{\pi^+}/(dpd\Omega)$ (mb/(GeV/c sr))			$d^2\sigma^p/(dpd\Omega)$ (mb/(GeV/c sr))		
160	210	0.75	1.00	331.6	$\pm$	53	137.4	$\pm$	22
		1.00	1.25	343.6	$\pm$	53	146.8	$\pm$	23
		1.25	1.50	271.8	$\pm$	33	127.2	$\pm$	19
		1.50	1.75	190.7	$\pm$	23	96.1	$\pm$	13
		1.75	2.00	168.9	$\pm$	18	89.7	$\pm$	12
		2.00	2.25	135.0	$\pm$	15	76.0	$\pm$	10
		2.25	2.50	103.9	$\pm$	14	75.8	$\pm$	11
		2.50	2.75	86.0	$\pm$	10	66.1	$\pm$	9
		2.75	3.00	67.0	$\pm$	10	55.3	$\pm$	8
		3.00	3.25	52.6	$\pm$	8	52.5	$\pm$	7
		3.25	4.00	40.5	$\pm$	6	46.9	$\pm$	6
		4.00	5.00	21.7	$\pm$	4	30.9	$\pm$	4

A.2   Positive kaons

12.9 GeV/c proton + aluminum						
$\theta_{\min}$ (mrad)	$\theta_{\max}$ (mrad)	$p_{\min}$ (GeV/c)	$p_{\max}$ (GeV/c)	$d^2\sigma^{K^+}/(dpd\Omega)$ (mb/(GeV/c sr))		
30	60	0.75	1.00	163.7	$\pm$	74
		1.00	1.25	102.6	$\pm$	55
		1.25	1.50	53.0	$\pm$	31
		1.50	1.75	41.2	$\pm$	20
		1.75	2.00	49.2	$\pm$	23
		2.00	2.25	44.7	$\pm$	18
		2.25	2.50	55.0	$\pm$	22
		2.50	2.75	63.8	$\pm$	22
		2.75	3.00	51.2	$\pm$	18
		3.00	3.25	46.7	$\pm$	15
		3.25	4.00	45.9	$\pm$	14
		4.00	5.00	53.2	$\pm$	33
60	90	0.75	1.00	89.5	$\pm$	52
		1.00	1.25	47.6	$\pm$	26
		1.25	1.50	32.6	$\pm$	17
		1.50	1.75	31.5	$\pm$	15
		1.75	2.00	23.5	$\pm$	13
		2.00	2.25	26.1	$\pm$	15
		2.25	2.50	28.6	$\pm$	15
		2.50	2.75	34.2	$\pm$	15
		2.75	3.00	39.9	$\pm$	14
		3.00	3.25	28.2	$\pm$	11
		3.25	4.00	27.0	$\pm$	10
		4.00	5.00	23.7	$\pm$	18

12.9 GeV/c proton + aluminum						
$\theta_{\min}$ (mrad)	$\theta_{\max}$ (mrad)	$p_{\min}$ (GeV/c)	$p_{\max}$ (GeV/c)	$d^2\sigma^{K^+}/(dpd\Omega)$ (mb/(GeV/c sr))		
90	120	0.75	1.00	91.8	±	49
		1.00	1.25	55.5	±	23
		1.25	1.50	38.3	±	12
		1.50	1.75	25.6	±	10
		1.75	2.00	17.7	±	11
		2.00	2.25	16.0	±	12
		2.25	2.50	25.6	±	12
		2.50	2.75	21.7	±	12
		2.75	3.00	15.0	±	11
		3.00	3.25	22.3	±	10
		3.25	4.00	26.8	±	8
		4.00	5.00	10.4	±	11
120	160	0.75	1.00	56.8	±	34
		1.00	1.25	41.5	±	16
		1.25	1.50	33.7	±	12
		1.50	1.75	16.8	±	9
		1.75	2.00	24.4	±	9
		2.00	2.25	23.3	±	8
		2.25	2.50	24.1	±	12
		2.50	2.75	22.7	±	10
		2.75	3.00	22.1	±	9
		3.00	3.25	21.6	±	7
		3.25	4.00	15.0	±	6
		4.00	5.00	7.0	±	5

12.9 GeV/c proton + aluminum				
$\theta_{\min}$ (mrad)	$\theta_{\max}$ (mrad)	$p_{\min}$ (GeV/c)	$p_{\max}$ (GeV/c)	$d^2\sigma^{K^+}/(dpd\Omega)$ (mb/(GeV/c sr))
160	210	0.75	1.00	54.8 $\pm$ 40
		1.00	1.25	31.1 $\pm$ 13
		1.25	1.50	19.1 $\pm$ 7
		1.50	1.75	16.3 $\pm$ 6
		1.75	2.00	18.5 $\pm$ 7
		2.00	2.25	13.8 $\pm$ 7
		2.25	2.50	8.9 $\pm$ 6
		2.50	2.75	10.1 $\pm$ 5
		2.75	3.00	9.4 $\pm$ 3
		3.00	3.25	9.3 $\pm$ 3
		3.25	4.00	4.3 $\pm$ 2
		4.00	5.00	2.1 $\pm$ 1

Appendix B

Cross-sections with statistical errors only

This appendix shows the measured π^+ and π^-, K^+ and protons production cross-sections from 12.9 GeV/c proton+aluminum collisions. The error bars are statistical uncertainties only and are obtained following the method presented in Section 4.10.1.
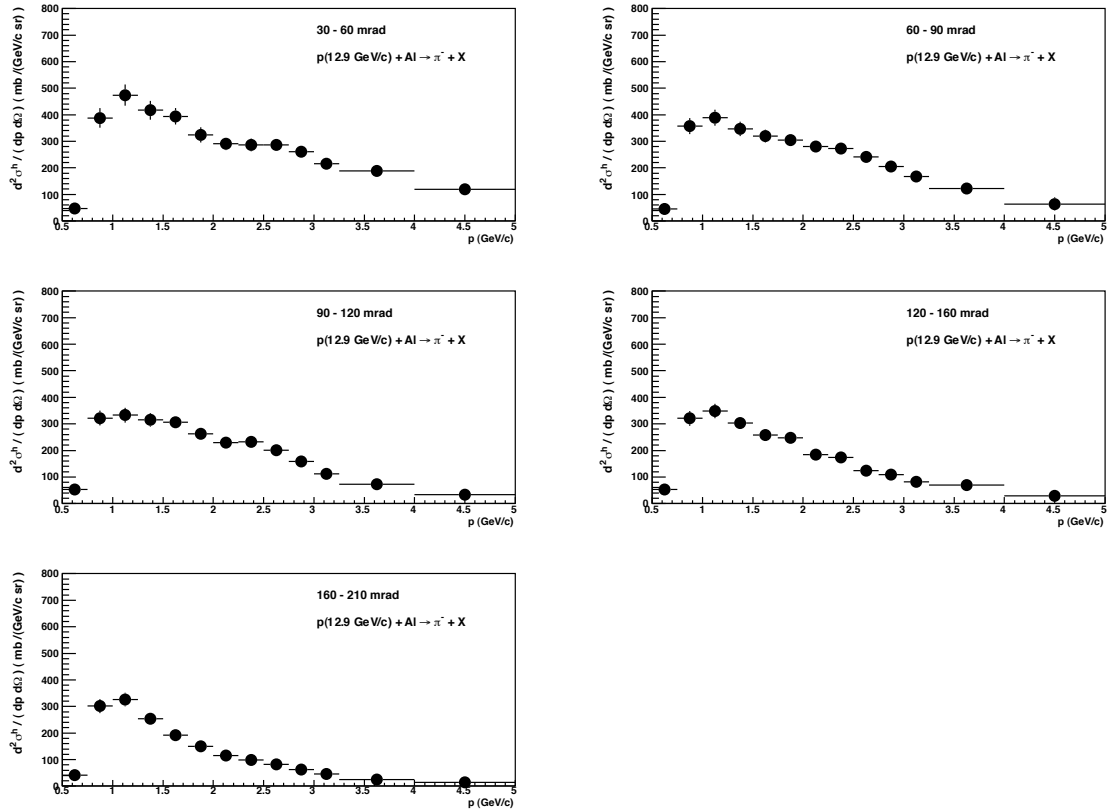
Figure B.1: Positive pion production cross-sections from 12.9 GeV/c proton+aluminum collisions, statistical errors only.
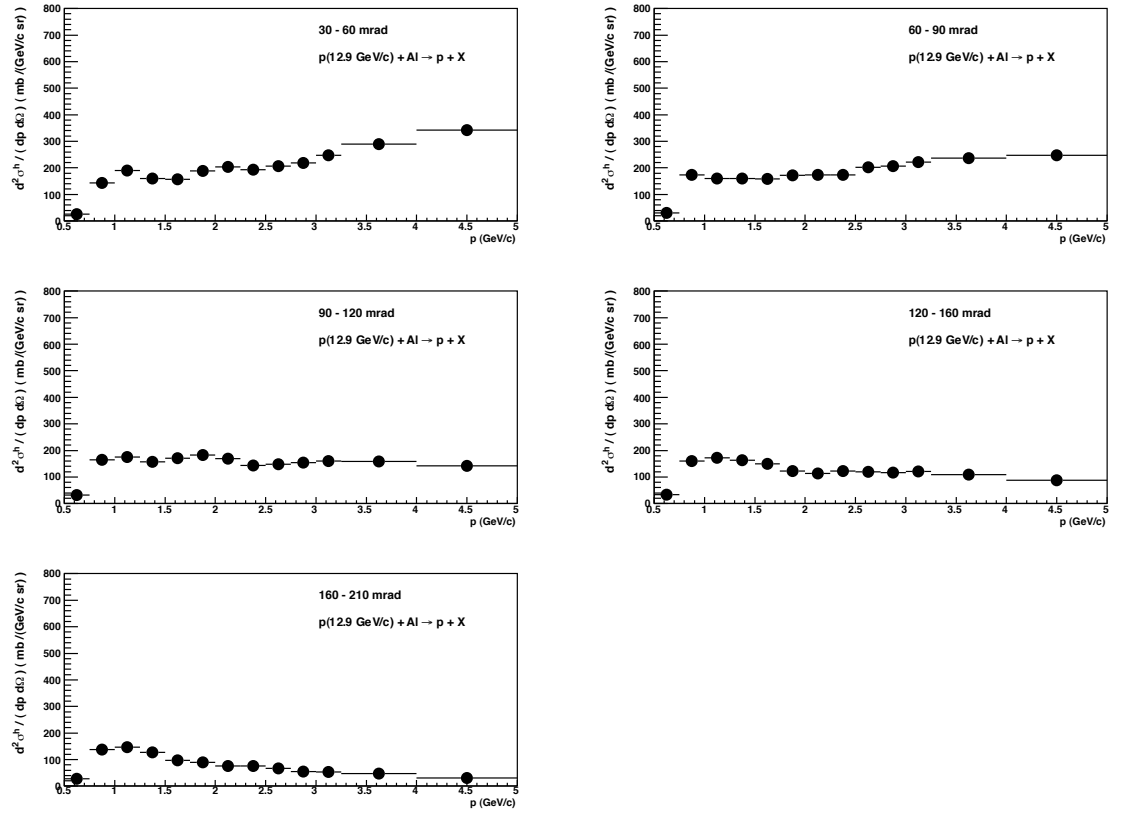
Figure B.2: Proton production cross-sections from 12.9 GeV/c proton+aluminum collisions, statistical errors only.
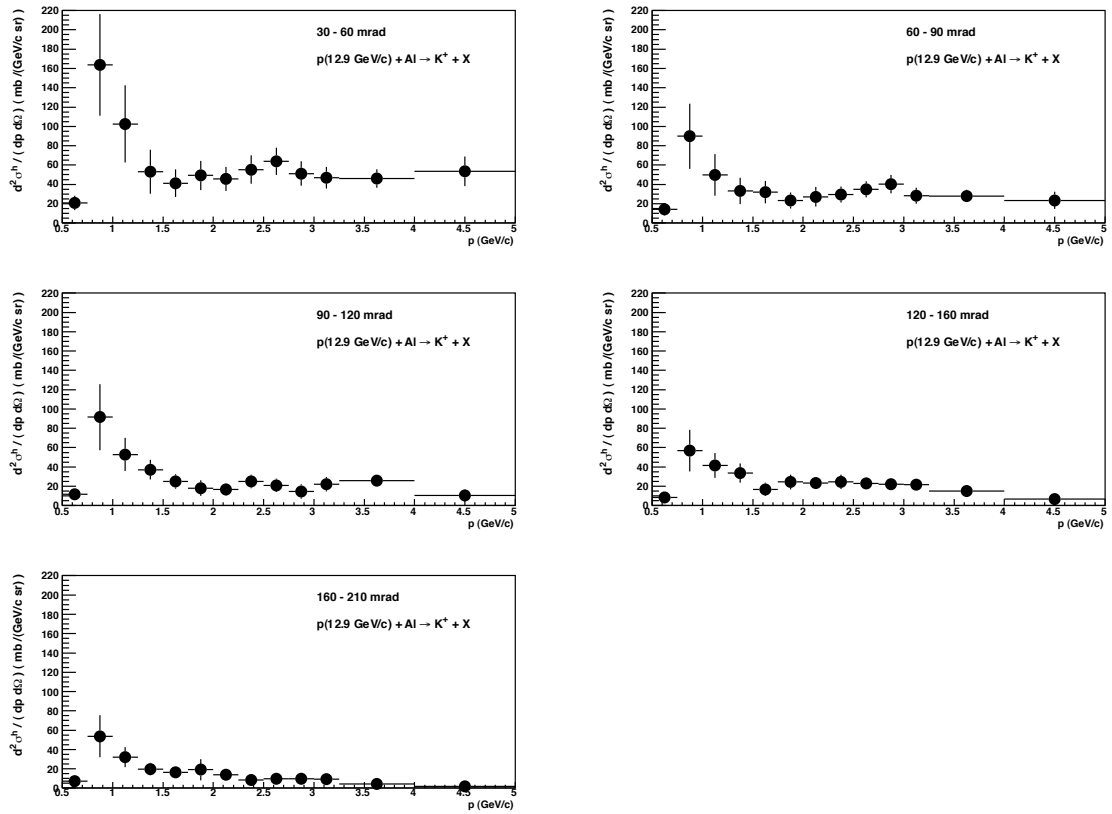
Figure B.3: Positive kaon production cross-sections from 12.9 GeV/c proton+aluminum collisions, statistical errors only.

Appendix C

Fitted $\boldsymbol{\beta}$ spectra

This appendix shows β spectra filled with the 12.9 GeV/c protons on aluminum target data set fitted according to the method presented in Section 4.8. The fits are presented in bins of reconstructed momentum and angle (p', θ') in the range 0.75 GeV/c $\leq p' \leq$ 5.0 GeV/c and 0.030 rad $\leq \theta' \leq$ 0.210 rad. Note that the total number of particles extracted in each bin, before applying post-fit corrections, is given by Eq. 4.22 and 4.23 and not by the numbers displayed directly on the folowing panels.

Figure C.1: *β* spectra fitted according to the method presented in Section 4.8. The reconstructed momentum and angle range of each fit is indicated on the panel. Left panel: all inclusive particles. Right panel: corresponding spectrum fit following the Cherenkov cut method (Section 4.8.1)
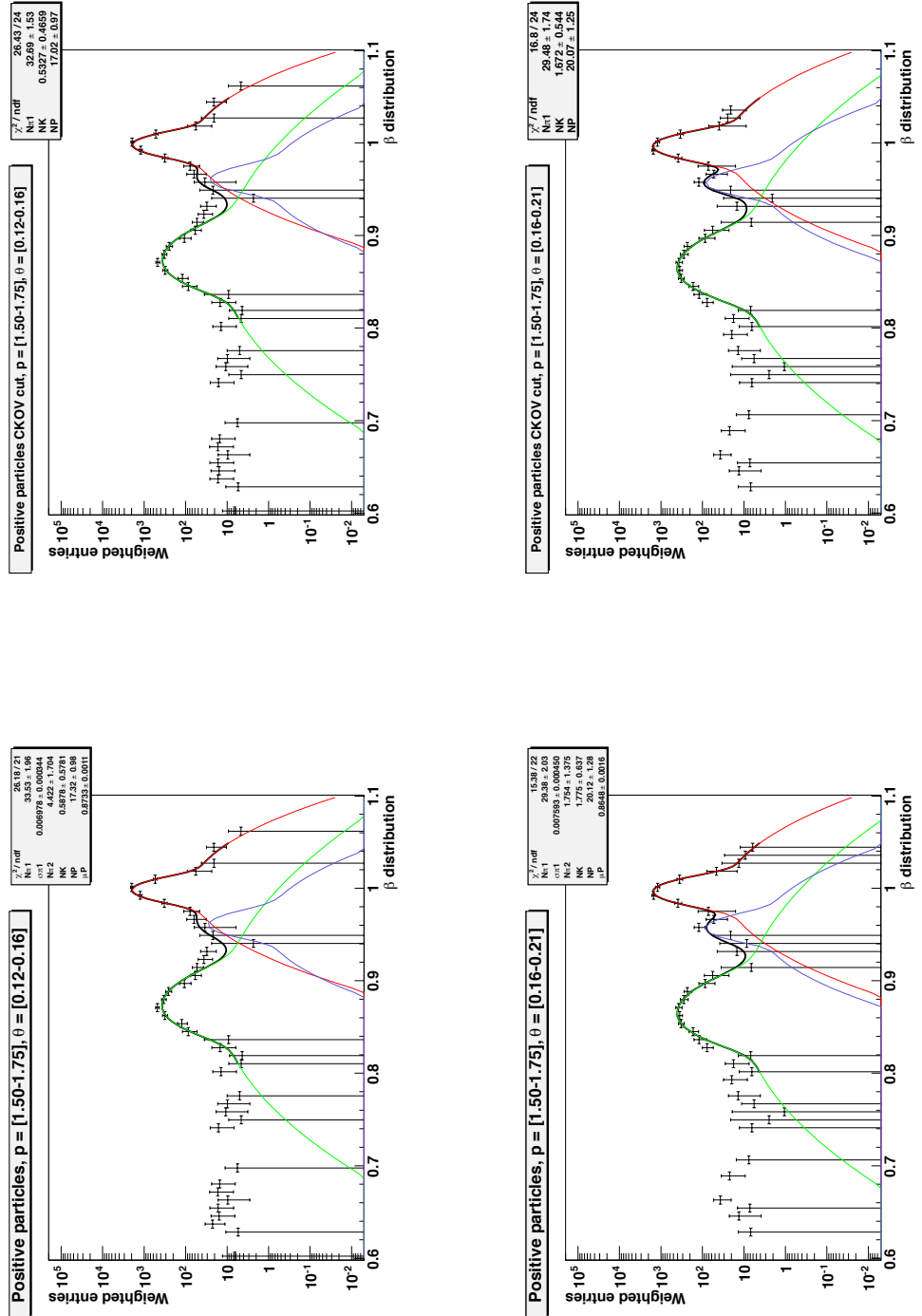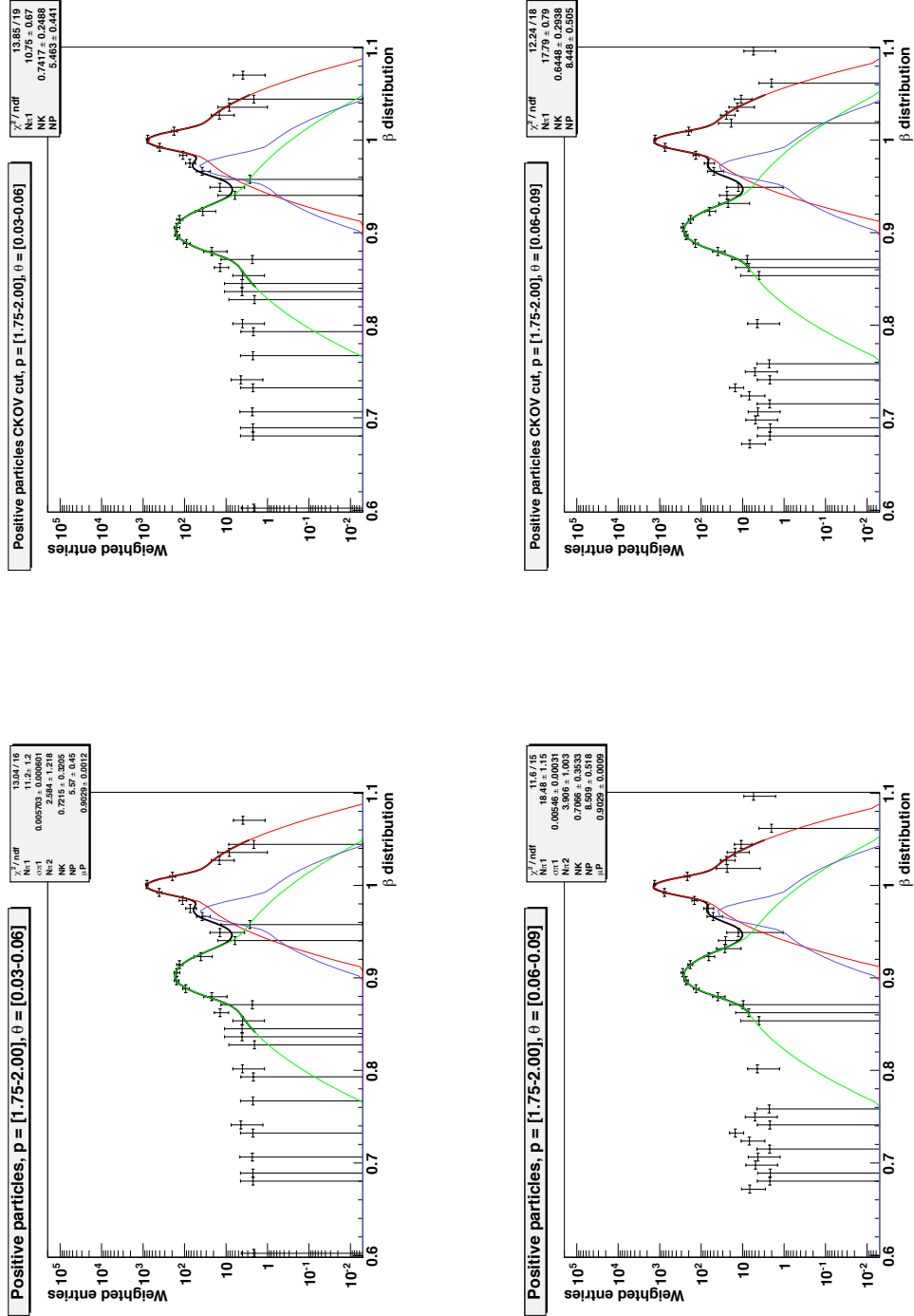
Figure C.2: β spectra fitted according to the method presented in Section 4.8. The reconstructed momentum and angle range of each fit is indicated on the panel. Left panel: all inclusive particles. Right panel: corresponding spectrum fit following the Cherenkov cut method (Section 4.8.1)

Figure C.3: *β* spectra fitted according to the method presented in Section 4.8. The reconstructed momentum and angle range of each fit is indicated on the panel. Left panel: all inclusive particles. Right panel: corresponding spectrum fit following the Cherenkov cut method (Section 4.8.1)
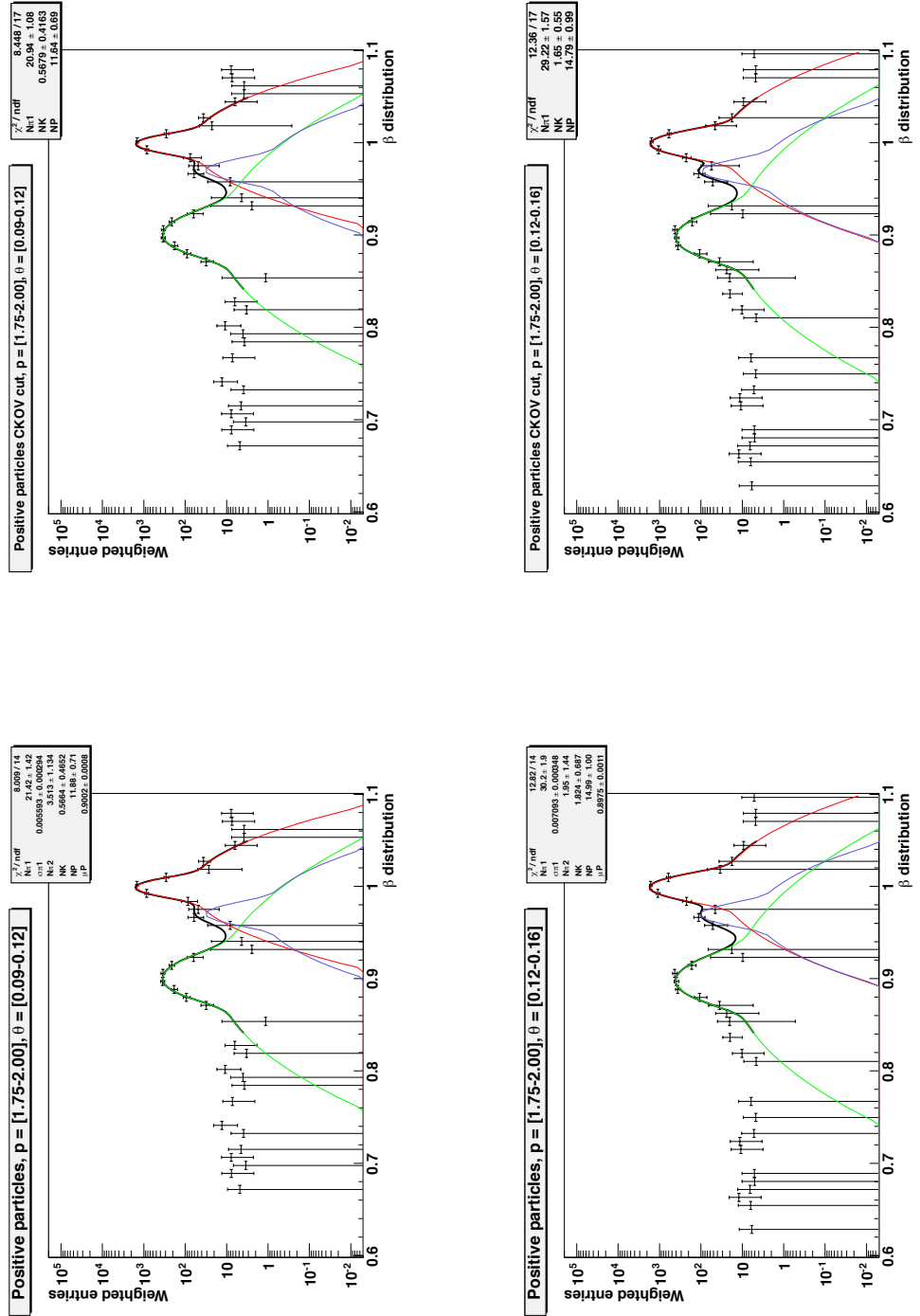
Figure C.4: β spectra fitted according to the method presented in Section 4.8. The reconstructed momentum and angle range of each fit is indicated on the panel. Left panel: all inclusive particles. Right panel: corresponding spectrum fit following the Cherenkov cut method (Section 4.8.1)
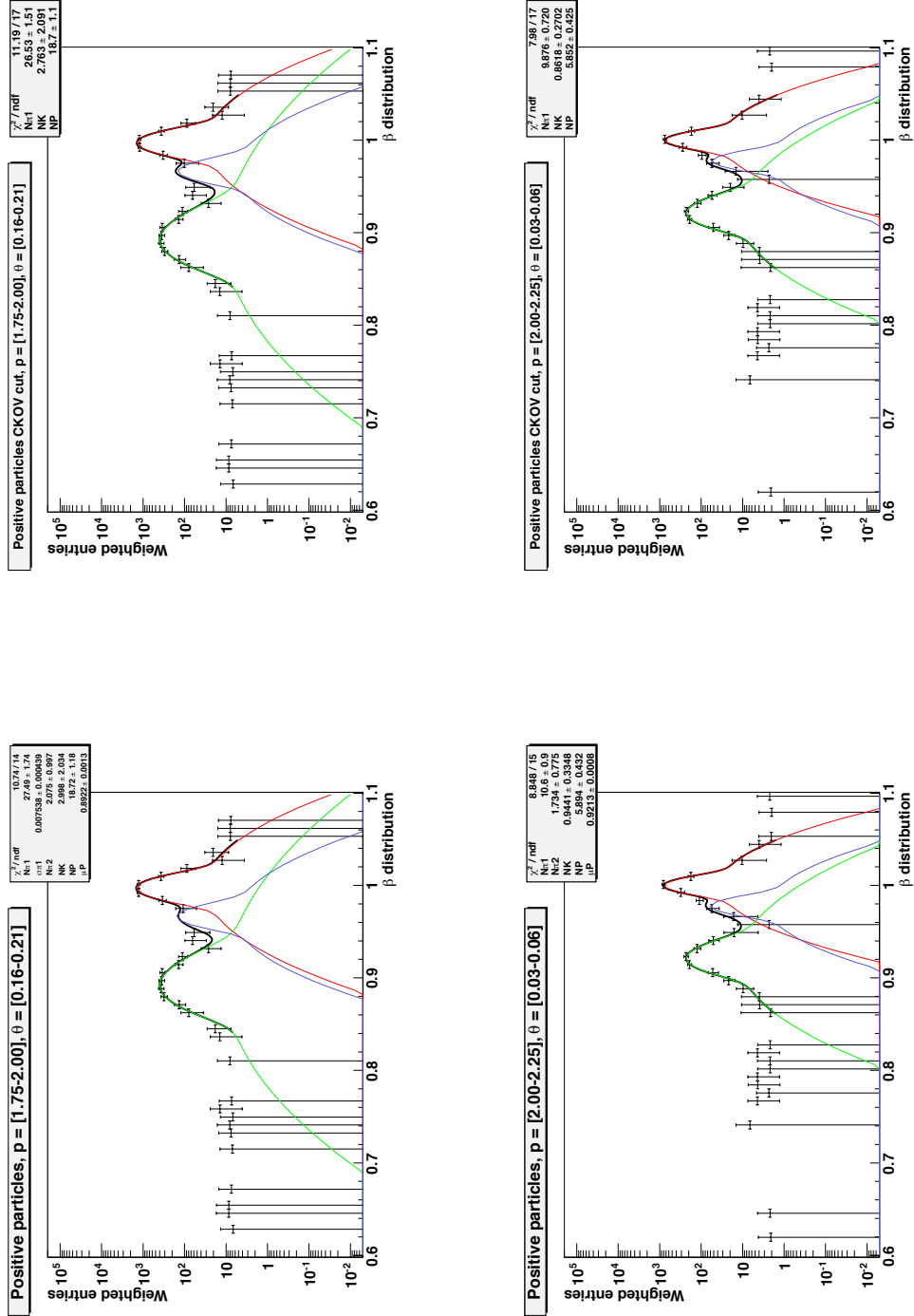
Figure C.5: *β* spectra fitted according to the method presented in Section 4.8. The reconstructed momentum and angle range of each fit is indicated on the panel. Left panel: all inclusive particles. Right panel: corresponding spectrum fit following the Cherenkov cut method (Section 4.8.1)

Figure C.6: β spectra fitted according to the method presented in Section 4.8. The reconstructed momentum and angle range of each fit is indicated on the panel. Left panel: all inclusive particles. Right panel: corresponding spectrum fit following the Cherenkov cut method (Section 4.8.1)
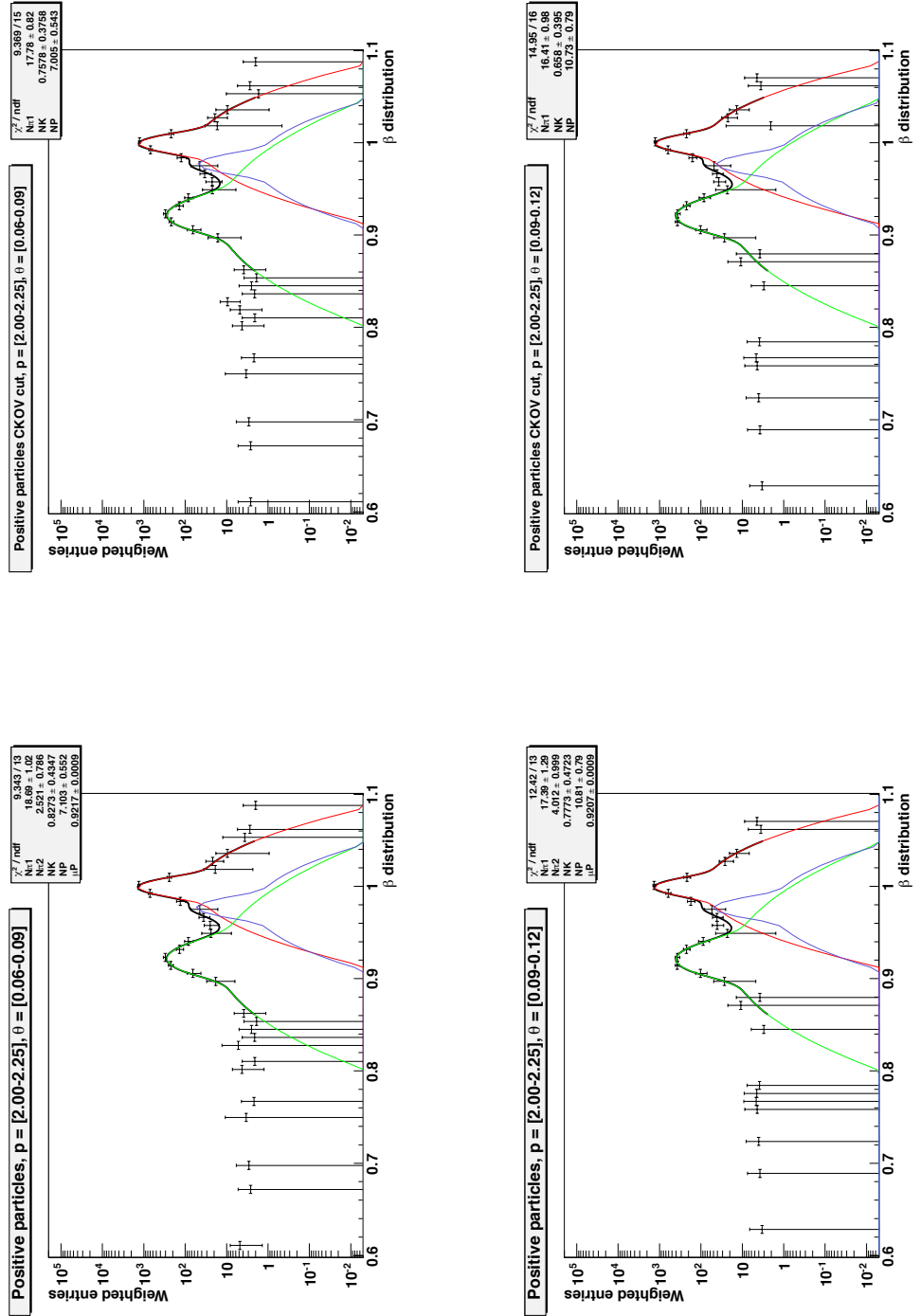
Figure C.7: *β* spectra fitted according to the method presented in Section 4.8. The reconstructed momentum and angle range of each fit is indicated on the panel. Left panel: all inclusive particles. Right panel: corresponding spectrum fit following the Cherenkov cut method (Section 4.8.1)
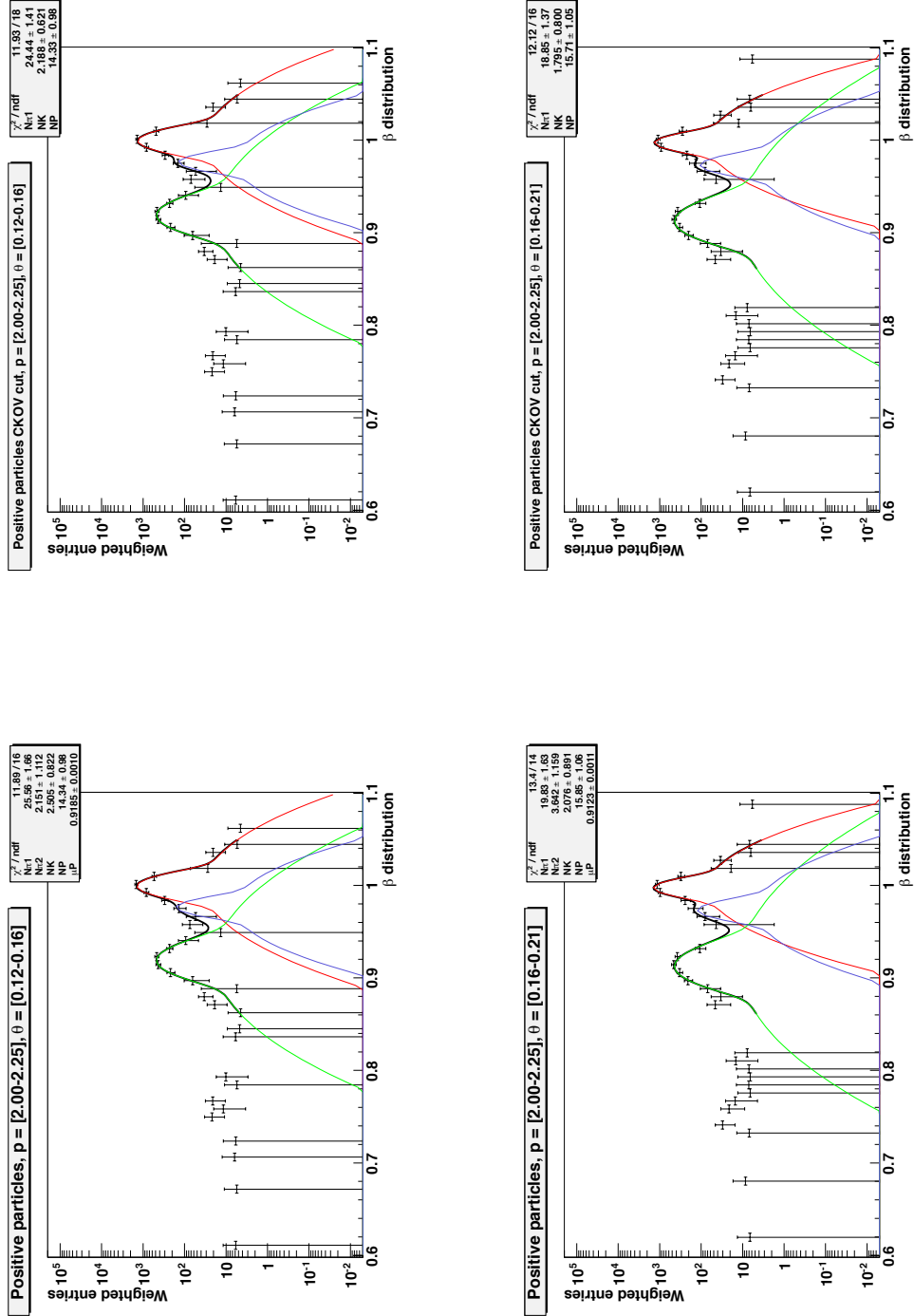
Figure C.8: β spectra fitted according to the method presented in Section 4.8. The reconstructed momentum and angle range of each fit is indicated on the panel. Left panel: all inclusive particles. Right panel: corresponding spectrum fit following the Cherenkov cut method (Section 4.8.1)

Figure C.9: *β* spectra fitted according to the method presented in Section 4.8. The reconstructed momentum and angle range of each fit is indicated on the panel. Left panel: all inclusive particles. Right panel: corresponding spectrum fit following the Cherenkov cut method (Section 4.8.1)
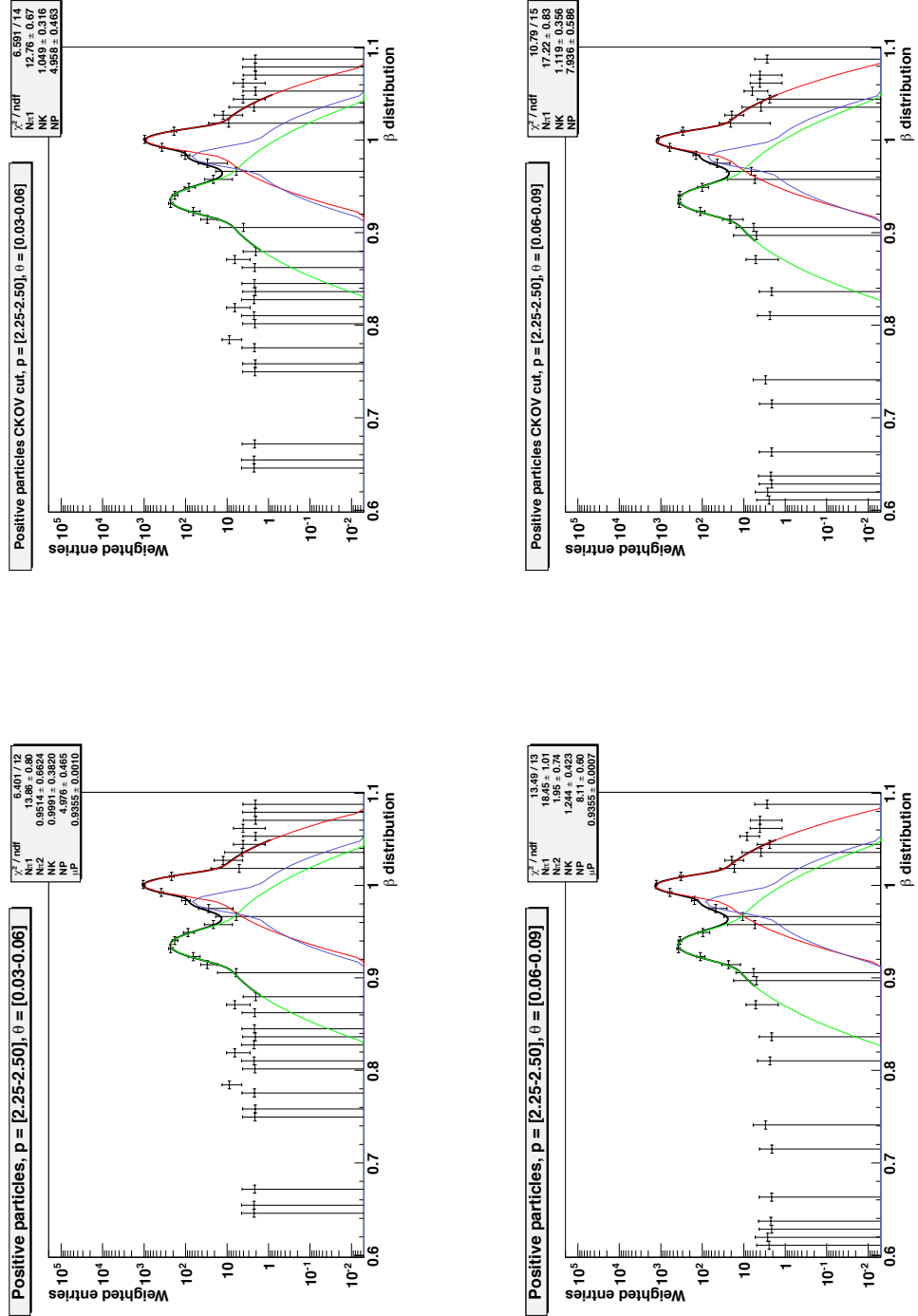
Figure C.10: β spectra fitted according to the method presented in Section 4.8. The reconstructed momentum and angle range of each fit is indicated on the panel. Left panel: all inclusive particles. Right panel: corresponding spectrum fit following the Cherenkov cut method (Section 4.8.1)
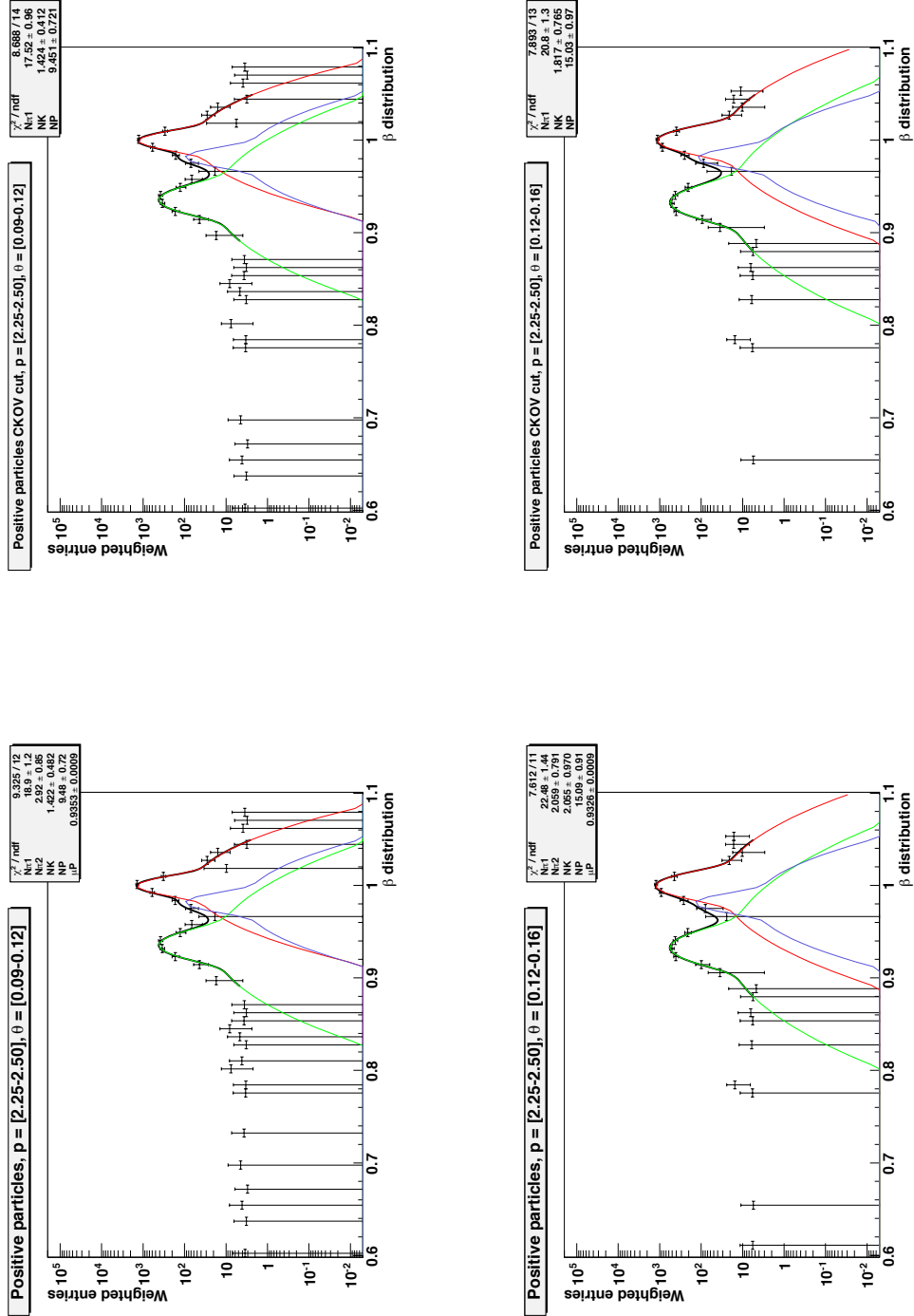
Figure C.11: *β* spectra fitted according to the method presented in Section 4.8. The reconstructed momentum and angle range of each fit is indicated on the panel. Left panel: all inclusive particles. Right panel: corresponding spectrum fit following the Cherenkov cut method (Section 4.8.1)
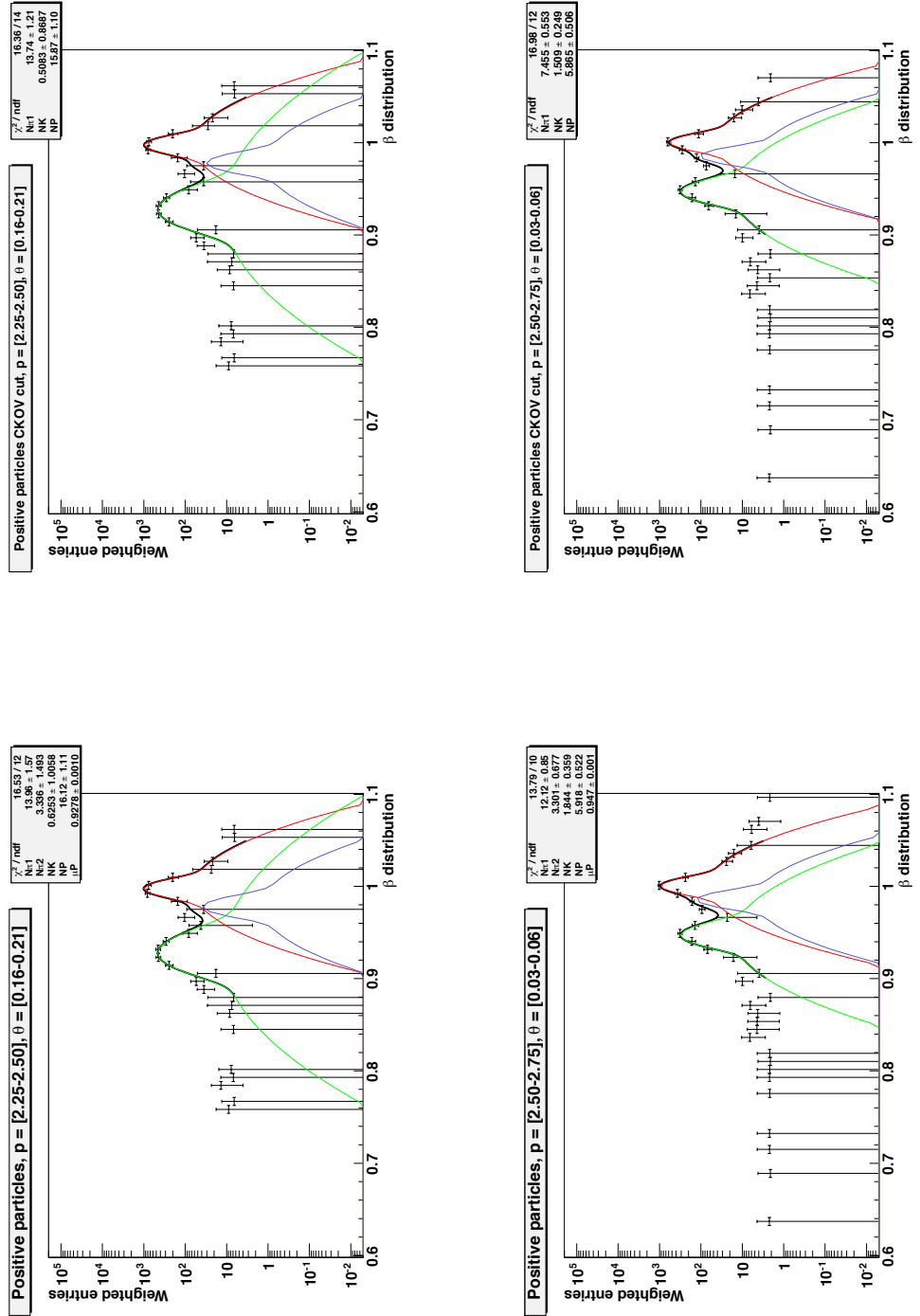
Figure C.12: *β* spectra fitted according to the method presented in Section 4.8. The reconstructed momentum and angle range of each fit is indicated on the panel. Left panel: all inclusive particles. Right panel: corresponding spectrum fit following the Cherenkov cut method (Section 4.8.1)

Figure C.13: *β* spectra fitted according to the method presented in Section 4.8. The reconstructed momentum and angle range of each fit is indicated on the panel. Left panel: all inclusive particles. Right panel: corresponding spectrum fit following the Cherenkov cut method (Section 4.8.1)
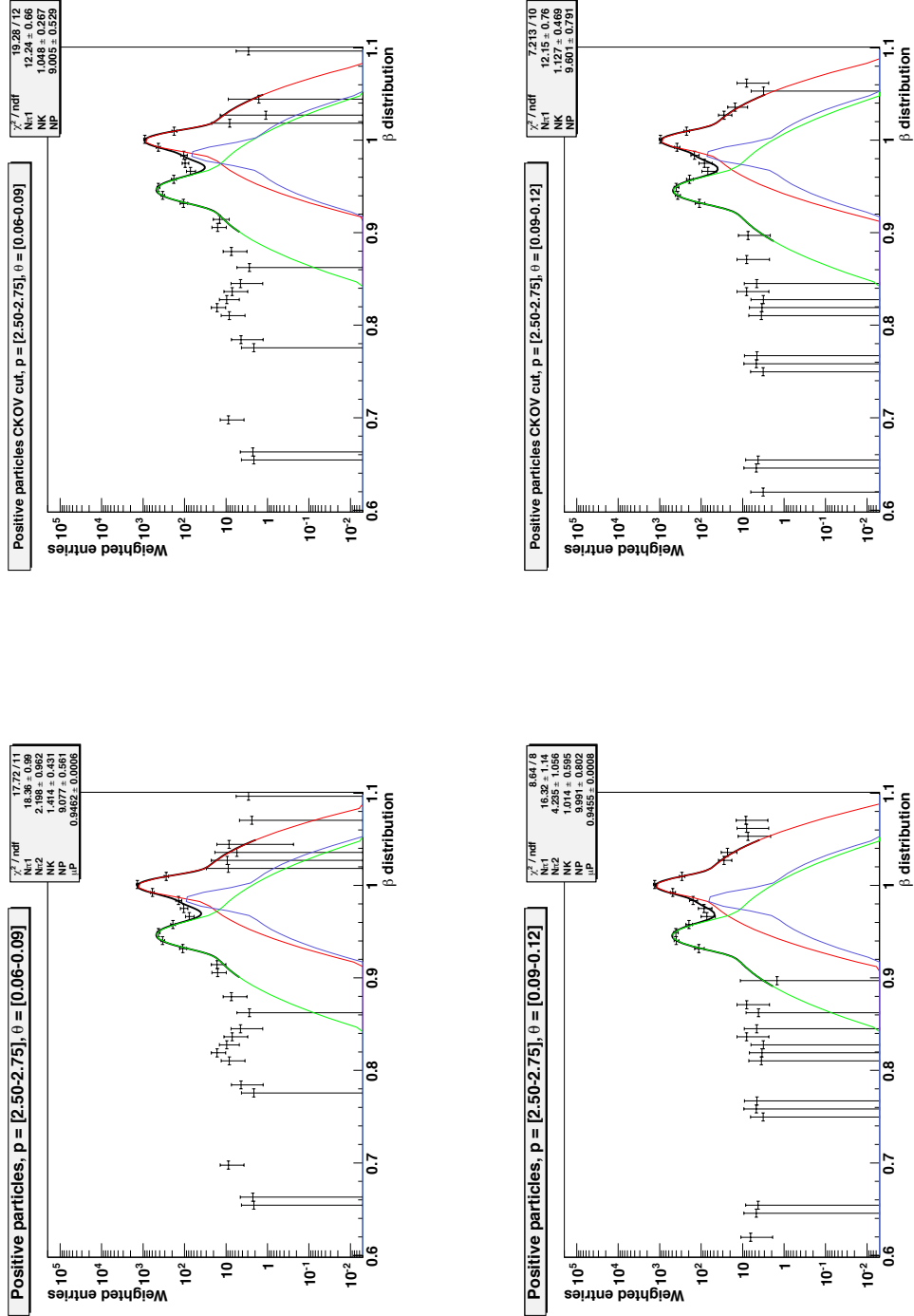
Figure C.14: β spectra fitted according to the method presented in Section 4.8. The reconstructed momentum and angle range of each fit is indicated on the panel. Left panel: all inclusive particles. Right panel: corresponding spectrum fit following the Cherenkov cut method (Section 4.8.1)
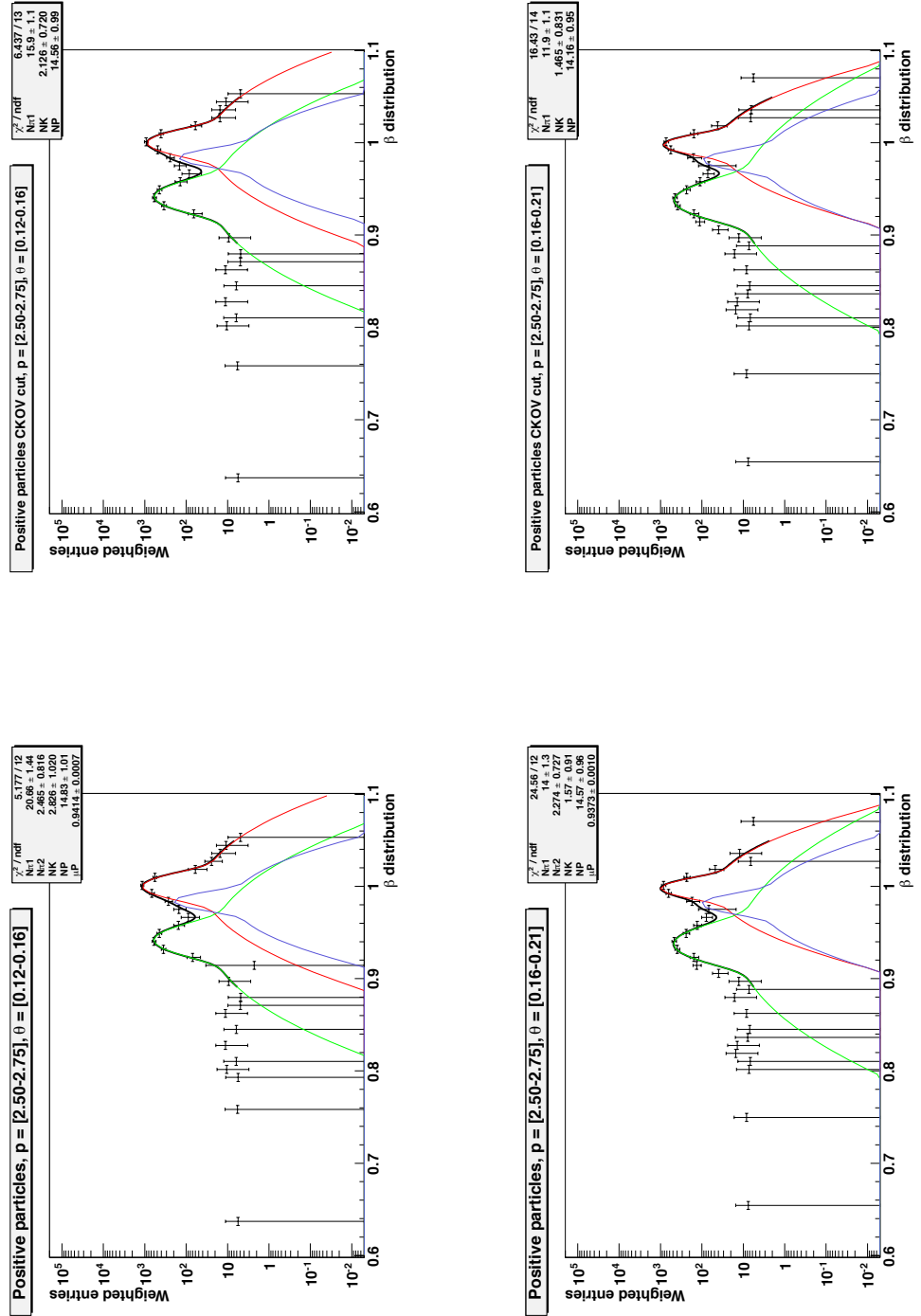
Figure C.15: *β* spectra fitted according to the method presented in Section 4.8. The reconstructed momentum and angle range of each fit is indicated on the panel. Left panel: all inclusive particles. Right panel: corresponding spectrum fit following the Cherenkov cut method (Section 4.8.1)

Figure C.16: *β* spectra fitted according to the method presented in Section 4.8. The reconstructed momentum and angle range of each fit is indicated on the panel. Left panel: all inclusive particles. Right panel: corresponding spectrum fit following the Cherenkov cut method (Section 4.8.1)
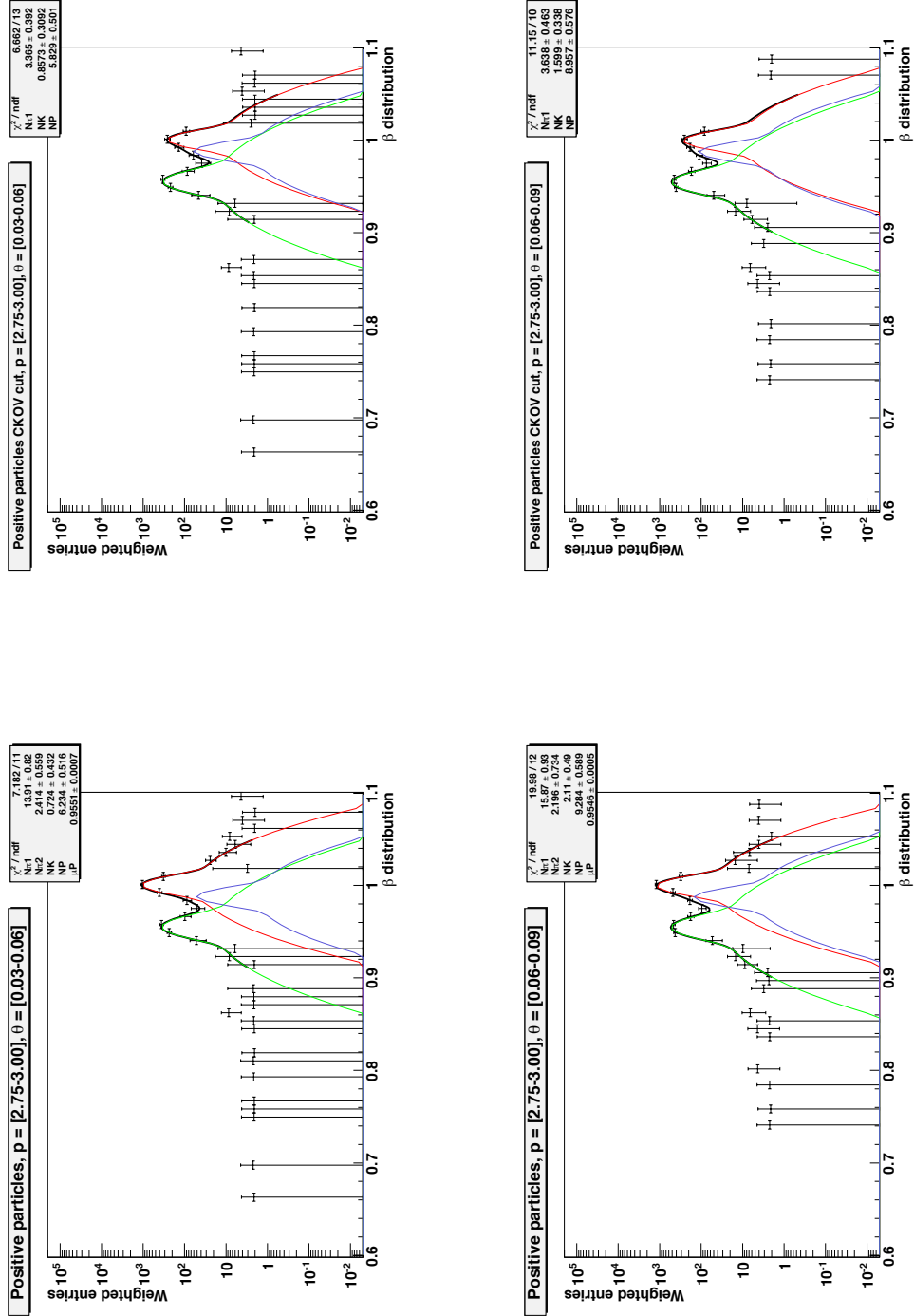
Figure C.17: β spectra fitted according to the method presented in Section 4.8. The reconstructed momentum and angle range of each fit is indicated on the panel. Left panel: all inclusive particles. Right panel: corresponding spectrum fit following the Cherenkov cut method (Section 4.8.1)
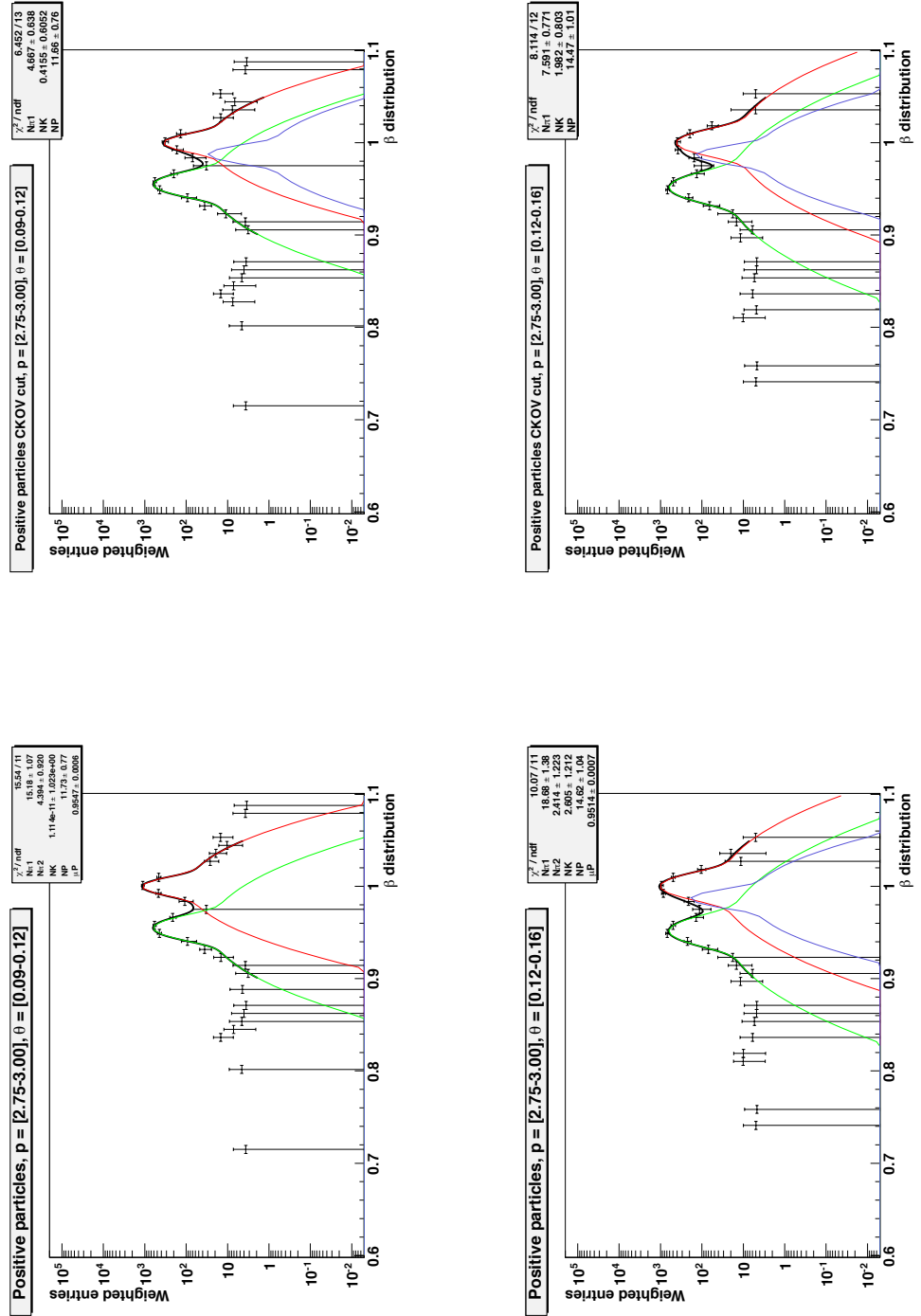
Figure C.18: *β* spectra fitted according to the method presented in Section 4.8. The reconstructed momentum and angle range of each fit is indicated on the panel. Left panel: all inclusive particles. Right panel: corresponding spectrum fit following the Cherenkov cut method (Section 4.8.1)

Figure C.19: *β* spectra fitted according to the method presented in Section 4.8. The reconstructed momentum and angle range of each fit is indicated on the panel. Left panel: all inclusive particles. Right panel: corresponding spectrum fit following the Cherenkov cut method (Section 4.8.1)
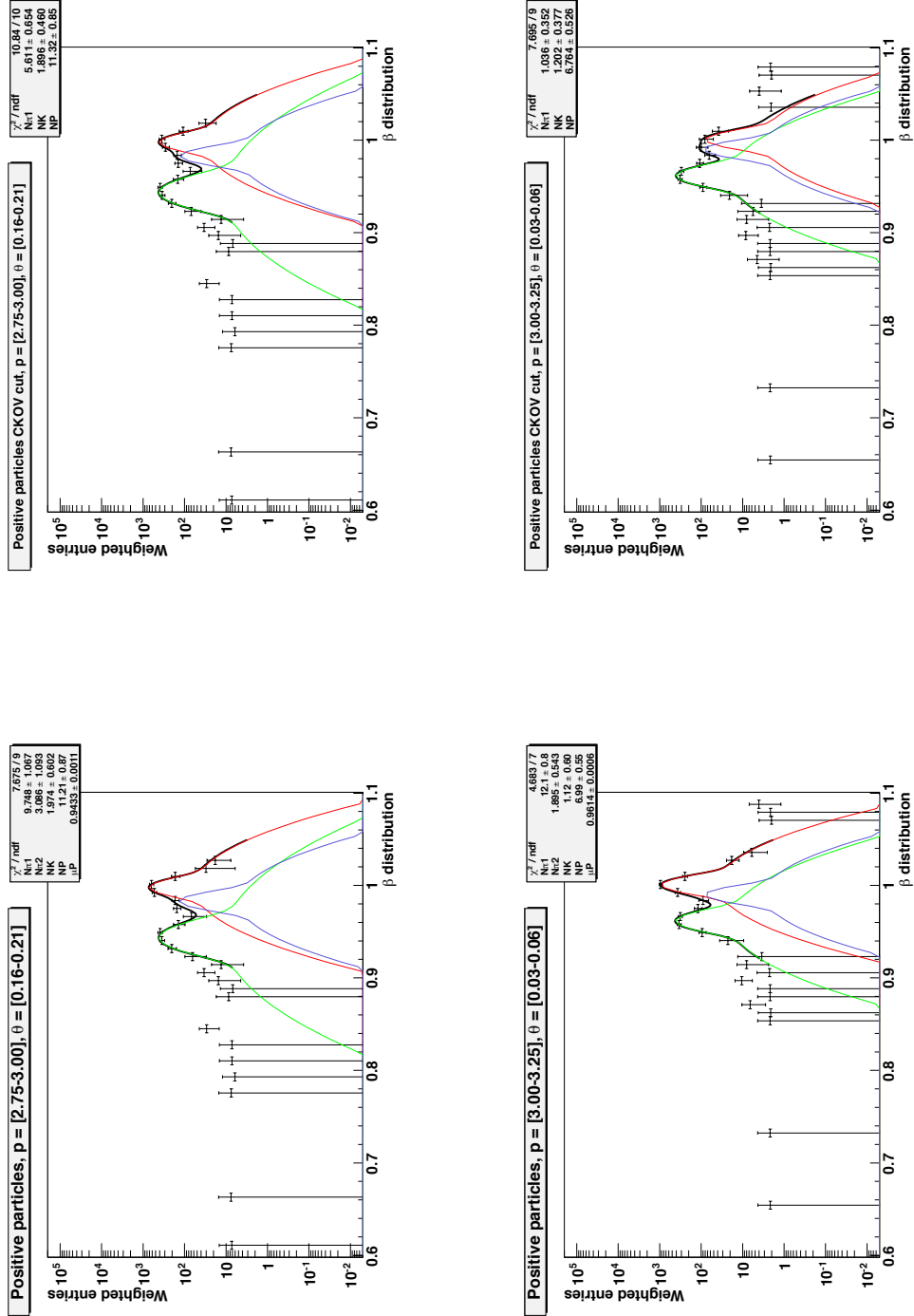
Figure C.20: β spectra fitted according to the method presented in Section 4.8. The reconstructed momentum and angle range of each fit is indicated on the panel. Left panel: all inclusive particles. Right panel: corresponding spectrum fit following the Cherenkov cut method (Section 4.8.1)
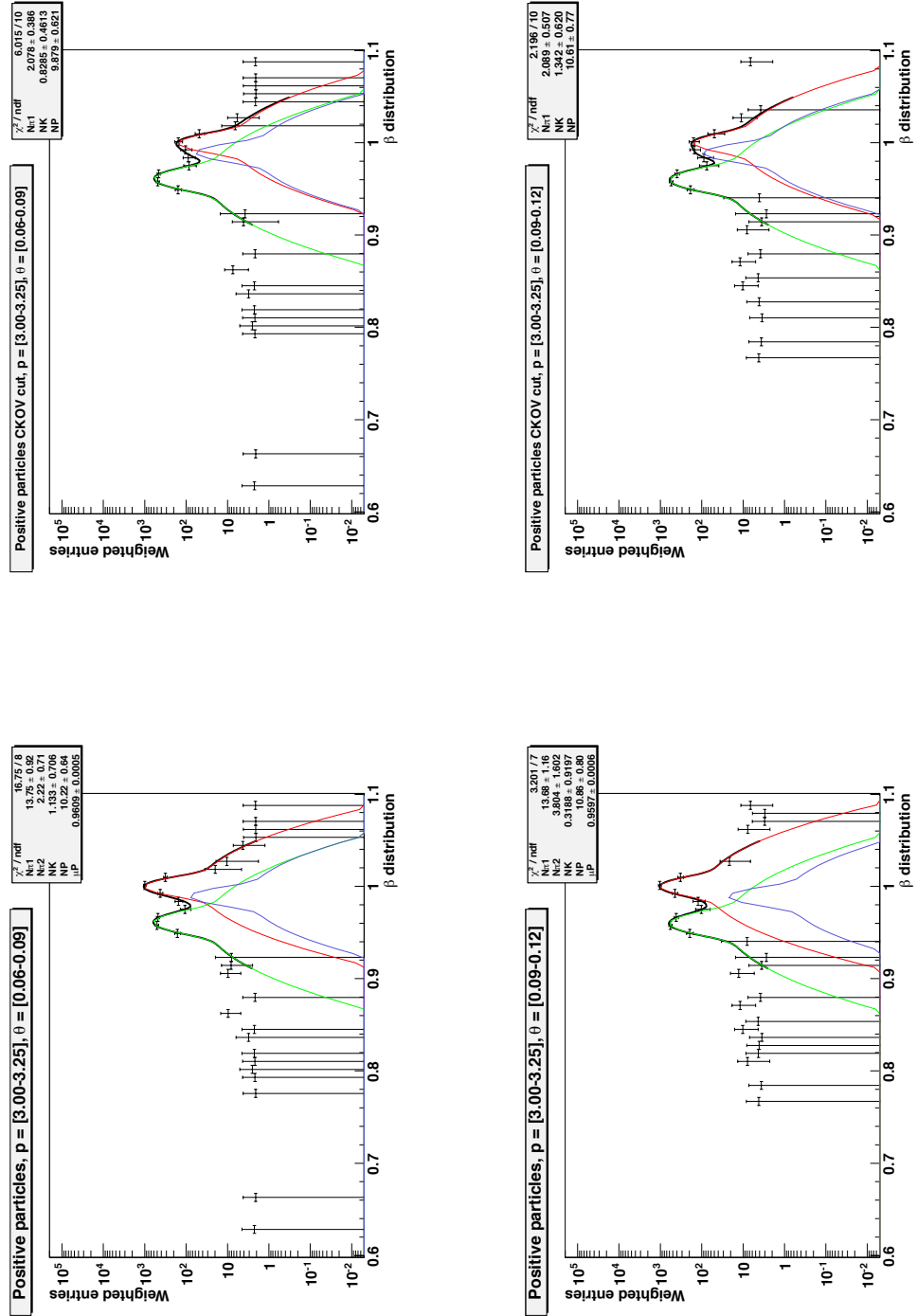
Figure C.21: *β* spectra fitted according to the method presented in Section 4.8. The reconstructed momentum and angle range of each fit is indicated on the panel. Left panel: all inclusive particles. Right panel: corresponding spectrum fit following the Cherenkov cut method (Section 4.8.1)

Figure C.22: β spectra fitted according to the method presented in Section 4.8. The reconstructed momentum and angle range of each fit is indicated on the panel. Left panel: all inclusive particles. Right panel: corresponding spectrum fit following the Cherenkov cut method (Section 4.8.1)
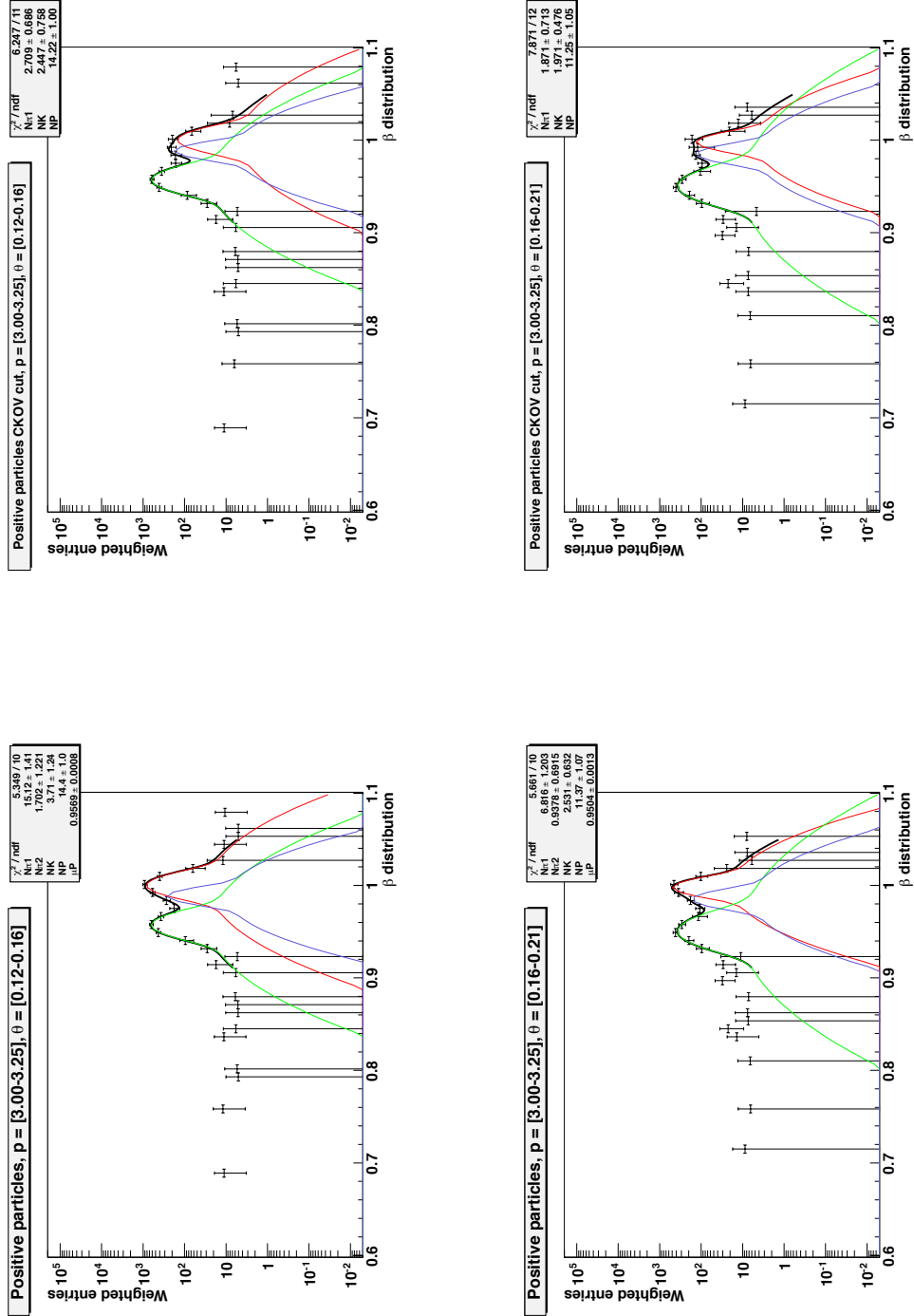
Figure C.23: *β* spectra fitted according to the method presented in Section 4.8. The reconstructed momentum and angle range of each fit is indicated on the panel. Left panel: all inclusive particles. Right panel: corresponding spectrum fit following the Cherenkov cut method (Section 4.8.1)
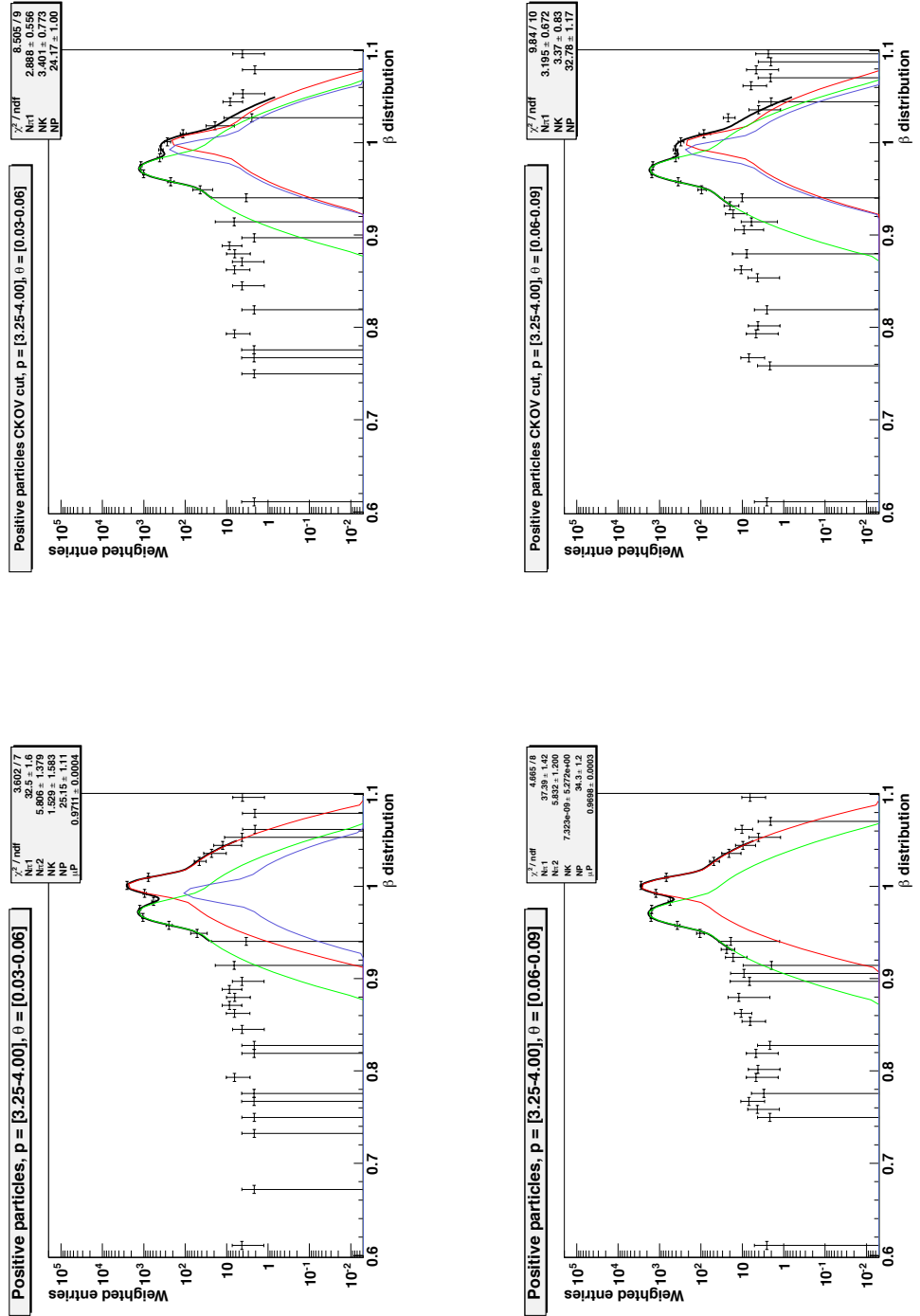
Figure C.24: β spectra fitted according to the method presented in Section 4.8. The reconstructed momentum and angle range of each fit is indicated on the panel. Left panel: all inclusive particles. Right panel: corresponding spectrum fit following the Cherenkov cut method (Section 4.8.1)

Figure C.25: *β* spectra fitted according to the method presented in Section 4.8. The reconstructed momentum and angle range of each fit is indicated on the panel. Left panel: all inclusive particles. Right panel: corresponding spectrum fit following the Cherenkov cut method (Section 4.8.1)
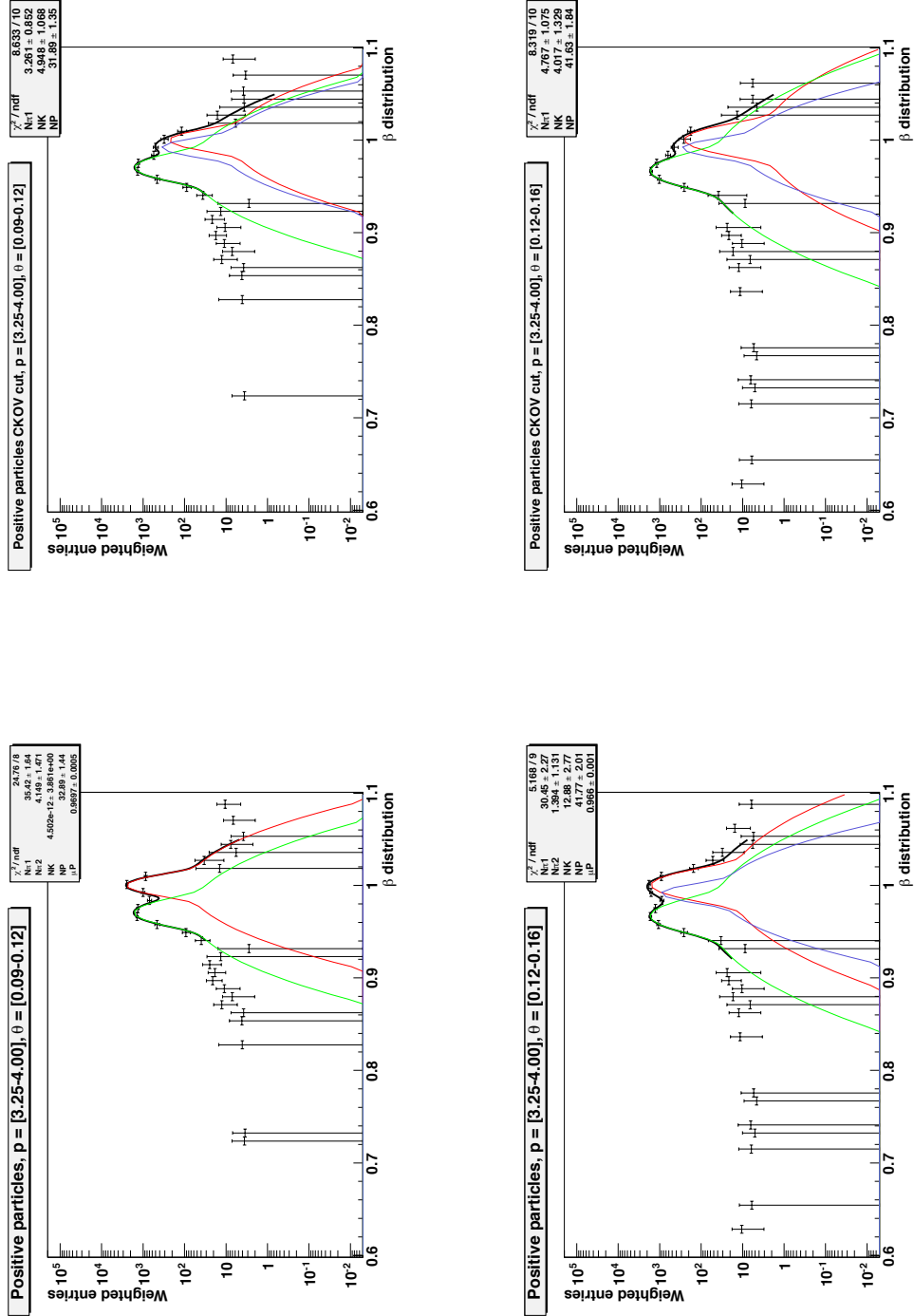
Figure C.26: *β* spectra fitted according to the method presented in Section 4.8. The reconstructed momentum and angle range of each fit is indicated on the panel. Left panel: all inclusive particles. Right panel: corresponding spectrum fit following the Cherenkov cut method (Section 4.8.1)
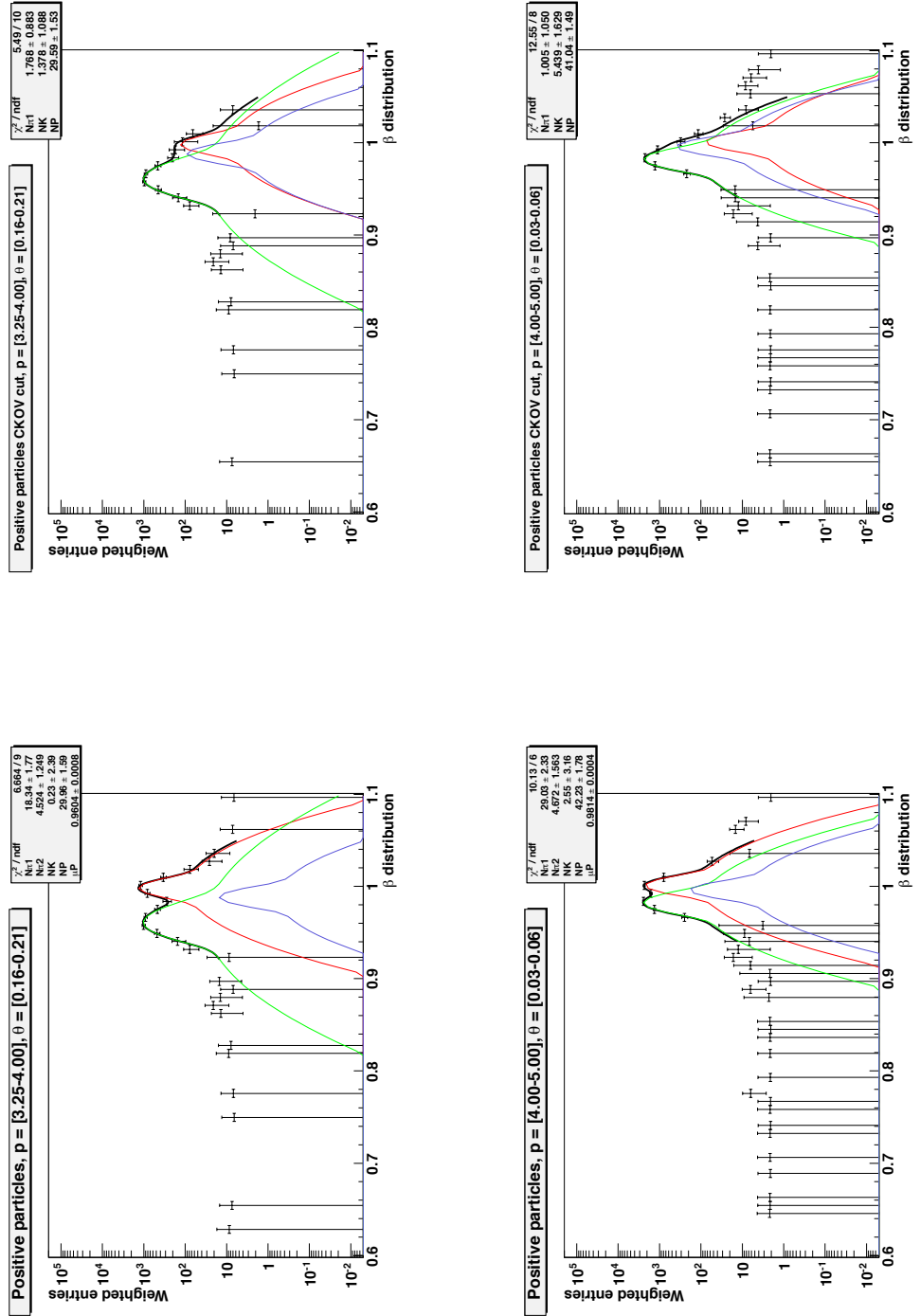
Figure C.27: *β* spectra fitted according to the method presented in Section 4.8. The reconstructed momentum and angle range of each fit is indicated on the panel. Left panel: all inclusive particles. Right panel: corresponding spectrum fit following the Cherenkov cut method (Section 4.8.1)

Figure C.28: *β* spectra fitted according to the method presented in Section 4.8. The reconstructed momentum and angle range of each fit is indicated on the panel. Left panel: all inclusive particles. Right panel: corresponding spectrum fit following the Cherenkov cut method (Section 4.8.1)
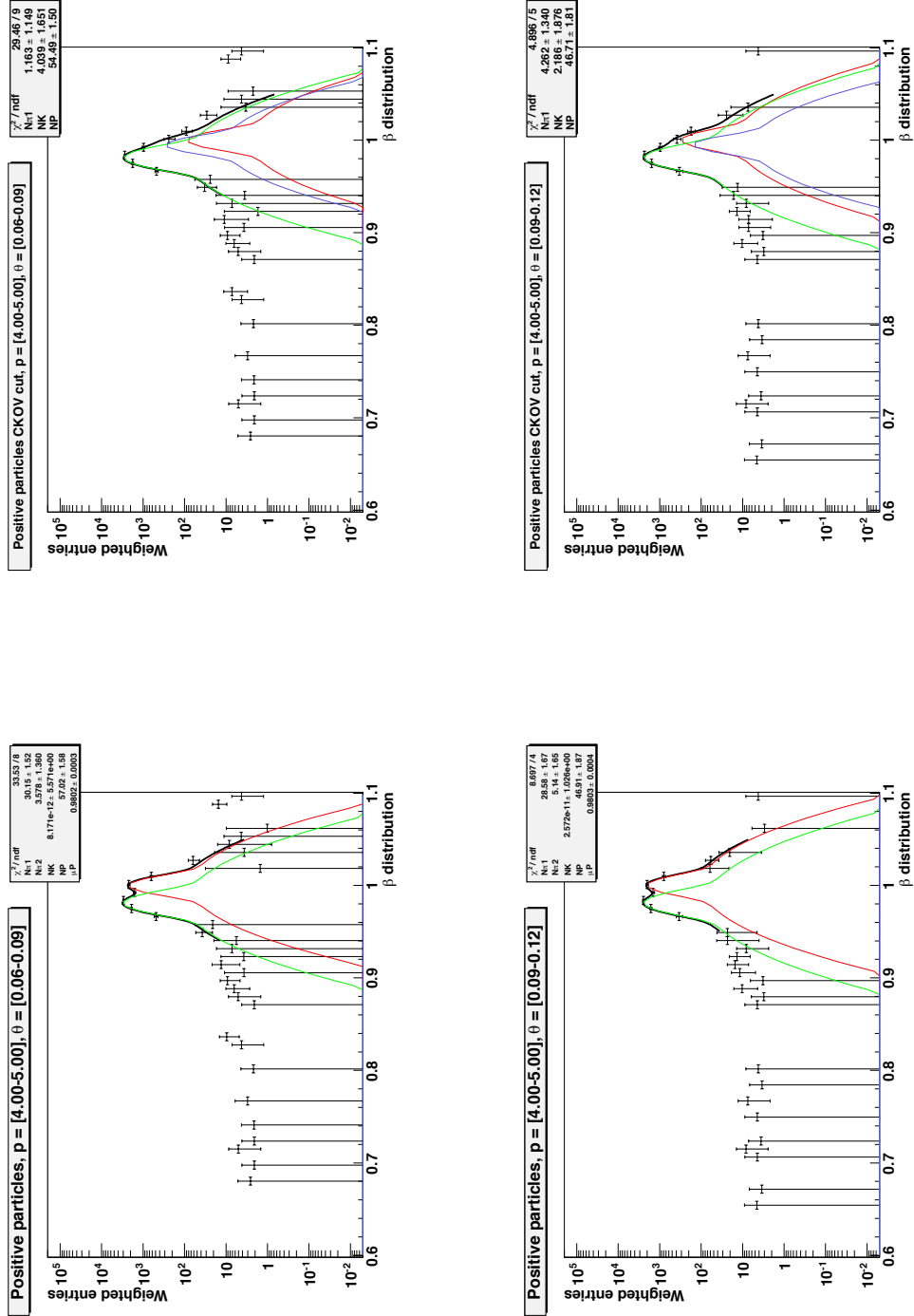
Figure C.29: *β* spectra fitted according to the method presented in Section 4.8. The reconstructed momentum and angle range of each fit is indicated on the panel. Left panel: all inclusive particles. Right panel: corresponding spectrum fit following the Cherenkov cut method (Section 4.8.1)
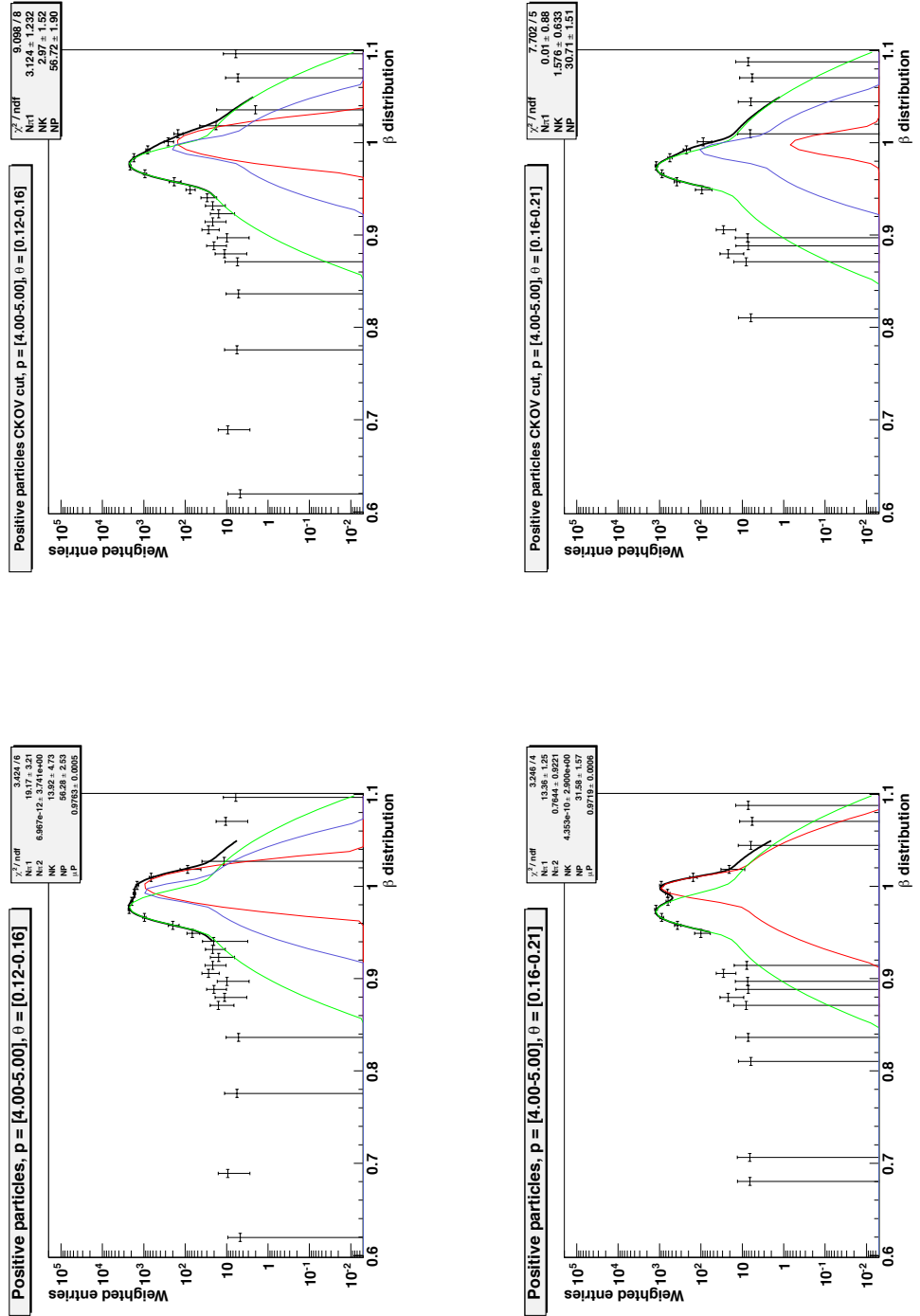
Figure C.30: *β* spectra fitted according to the method presented in Section 4.8. The reconstructed momentum and angle range of each fit is indicated on the panel. Left panel: all inclusive particles. Right panel: corresponding spectrum fit following the Cherenkov cut method (Section 4.8.1)